Towards an improved understanding of wind turbine wakes in complex terrain

Présentée le 3 juin 2024

Faculté de l'environnement naturel, architectural et construit
Laboratoire d'ingénierie éolienne et d'énergie renouvelable
Programme doctoral en mécanique

pour l'obtention du grade de Docteur ès Sciences

par

Arslan Salim DAR

Acceptée sur proposition du jury

Prof. F. Gallaire, président du jury
Prof. F. Porté Agel, directeur de thèse
Prof. J. Mann, rapporteur
Prof. R. B. Cal, rapporteur
Prof. K. Mulleners, rapporteuse

École
polytechnique
fédérale
de Lausanne

2024

To the loving memory of my father Salim,
to my mother Firdousia,
and to my brother Waqas.

Acknowledgements

Even though this thesis bears my name on the title, my academic journey leading to the Ph.D. and the work carried out within it could not have been possible without the support of numerous people. First and foremost, I would like to remember my father Salim Akbar Dar, who left us during the course of this Ph.D. He was the kindest person I have ever known and a role model of hard work, perseverance, and discipline. He encouraged me to pursue my dreams at every stage of my academic career, and always supported my academic endeavors. I would like to express my gratitude toward my thesis advisor Prof. Fernando Porté-Agel, who gave me the opportunity to work in his group. I have thoroughly enjoyed working with him during the course of my Ph.D. He provided me with the right environment to develop my research and with state-of-the-art experimental resources. He always made himself available for timely and useful discussions on conception of ideas, interpretation of results, and effective writing skills. His expertise and passion for research were pivotal to the success of my work. I would also like to thank the jury members of my oral exam, Prof. François Gallaire, Prof. Karen Mulleners, Prof. Jakob Mann, and Prof. Raúl Bayoán Cal, for taking the time to critically read the thesis, and for their insightful comments on the work.

My friends and colleagues at the WiRE laboratory have been instrumental in the successful completion of this thesis. Special thanks to Dara Vahidi and Guiyue Duan for being my office mates, for all the academic and non-academic discussions, and for all the laughs. I came to this lab without significant practical knowledge of experimental techniques, therefore I would like to acknowledge Haohua Zong and Vincent Rolin for teaching me the basics of conducting experiments and for offering their advice during my first experiments. I would also like to thank my friends at WiRE: Tristan Revaz, Marwa Souaiby, Mou Lin, Peter Brugger, Nicolas Kirchner-Bossi, Sina Shamsoddin, Jiannong Fang, and Konstantinos Kostarinis. A special thanks to all the students I had a chance to supervise and collaborate with over the course of my Ph.D.: Guillem Armengol Barcos, Abraham Starbuck Gertler, Fabien Waridel, and Stefano Elikplim Tamo. Working with them, I had a chance to learn the skills of supervision, management, and knowledge transfer. Their insightful questions at times forced me to learn new things and re-learn things I had already known.

Finally, I would like to thank the dearest and most important people in my life. My mother Firdousia Tasneem, who always encouraged me to pursue higher studies, supported my

Abstract

This work investigates how various terrain-induced flow phenomena such as flow separation, varying levels of flow shear, and pressure gradient, impact the wake and performance of wind turbines. We use a combined experimental and analytical approach to study wind turbines in different complex terrains.

In the first part, wake of a wind turbine sited on an escarpment is investigated. We test five distinct escarpment shapes, ranging from forward-facing steps (FFS) to ramp-shaped designs. Flow separation at the leading edge of FFS escarpments induces high turbulence, resulting in a faster wake recovery and higher turbulence kinetic energy in the turbine wake. A slight curvature of the leading edge significantly reduces turbulence in the wake, while ramp-shaped escarpments display slower wake recovery and lower turbulence. The shape of the escarpment also affects wake growth rate, meandering, and the behavior of tip and hub vortices.

Furthermore, we investigate the influence of wind direction over cliffs and its impact on wind turbine wakes. With the increase in the obliqueness in the wind direction, the flow becomes heterogeneous in the spanwise direction, causing spanwise recirculation. This development of spanwise recirculation in the base flow significantly affects the wake's shape, recovery, and deflection.

In the second part, we analyze the effect of terrain-induced pressure gradient on wind turbine wakes. We introduce an analytical model to account for the impact of pressure gradient on the velocity deficit in the near wake. This new model is coupled with an existing model for far wake evolution under pressure gradient conditions and applied to various escarpment shapes. Our model agrees well with the experimental data and outperforms existing models.

We systematically study the effect of pressure gradient on wind turbine wakes using linear ramps with different slopes to create a linear speed-up or slow-down in velocity. The wind turbine power coefficient increases under favorable pressure gradients (FPG) and decreases under adverse pressure gradients (APG). The wake's recovery, expansion, and transition from near to far wake exhibit a systematic relationship with the imposed pressure gradient. Additionally, we propose an analytical relation to estimate the length of the near wake under a pressure gradient. The analytical model for wake velocity deficit, along with the new relation for near wake length, successfully predicts the wake velocity deficits.

We expand this investigation into the cumulative wake of multiple turbines. The cumulative wake of multiple turbines is shown to be affected by the pressure gradient imposed by the

Abstract

upstream turbine(s). We propose a novel approach to model the cumulative wake velocity deficit of multiple turbines, considering the pressure gradient imposed by upstream turbines on downstream ones, eliminating the need for subsequent superposition of individual wakes. This approach seems to outperform a linear summation method for superposing individual wake velocity deficits and aligns well with the experimental data.

The third part of our research explores wind turbines within urban environment. We set up a cubic building surrounded by an urban canopy to install a roof-mounted turbine. We investigate the impact of roof edge shapes on the turbine's power generation and wake. Curved roof edges are found to yield the best performance, while a solid boundary fence around the roof leads to the worst performance. The shape of the roof edge also affects the turbine wake. Roof boundary fences are integral to the safety of the building. Therefore, we examine the influence of fence height, porosity, angle, and curvature on wind turbine performance. Higher fence heights negatively affect the turbine's power and thrust performance, while fences with more than 20% porosity significantly increase available power compared to solid fences. Inward-angled fences outperform outward ones, with a 60° inward angle delivering performance similar to a building with no fence. Similarly, inward curved fences enhance power generation and thrust, outperforming outward curved fences. Therefore, we recommend using angled and curved fences to enhance the performance of roof-mounted turbines.

Keywords: Wind energy, wind turbines, wakes, wind tunnel experiments, analytical modeling

Résumé

Ce travail explore comment divers phénomènes d'écoulement induits par le relief, tels que la séparation de l'écoulement, les niveaux variables de cisaillement de l'écoulement et le gradient de pression, affectent le sillage des éoliennes et leur performance. Nous utilisons une approche expérimentale et analytique combinée pour étudier les éoliennes dans différents terrains complexes.

Dans la première partie, le sillage d'une éolienne implantée sur un escarpement est étudié. Nous testons cinq formes d'escarpements distinctes, allant des marches orientées vers l'avant (FFS) aux design en forme de rampe. La séparation de l'écoulement au bord d'attaque des escarpements FFS provoque une forte turbulence, entraînant une récupération plus rapide du sillage de l'éolienne et une plus grande énergie cinétique turbulente dans le sillage. Une légère courbure du bord d'attaque réduit significativement la turbulence dans le sillage de l'éolienne, tandis que les escarpements en forme de rampe montrent un récupération plus lent du sillage et une turbulence plus faible. La forme de l'escarpement affecte également le taux d'expansion du sillage de l'éolienne, le méandre du sillage et le comportement des tourbillons de bout de pale et de moyeu.

De plus, nous examinons l'influence de la direction du vent sur les falaises et son impact sur les sillage des éoliennes. À mesure que la direction oblique du vent augmente, l'écoulement devient hétérogène dans la direction latérale, provoquant une recirculation dans la direction latérale. Ce développement de la recirculation dans l'écoulement de base affecte significativement la forme du sillage, sa récupération, et sa déflexion.

Dans la deuxième partie, nous analysons l'effet des gradient de pression induits par le relief sur les sillage des éoliennes. Nous introduisons un modèle analytique pour prendre en compte l'impact du gradient de pression sur le déficit de vitesse dans le sillage proche. Ce nouveau modèle est couplé à un modèle existant pour l'évolution du sillage lointain dans des conditions de gradient de pression et appliqué à différentes formes d'escarpements. Notre modèle concorde bien avec les données expérimentales et surpasse les modèles existants.

Nous étudions systématiquement l'effet du gradient de pression sur les sillage des éoliennes en utilisant des rampes linéaires avec différentes pentes pour créer une accélération ou un ralentissement linéaire de la vitesse de base. Le coefficient de puissance de l'éolienne augmente sous des gradients de pression favorables (FPG) et diminue sous des gradients de pression défavorables (APG). La récupération du sillage, son expansion et la transition du

Abstract

sillage proche au sillage lointain présentent une relation systématique avec le gradient de pression imposé. De plus, nous proposons une relation analytique pour estimer la longueur du sillage proche sous l'effet du gradient de pression. Le modèle analytique du déficit de vitesse du sillage, associé à la nouvelle relation pour la longueur du sillage proche, prédit avec succès le déficit de vitesse du sillage.

Nous étendons cette étude au sillage cumulatif de plusieurs éoliennes. Le sillage cumulatif de plusieurs éoliennes est affecté par le gradient de pression imposé par la (les) éolienne(s) en amont. Nous proposons une nouvelle approche pour modéliser le déficit de vitesse cumulatif du sillage de plusieurs éoliennes, en tenant compte du gradient de pression imposé par les éoliennes en amont sur les éoliennes en aval, éliminant ainsi la nécessité d'une superposition additionelle des sillages. Cette approche semble surpasser une méthode de sommation linéaire pour superposer les déficits de vitesse du sillage et concorde bien avec les données expérimentales.

La troisième partie de notre recherche explore les éoliennes dans des environnements urbains. Nous installons une éolienne sur le toit d'un bâtiment cubique entouré d'une canopée urbaine. Nous examinons l'impact de la forme du bord du toit sur la génération de puissance de l'éolienne et sur le sillage. Les bords de toit incurvés donnent les meilleurs résultats, tandis qu'une barrière de bordure solide autour du toit entraîne les moins bonnes performances. La forme du bord du toit affecte également le sillage de l'éolienne.

Les barrières du toit sont essentielles pour la sécurité du bâtiment. Par conséquent, nous étudions l'influence de la hauteur, de la porosité, de l'angle et de la courbure de la barrière sur les performances de l'éolienne. Les barrières plus hautes ont un impact négatif sur la puissance de l'éolienne, tandis que les barrières avec plus de 20% de porosité augmentent significativement la puissance disponible par rapport aux barrières solides. Les barrières inclinées vers l'intérieur surpassent celles inclinées vers l'extérieur, avec un angle de 60° vers l'intérieur offrant des performances similaires à un bâtiment sans barrière. De même, les barrières incurvées vers l'intérieur améliorent la génération de puissance et la poussée de l'éolienne par rapport à celles incurvées vers l'extérieur. Par conséquent, nous recommandons l'utilisation de barrières inclinées et incurvées pour améliorer les performances des éoliennes sur les toits.

Mots-clés : Énergie éolienne, éoliennes, sillages, expériences en soufflerie, modélisation analytique

Contents

List of Figures

List of Tables

1 Introduction

Climate change is one of the most pressing issues faced by mankind today. A major part of tackling climate change involves decarbonization of the energy sector. An ever-increasing demand for electricity with the increase in the world population and electrification of the energy sector further complicates the situation. In light of these challenges, renewable energy sources such as wind, solar, hydro, geothermal, tidal and biomass are increasingly being promoted to replace fossil fuel-based energy sources. According to the international renewable energy agency (IRENA), onshore wind energy together with solar energy are now cheaper and more economically viable than their fossil fuel counterparts (IRENA, 2021).

Wind is an abundant resource of energy, and is harvested mainly using wind turbines. A wind turbine extracts the kinetic energy from the wind and converts it into electrical energy. Wind energy has experienced an exponential growth in the last few decades, which is associated with the increase in the demand for clean energy, increase in the size of wind turbines, and continued improvements in the aerodynamic design of wind turbines. By the end of 2022, the total installed wind energy capacity stood at 906 GW (GWEC, 2023). However, it is also estimated that the current growth of wind energy is below the target set to achieve net zero emissions by 2030 (GWEC, 2023). Therefore, an acceleration in the growth of wind energy sector can very well be expected over the next decade.

Onshore wind energy currently dominates the wind energy market with a 93% share in the global installed wind energy capacity. In the onshore environment, wind turbines are often sited in complex, non-flat topography (Alfredsson and Segalini, 2017). Flow in topography exhibits several complex features such as varying levels of flow shear and turbulence, localized flow structures, and terrain-induced pressure gradients. This makes wind resource assessment in a complex terrain a challenging task. In modern days, wind energy is harvested mainly from wind farms, which comprise several wind turbines sited in close proximity to each other. As wind flows through a wind farm, the upstream-most turbines extract the most kinetic energy from the wind and generate a low-speed and high-turbulence region known as a wake behind them. As the inter-turbine spacing in a wind farm is finite (typical spacing values range between 3 to 10 rotor diameters), downstream turbines often experience the wake

of the upstream ones. This means that the turbines exposed to the wake flow have lesser available power and experience higher fatigue loads compared to the turbines exposed to the undisturbed flow.

Understanding how wind turbines interact with the atmospheric boundary layer flow is identified as a grand challenge in the expansion of wind energy (Veers et al., 2019). The characteristics of wind turbine wakes are significantly affected by the atmospheric conditions and terrain features. The development of wind turbine and wind farm wakes in a flat terrain under a variety of atmospheric flow conditions such as flow shear, Coriolis force, and thermal stratification have been explored in great detail in the literature (Porté-Agel et al., 2020; Stevens and Meneveau, 2017). The interaction between terrain-induced flow features and wind turbine wakes has recently gained attention from the scientific community. A brief review of some recent developments in the field of wind turbines in complex terrain is provided by Elgendi et al. (2023).

The current thesis is motivated by the lack of understanding of complex interactions between wind turbine wakes and topographical flows. In this thesis, we focus on three distinct types of complex terrains: (i) escarpments, which induce a flow speed-up, variable flow shear, and flow separation in some cases; (ii) linear ramps, which are used to impose a linear flow speed-up and slow-down; and (iii) urban environment, where the flow is significantly affected by the building morphology. The objective of this thesis is two-fold: to provide physical insights into the complex interactions between wind turbine wakes and topographical flows, and to advance analytical tools that provide computationally inexpensive but reliable estimates of wake velocity deficit in complex terrain. For this purpose, we carry out a series of experimental and analytical studies on wind turbines in complex terrain.

The rest of the thesis is structured as follows. The thesis is divided in three parts. The first part investigates wind turbine wakes on escarpments, and comprises three chapters: Chapter 2 provides a three-dimensional characterization of a wind turbine wake sited on two distinct escarpments; Chapter 3 characterizes the effect of escarpment shape on the wake of a wind turbine; and Chapter 4 explores the effect of wind direction on the flow over a cliff and its interaction with the wake of a wind turbine. The second part of the thesis deals with the effect of terrain-induced pressure gradient on the wake of a wind turbine. This part of the thesis also comprises three chapters: Chapter 5 validates an analytical framework to model wind turbines exposed to pressure gradient; Chapter 6 presents a systematic experimental and analytical study of wind turbines exposed to a pressure gradient; and Chapter 7 investigates the cumulative wake of multiple turbines exposed to a pressure gradient and validates an analytical approach to model these wakes. In the third part of this thesis, we focus on wind turbines in an urban environment. This part consists of two chapters: Chapter 8 investigates the effect of three different roof edge shapes on the power and wake of a roof-mounted wind turbine; and Chapter 9 presents a parametric study on the effect of roof boundary fence shape on the performance of a roof-mounted wind turbine. Finally, a summary of the thesis and some perspectives for future work are given in Chapter 10.

Part - I: Wakes on escarpments

2 Three-dimensional wind-turbine wake characterization via tomographic particle-image velocimetry [I]

Abstract

Wind turbines are often sited on different topographical features. In the current work, we performed wind-tunnel measurements of the wake behind a single wind turbine sited on two escarpments differing in the windward side shape using tomographic particle-image velocimetry. The escarpments are classified as forward facing step (FFS) and ramp-shape. The turbine sited on the FFS experiences an inflow with high flow shear and turbulence due to flow separation from the escarpment leading edge compared to the one on the ramp-shaped escarpment. As a consequence, the wake characteristics behind the turbine are strongly affected by the shape of the topography. The velocity deficit in the wake of the turbine is relatively higher in the forward facing step shape, but it also shows a faster recovery. The rotation of the wake is stronger for the turbine on the ramp-shaped escarpment, whereas the meandering of the wake is higher for the FFS case. The spatial coherence is observed to be higher in the near wake of the turbine sited on the FFS escarpment, while it is very similar in the far wake for both cases. Instantaneous vortices identified by the Q-criterion show that the development of tip and hub vortices is affected by the topography as well.

2.1 Introduction

Wind turbine wakes are characterized by highly complex three-dimensional flows due to the effects of boundary-layer flow shear, rotor rotation and multiple sources of vortex generation (Vermeer et al., 2003; Zhang et al., 2012). The development of these wakes is further dependent on different atmospheric conditions: thermal stratification, turbulence intensity and Coriolis force, to name a few (Abkar and Porté-Agel, 2016; Bhaganagar and Debnath, 2014; Chamorro and Porté-Agel, 2010; Vollmer et al., 2016). In complex terrain, the presence of different topographical features further complicates the three-dimensional structure of wind turbine wakes. Understanding and quantifying these effects is, therefore, of great importance to predict wake effects in wind farms sited on topography (Fernando et al., 2019; Porté-Agel et al., 2020). The information on the three-dimensional evolution of the wind turbine wakes can be useful for accurate estimation of the flow experienced by downstream wind turbines. This can facilitate the optimization of the turbine placement in a wind farm and provide basis for accurate power and load predictions. The most common laboratory measurement techniques, such as hot-wire anemometry, laser-doppler velocimetry and two-component or stereoscopic particle-image velocimetry (PIV), however, only provide point or planar measurements.

Tomographic particle-image velocimetry (Elsinga et al., 2006) is a powerful technique that enables instantaneous flow measurements in a volume. The working principle behind the technique is briefly described in the following. The measurement volume filled with tracer particles is illuminated by a laser source. Multiple cameras are used to capture the light scattered by the particles from different angles. The numerical aperture of the cameras is increased in order to cover the depth of the measurement volume. A three-dimensional volume reconstruction is done from the acquired images using an iterative algebraic reconstruction technique. Finally, a three-dimensional cross-correlation is done on the reconstructed volume to obtain the velocity field. This technique has been proven useful to study three-dimensional flows, e.g., turbulent boundary layers (Elsinga et al., 2007) and trailing edge vortices (Ghaemi and Scarano, 2011). The application of the technique for wind turbine wakes on topography is yet to be explored (to the best of the authors' knowledge).

In this study we attempt to characterize the three-dimensional flow field behind a single wind turbine sited on two different topographical features, namely, escarpments with a different windward side shape. The objective is to highlight the differences in the wake development that arise solely due to the change in the shape of the escarpment.

The rest of the article is outlined as follows. The experimental setup is presented in section 2.2. The two cases are analyzed in section 2.3. Finally, a summary of the work is given in section 2.4.

2.2   Experimental Setup

The experiments are performed in the boundary-layer wind tunnel at the WIRE laboratory of EPFL. The wind tunnel has a test section of $28 \times 2.56 \times 2\ m^3$, and a 130 kW fan drives the flow in the closed-loop tunnel. A contraction with a 5:1 area ratio is present at the inlet of the test section. Due to the length of the test section a natural boundary-layer develops over the surface without any tripping mechanism. A three-bladed horizontal axis wind turbine model (Bastankhah and Porté-Agel, 2017a) with a rotor diameter of 15 cm and hub height of 12.5 cm is placed one rotor diameter downstream from the leading edge of the escarpment. The turbine model is operated at a tip speed ratio $\lambda \approx 3.8$, which corresponds to the maximum power coefficient of the turbine.

Two topography models are used for the current study. The models are escarpments differing in the shape of the leading edge of the model. The length and width of the models is 3 m and 2.5 m respectively. The height is equal to the turbine hub height, i.e. 12.5 cm. One escarpment model is characterized by a sharp 90° edge (referred to as forward-facing step), whereas the second model has a sinusoidal ramp shape at the leading edge (referred to as ramp-shape). The ramp shape z_r is computed using the following equation:

$$z_r(x) = \frac{1}{2}H[1 + cos(\frac{\pi x}{2L})], \tag{2.1}$$

where H is the escarpment height and L is the half-length of the ramp, equal to 1.25 times the height, resulting in a maximum slope of about 33°. Figure 2.1 shows the side view of the escarpment model shapes.
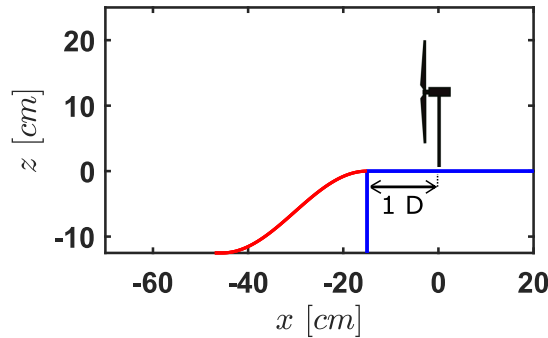
Figure 2.1: Side view of the topography leading edge. Blue: forward-facing step, and red: ramp-shaped escarpment.

The incoming velocity profile is characterized by a two-dimensional two-component (2D2C) PIV setup. The free stream velocity U_∞ is 4.37 ms^{-1}, whereas the velocity and streamwise turbulence intensity at the escarpment height are 3.55 ms^{-1} and 6% respectively. Figure 2.2 shows the incoming velocity and streamwise turbulence intensity profiles. The boundary layer thickness is 39 cm, and the roughness length and friction velocity are computed to be 0.04 mm and 0.17 ms^{-1} respectively.
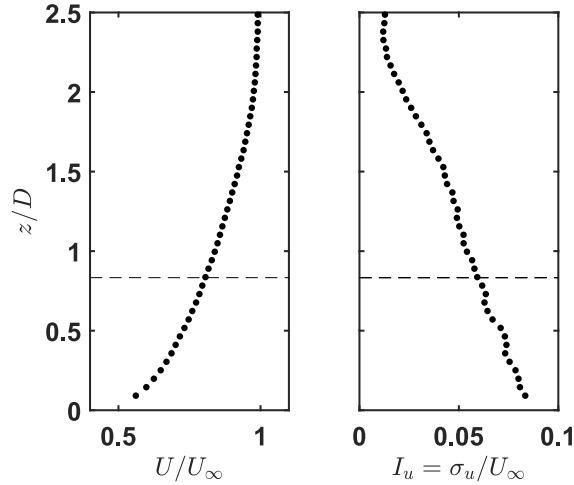
Figure 2.2: Vertical profiles of the normalized streamwise velocity (left) and streamwise turbulence intensity (right) in the upstream boundary-layer. The horizontal line indicates the projected topography height.

2.2.1 Tomographic particle-image velocimetry

A tomographic particle-image velocimetry system is used to measure the flow in a volume of $2D \times 2D \times 1.5D$ ($x \times y \times z$) at a spatial resolution of $0.023D$, where D is the rotor diameter. The camera setup consists of four 16-bit sCMOS cameras (2560×2160 pixels), mounted on Scheimpflug adapters with 55 mm objectives. To cover the depth of focus of the target volume, the aperture of the objectives is set to $f/16$ (with f being the focal length), and the center of the focal depth is aligned with the center of the illuminated volume. A double-pulse 435 mJ Nd:YAG laser is used as the laser source, and a combination of converging and diverging lenses is used to expand the laser beam into a volume. A helium-filled soap bubble generator system developed by LaVision is used to generate neutrally buoyant soap particles with a diameter on the order of 1 mm. The soap bubbles produced this way are much brighter compared to the conventional oil/aerosol particle seeding methods and facilitate PIV measurements at low light intensity. The bubbles are injected into the flow using a fluid supply unit at approximately 15 m upstream of the measurement volume. Figure 2.3 shows a schematic representation of the tomo-PIV setup.

A target calibration using a 3D calibration plate developed by LaVision is initially conducted, where images at five equidistant planes within the target volume are used. Following the physical calibration, images are acquired at a sampling rate of 10 Hz and a total of 1000 image pairs are used to obtain the ensemble averaged flow field. The captured images are pre-processed by subtracting a sliding minimum over each 3 pixels, normalizing with a local average over 50 pixels and, finally, performing a Gaussian smoothing over a 3×3 pixel window. The physical calibration is further improved by a self-calibration method (Wieneke, 2008), following which the volume reconstruction is done. A multiplicative algebraic reconstruction technique (MART) (Herman and Lent, 1976) is used for this purpose. For the current study, we
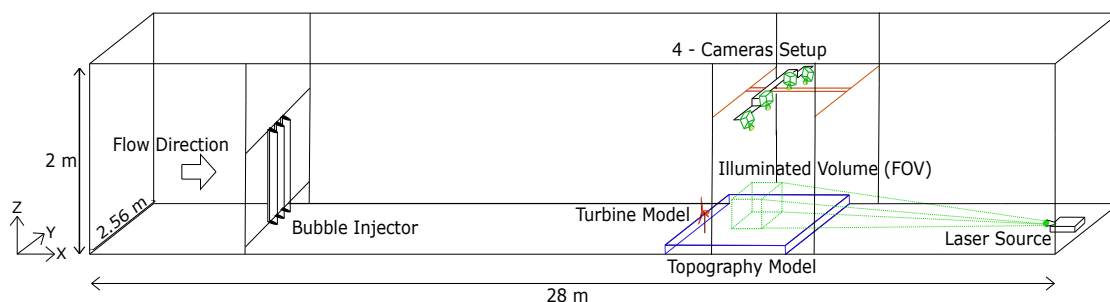
Figure 2.3: Schematic representation of the tomographic PIV setup.

perform six MART iterations for each volume reconstruction. The quality of the reconstructed volume is ensured by maintaining the signal-to-noise ratio above 5. The reconstructed field is then used for volume correlation, which is done in three decreasing interrogation volumes from $96 \times 96 \times 96$ voxels to $64 \times 64 \times 64$ voxels to $48 \times 48 \times 48$ voxels. Each interrogation volume has 75% overlap and the correlation is obtained after two passes through each volume. A total of three fields of view are obtained for each case, and an overlap of approximately 10% is kept between different fields of view.

2.3 Results

2.3.1 Mean flow characteristics

We first focus on the mean characteristics of the wake behind the turbine. Figure 2.4 shows the normalized mean streamwise component of the flow velocity for the two cases. The hub height
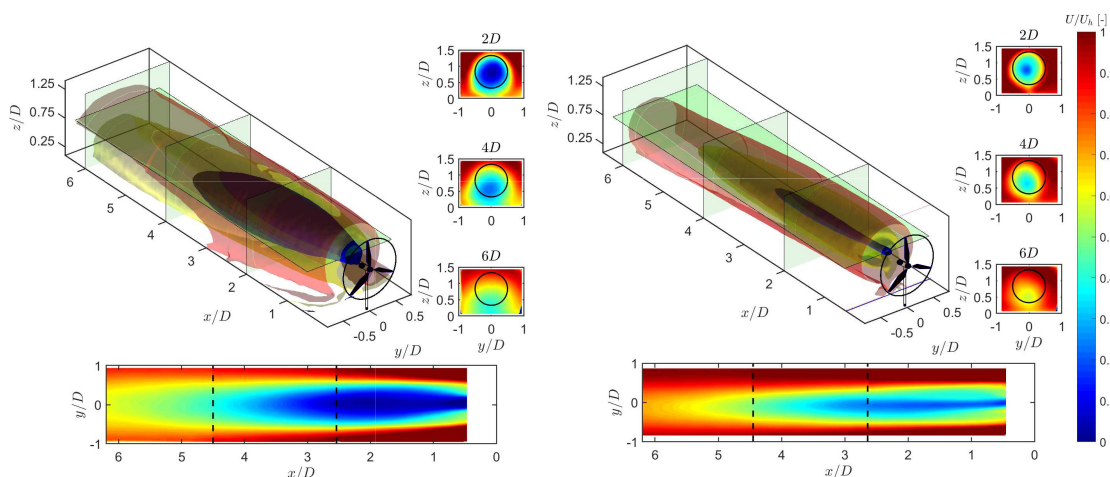
Figure 2.4: Normalized mean streamwise velocity component for the turbine sited on forward facing step (left) and ramp-shaped (right) escarpments. Isosurfaces correspond to: U/U_h=0.75 (red), U/U_h=0.5 (yellow) and U/U_h=0.25 (blue). Contour plots correspond to information extracted from highlighted planes in the three-dimensional plot.
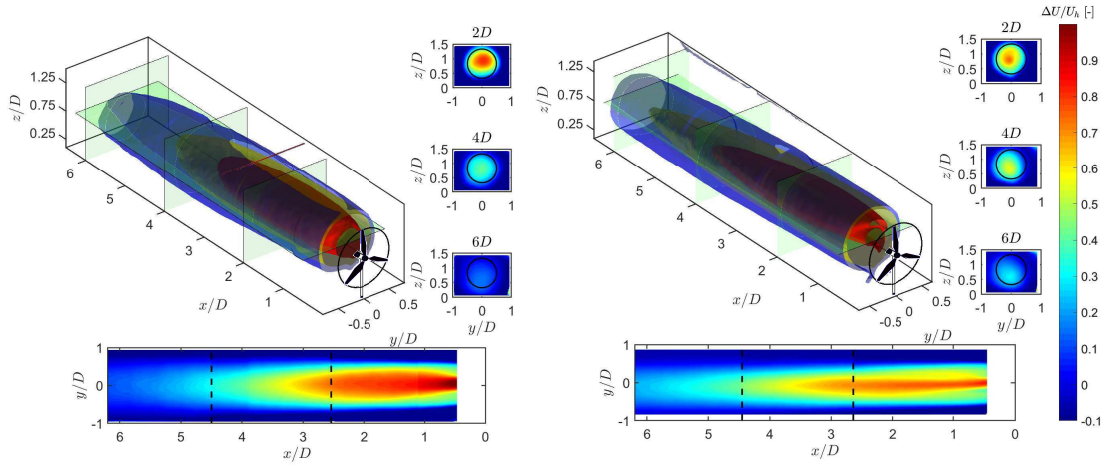
Figure 2.5: Normalized mean streamwise velocity deficit for the turbine sited on forward facing step (left) and ramp-shaped (right) escarpments. Isosurfaces correspond to: $\Delta U/U_h$=0.5 (red), $\Delta U/U_h$=0.3 (yellow) and $\Delta U/U_h$=0.1 (blue). Contour plots correspond to information extracted from highlighted planes in the three-dimensional plot.

streamwise velocity at the turbine location without the turbine U_h is chosen for normalization in respective cases throughout the article. Using isosurfaces, we isolate different features of the wake flow. In the case of the turbine on the FFS escarpment, the wake appears to be stronger and has a higher expansion rate compared to the one on the ramp-shaped escarpment. A downward shift in the wake position is also observed as it moves downstream. The shape of the wake is relatively more asymmetric for the turbine on the FFS escarpment than for the one on the ramp-shaped escarpment. This is because the shear induced by the FFS escarpment is higher than that induced by the ramp-shaped escarpment.

While the streamwise velocity component shows the combination of the wake and the ambient flow, the streamwise velocity deficit, computed as $\Delta U = U_{nw} - U_w$, is used to determine the effect of the turbine on the flow. Here, U_{nw} is the velocity without the turbine and U_w is the velocity in the presence of the turbine. In the current study, U_{nw} is obtained from stereoscopic PIV measurements and figure 2.5 shows the velocity deficit for the two cases. The isosurface corresponding to $\Delta U/U_h = 0.5$ encloses the region with high velocity deficit and is observed to be wider for the FFS case. This isosurface allows to identify the downstream location where the wake is recovered by 50%, which is around 3.65D and 4.35D for the turbine on the FFS and ramp-shaped escarpment, respectively. The location where the wake is recovered by 70% is shown by the yellow isosurface ($\Delta U/U_h = 0.3$), which also happens earlier for the turbine on the FFS compared to the one on the ramp-shaped escarpment. The blue isosurface ($\Delta U/U_h = 0.1$) shows the size of the wake itself, and is observed to be bigger for the FFS case. In general, the velocity deficit is comparatively higher for the turbine on the FFS escarpment, but it also exhibits a faster rate of recovery.

The information gained from the three-dimensional development of the streamwise velocity

can be used to estimate the power available for an in-wake turbine. To compare the power available in the wake of the turbine we use the following expression by Vollmer et al. (2016):

$$f_{AP} = \frac{1}{2}\rho \int_{y_1}^{y_2} \int_{z_1}^{z_2} U^3(y,z)dzdy, \tag{2.2}$$

where $y^2 + (z - z_h)^2 \leq (D/2)^2$ and z_h is the hub height of the turbine. The computed available power is then normalized by the reference $f_{AP,ref} = 1/2\rho AU_h^3$. Figure 2.6 shows a comparison of the normalized available power for the two escarpment cases. As can be seen, the available power is higher in the wake of the turbine sited on the ramp-shaped escarpment than in that on the FFS escarpment. For instance, at a downstream distance of 5 rotor diameters, the f_{AP} is almost double for the ramp-shaped escarpment case than for the FFS case. This indicates that a potential wind farm sited on the ramp-shaped escarpment could have a better power performance compared to a wind farm sited on the forward facing step escarpment.
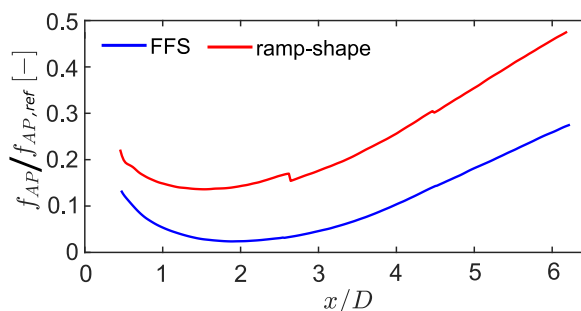
Figure 2.6: Comparison of the normalized available power in the turbine wake for the two escarpment cases.

We now compare the strength of the wake rotation in the two cases. Figure 2.7 shows the streamlines tracking mean flow from different initial points, overlaid by the in-plane velocity vectors at different planes parallel to the rotor plane. Comparing the two cases, the wake rotation is relatively stronger for the turbine sited on the ramp-shaped escarpment. It also lasts a longer distance for the turbine on the ramp-shaped escarpment than for the one on the FFS escarpment. The relatively weaker rotation of the wake behind the turbine sited on the FFS escarpment can be associated with higher turbulence in the inflow originating from the separated flow from the leading edge of the escarpment. In the far wake, the entrainment of outer flow into the wake can be observed around the rotor top, which plays a role in the recovery of the wake. In order to understand the trajectory of the wake, the streamlines tracking the mean flow are discussed here. We first look at the streamlines numbered 1-4 in figure 2.7 side panels. The streamlines 1,2 originate around the bottom left of the rotor and the streamlines 3,4 initiate from the upper right part of the wake. These streamlines show a higher deflection from the wake center with the increase in downstream distance for the turbine on the FFS escarpment compared to the one on the ramp-shaped escarpment. This can be associated with the size of the wake observed in figure 2.4 and indicates that the wake has a comparatively higher expansion rate in the FFS case. Another important observation is

the downward trajectory of the streamlines, showing a downward motion of the wake with downstream distance. This downward motion is higher for the turbine on the FFS escarpment, which shows that the wake gets more attached to the surface in this case compared to the case of the ramp-shaped escarpment.
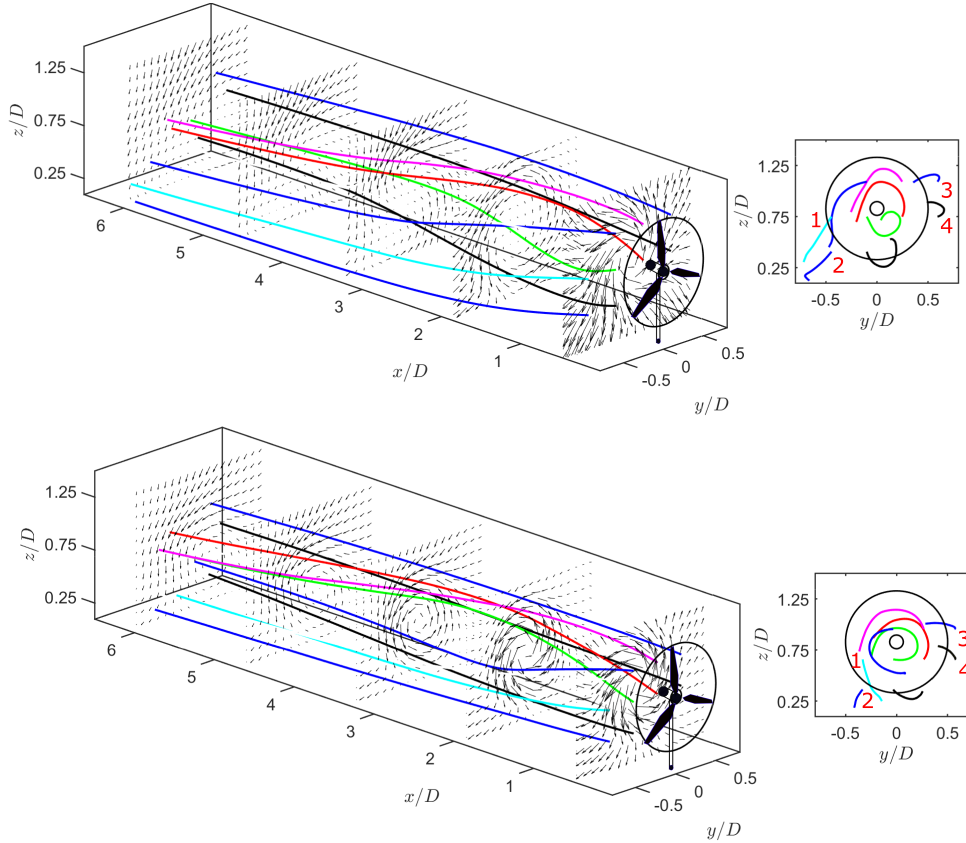
Figure 2.7: Streamlines tracking the mean flow trajectory in the wake of the turbine sited on forward facing step (top) and ramp-shaped (bottom) escarpments. In-plane velocity vectors are displayed at selected planes parallel to the rotor plane. Side panels show the front view of the three-dimensional plot.

2.3.2 Dynamic characteristics

The difference in the ambient flow conditions the turbine is exposed to in the two escarpment cases has an effect on the dynamic wake characteristics. Herein this section we study the wake meandering, flow coherence and vortical structures from the tomo-PIV measurements.

Meandering is an important dynamic characteristic due to its implications for the fluctuating loads on the downwind turbines. Here, we characterize the magnitude of the meandering motions using the three-dimensional distribution of the instantaneous streamwise velocity minimum (Howard et al., 2015). To obtain a smooth meandering profile, a spatial moving average filter with a window length of 0.5D is applied on the instantaneous streamwise velocity
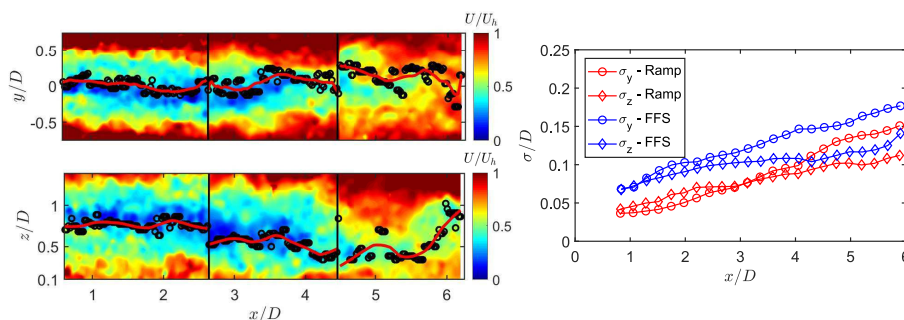
Figure 2.8: Left panel: instantaneous streamwise velocity contours in the lateral and vertical planes passing through the turbine hub and centerline, respectively, for the ramp-shaped escarpment case. The projections of the three-dimensional distribution of the streamwise velocity minimum and spatially filtered meandering profile on two-dimensional planes are represented by black circles and red line, respectively. Different fields of view are separated by the black vertical lines. Right panel: normalized standard deviation of the Gaussian fit to the spatially filtered instantaneous streamwise velocity minimum as a function of the downstream distance.

minimum. The size of the window length is chosen such as to remove the effect of the small scale velocity fluctuations, meanwhile maintaining the coherent structure of the meandering motion. An example of the obtained meander profile in three separate time instants (one for each field of view) for the turbine on the ramp-shaped escarpment is shown in figure 2.8 (left panel).

Figure 2.9 shows the distribution of the spatially filtered instantaneous streamwise velocity minimum for the two escarpment cases. The magnitude of meandering is observed to increase with the downstream distance, and the instantaneous velocity minimum distribution shows a downward trajectory for both cases. To characterize the increase in meandering with the downstream distance, we plot the normalized standard deviation of the Gaussian fit to the lateral and vertical instantaneous streamwise velocity minimum distribution in figure 2.8 (right
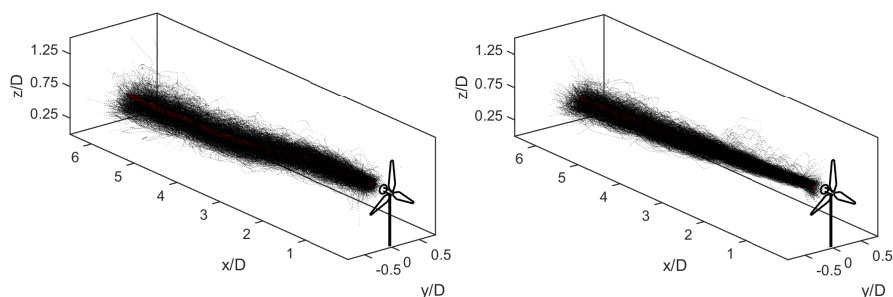
Figure 2.9: Three-dimensional distribution of the spatially filtered instantaneous streamwise velocity minimum for the turbine sited on the forward facing step (left) and ramp-shaped (right) escarpments.

panel). In the near wake, the lateral and vertical standard deviations are very close to each other for the respective cases. The difference in these standard deviations, however, increases with the increase in downstream distance with the lateral standard deviation showing higher values than the vertical one. Comparing the two escarpment cases, the turbine on the FFS escarpment shows higher standard deviation values, both in the vertical and lateral direction than the turbine on the ramp-shaped escarpment. This shows that the meandering of the turbine wake is higher when it is sited on the FFS escarpment than when it is sited on the ramp-shaped escarpment. This can be related to the higher turbulence and unsteadiness in the incoming flow for the turbine on the FFS than for the one on the ramp-shaped escarpment.

The spatial coherence of the streamwise velocity fluctuations is investigated using two-point spatial correlation in a three-dimensional space. The spatial correlation is computed for the streamwise velocity fluctuation component as follows:

$$R_{uu} = \frac{\overline{u'(x_{ref}, y_{ref}, z_{ref}) u'(x, y, z)}}{\sqrt{\overline{u'(x_{ref}, y_{ref}, z_{ref})^2} \times \overline{u'(x, y, z)^2}}}, \tag{2.3}$$

where $u'(x_{ref}, y_{ref}, z_{ref})$ is the reference indicated by black points in the isosurface plots shown in figure 2.10. In general, the spatial coherence is small for the region closest to the turbine and it increases with increasing downstream distance. In the near wake region of the two cases, the spatial coherence is observed to be higher for the turbine on the forward facing step escarpment, whereas in the far wake it is similar for both cases. As discussed by Bastankhah and Porté-Agel (2017b), the spatial coherence in the near wake is influenced by the shear layer developed around the turbine nacelle. The small coherence observed in the near-wake of the turbine on the ramp-shaped escarpment is found to be consistent with the fact that the shear layer developed around the turbine nacelle is stronger in this case compared
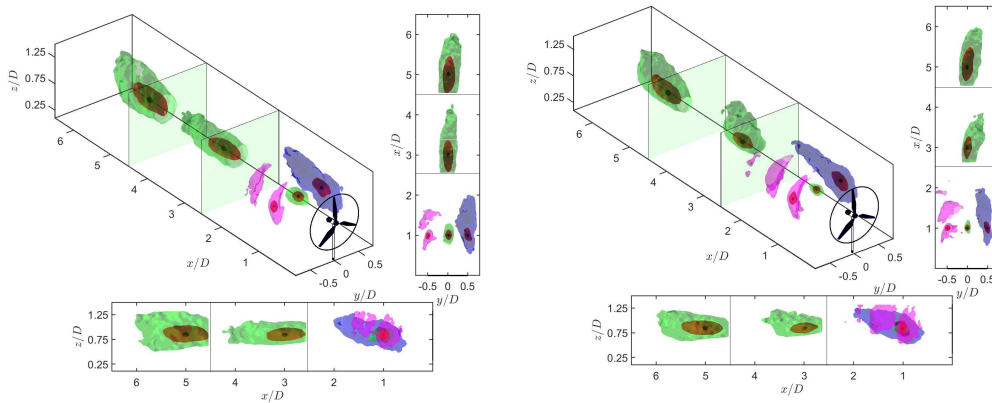
Figure 2.10: Two-point spatial correlation of the streamwise velocity fluctuations at different spatial locations for the turbine sited on the forward facing step (left) and ramp-shaped (right) escarpments. The isosurfaces correspond to $R_{uu} = 0.95$ (black) (location of the reference point), $R_{uu} = 0.5$ (red) and $R_{uu} = 0.25$ (green, magenta, purple). Green planes separate consecutive fields of view.
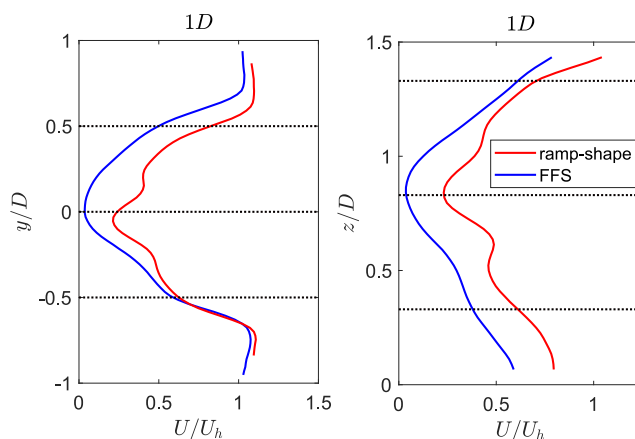
Figure 2.11: Lateral (left) and vertical (right) profiles of the normalized mean streamwise velocity component at a downstream distance of 1 rotor diameter. The horizontal black lines show rotor tips and hub locations.

to the one of the turbine on the FFS (see figure 2.11).

Vortices generated by the rotor blades and the hub are an important dynamic characteristic of the turbine wake. To identify vortices in the instantaneous three-dimensional field we use Q-criterion, which quantifies the relative amplitude of the rotation rate and strain rate, revealing the vortex cores. The Q-criterion is computed as follows:

$$Q = \frac{1}{2}(||\Omega_{ij}||^2 - ||S_{ij}||^2),\tag{2.4}$$

where $\Omega_{ij} = \frac{1}{2}(\frac{\partial u_i}{\partial x_j} - \frac{\partial u_j}{\partial x_i})$ is the vorticity tensor, $S_{ij} = \frac{1}{2}(\frac{\partial u_i}{\partial x_j} + \frac{\partial u_j}{\partial x_i})$ is the strain rate tensor and $||.||$ represents the Euclidean norm (Haller, 2005). Figure 2.12 shows the isosurface plots
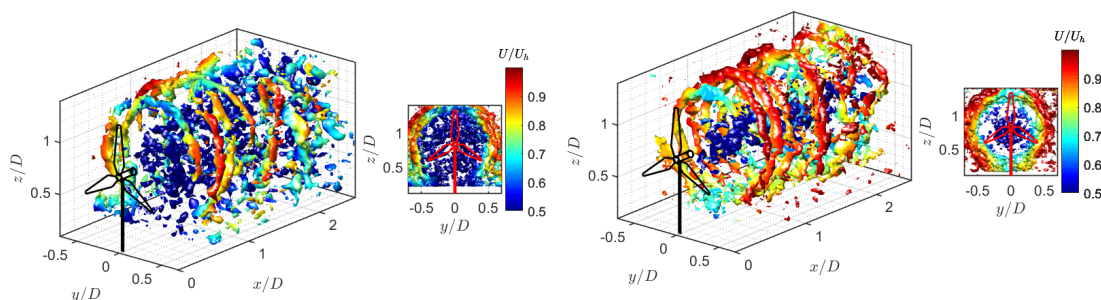
Figure 2.12: Isosurfaces of the normalized instantaneous Q-criterion ($QD^2/U_h^2 = 5$) for the turbine sited on the forward facing step (left) and ramp-shaped (right) escarpments. The isosurfaces are colored by the instantaneous normalized streamwise velocity. Side panels show the front view of the three-dimensional plot.

of the normalized instantaneous Q-criterion for the two cases, colored by the normalized instantaneous streamwise velocity. Individual spirals from the tip vortices can be identified in the near wake of the two cases. The helical shape of the tip vortices lasts up to a downstream distance of about 2 times the rotor diameter for the turbine on the FFS, beyond which breakdown of tip vortices happens. For the case of the turbine on the ramp-shaped escarpment, these tip vortices last up to 2.5D. The strength of the tip vortices is also higher for the turbine on the ramp-shaped escarpment compared to the one on the FFS. The weaker strength and earlier breakdown of the tip vortices in the FFS case can be associated with the relatively higher turbulence in the inflow compared to the case of the ramp-shape. Another important observation is the hub vortex, which is broken in the forward facing step case but is still intact in the near wake of the turbine on the ramp-shaped escarpment. The broken hub vortex in the FFS case can be seen hitting the tip vortices, which also plays a role in the reduced strength and breakdown of the tip vortices in this case.

2.4   Summary

Experimental observations of complex three-dimensional flows in a volume are a powerful tool to understand the spatial development of such flows. In the current work, we performed tomographic particle-image velocimetry for a single turbine wake sited on two different topographical features: a forward facing step and a ramp-shaped escarpment. The two topographies induced different levels of flow shear and turbulence which eventually had a strong influence on the wake characteristics of the turbine sited on them. Focusing on mean flow characteristics, we highlighted key differences in the development of the turbine wake caused primarily by the difference in the shape of the topography. The wake showed a higher velocity deficit for the turbine on the forward facing step escarpment, but also recovered quicker compared to the one on the ramp-shaped escarpment. The rotation of the wake was found to be comparatively stronger for the turbine on the ramp-shaped escarpment. Extending the analysis to the dynamic wake characteristics, the wake meandering was observed to be stronger for the turbine wake on the FFS escarpment due to higher turbulence in the inflow and unsteady nature of the flow separation from the leading edge of the escarpment. The spatial coherence was higher in the near wake of the turbine on the FFS escarpment which was associated with the shear in the flow, however it was similar in the far wake for both cases. Finally, we studied vortex shedding from the rotor tips and hub. The tip vortices shed by the turbine on the ramp-shaped escarpment lasted longer distance than by the turbine on the FFS escarpment. The hub vortex in the near wake was broken in the FFS case, whereas it was intact in the ramp-shaped escarpment case.

3 Wind turbine wakes on escarpments: A wind-tunnel study [I]

Abstract

In this study, the wake behind a wind turbine located on an escarpment is investigated using particle-image velocimetry in a wind tunnel. Five different escarpment models are used, which vary in the windward side shape from forward facing steps (FFS) with different curvatures at the leading-edge to sinusoidal ramp shapes with varying slopes. The difference in the base flow (flow without the turbine) resulting from the change in the geometry of the escarpment leads to significant differences in the average and dynamic characteristics of the turbine wake. The relatively high level of turbulence intensity in the base flow induced by the FFS escarpments leads to a faster wake recovery accompanied by higher turbulence kinetic energy, compared with the ramp-shaped ones. The self-similar behavior of the velocity deficit profiles in the far wake is confirmed for all the cases; unlike turbine wakes over flat terrain, the wake growth rate is found to be larger in the vertical direction than in the lateral direction. Meandering of the wake is observed to be higher on the FFS escarpment with an upward wake trajectory, compared to the ramp-shaped one. Finally, an analytical model is assessed to predict the wake velocity deficit of the turbine.

3.1 Introduction

The global wind energy capacity has exceeded 600 GW in the year 2019 (Council, 2020). Onshore wind energy, in particular, has experienced a tremendous growth since the dawn of this century, accounting for about 96% of the total installed wind energy capacity. With the new onshore wind energy installations expected to cost less than the cheapest fossil fuel alternatives from 2020 onward (IRENA, 2020), it has a vital role to play in our transition from fossil fuel to clean energy sources. Some key contributors to the success of wind energy projects are accurate wind resource assessment, wind farm power prediction and layout optimization. Turbine wakes, characterized by high velocity deficit and enhanced turbulence intensity, are one of the most important turbine-induced flow phenomena responsible for reduced power generation (up to 40% when the wind direction is aligned with the turbine rows/columns in wind farm arrays (Porté-Agel et al., 2020; Stevens and Meneveau, 2017)) and enhanced fluctuating loads on the downstream turbines. Developing a thorough understanding of these wakes remains, however, a non-trivial task due to the complex nature of interactions between the wakes, the atmosphere and the underlying terrain. As wind farms operate in the inherently turbulent atmospheric boundary layer (ABL), characterizing wakes under different atmospheric conditions (thermal stability, turbulence intensity, wind shear and veer), wind farm configurations (size and layout) and surface characteristics (roughness, heterogeneity and topography) is crucial for the improvement of existing power prediction and optimization tools, as well as for ensuring optimal integration of wind energy in the electrical grid.

Wake characteristics of wind turbines and farms sited on flat terrain have been studied in great detail over the last two decades. Earlier works investigating single turbine wakes ranged from uniform inflow velocity (Medici and Alfredsson, 2006; Troldborg et al., 2010) to accounting for boundary layer effects (Bastankhah and Porté-Agel, 2017b; Chamorro and Porté-Agel, 2009; Hu et al., 2012) under neutral atmospheric conditions. Further research incorporated atmospheric stability (Abkar and Porté-Agel, 2015; Bhaganagar and Debnath, 2014; Chamorro and Porté-Agel, 2010; Vollmer et al., 2016) and wind veer (Abkar and Porté-Agel, 2016) effects in wake development due to thermal stratification and the Coriolis force. While studying single turbines is important for a fundamental understanding of wake flows, wind farms often comprise of multiple turbines grouped together. Flow characteristics inside and above wind farms, including multiple wake interactions, wind direction effects and the influence of wind farms on local meteorology have been extensively explored under different atmospheric conditions (Abkar and Porté-Agel, 2014; Abkar et al., 2016; Allaerts and Meyers, 2015; Baidya Roy et al., 2004; Calaf et al., 2010, 2014; Camp and Cal, 2016; Chamorro et al., 2011; Porté-Agel et al., 2011, 2013; Roy, 2011; Siedersleben et al., 2018; van der Laan and Sørensen, 2017). Insights gained from these works led to the development of computationally fast analytical tools for single turbine wakes (Abkar and Porté-Agel, 2015; Abkar et al., 2018; Bastankhah and Porté-Agel, 2014; Katic et al., 1986; Xie and Archer, 2015) and wind farm power predictions (Niayifar and Porté-Agel, 2016; Stevens et al., 2015, 2016), which are widely used today by wind farm developers.

In reality, however, there is a high probability that wind turbines and farms are sited on different topographical features, such as hills, ramps and escarpments. Although the flow speed-up induced by the presence of the topography presents a lucrative incentive, the complex flow characteristics such as varying levels of flow shear, enhanced turbulence generation and hill-induced pressure gradients require a comprehensive understanding of the flow in such terrain. Current literature is rich in studies dealing with flows over complex topography, including analytical solutions (Jackson and Hunt, 1975), experimental (Ishihara et al., 1999; Mason and Sykes, 1979; Pearse et al., 1981; Takahashi et al., 2005) and numerical (Clark, 1977; Wan and Porté-Agel, 2011) works. Field measurements of flow over topography have been carried out with great success, such as the benchmark studies of flow around the Askervein Hill (Mickle et al., 1988; Taylor and Teunissen, 1987) and the Bolund experiment (Bechmann et al., 2011; Berg et al., 2011). The study of flow over escarpments was pioneered by Bowen and Lindley (1977), who characterized the flow over sharp edged escarpments with varying slopes. Wind turbine wake behavior in such challenging terrains is far from understood and has resulted in overestimation of power output and underestimation of mechanical loads in wind farms sited close to escarpments (Lange et al., 2017). Some examples of wind farms potentially affected by flow separation across steep escarpments are given by Rowcroft et al. (2019). In the following, a brief account of recent developments pertaining to wind turbines sited on topography is presented.

Politis et al. (2012) used two different Reynolds Averaged Navier Stokes (RANS) solvers to simulate wake effects of wind farms in complex terrain, highlighting challenges in the modeling of such complex flows. In addition, they showed that a linear superposition of terrain and wake effects is insufficient to model wakes in complex terrain. Tian et al. (2013) did an experimental investigation of a wind farm sited on a Gaussian hill to assess the interaction between the turbine wakes and the topography. They showed that the presence of the hill affects the power performance of the turbines and also influences the wake of the turbines. Shamsoddin and Porté-Agel (2017b) performed large-eddy simulation (LES) of a wind farm located on topography and validated the results with the experimental data of Tian et al. (2013). Hyvärinen and Segalini placed wind turbines on periodic sinusoidal hills and reported that topography improves turbine performance (Hyvärinen and Segalini, 2017a) and wake interaction with the terrain leads to a faster recovery (Hyvärinen and Segalini, 2017b). Recently, an extensive field campaign in Perdigão, Portugal, which aimed at understanding the flow over a double ridged complex site and its interaction with a turbine wake, was conducted (Fernando et al., 2019; Mann et al., 2017). A series of studies using data from the Perdigão campaign look to answer some fundamental questions about wakes in challenging terrains. Menke et al. (2018) analyzed the wake of the turbine to determine whether it follows the topography or not. Their results found a dependency on atmospheric stability where the wake followed the terrain in stable conditions, was deflected upward in unstable conditions, whereas no deflection was observed in neutral conditions. Han et al. (2018) also found that the wind turbine power performance and wake has significant dependence on the atmospheric stability. Barthelmie and Pryor (2019) developed an algorithm to automate the wake identification and characterization over

a downstream distance of up to 4.5 rotor diameters. Dar et al. (2019) extended the work of Berg et al. (2017) to study the wakes under different levels of terrain complexity and turbine locations using large-eddy simulation. They found that wakes remain self-similar in complex terrain, although, for a very short downstream distance due to faster wake recovery and higher turbulence compared to the flat terrain. The faster wake recovery is a commonly observed feature among turbines located in highly complex terrains (Astolfi et al., 2018; Politis et al., 2012; Tabib et al., 2016).

To analytically model the effect of topography on wakes, the most common practice is to superimpose the velocity deficit in a flat terrain on topography (Crespo et al., 1993; Hyvärinen and Segalini, 2017b). This method, however, only works for hills with gentle slopes and yields inaccurate results for steeper terrains. Recently, Shamsoddin and Porté-Agel (2018b) proposed a new analytical model for turbine wake development over hills, which accounts for the hill-induced pressure gradients and the modified trajectory of the wake. Barthelmie et al. (2016) presented a data set from field measurements across an escarpment located at a coastline. The height of the escarpment, however, was limited to 14 m compared to the hub height of 80 m for the turbines located on the escarpment. Lutz et al. (2017) performed detached-eddy simulation of a wind turbine wake in a complex terrain, which can be approximated by an escarpment with a certain slope upstream. A comparison with a wind turbine in flat terrain was carried out to highlight the influence of topography. Qian and Ishihara (2019) numerically simulated a turbine sited on an escarpment and showed that the wake development is affected by the ratio between the turbine hub height and the hill height. More recently, Dar and Porté-Agel (2020) performed a three-dimensional characterization of the wake behind a turbine sited on two different escarpments using tomographic particle-image velocimetry. They showed that the shape of the escarpment has an influence on the mean, as well as the dynamic characteristics of the wake.

The current work is motivated by the need of a systematic study of wind turbine wakes sited on topography. The choice of escarpments as the topographical feature originates from their common existence in the real world. Coastlines, for instance, have the potential to be very good sites for wind farms, as they can benefit from the high winds coming from the oceans and low costs of onshore wind energy installations. Approximately 80% of the ocean coasts are known to have escarpments of varying heights (Emery and Kuhn, 1982). In addition, escarpments in an onshore environment are also a common site for wind farms (Lutz et al., 2017; Uchida, 2017). One distinguishing feature of escarpments is the shape of their windward side, which can vary from a steep, forward facing step shape to a sloped ramp shape (Lutz et al., 2017; Qian and Ishihara, 2019; Uchida, 2017). The sensitivity of a turbine wake to changes in the shape of the windward side of an escarpment is not well understood. In the current work, we have developed five escarpment models, varying systematically in the shape of the windward side of the escarpments, where a model wind turbine is placed at a distance of one rotor diameter from the leading edge of the escarpment. The objective is to characterize the differences in the wake flow that arise solely due to the change in the shape of the escarpment. The rest of the article is structured as follows: a description of the wind tunnel, wind turbine

model, details of escarpment models and flow measurement setup are provided in section 3.2; key findings from the study are presented in section 3.3; finally, a summary and conclusions are given in section 3.4.

3.2 Experimental Setup

3.2.1 Wind tunnel

The experiments were carried out in the boundary-layer wind tunnel at the WiRE laboratory of EPFL. The wind tunnel is a closed-loop low-speed one, where a 130 kW fan drives the flow in the test section of dimensions 28 m × 2.56 m × 2 m. A contraction with a 5:1 area ratio is present at the inlet of the test section. A natural boundary layer develops over the surface of the wind tunnel without the use of an external tripping mechanism.

3.2.2 Wind turbine model

The wind turbine model used in the current study is a three bladed model with a rotor diameter D of 15 cm and a hub height z_h of 12.5 cm. The blade profile has a circular arc shape with 5% camber and 5% thickness with respect to the chord length. The chord length varies from 12 mm at the blade root to 8.4 mm at the blade tip. The model is specifically designed to have power and thrust coefficients comparable to those of full-scale commercial turbines. The turbine rotor results in an aerodynamic blockage ratio of 0.34%. For more details on the turbine model, the reader is referred to Bastankhah and Porté-Agel (2017a).

3.2.3 Escarpment model

Five escarpment models are studied in this work. The models differ in the shape of the windward side of the escarpment. The length of the models is 3 m ($\sim 20D$) and the width is equal to 2.5 m (i.e. covering the width of the tunnel cross-section). The height H of the escarpments is chosen to be equal to the hub height of the turbine model (i.e. 12.5 cm), resulting in a solid blockage ratio of about 6.25%. The wind turbine model is placed one rotor diameter downstream of the leading edge of the models. The escarpments can be sub-divided into two categories: forward-facing step (FFS) models, and models with a ramp shape upstream. A description of the model shapes is given in the following.

Forward-facing steps with:

- sharp corner at the leading edge (labeled 90° Edge)

- 5% radius of curvature with respect to the escarpment height at the leading edge (labeled 5% r/H)

- 10% radius of curvature with respect to the escarpment height at the leading edge (labeled 10% r/H)

The flow separation and turbulence intensity generated by the escarpment are known to be highly sensitive to the shape of the leading edge (Lange et al., 2017). It will, therefore, be interesting to see how the turbine wake is affected by adding a radius of curvature as small as 5% with respect to the escarpment height.

The ramp shapes are sinusoidal and defined by the following mathematical expression:

$$z_r(x) = \frac{1}{2}H[1 + cos(\frac{\pi x}{2L})], \tag{3.1}$$

where H is the escarpment height and L is the half-length of the ramp. The two ramp models are described by:

- half-length $L = 2H$, leading to a maximum local slope of ~21.5° (labeled 21.5° Slope)

- half-length $L = 1.25H$, leading to a maximum local slope of ~33° (labeled 33° Slope)

Figure 3.1 shows the shapes of the five escarpment models.

3.2.4   PIV setup

Stereoscopic particle-image velocimetry (S-PIV) is used to obtain high spatial resolution flow measurements. The flow is seeded with olive oil particles with a diameter on the order of 1 μm. The field of view is illuminated by a dual head 425 mJ Nd:YAG laser. Two 16-bit sCMOS cameras (2560 × 2160 pixels) with 55 mm objectives and mounted on Scheimpflug adapters are used for capturing images. The images are taken at a sampling rate of 10 Hz and mean flow
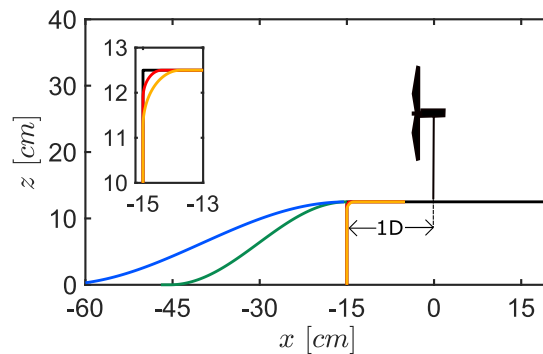
Figure 3.1: Side view of the escarpment leading edge for the five topography models. The inset shows a close-up of the leading edge of the forward-facing step models. Black: 90° Edge; red: 5% r/H; orange: 10% r/H; green: 33° Slope; blue: 21.5° Slope.
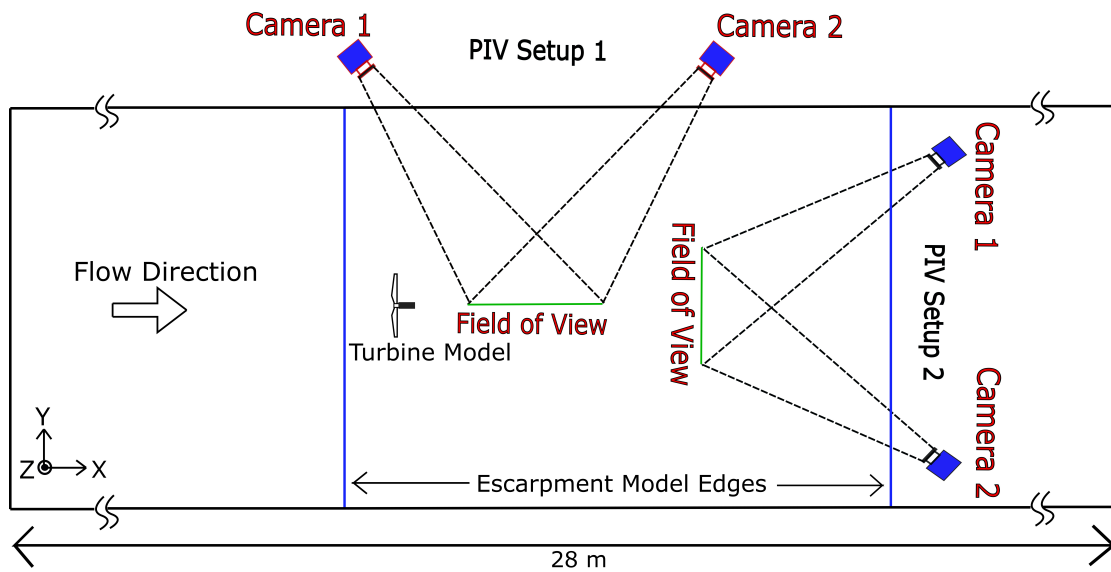
Figure 3.2: Schematic representation of the experimental setup and stereoscopic PIV setups (top view).

quantities are obtained by averaging over 1000 images. The sampling rate used in this study is not fast enough to resolve the smallest temporal scales, but it is sufficient to provide data for computing Reynolds averaged flow characteristics. Moreover, the PIV system also provides instantaneous information on spatial development of the flow in a two-dimensional plane.

Flow fields in the XZ plane passing through the turbine centerline and YZ planes in the turbine wake are sampled. Figure 3.2 shows a schematic representation of the two S-PIV setups. Details of the two setups are given in the following:

- PIV Setup 1: the size of the field of view (FOV) is $4D \times 3D$ with a resolution of 0.0106D. The angle between the cameras is about 45°.

- PIV Setup 2: the size of the field of view (FOV) is $3D \times 2D$ with a resolution of 0.014D. The angle between the cameras is about 42°.

The post-processing is performed in two steps, with an interrogation window size of 64×64 pixels in the first step and 32×32 pixels in the second step. An overlap of 75% is kept within the interrogation windows and the correlation is obtained after two passes through each window size. In addition to the PIV setups described above, a two-dimensional two-component (2D2C) PIV setup using one 16-bit sCMOS camera is used to sample the streamwise and vertical velocity components upstream of the escarpment. The spatial resolution of this PIV setup is also 0.0106D.

3.3 Results

3.3.1 Upstream boundary layer and base flow

The upstream boundary layer is characterized using a 2D2C PIV setup. Figure 3.3 shows the averaged streamwise velocity U seven rotor diameters upstream of the topography, normalized by the free stream velocity U_∞ (= 4.37 ms^{-1}) at the same streamwise position. The vertical coordinate $z/D = 0$ in figure 3.3 represents the surface, whereas it represents the center of the turbine on the escarpment in the rest of the article. The boundary-layer height δ is approximately 39 cm and the mean hub height wind speed $U_{h,up}$ is 3.55 ms^{-1}. A power law is fitted to the velocity profile $U = U_{h,up}(z/z_h)^n$, where the scaling exponent n is 0.17. The streamwise turbulence intensity $I_u = \sigma_u/U_\infty$, where σ_u is the standard deviation of the streamwise velocity component, is around 0.06 at the hub height. The normalized vertical momentum flux is higher near the surface due to high shear in that region. A friction velocity u_* of 0.17 ms^{-1} and surface roughness length z_o of 0.04 mm are estimated by fitting a logarithmic profile to the lowest 15% of the boundary layer. The logarithmic fit is done according to the following relation: $U = \frac{u_*}{\kappa}log(\frac{z}{z_o})$, where $\kappa = 0.41$ and the fitted line is shown in figure 3.3 (d). The ratio $z_o/D = 2.67 \times 10^{-4}$ scales to a roughness length of about 0.0267 m for a full-scale turbine of 100 m diameter, corresponding to a terrain with grass and shrubs (Stull, 1988) upstream of the escarpments. The flow over the escarpments, especially the forward-facing steps, is affected by the ratio of boundary-layer to step height (δ/H) (Sherry et al., 2010). The δ/H ratio in the current study is 3.12, which is similar to previous experimental studies of flows on escarpments, e.g. see Kilpatrick et al. (2016).

The flow characteristics over the escarpments in the absence of the turbine, termed as the base flow, are now discussed. Figure 3.4 shows the normalized averaged streamwise component of
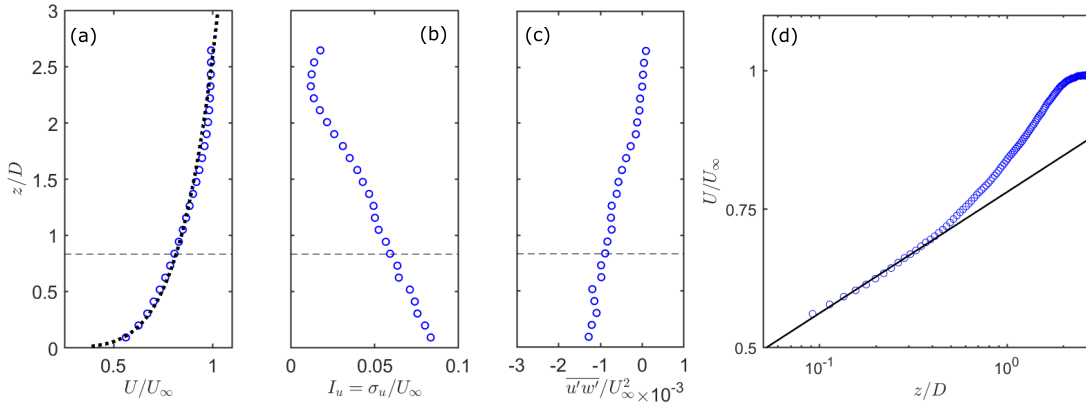
Figure 3.3: Vertical profiles of the normalized averaged streamwise velocity component (a), streamwise turbulence intensity (b) and normalized averaged vertical momentum flux (c) in the upstream boundary layer. The horizontal dashed black line shows the height of the escarpment (equal to the hub height). (d) Normalized averaged streamwise velocity in semi-logarithmic coordinates, with the logarithmic fit in black solid line.
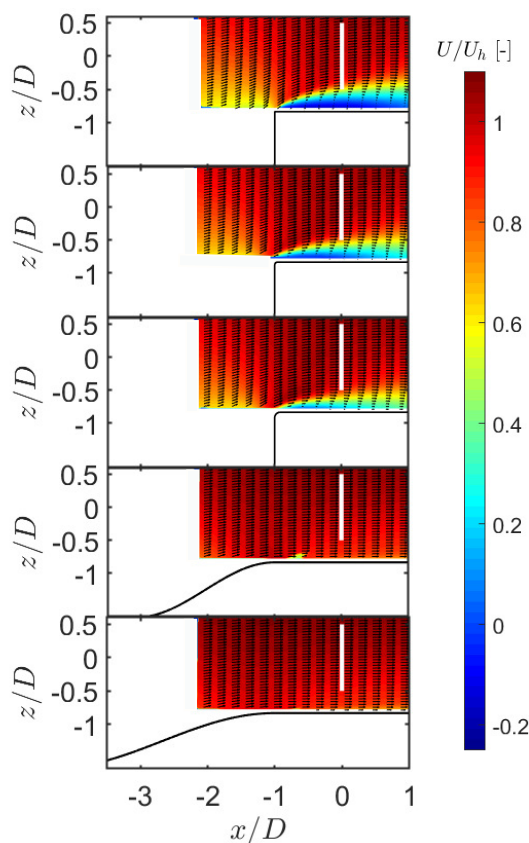
Figure 3.4: Contours of the normalized averaged streamwise velocity component without the turbine from top to bottom: 90° Edge, 5% r/H, 10% r/H, 33° Slope and 21.5° Slope. In-plane velocity vectors are overlaid. The prospective turbine rotor is shown by the vertical white line.

the flow velocity on the escarpments in the base flow. A separated flow region can be observed in the 90° Edge escarpment case. The reverse flow region is identified by the dark blue contour in the figure. This reverse flow zone has a maximum height of about 0.17 times the escarpment height and the flow reattaches to the surface around two rotor diameters downstream of the leading edge ($x/D = -1$). High flow shear induced by the flow recirculation can be observed. The strength of the flow separation is significantly reduced by just adding a curvature of 5% radius with respect to the escarpment height at the leading edge. The flow reattachment occurs around one rotor diameter from the leading edge. As a result, the shear in the flow is also relatively less in this case. For the forward facing step with a 10% radius of curvature, no recirculation region is observed in the captured field of view. The ramp-shaped escarpments show lesser shear closer to the surface. This is due to the absence of any flow separation, and due to the speed-up of flow closer to the surface over the escarpment.

An important feature of the flow over escarpments (or, in general, topography) is the flow speed-up across the streamwise transect. This flow speed-up is quantified as the ratio of velocity across the escarpment to a reference velocity in the upstream at the same height

25
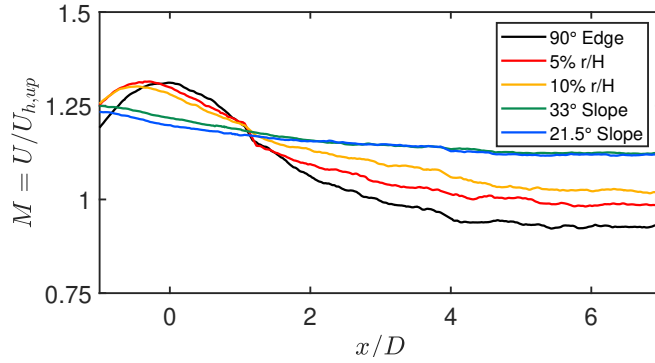
Figure 3.5: Flow speed-up across the escarpments (without the turbine). $x/D = 0$ shows the location of the turbine model and $U_{h,up}$ is the streamwise velocity at the hub height in the upstream boundary layer.

relative to the local surface. Figure 3.5 shows the speed-up across all the different escarpment models at the hub height. The FFS escarpments have a higher speed-up, with the 90° Edge escarpment showing the highest velocity at the chosen turbine location. The FFS escarpments, however, have a faster decay in the speed-up with the increase in the downstream distance. The escarpments with a ramp upstream have a lower speed-up, but also show a slower decay with the downstream distance compared to the FFS escarpments, which can prove beneficial from the point of view of siting a wind farm on the escarpment.

Table 3.1 presents some basic flow parameters at the chosen turbine location without the presence of the turbine. The mean streamwise velocity in the base flow at the hub height of the chosen turbine location U_h is used to normalize all the flow quantities in the respective cases. The streamwise turbulence intensity at the hub height is between 0.069 and 0.051 for different cases. It is to be noted that the turbulence intensity in the FFS escarpments is much higher closer to the ground due to high flow shear induced by the flow separation from the escarpment leading edge. The shear exponents are computed over the rotor diameter as $n = ln(U_{z_1}/U_{z_2})/ln(z_1/z_2)$ (Barthelmie et al., 2016), where z_1 and z_2 are the heights of the rotor top and bottom, respectively. The values of the shear exponents for the FFS escarpments are considerably higher than the recommended value of 0.2 (IEC, 2005) as per IEC standards. This is understandable, as the IEC recommendation is based on turbines sited on flat terrain. High shear exponents have been observed for escarpments (Barthelmie et al., 2016; Lange et al., 2017) and imply high fluctuating loads on the blades. For the ramp-shaped escarpments, the flow shear is reduced compared to the incoming flow due to the effect of flow speed-up closer to the ground.

As per IEC standard 61400-1 edition-3 (IEC, 2005), the inclination angle α with respect to the horizontal axis of the mean flow should be less than 8°. High inclination angles can induce significant additional loads on the rotor. Using the streamwise and vertical velocity components, we compute the flow inclination angles in the absence of the turbine. Very

	90° Edge	5% r/H	10% r/H	33° Slope	21.5° Slope
$U_h\ (ms^{-1})$	4.70	4.60	4.52	4.34	4.27
$I_u = \sigma_u/U_h$ (%)	6.9	6.25	6	5.15	5.26
n	0.8171	0.48	0.28	0.12	0.1265

Table 3.1: Overview of key flow parameters at turbine location without the presence of turbine.

high inclination angles are observed over the leading edge of the FFS escarpments, whereas, ramp-shaped escarpments have inclination angles around 5° (see figure 3.6). At the turbine location, the flow inclination angle ranges from 0° to 6° for the 90° Edge, with a high variation in the lower half of the rotor. The other two FFS cases show very similar trends with α varying between −3° to 3°. The ramp-shaped cases have α less than 3°. It is to be noted that, the inclination angles are within the 8° IEC recommendation for all the escarpment shapes.

3.3.2 Power and thrust coefficients

The turbine rotor is mounted on a permanent magnet direct current machine. To extract energy from the wind, the DC machine is operated in the 'generator mode'. The power coefficient C_p is calculated by:

$$C_p = \frac{Q\Omega}{\frac{1}{2}\rho A U_r^3},\tag{3.2}$$

where Q is the torque generated by the rotor, Ω the rotational speed, A the rotor area and U_r is the rotor averaged velocity in the base flow at the turbine location. In addition, to measure the thrust force T of the turbine, the tower of the turbine is mounted on a multi-axis strain
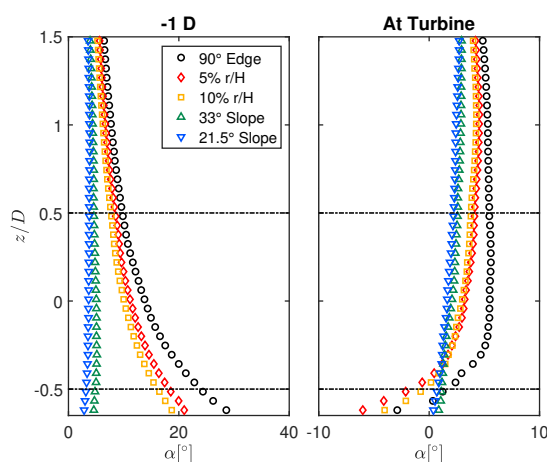
Figure 3.6: Flow inclination angle α at the leading edge of the escarpments (-1D) and prospective turbine location. The horizontal lines trace the rotor top and bottom tips.

gauge sensor. The thrust coefficient C_T is calculated by:

$$C_T = \frac{T}{\frac{1}{2} \rho A U_r^2}. \tag{3.3}$$

Figure 3.7 shows the variation of power and thrust coefficients with tip-speed ratio λ for all escarpment models. The maximum power coefficient is between 0.31 and 0.35 for the different cases, with the 90° Edge escarpment case showing the maximum C_p out of all the cases. The thrust coefficient is fairly constant between different cases, with an approximate value of 0.8 for the tip speed ratio corresponding to maximum C_p. The tip-speed ratio is adjusted by changing the rotational speed of the rotor while keeping the incoming velocity constant. For PIV measurements, the turbine is operated at the tip-speed ratio corresponding to the maximum C_p for each case.

3.3.3 Mean flow and turbulence characteristics

We now present some key features of the flow in the wake of the turbine. Figure 3.8 shows the averaged normalized streamwise component of the flow velocity. In the FFS escarpments, the recirculation near the surface in the base flow is removed in the presence of the turbine. The normalized streamwise velocity is lowest in the turbine wake for the 90° Edge case, with values getting higher with the increase in the leading edge curvature. The ramp-shaped escarpments show even higher normalized streamwise velocity in the turbine wake. This can be explained by the fact that, as the normalized streamwise velocity in the base flow near the surface increases with the increase in the leading edge curvature and with the addition of the ramp, the normalized streamwise velocity in the turbine wake also increases.

The turbulent momentum fluxes play a role in the exchange of energy between the outer and wake flow, thereby contributing to the recovery of the wake. In addition, these fluxes are
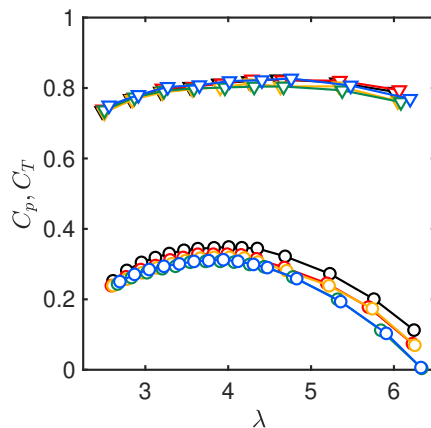
Figure 3.7: Power (circles) and thrust (triangles) coefficient as a function of tip-speed ratio for different escarpment models. The colors correspond to same cases as in figure 3.5.
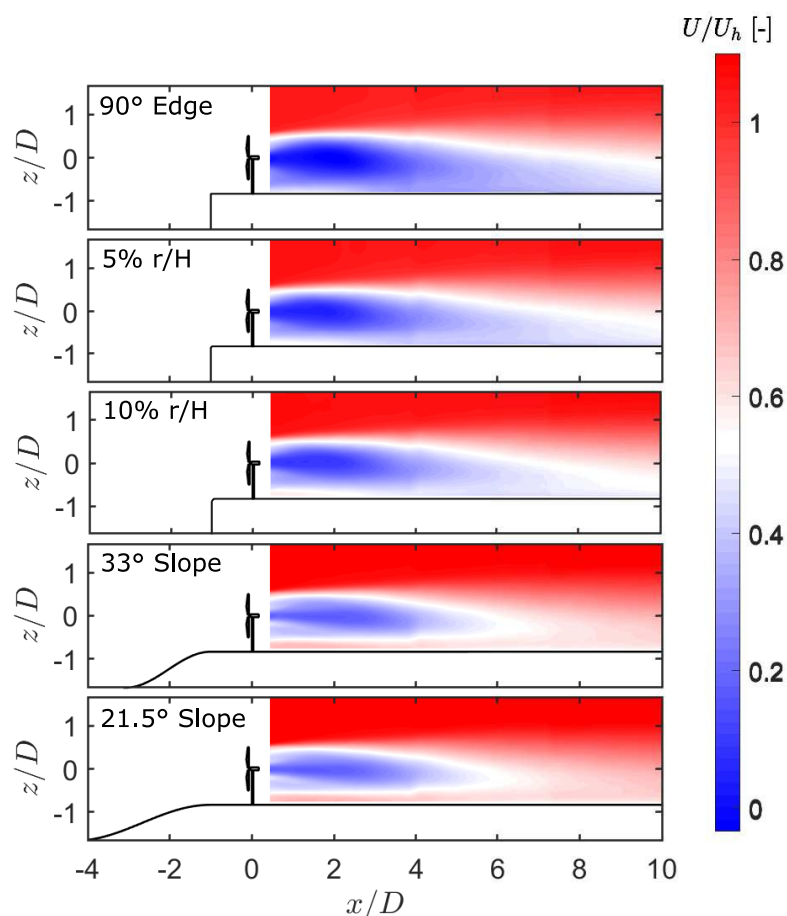
Figure 3.8: Contours of the normalized averaged streamwise velocity component in the wake of the turbine for all cases.

responsible for the mechanical production of turbulence along with the mean shear in the flow. Figures 3.9 & 3.10 show the normalized vertical and lateral momentum fluxes, respectively, in the turbine wake for different escarpment cases. The magnitude of these fluxes is highest in the 90° Edge case and shows a gradual decrease with the increase in the leading edge curvature. The magnitude of these fluxes gets even smaller with the addition of the ramp in front of the escarpment. An exchange of momentum between the turbine wake and the outer flow near the surface can also be observed in the FFS escarpments at shorter downstream distances from the turbine.

Contours of the normalized turbulence kinetic energy ($tke = \frac{1}{2}(\overline{u'^2} + \overline{v'^2} + \overline{w'^2})$), where u', v' and w' are the fluctuating part of the streamwise, spanwise and vertical velocity components, respectively) in the turbine wake are shown in figure 3.11. The highest magnitude of the normalized tke is observed in the 90° Edge case, with maximum energy at around 3 rotor diameters downstream. The magnitude of the normalized tke decreases with the increase in the leading edge curvature, and it is almost half for the ramp-shaped cases when compared to the 90° Edge case. In general, the trend observed in the magnitude of the tke with respect to

29
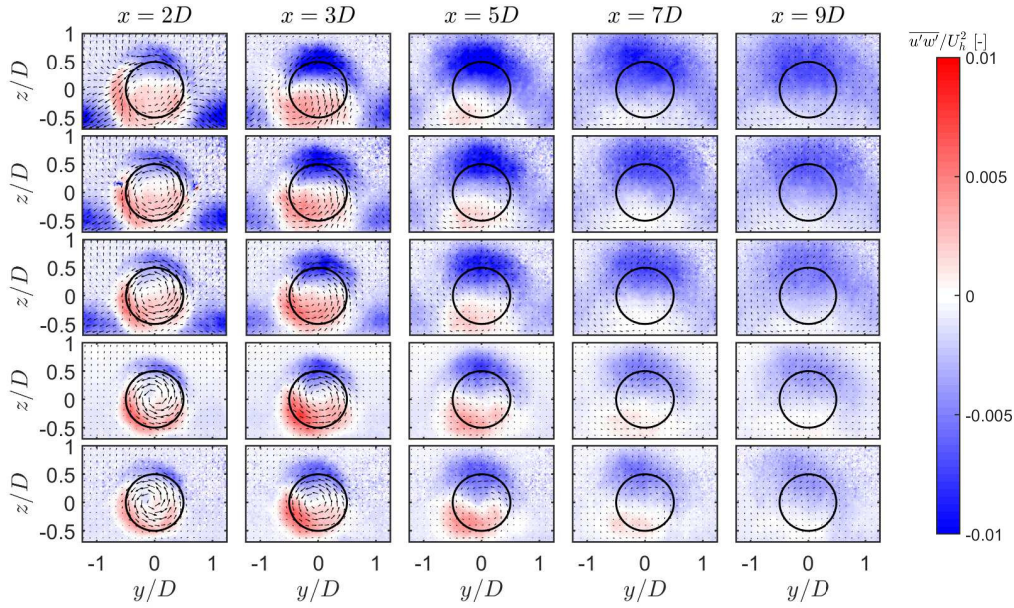
Figure 3.9: Contours of the normalized vertical momentum flux in the wake of the turbine. From top to bottom: 90° Edge, 5% r/H, 10% r/H, 33° Slope, 21.5° Slope. In-plane velocity components are overlaid. Black circles represent the rotor position.
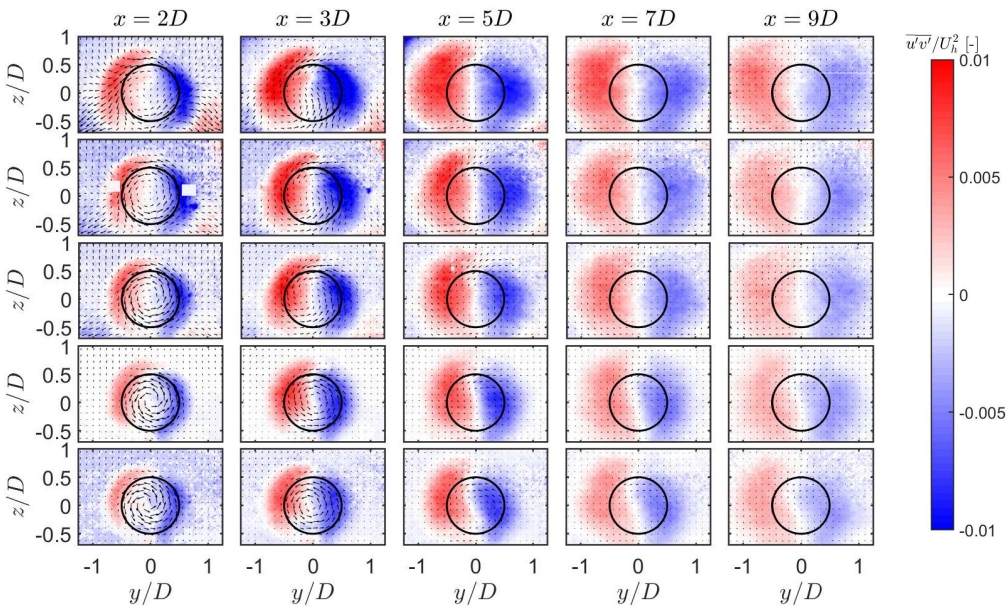
Figure 3.10: Contours of the normalized lateral momentum flux in the wake of the turbine. From top to bottom: 90° Edge, 5% r/H, 10% r/H, 33° Slope, 21.5° Slope. In-plane velocity components are overlaid. Black circles represent the rotor position.

the escarpment shape is consistent with that of the turbulent momentum flux. As explained by Wu and Porté-Agel (2012), the flow shear around the rotor bottom tip is small which leads
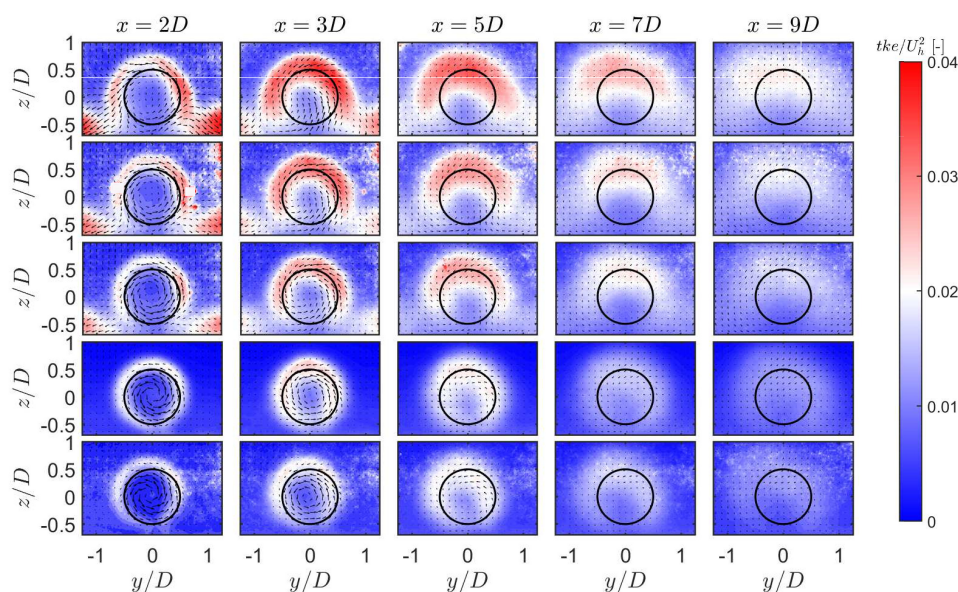
Figure 3.11: Contours of the normalized turbulence kinetic energy in the wake. From top to bottom: 90° Edge, 5% r/H, 10% r/H, 33° Slope, 21.5° Slope. In-plane velocity components are overlaid. Black circles represent the rotor position.

to less turbulence production in this region compared to the rotor top tip, even though the magnitude of the turbulent momentum flux is almost the same in both regions. As a result, the region of high tke resembles a horseshoe shape, whose width is highest for the 90° Edge case and decreases for the curved edged FFS and ramp-shape cases. Another interesting observation is the presence of high turbulence kinetic energy close to the surface surrounding the turbine wake in the FFS escarpment cases. This high tke region is a result of the high shear induced by the flow separation from the escarpment leading edge.

3.3.4 Wake structure

In order to characterize the difference in the turbine wake flow with respect to the base flow, the streamwise velocity deficit is computed. For this purpose, the streamwise velocity in the base flow is subtracted from that in the wake flow as $\Delta U = U_b - U_w$, where U_b and U_w is the time averaged streamwise velocity in the base and wake flow , respectively. Figure 3.12 shows the two dimensional velocity deficit fields in several y-z planes at different downstream distances from the turbine. The presence of the turbine has an impact on the surrounding flow over the FFS escarpments. This is evident from the negative velocity deficit region surrounding the lower part of the rotor up to a downstream distance of 3D in these cases. The magnitude of this negative velocity deficit decreases with the increase in the curvature of the escarpment leading edge. This negative velocity deficit region is generated as the presence of the turbine suppresses the development of separated flow from the escarpment leading edge,
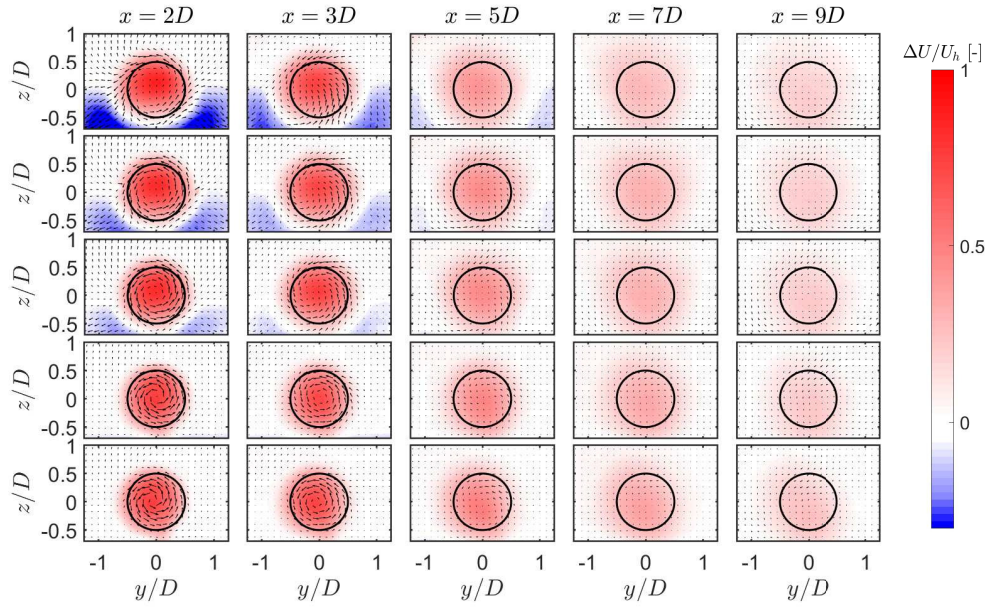
Figure 3.12: Contours of the normalized averaged streamwise velocity deficit in the wake of the turbine. From top to bottom: 90° Edge, 5% r/H, 10% r/H, 33° Slope, 21.5° Slope. In-plane velocity components are overlaid. Black circles represent the rotor position.

which causes a decrease in the mean flow shear in the surrounding flow and higher velocity compared to those in the base flow, thereby leading to a negative velocity deficit region in the FFS escarpments.

The rotation of the wake up to a downstream distance of 3D is also affected by the escarpment geometry. Specifically, the vertical velocity induced by the escarpment in the base flow can affect the wake rotation; high vertical velocity in the base flow of the turbine sited on the 90° Edge escarpment results in a weaker rotation. As the base flow vertical velocity component reduces with the increase in the curvature of the escarpment leading edge and by the addition of the ramp, the wake rotation gets stronger in these cases. To compare the streamwise velocity deficit quantitatively, figure 3.13 shows the lateral and vertical profiles in y-z and x-z planes passing through the turbine axis. The velocity deficit is observed to be higher in the FFS cases and it also appears to recover faster than in the ramp cases.

To elaborate on the recovery of the wake center velocity deficit, we plot the maximum velocity deficit for each case as a function of the downstream distance in figure 3.14. The three FFS escarpment cases have higher velocity deficit maxima in the near wake than the ramp-shaped escarpment cases. This can be related to the effect of pressure gradient induced by the topography on the turbine wake. As shown earlier, the thrust coefficient of the turbine is almost unchanged for different escarpments (see figure 3.7). In topography, however, the wake velocity deficit also has a contribution from the pressure gradient induced by the terrain (Shamsoddin and Porté-Agel, 2018a). The streamwise variation in base flow velocity is higher
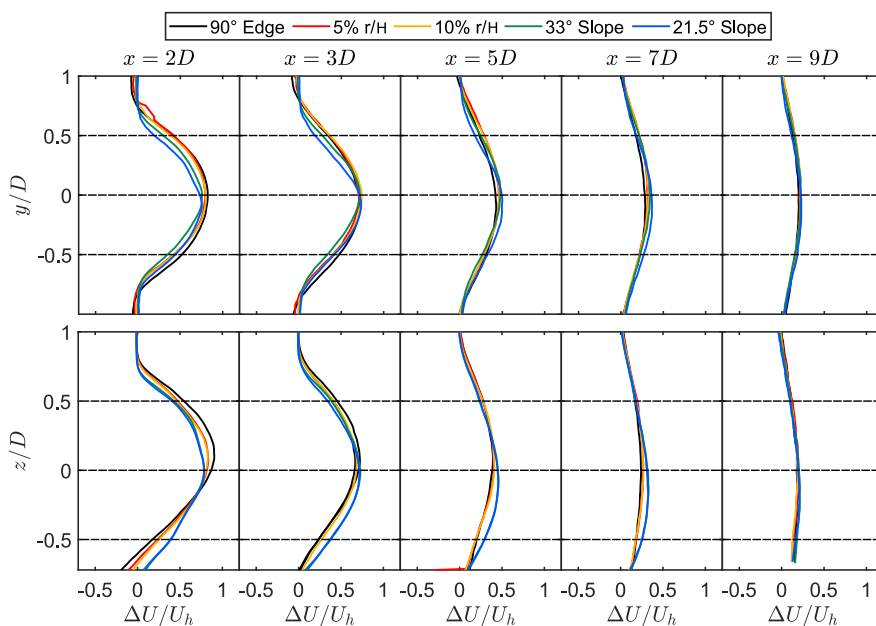
Figure 3.13: Normalized averaged streamwise velocity deficit: lateral (top) and vertical (bottom) profiles passing through the turbine axis. Horizontal dashed lines trace the rotor axis and tip positions.
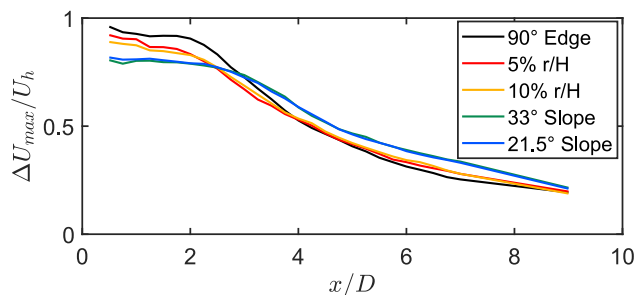
Figure 3.14: Maximum velocity deficit as a function of downstream distance.

in the FFS escarpments compared to the ramp-shaped ones (see figure 3.4), which implies a higher contribution from the pressure gradient, and thereby, a higher wake velocity deficit. The maximum velocity deficit also shows a minimal change in this near wake region. This is because the shear layer around the rotor tips, which brings outer flow into the wake, has not grown enough to re-energize the wake center. In the far wake, the recovery of the wake center velocity deficit is faster for the FFS cases compared to that for the ramp-shape cases. This is due to the higher levels of turbulence and momentum fluxes for the FFS cases compared to the ramp-shaped escarpment cases. The far wake region is also characterized by the Gaussian profile of the velocity deficit and linear expansion of the wake with the increase in the downstream distance. Both characteristics will be discussed later in this section.

To understand the impact of the wind turbine on the streamwise turbulence intensity in the

wake, we compute the added streamwise turbulence intensity as follows:

$$I_{add} = \begin{cases} +\sqrt{I_{u,w}^2 - I_{u,b}^2}, & I_{u,w} \geq I_{u,b} \\ -\sqrt{I_{u,b}^2 - I_{u,w}^2}, & I_{u,w} < I_{u,b}, \end{cases}$$

where $I_{u,b}$ and $I_{u,w}$ are the streamwise turbulence intensities without and with the turbine at the same physical location. Figure 3.15 shows the streamwise contours of added streamwise turbulence intensity for two selected cases. The added turbulence intensity is positive in the upper half of the rotor due to high turbulence production behind the rotor tip. Its magnitude is larger for the FFS escarpment compared to the ramp-shaped escarpment. The magnitude of I_{add} is highest at a downstream distance of around 3D where the tke production is highest and the transition from near to far wake happens. The I_{add} is observed to be negative below the turbine hub height for the FFS escarpment throughout the downstream extent of the domain, whereas in the ramp-shaped escarpment it is positive except for a small region around the rotor bottom tip in the near wake region. Change in the flow shear close to the rotor bottom tip is responsible for the negative I_{add} in the ramp-shaped escarpment. In the FFS escarpment, the negative I_{add} appears because the high turbulence intensity region generated due to the flow shear induced by the leading edge flow separation in the base flow is suppressed in the wake flow due to the change in the flow shear caused by the turbine.

For a quantitative comparison between all cases, profiles of I_{add} in lateral and vertical planes passing through the turbine axis are plotted in figure 3.16. The FFS escarpment cases show a gradual decrease in the magnitude of the added turbulence intensity with the increase in the curvature. The two ramp cases have a lower magnitude of the added turbulence intensity compared to the FFS cases and show very similar values compared to each other.

Another important characteristic of the turbine wakes is their rate of expansion as a function of the downstream distance, known as the wake growth rate. The wake is shown to grow linearly in the far wake (Chamorro and Porté-Agel, 2010; Wu and Porté-Agel, 2012) and, therefore, its width can be estimated by the following relation:

$$\frac{\sigma}{D} = k\frac{x}{D} + \epsilon, \tag{3.4}$$

where the slope k of the linear relation is the wake growth rate and ϵ is the initial wake width. The wake width σ, defined as the standard deviation of the Gaussian fit to the lateral and vertical velocity deficit profiles, is plotted in figure 3.17. A linear fit is done on the normalized standard deviation, the slope of which yields the wake growth rate k. As can be seen, the wake growth rate in the lateral direction is similar for all the cases. In the vertical direction, however, the 90° Edge case shows the highest wake growth rate, with values gradually decreasing for the rest of the cases. A relatively higher mean flow shear and enhancement of turbulence in the vertical direction, compared to that in the lateral direction, can explain the observed trend. Figure 3.18 shows the maxima of the vertical and lateral turbulence intensities in the vertical and lateral profiles at the turbine centerline and hub height, respectively. The vertical
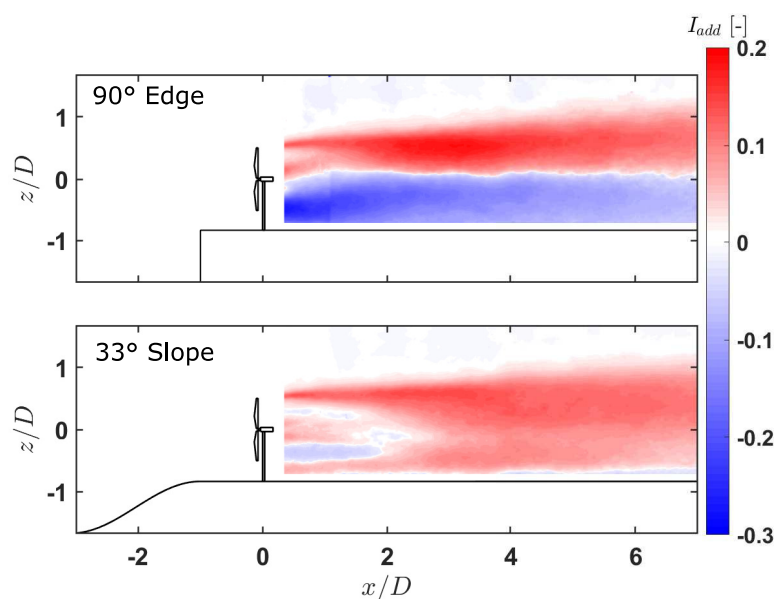
Figure 3.15: Contours of the added streamwise turbulence intensity in the turbine wake for two selected cases.
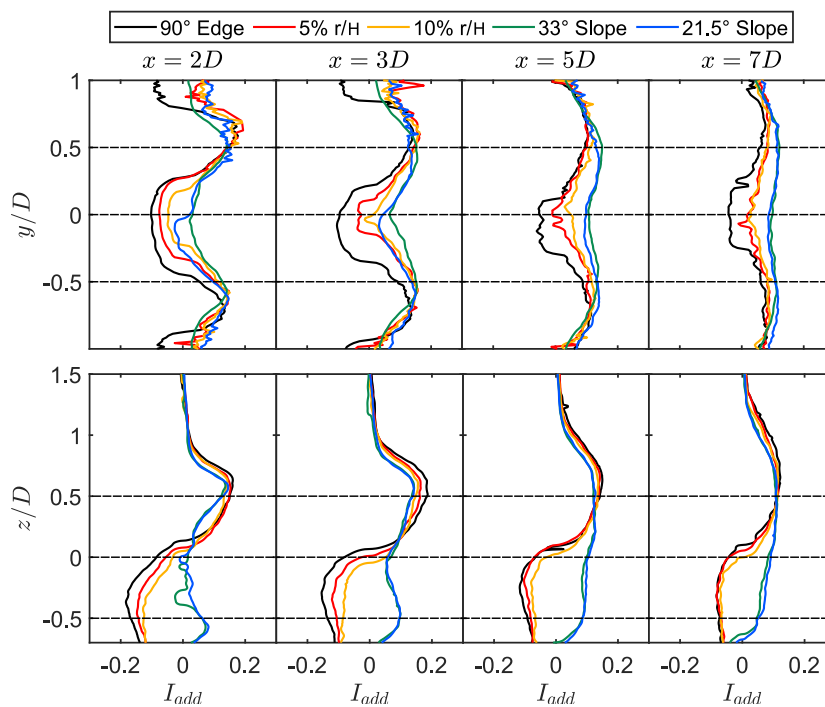
Figure 3.16: Added streamwise turbulence intensity: lateral (top) and vertical (bottom) profiles passing through the turbine axis. Horizontal dashed lines trace rotor axis and tip positions.

turbulence intensity is observed to be higher than the lateral one in the FFS cases, whereas their difference decreases in the ramp-shaped escarpment cases. This is consistent with the larger magnitude of the momentum fluxes and, consequently, the wake growth rates in
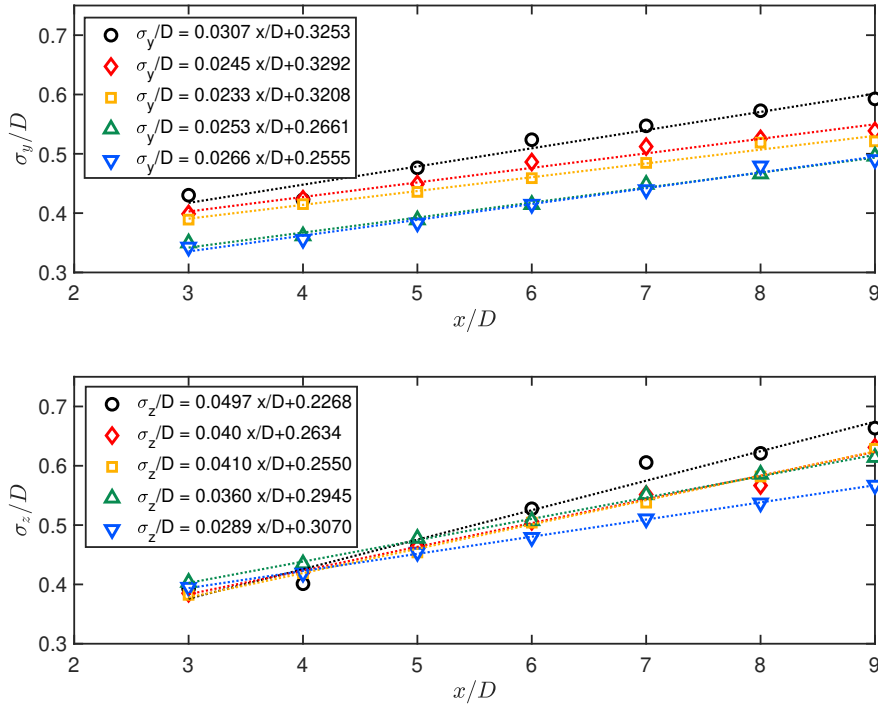
Figure 3.17: Normalized standard deviation of the streamwise velocity deficit for the lateral (top) and vertical (bottom) profiles at the turbine hub height and centerline, respectively. Black: 90° Edge; orange: 5% r/H; red: 10% r/H; green: 33° Slope; blue: 21.5° Slope. The legend shows the linear fits according to equation 3.4 for each case.

the vertical direction compared with the lateral one. This is, however, in contrast with what is reported over flat terrain, where the momentum fluxes and, thus, the wake growth rates are higher in the lateral direction compared to the vertical one (Abkar and Porté-Agel, 2015; Bastankhah and Porté-Agel, 2017c).

Finally, wind turbine wakes are known to depict self-similar behavior in both flat (Abkar and Porté-Agel, 2015; Bastankhah and Porté-Agel, 2014; Xie and Archer, 2015) and complex (Dar et al., 2019) terrains. Here, we plot the normalized streamwise velocity deficit profiles as a function of distance from the wake center normalized by the wake half-width $r_{1/2}$. The wake half-width is defined as the distance from the velocity deficit maximum to the point where the velocity deficit is reduced to 50% of its maximum value. We verify that the self-similarity holds for both vertical and lateral profiles in all escarpment cases and the velocity deficit can be approximated by a Gaussian profile (see figure 3.19). This is important, especially for the FFS escarpments, as it shows that the interaction between the wake and flow separation does not affect the self-similarity of the velocity deficit in the far wake.
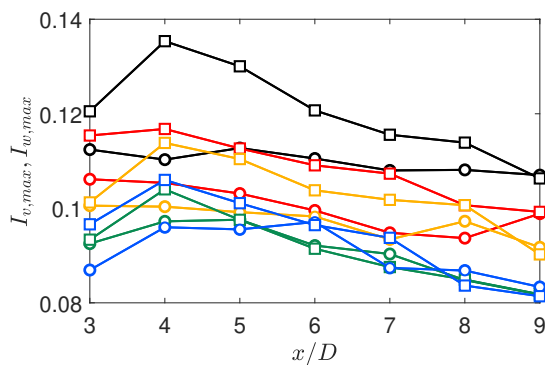
Figure 3.18: Maximum of the lateral and vertical turbulence intensity in the lateral and vertical direction at the turbine hub height and centerline, respectively. The circles and squares represent the lateral and vertical turbulence intensity values, respectively.
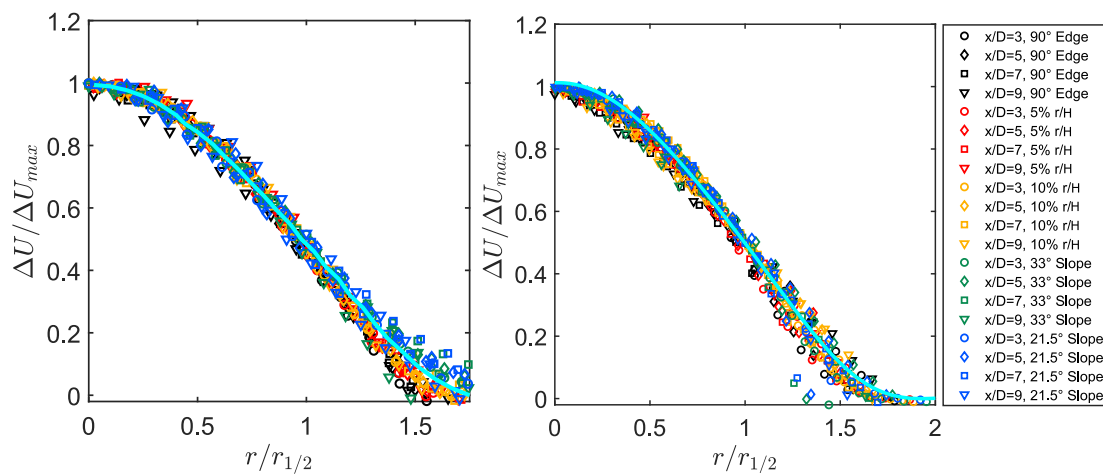
Figure 3.19: Self-similar normalized streamwise velocity deficit lateral (left) and vertical (right) profiles at the turbine hub height and centerline, respectively. A Gaussian curve is overlaid for comparison.

3.3.5 Comparison of experimental and analytically modeled velocity deficit profiles

In this section, we test an existing analytical tool to model wakes behind wind turbines sited on escarpments. The problem under focus is stated as: given that the mean streamwise velocity at the hub height in the base flow $U_b(x)$ is known, can we then predict the wake using an analytical model? The dominating effect of the escarpment on the flow is a pressure gradient that is induced due to the presence of the topography. Therefore, we choose the model for turbulent axisymmetric wakes under a pressure gradient proposed by Shamsoddin and Porté-Agel (2018a). For details on the model, the reader is referred to the original work; here, we will briefly describe the procedure followed to obtain the velocity deficit profiles.

We generate a velocity profile using the power law fit in figure 3.3 to represent the upstream flow. For model inputs, we choose a thrust coefficient C_T of 0.8 (figure 3.7). The wake width $\sigma_0(x)$ for the miniature wind turbine is computed using the linear relation in equation 3.4, where the wake growth rate is estimated using the empirical relation $k = 0.3TI$ (Brugger et al., 2019) and TI is the rotor averaged turbulence intensity in the base flow at the turbine location; and ϵ is taken equal to $1/\sqrt{8}$ (Bastankhah and Porté-Agel, 2016). Using these parameters, the model returns the maximum velocity deficit under zero pressure gradient C_0:

$$C_0(x) = 1 - \sqrt{1 - \frac{C_T}{8(\frac{\sigma_0(x)}{D})^2}}, \qquad (3.5)$$

and the invariant ratio of velocity deficit to wake width:

$$\Lambda_0(x) = \Lambda(x) = \frac{C_0(x)U_{in}}{\sigma_0(x)}, \qquad (3.6)$$

where U_{in} is the upstream velocity at the hub height, Λ_0 is the invariant ratio under zero pressure gradient and Λ is the invariant ratio under pressure gradient. As a next step, the base flow information and the invariant ratio are used to compute the maximum velocity deficit C under the pressure gradient induced by the escarpments:

$$\frac{dC(x)}{dx} = \frac{-1}{\left(\frac{U_b^4(x)}{\lambda_0^2(x)}\right)(3C^2(x) - 2C^3(x))} \left[\frac{1}{4} \frac{dU_b^4(x)}{dx} \frac{C^3(x)}{\lambda_0^2(x)} + \left(C^3(x) - \frac{C^4(x)}{2}\right) \frac{d}{dx}\left(\frac{U_b^4(x)}{\lambda_0^2(x)}\right) \right], \quad (3.7)$$

with the following boundary condition:

$$C(x_i) = C_0(x_i), \qquad (3.8)$$

where x_i represents the start of the far wake, taken as the streamwise position where the maximum velocity deficit (in experiments) is equal to the theoretical value $(1 - \sqrt{1 - C_T})$. Furthermore, the wake width $\sigma(x)$ is computed using the new velocity deficit and base flow
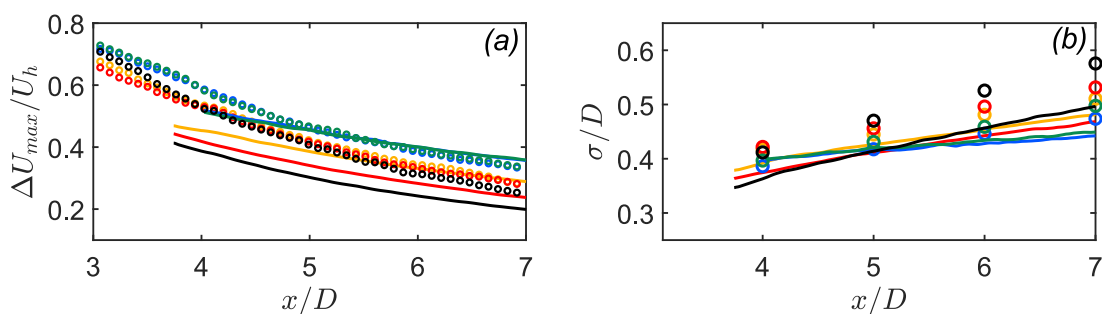
Figure 3.20: Comparison of the maximum normalized streamwise velocity deficit (a) and the equivalent wake width (b) between the analytical models and experiments. Circles mark the experimental data and solid lines represent the PG model. Color codes for different cases are same as figure 3.17.

information:

$$\sigma(x) = \frac{U_b(x)C(x)}{\Lambda(x)}. \tag{3.9}$$

Finally, the velocity deficit profiles are computed using the Gaussian shape function:

$$\frac{U_b(x) - U_w(x,r)}{U_b(x)} = C(x)e^{-\left(\frac{r^2}{2\sigma^2}\right)}, \tag{3.10}$$

where U_w is the streamwise velocity in the wake and r is the distance from the maximum velocity deficit position. It is to be noted that the turbine wakes in the current study are not perfectly axisymmetric and experience flow shear in the vertical direction due to the effect of the surface. As stated by Shamsoddin and Porté-Agel (2018a), in such case the wake width obtained from the model is the equivalent wake width of the lateral and vertical wake widths, which is computed as the geometric mean of the two wake widths: $\sigma_{eq} = \sqrt{\sigma_y \sigma_z}$.

Figure 3.20 shows the comparison between the experimentally and analytically obtained maximum velocity deficit and equivalent wake width. The degree of agreement between the experiments and the model is observed to be dependent on the escarpment shape. For the ramp-shaped escarpment cases, the maximum velocity deficit is predicted reasonably well, with slight underestimation until a downstream distance of 4.75 rotor diameters. For the forward facing step cases, however, the velocity deficit prediction gets worse with the increase in the edge sharpness. The escarpment with 10% curvature at the edge (with respect to the escarpment height) shows good agreement between the experiments and the model beyond 5 rotor diameters. The other two forward facing step escarpments show an underestimation of the maximum velocity deficit by the model, with the highest difference for the case with a sharp edge. The equivalent wake width shows a similar trend, with the best agreement between the experiments and the model in ramp-shaped escarpment cases and worst in the sharp-edged escarpment. The equivalent wake width width is observed to be underestimated

by the model.

Finally, a comparison of the averaged streamwise velocity deficit profiles is shown in figure 3.21. As can be seen, the velocity deficit are well reproduced for the ramp-shaped escarpments and forward facing step with 10% curvature beyond 5 rotor diameters, even though the effect of wake width underestimation is seen in the vertical profiles. For the rest of the two forward facing step cases, an underestimation of velocity deficit profiles is observed.

The underestimation of the maximum velocity deficit, as well as the equivalent wake width in some cases (as shown in figure 3.20) can be related to the fact that the analytical model used here assumes no pressure gradient in the base flow at the turbine location. This assumption is embedded in the boundary condition given in equation 3.8. In the ramp-shaped escarpments, the pressure gradient imposed by the base flow at the turbine location is not very high, which is why the model gives acceptable results. In the forward facing step escarpments, the agreement between the model and experiments gets worse with the increase in the sharpness of the escarpment edge. As a sharper edge induces a higher pressure gradient via the base flow at the turbine location, the difference between the model and the experiments gets higher. This highlights the need to develop analytical models capable of capturing pressure gradient effects in the base flow at the turbine location.

3.3.6   Wake meandering and trajectory

Defined by low-frequency and large-scale coherent oscillations, meandering is an important dynamical feature of the wake, contributing to the unsteady wake dynamics. To characterize meandering of the turbine wake over different escarpments, we employ a 'center of mass' method (Bastankhah and Porté-Agel, 2017c; Bastine et al., 2015; Howland et al., 2016). The method quantifies the displacement of the center of the instantaneous velocity deficit in the lateral and vertical directions using the following equations:

$$y_c = \frac{\iint \Delta U y \, dy \, dz}{\iint \Delta U \, dy \, dz},$$
(3.11)

$$z_c = \frac{\iint \Delta U z \, dy \, dz}{\iint \Delta U \, dy \, dz}.$$
(3.12)

The information on the instantaneous wake center location in the lateral and vertical direction is then used to compute the joint probability density function (PDF) for different cases. Figure 3.22 shows the joint PDFs for two cases at different streamwise locations. In general, the spread of the instantaneous wake centers is observed to increase with the downstream distance. This spread is higher in the lateral direction compared to the vertical one. The spread in the joint PDFs is higher for the turbine on the FFS escarpment compared to that for the turbine on the ramp-shaped escarpment. This indicates that the FFS escarpment enhances the
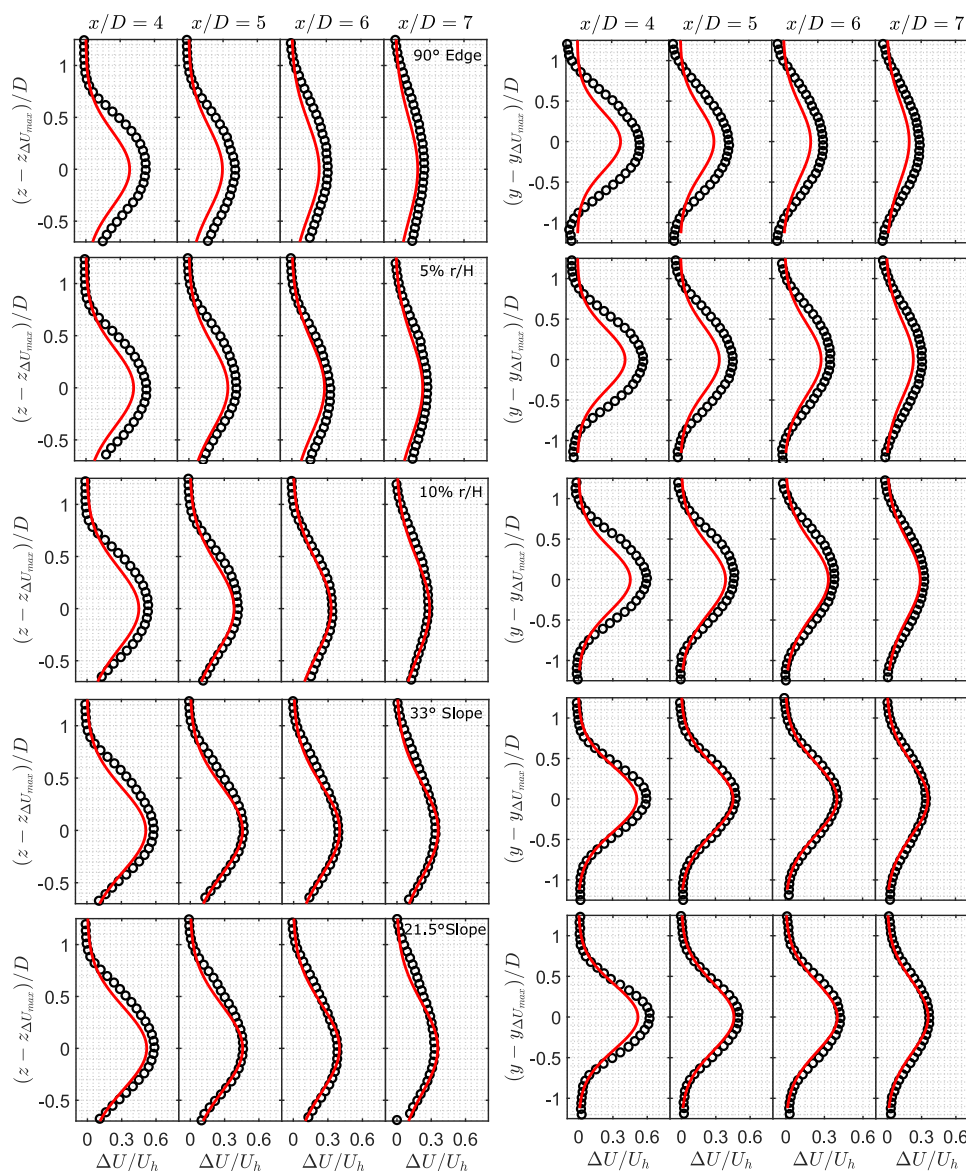
Figure 3.21: Comparison of the normalized averaged streamwise velocity deficit profiles between the analytical models and experiments for different cases. Experimental data is marked by circles and solid line represents the PG model.

meandering of the wake compared to the ramp-shape escarpment. The unsteady nature of the flow separation in the base flow of the FFS escarpment can explain the relatively higher meandering observed in this case.

Another important observation is the vertical displacement of the mean wake center from the turbine axis in figure 3.22. In the near wake, the mean wake center is shifted above the turbine axis, followed by a gradual downward shift with the increase in the downstream distance. This mean wake center displacement is comparatively higher for the turbine on the FFS escarpment
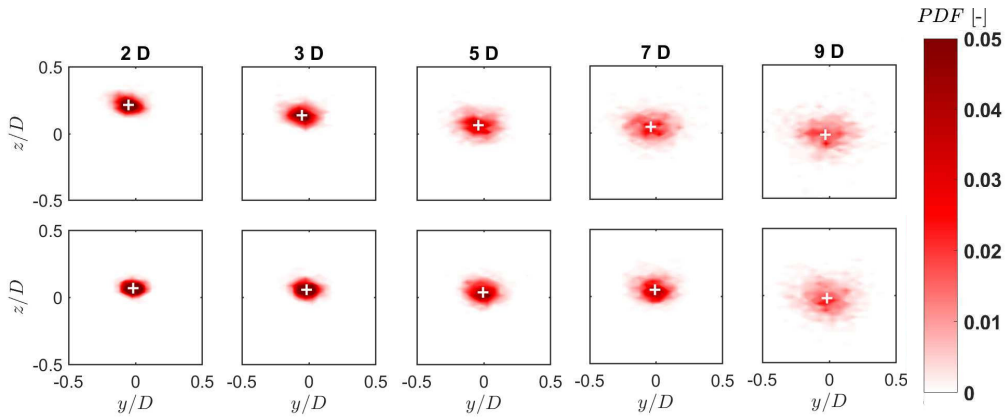
Figure 3.22: Normalized joint probability density function of the instantaneous wake center at different downstream locations for the 90° Edge (top row) and 33° Slope (bottom row). Plus signs indicate the mean wake center.

than for the one on the ramp-shaped escarpment. In addition, the wake trajectory, defined as the vertical position of the maximum velocity deficit $z_{\Delta U_{max}}$ at each streamwise location, is plotted in figure 3.23 for all the cases. The wake is observed to have an upward trajectory in the near wake region with a downward shift in the far wake for the FFS escarpments. For the ramp-shaped escarpments, however, the wake is more attached to the surface and shows a lower trajectory than for the three FFS escarpments. In order to understand this, we first look at the normalized vertical velocity component without the turbine in figure 3.24 (a). The vertical velocity component in the base flow is much higher for the turbine on the FFS escarpment compared to the one on the ramp-shaped escarpment. This high positive vertical velocity component causes the wake to shift upward in the near-wake region for the turbine on the FFS escarpment. As the difference in the mean wake center between the two cases is highest at a downstream distance of 2D, we show the vertical velocity component at this position in figure 3.24 (b). In the case of the ramp-shaped escarpment, the vertical velocity component is solely caused by the wake rotation, with positive and negative vertical velocity in the right and left halves of the wakes, respectively. In the case of the FFS escarpment, however, there is a positive vertical velocity component around the center of the rotor. This positive vertical velocity component is a result of the higher vertical velocity faced by the turbine, and pushes the wake center in the upward direction for the turbine on the FFS escarpment.

3.3.7 Counter-rotating vortex pair and energy entrainment

The non-zero mean vertical velocity component in the base flow also leads to the development of a counter-rotating vortex pair (CVP) in the far wake of the wind turbines sited on the escarpments. The CVP is fully developed in the case of the sharp edge escarpment; therefore, we will focus on the mentioned case in this section. To visualize the formation of the CVP, we show the normalized out-of-plane vorticity in figure 3.25. In the near wake, there is an outward flow from the wake, which creates a negative vorticity region surrounding the rotor. However,
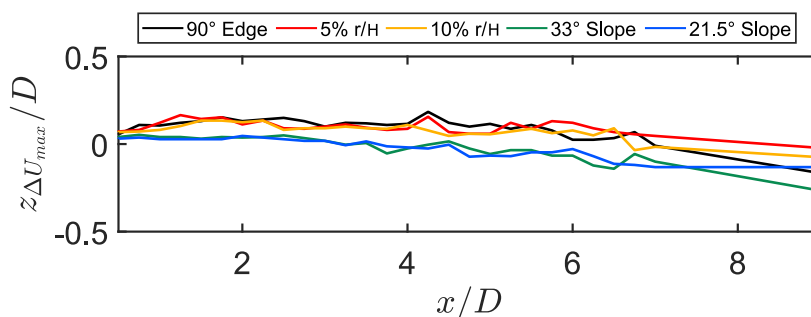
Figure 3.23: Wake trajectory as a function of the downstream distance.
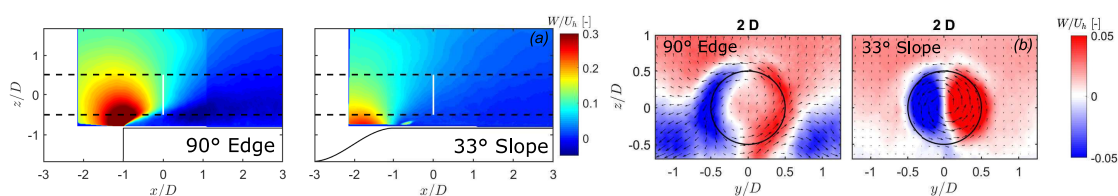
Figure 3.24: (a) Contours of the normalized vertical velocity component on the escarpments without the turbine. White vertical line shows the position of the prospective turbine. (b) Contours of the normalized vertical velocity component at a distance of 2D in the wake of the turbine. The black circle indicates the rotor outline.

as we move downstream ($x/D = 3$), the positive vertical velocity component around the top of the wake diminishes and we observe outer flow moving into the wake due to the presence of a negative vorticity region at the top of the wake. In the far wake, the distribution of the in-plane velocity components becomes almost perpendicular to the surface at the turbine center, depicting a strong vertical component. This vertical velocity component is positive in the region under the rotor center and negative above it, and is believed to give rise to the development of the CVP in order to satisfy continuity. This mechanism is similar to the one observed by Bastankhah and Porté-Agel (2016) in yawed wind turbines, where the formation of a CVP is due to the strong lateral velocity component.

It is to be noted that the vertical velocity component is not as high as the lateral velocity component in yawed turbines, such that it does not cause a significant distortion in the shape of the wake. However, it does appear to play a role in the entrainment of energy from the outer flow into the wake and, thus, contributes to the re-energization of the wake. To explain this, we show two dimensional fields of the advection term of mean kinetic energy in figure 3.26. The advection term is negative in the near wake surrounding the rotor area, where the vorticity is negative, showing an outward flow of energy. As we move downstream, however, when the formation of the vortex pair starts bringing outer flow into the wake, the advection term becomes positive at the rotor top and around the vortex cores, leading to a faster wake recovery in the far wake.
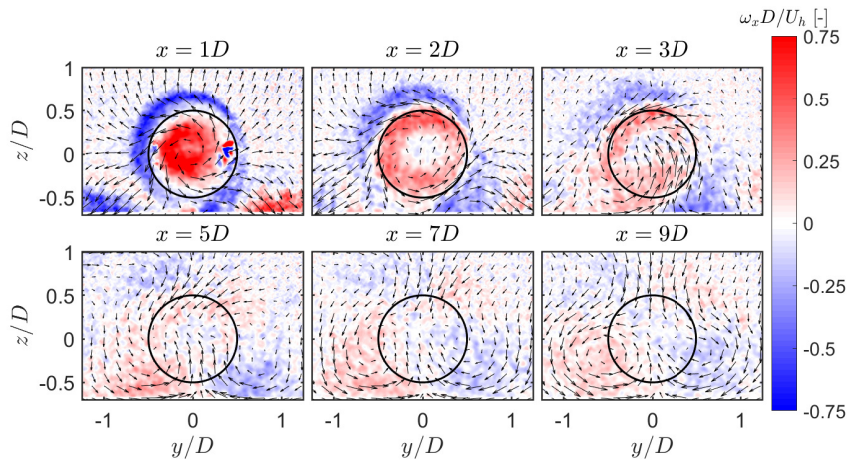
Figure 3.25: Contours of the normalized out-of-plane vorticity with in-plane velocity vectors overlaid for the 90° Edge escarpment. The black circle indicates the rotor outline.
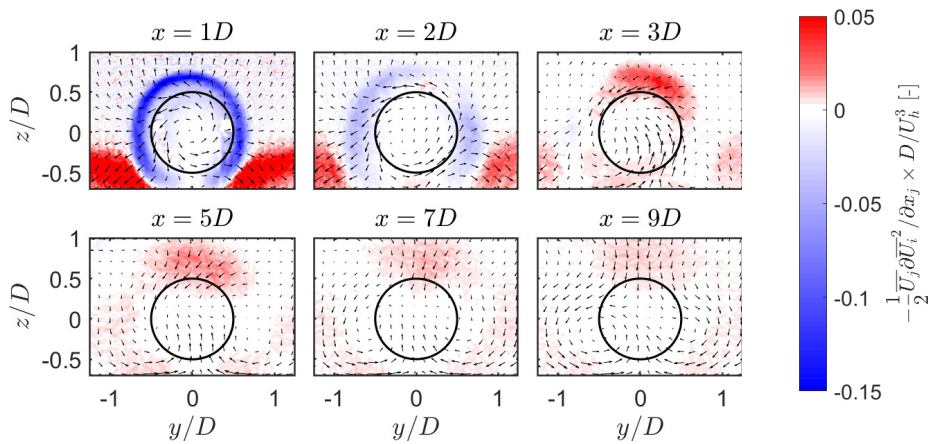
Figure 3.26: Contours of the normalized advection of mean kinetic energy with in-plane velocity vectors overlaid for the 90° Edge escarpment. The black circle indicates the rotor outline.

3.4 Summary

Onshore wind energy has grown tremendously over the last two decades, with wind farms often located in complex terrain. Lack of adequate knowledge of wind turbine behavior in such challenging terrains is known to result in inaccurate estimation of power performance and dynamic loads. Understanding wakes in complex terrain, therefore, has become crucial in today's renewable energy market for better resource assessment, power optimization and layout design of wind farms in such sites. In the current study, we have characterized the wake generated by a single wind turbine sited on different escarpments using stereo-PIV measurements. Escarpments are a common topographical feature and a potential location for wind farms.

Focusing on the sensitivity of the wind turbine wake to the geometrical details of the topography, we have studied five different escarpment models approximated by forward facing steps (FFS) and ramp-shaped escarpments. The shape of the escarpment leading edge is found to have a strong influence on the base flow (flow without the turbine) velocity, shear, speed-up and turbulence over the topography, which eventually have an impact on the wake of the turbine. The presence of the turbine suppresses the development of the flow recirculation near the surface in the wake for the FFS escarpments, and the normalized streamwise velocity in the turbine wake is lowest for the FFS with a sharp edge.

The turbine wake velocity deficit shows fastest recovery and the turbulence kinetic energy is observed to be highest in the case of the FFS with a sharp edge, which is consistent with the highest magnitude of momentum fluxes in this case. By adding a curvature as little as 5% at the leading edge with respect to the escarpment height, the turbulence kinetic energy is significantly reduced compared to the sharp edge case. The turbine wake on the ramp-shaped escarpments shows lower turbulence kinetic energy than the one on the FFS escarpments. Consistent with the amount of turbulence in the base flow, the near wake length is also observed to be shorter for the turbine on the FFS escarpments compared to that on the ramp-shaped escarpments. The streamwise added turbulence intensity in the wake shows that, in comparison to the base flow, the turbine suppresses the production of turbulence below the hub height and enhances it above the hub height for the FFS escarpments. This is because the shear layer formed due to the leading edge flow separation is suppressed in the turbine wake. For the ramp-shaped escarpments, however, the wake flow is more turbulent compared to the base flow except for a small region around the rotor bottom tip level in the near wake region. The wake growth rate in the lateral direction is found to be very similar in all cases; in contrast, it differs in the vertical direction. The vertical growth rate is also observed to be higher than the lateral one, which is related to comparatively higher turbulence and mean flow shear in the vertical direction compared to the lateral one in the turbine wake. The velocity deficit profiles show self-similarity in the far wake for all the cases.

We have also assessed an analytical model for the prediction of velocity deficit in the wake of the turbine sited on escarpments. It is found that the performance of the model depends on

the escarpment shape, as the model works reasonably well for the ramp-shaped escarpments, but underestimates the maximum velocity deficit and wake width for the forward facing step cases. This is due to the fact that the analytical model assumes no pressure gradient induced by the base flow at the turbine location, whereas, in the forward facing step cases, the induced pressure gradient by the base flow at the turbine location is not negligible. Future research should address this limitation of the analytical model.

The shape of the escarpment is also observed to affect the instantaneous location of the turbine wake center and, thereby, the dynamics of wake meandering, with higher meandering in the FFS escarpments compared to the ramp-shaped ones. This is associated with the unsteadiness of the base flow, which is higher for the FFS due to the dynamic nature of the flow separation. The center of the wake is shifted above the turbine hub height in the near wake of the turbine on the FFS escarpment, with a gradual downward shift in the far wake. This is associated with a higher vertical velocity component in the base flow. The relatively large vertical velocity component also leads to the formation of a counter-rotating vortex pair in the far wake of the 90° Edge FFS escarpment, which plays a role in the energy entrainment from the outer flow into the wake.

4 Influence of wind direction on flow over a cliff and its interaction with a wind turbine wake [I]

Abstract

This work investigates the effect of wind direction on the flow over a cliff and its interaction with the wake of a wind turbine sited on the cliff. The cliff is modeled as a forward-facing step, and five wind directions are tested (θ = 0°, 15°, 30°, 45° and -45°). The flow becomes increasingly three-dimensional with the increase in the wind direction and a cross-stream flow separation develops from the cliff leading-edge. The turbulence kinetic energy decreases for wind directions higher than 15°, which is due to the absence of the streamwise flow separation for higher wind directions. The cross-stream flow development in the base flow affects the shape of the turbine wake. A two-dimensional Gaussian fit is performed on the wake velocity deficit, where the wake recovery slows down for wind directions higher than 15°, and the wake width is larger for higher wind directions. The wake shows higher deflection and tilt angle for higher wind directions. Analysis of the streamwise momentum in the wake reveals that the advection terms play a role in slowing the wake recovery for higher wind directions.

[I]The contents of this chapter are under review for publication in *Physical Review Fluids*.

4.1 Introduction

Concerns over the role of fossil-fuel-based energy sources in climate change have resulted in a push towards renewable energy sources. According to the International Renewable Energy Agency (IRENA, 2021), new renewable energy installations are now economically more viable than their fossil fuel counterparts. Onshore wind energy, in particular, is one of the cheapest available sources of energy, with the levelized cost of energy falling 56% over the last decade (IRENA, 2021) while accounting for 95% of the global wind energy capacity (GWEC, 2021). As countries across the world are setting ambitious goals towards renewable energy, wind energy is expected to grow at an unprecedented rate. To ensure the successful growth of wind energy, an improved understanding of the interactions between wind turbines and the atmospheric boundary layer is needed. Wind turbines are often installed in groups forming wind farms, where due to spatial constraints, certain turbines have to operate in the wake of the upstream ones. The low velocity and enhanced turbulence experienced by the in-wake turbines result in reduced power production and enhanced fatigue loads. Turbine wakes are very complex and their characteristics depend on a multitude of factors such as the boundary layer flow shear, surface roughness, terrain features, thermal stability, and turbulence intensity. Extensive efforts have been made to understand the interaction between wind turbines and the atmospheric flow under a variety of scenarios. For a detailed review of the state-of-the-art, the reader is referred to Porté-Agel et al. (2020) and Stevens and Meneveau (2017).

As onshore wind energy grows, the likelihood of wind farm installations in complex terrain also increases. This is motivated, in part, by the high available resources on top of hills and partly due to a lack of better alternatives (Alfredsson and Segalini, 2017). However, as stated by Porté-Agel et al. (2020), most of the existing literature concerning wind turbine and wind farm flows is limited to flat terrain. Although, the first studies investigating wind turbine wakes in complex terrain date back to the early 90s (Helmis et al., 1995; Stefanatos et al., 1994; Taylor and Smith, 1991), the topic has gained a renewed interest from the scientific community in recent years. For boundary layer flows over complex topography, on the other hand, the literature is very rich, thanks to a wide range of analytical, numerical and experimental efforts over the last 50 or so years.

The seminal work of Jackson and Hunt (1975) laid foundations for analytical studies of flow over hills with low slopes. They presented an expression for two-dimensional flow over arbitrary hills using perturbation methods. Their work was extended to three-dimensional hills by Mason and Sykes (1979), and a more rigorous attempt was made by Sykes (1980), who presented an asymptotic approach to flows over two-dimensional hills. Several studies attempted to validate the analytical model by Jackson and Hunt (1975) against wind tunnel (Britter et al., 1981) and field (Taylor et al., 1987) measurements. Attempts to include non-linear effects into the analytical expressions were made by Xu et al. (1994). Among the most notable experimental campaigns are the Askervein hill project (Taylor and Teunissen, 1987) and the Bolund hill experiment (Berg et al., 2011), which have served as benchmarks for numerical models attempting to capture flow in complex terrain. Since the 90s, large-eddy simulation

(LES) based numerical approaches have become increasingly popular for investigating flow over topography (Bechmann et al., 2011; Diebold et al., 2013; Gong et al., 1996; Liu and Stevens, 2020b; Mason, 1994; Wan and Porté-Agel, 2011). It is to be noted that the list of studies concerning boundary layer flows in complex terrain presented here is not exhaustive by any means, and for a more detailed review, the reader is referred to Finnigan et al. (2020).

Changes in terrain elevation can lead to high levels of flow shear, high spatial variability in flow characteristics, formation of localized flow structures (such as regions of flow separation from cliffs and wakes of hills), and terrain-induced local pressure gradients. Wake characteristics of wind turbines sited in complex terrain are strongly dependent on terrain characteristics, which is why a number of studies exploring turbine wakes in various idealized and real complex terrains have recently emerged. Mattuella et al. (2016) tested a scaled-down model of a complex site located in Spain inside a wind tunnel. They concluded that very careful layout optimization for wind farms in complex terrains is required due to high variation in mean velocity and turbulence across the terrain. Tian et al. (2013) experimentally investigated the power performance and wake of a wind farm sited on a sinusoidal hill. They showed that, compared to a wind farm in flat terrain, the hill influenced the power and wake characteristics of the wind farm. Yang et al. (2015) performed a numerical investigation of a wind turbine sited downstream of a three-dimensional hill. They showed that wake characteristics of the turbine were affected by both the height of the upstream hill, and spacing between the hill and the turbine. In their experimental study of wind turbine on periodic hills, Hyvärinen and Segalini (2017b) showed that a hilly terrain leads to a faster wake recovery. Shamsoddin and Porté-Agel (2018b) presented a combined analytical and numerical study of the wake of a wind turbine sited upstream of a hill. By dividing the flow over the hill into two regions corresponding to favorable and adverse pressure gradients, they showed that the wake recovery can be faster or slower compared to a flat terrain depending on the turbine location across the hill.

Wake trajectory in a complex terrain sited in Perdigão was investigated by Menke et al. (2018), who showed that the wake follows the terrain under stable conditions, deflects upwards under unstable conditions and shows no deflection in neutral conditions. Self-similarity of the wake velocity deficit is a common assumption in many analytical models. This assumption was verified by Dar et al. (2019) for a real complex terrain. Liu and Stevens (2020a) investigated the effect of two-dimensional hills on power performance of wind turbines and wind farm sited across them. They found that, for turbines taller than the hill, a power boost can be observed due to speed up from the hill. For turbines smaller than the hill, on the other hand, their performance depend on the location along the hill. For a hill located in the middle of a wind farm, turbines located downstream of the hill experience the wake of the hill, which can affect their performance. Liu et al. (2021) performed large-eddy simulation of wind turbine wake across two- and three- dimensional hills, and varied the ratio of turbine height to hill height. Interested in the wind turbine wake superposition over complex terrain, they investigated two different strategies, where one was based on superposition along the turbine hub height and the other along the streamline of the flow originating from the turbine hub height. From their results, they concluded that the second superposition method produced better results.

More recently, Dar et al. (2023) performed an experimental and analytical investigation of a wind turbine exposed to a range of pressure gradients. They showed that the wake deficit, expansion and power coefficient vary systematically with the change in the pressure gradient. Atmospheric stability is another important factor that can have significant effect on turbine performance and wakes, and its importance in complex terrain has instigated several recent studies (de Sá S. et al., 2022; Han et al., 2018; Liu and Stevens, 2021; Radünz et al., 2021).

Cliffs are a common topographical feature and a potential site of wind farms. Rowcroft et al. (2019) presented a brief list of wind farms across the world which are sited close to cliff edges and potentially affected by the leading edge flow separation. Bowen and Lindley (1977) were the first to investigate the effect of the cliff shape on the flow over it. Lange et al. (2017) showed that the flow over the cliff is highly sensitive to minor modifications to the leading edge shape, which can have significant effects on the power available to the wind turbines. Schulz et al. (2016) compared the performance of a turbine sited on flat terrain and on a steep escarpment. They found that the turbine sited on the escarpment experienced higher loads compared to the one on the flat terrain. Qian and Ishihara (2019) performed detached-eddy simulation of a wind turbine sited close to the edge of an escarpment. They showed that the turbine wake characteristics depend on the ratio between turbine hub height and escarpment height. Dar and Porté-Agel (2020, 2022b) performed wind tunnel experiments to investigate the wake of a wind turbine sited close to an escarpment edge. They tested different leading edge shapes of the escarpment and showed that the wake characteristics of the turbine were affected by the escarpment shape. In addition, they used the experimental data to validate an analytical model for wind turbines experiencing a pressure gradient imposed by the base (without turbine) flow (Dar and Porté-Agel, 2022a).

Flow over cliffs has often been approximated by the flow over forward facing steps. A comprehensive body of literature has explored flow over forward facing steps and its dependence on a number of flow and geometrical parameters (Awasthi et al., 2014; Graziani et al., 2017, 2018; Largeau and Moriniere, 2007; Ren and Wu, 2011; Sherry et al., 2010). Most of the literature deals with the flow direction perpendicular to the leading edge of the forward facing step. In the atmospheric boundary layer, however, wind direction is not always perpendicular to the leading edge. Only a handful of studies deal with the effect of direction on flow over forward facing steps. Rowcroft et al. (2016) investigated the flow over forward facing steps under different yaw angles and found that half a cliff height above and downstream of the leading edge is the optimal position with respect to flow speed-up and turbulence intensity for turbine placement. Barthelmie and Pryor (2018) performed a combined field and modeling study to understand the effect of changing wind direction on flow speed-up over a cliff. The height of the cliff was 12 m, which is relatively small compared to the hub height of modern wind turbines. They observed that the flow speed-up over the cliff was maintained for wind directions within ±25° from the direction perpendicular to the cliff edge. Hesp and Smyth (2021) performed numerical simulation of flow over scarps modeled as forward facing steps. Concerning the wind direction, they found that the flow deceleration decreases with increasing obliqueness of the wind direction, and showed the flow pattern using streamlines. To the

best of the authors' knowledge, the interaction of wind turbine wake with the flow over a cliff under different wind directions has not been investigated in the literature yet.

This work aims at providing useful insights into the physics of the flow over a cliff modeled as a forward facing step under different wind directions. A comprehensive analysis of the interaction between such flow and a wind turbine wake is also performed. Wind farms sited on cliffs are known to under-perform in terms of power and experience high loads due to the lack of sufficient understanding of the base flow (Lange et al., 2017), which makes it extremely important to explore this topic in further detail. Wind tunnel experiments are performed, where the effect of wind direction is simulated by yawing the leading edge of the cliff. The rest of the article is organized as follows: the description of the experimental setup is provided in section 4.2; the results from the study are presented in section 4.3; and finally, a summary and some concluding remarks are given in section 4.4.

4.2 Experimental setup

The experiments are performed in the closed-loop boundary-layer wind tunnel at the WiRE laboratory of EPFL. The wind tunnel has a maximum wind speed of 25 ms^{-1}, with an area contraction ratio of 5:1 at the inlet of the test section. The height and width of the test section are adjusted to yield an approximately zero pressure gradient along the length of the test section. At about 20 m downstream of the test section, the height and width are 2 m and 2.56 m, respectively. The test section is 28 m in length, with a smooth aluminum floor. A turbulent boundary layer develops along the length of the test section without the use of any external tripping mechanism. The flow in the wind tunnel is driven by a 130 kW fan.

A three-bladed miniature horizontal axis wind turbine named WiRE-01 is used in the experiments Bastankhah and Porté-Agel (2017a). The turbine has a rotor diameter D of 15 cm and a hub height z_h of 12.5 cm. The blade profile is a thick plate with a circular arc shape with a 5% camber and 5% thickness with respect to the chord length. The chord length varies from 12 mm at the root to 8.4 mm at the tip. The rotor is manufactured by 3d printing using a liquid photopolymer resin. The nacelle of the turbine is a direct current motor manufactured by Maxon motors (model: DCX10L), which has a diameter and length of 10 mm and 25 mm, respectively. The motor is controlled by a servo controller also manufactured by Maxon motors (model: ESCON 36/2 DC) via a digital encoder (model: ENX10).

The cliff is modeled as a forward facing step with a height H equal to the hub height of the miniature turbine (i.e. 12.5 cm). The width of the model is 2.5 m and its length varies between 3-3.5 m along the center of the span in different cases. It is to be noted that the ratio of length L and width W of the forward facing step to its height H are high enough such that the flow separation and reattachment from the leading edge are independent from the dimensions of the step. The reattachment length of the separated flow from the leading edge is known to become independent from the geometrical dimensions for $L/H > 4$, and for flow direction perpendicular to the leading edge $W/H > 9$ yields a two-dimensional flow
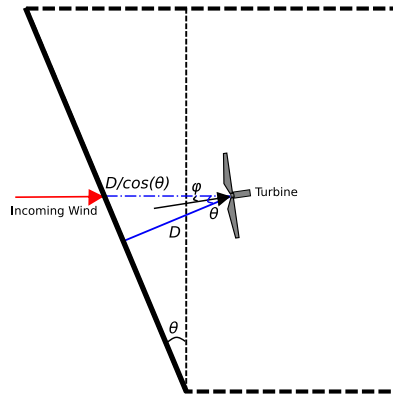
Figure 4.1: A sketch of the directional and angular conventions (not to scale). Black arrow shows the local wind direction at the turbine hub height.

(Bergeles and Athanassiadis, 1983; Graziani et al., 2017). As the incoming wind direction is fixed in the wind tunnel, the leading edge of the forward facing step is yawed at different angles to simulate the effect of changing wind direction. Five different wind directions are simulated: $\theta = \{0°, 15°, 30°, 45°, -45°\}$, where $0°$ represents the wind direction perpendicular to the leading edge of the cliff. The negative angle is simulated to investigate if the rotational direction of the turbine relative to the incoming wind direction can have an impact on its wake. The turbine is placed $D/cos(\theta)$ from the leading edge of the cliff along the centerline. This is done considering that in reality, with increasing wind direction, the wind will travel a longer distance on the cliff to reach the turbine. The resulting distance d from the leading edge along the centerline is 15 cm, 15.5 cm, 17.3 cm and 21.2 cm for wind directions $0°$, $15°$, $30°$ and $\pm 45°$, respectively. To account for the wind veering effect caused by the interaction of incoming flow with the yawed leading edge of the cliff, the wind turbine is aligned with the local wind direction at the turbine hub height. This is done in consideration with the fact that for commercial wind turbines, the wind vane mounted on the nacelle is used to align the turbine with the incoming flow. The wind veer ϕ is extracted from the base flow data at the turbine hub location: $\phi = \{0°, 4°, 7°, \pm 8.5°\}$ for wind directions $\theta = \{0°, 15°, 30°, \pm 45°\}$, respectively. Figure 4.1 shows a sketch of the directional and angular conventions used in the study.

A stereoscopic particle-image velocimetry (S-PIV) system is used to obtain high spatial resolution cross-stream (yz-plane) flow measurements on the cliff. The S-PIV system comprises of two 16-bit sCMOS cameras (2560 × 2160 pixels) with 50 mm objectives and mounted on Scheimpflug adapters to correct the camera focus on to the measurement plane. The camera aperture is fixed at $f/2.8$ with f being the focal length of the objective (i.e. 50 mm). An angle of 45° is kept between the two cameras and the size of the field-of-view (FOV) is $4D \times 3D$ at a spatial resolution of about $0.016D$. The field of view is illuminated with a double-pulsed Nd:YAG laser at a wavelength of 532 nm. Following Zong and Porté-Agel (2020a), the thickness of the laser sheet is kept at 10 mm to minimize the loss of particle pairs due to out-of-plane motion. Measurements are acquired at a sampling rate of 10 Hz and 1000 instantaneous
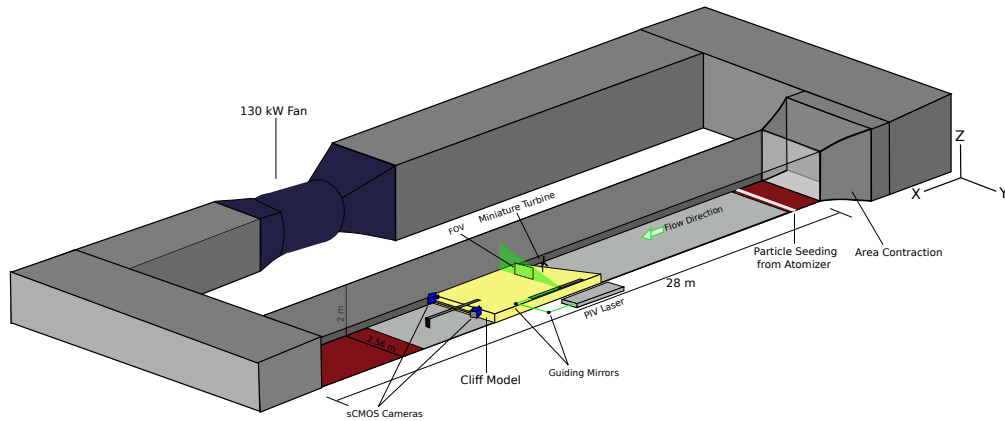
Figure 4.2: A schematic of the experimental setup in the wind tunnel.

fields are used to obtain time-averaged flow statistics. A programmable timing unit (LaVision, PTU-v9) is used to synchronize the cameras and the laser. Olive oil droplets of several microns in diameter are generated using an in-house atomizer array and injected into the wind tunnel through a slot in the floor close to the inlet of the test section. Both cameras and the laser optics used to expand the laser beam into a sheet are mounted on synchronized high precision motorized traversing systems (ZABER X-LRT) to facilitate cross-stream measurements at different downstream positions. For flow measurements without the turbine (base flow), measurements are taken from the prospective turbine location until 8 rotor diameters downstream, whereas for the turbine wake flow, measurements are taken from 1.5 rotor diameters behind the turbine until 8 rotor diameters. The streamwise interval between measurement planes is 0.25 rotor diameter for downstream distance up to 5 rotor diameters, whereas it is 0.5 rotor diameters for downstream distance greater than 5 rotor diameters. Following this procedure, 27 FOVs in the base flow and 21 FOVs in the wake flow are captured for each wind direction, resulting in a total of 240 FOVs.

The image post-processing is performed in double-pass reducing size interrogation windows of 64 × 64 pixels and 32 × 32 pixels with a 75% overlap between neighboring windows. A universal outlier detection method is used to filter any bad vectors from the PIV data. The maximum uncertainty in mean velocity is estimated to be around $0.05\ ms^{-1}$ using a correlation statistics approach (Wieneke, 2015). A schematic sketch of the experimental setup is shown in figure 4.2.

The performance of the turbine on the cliff is also characterized. The power and thrust coefficients of the turbine are measured and plotted in figure 4.3 for different wind directions as a function of tip speed ratio. The mean power P generated by the turbine is measured by multiplying the torque generated by the motor Q with its rotational speed Ω, where the generated torque is estimated by multiplying the generated current I with the torque constant K of the motor and adding the frictional torque Q_f of the motor. For more details on power measurement, the reader is referred to Bastankhah and Porté-Agel (2017a). The power
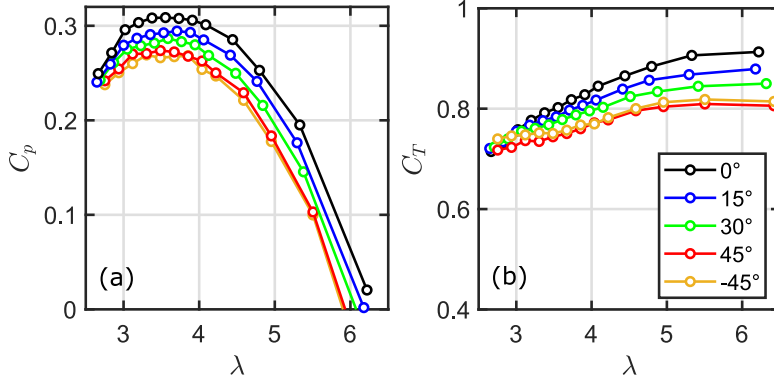
Figure 4.3: (a) Power coefficient and (b) thrust coefficient of the turbine on the cliff for different wind directions as a function of tip speed ratio.

coefficient C_p is then computed as:

$$C_p = \frac{P}{\frac{1}{2}\rho A U_h^3} = \frac{Q\Omega}{\frac{1}{2}\rho A U_h^3},$$ (4.1)

where ρ is the air density, A is the rotor area and U_h is the hub height velocity at the turbine hub position. A maximum power coefficient C_p of 0.31 is observed for the 0° wind direction, which decreases with the increase in the wind direction. This decrease in the C_p can be related to the increased wind veer with increasing wind direction and a lower hub height velocity. The maximum C_p is observed at a tip speed ratio λ of around 3.5, which is used to operate the turbine for flow measurements. It is to be noted that the tip speed ratio is varied by changing the rotor rotational speed while keeping the incoming wind at a constant value.

The thrust force T experienced by the turbine rotor is measured using a multi-axis strain gauge sensor (model: ATI-nano-17Ti). The thrust coefficient C_T is computed as:

$$C_T = \frac{T}{\frac{1}{2}\rho A U_h^2}.$$ (4.2)

Similar to the power coefficient, the thrust coefficient shows a slight decrease with increase in the wind direction and varies between 0.75-0.8 at the optimal tip speed ratio. The thrust coefficient C_T measured here is comparable to that of real-scale commercial wind turbines. The hub height velocity U_h for different cases is $U_h = \{4.56, 4.45, 4.4, 4.15, 4.25\}\ ms^{-1}$ for wind directions $\theta = \{0°, 15°, 30°, 45°, -45°\}$, respectively. The hub height velocity for each case is used to normalize all flow quantities in the respective cases.

The turbulent boundary layer upstream of the cliff is measured using a two-dimensional, two-component (2D2C) particle-image velocimetry system with a single sCMOS camera. Figure 4.4 shows the normalized averaged streamwise velocity U/U_h and streamwise turbulence intensity $I_u = \sigma_u/U_h$ in the upstream boundary layer flow with σ_u as the standard deviation in the streamwise velocity. A power law fit according to $U = U_h(\frac{z}{z_h})^n$ is also shown in figure
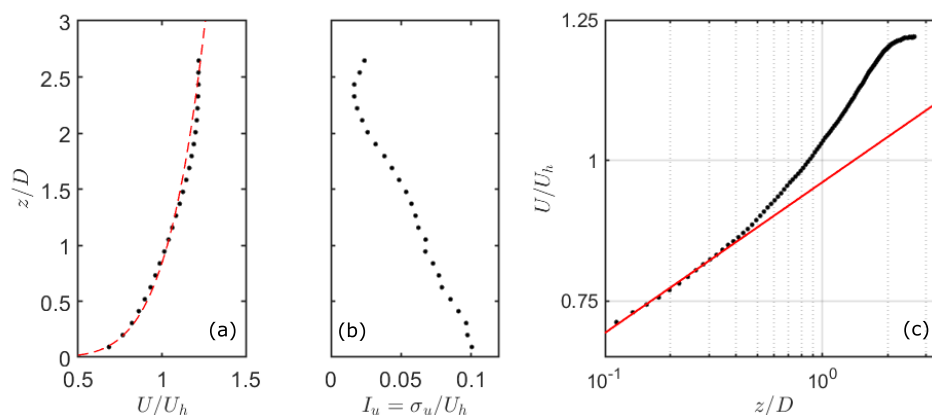
Figure 4.4: Upstream boundary layer profile: (a) normalized averaged streamwise velocity with a power law fit shown with red dotted line and (b) streamwise turbulence intensity and (c) normalized averaged streamwise velocity in logarithmic coordinates with a logarithmic law fit in red line.

4.4 (a), which yields an exponent n equal to 0.17. The boundary layer height is estimated to be around 36 cm, and the streamwise turbulence intensity at the height of the cliff is 7.3%. A logarithmic fit according to $U = \frac{u_*}{\kappa} log(\frac{z}{z_0})$ is done on the lowest 15% of the boundary layer, which corresponds roughly to the height of the surface layer. Here, u_* is the friction velocity, which is estimated to be 0.17 ms^{-1}, κ is the von-Karman constant assumed to be 0.41, and z_0 is the aerodynamic roughness length estimated to be 0.04 mm. The logarithmic fit is shown in figure 4.4 (c).

4.3 Results

In this section, we present results from the experiments. First, we discuss the flow over the cliff under different incoming wind directions without any wind turbine (termed as base flow). Understanding how wind direction affects the flow over a forward facing step is important from a fundamental perspective. Following the base flow, we analyze the wake flow, which mainly deals with investigating the interaction between the base flow and the wake of the wind turbine sited on the cliff. It is to be noted that averaging in the current work refers to time-averaging, unless otherwise mentioned.

4.3.1 Base flow

For wind directions perpendicular to the leading-edge of the FFS, a flow separation occurs from the leading edge with a recirculation. This flow separation and subsequent reattachment has been found to depend on many factors such as the Reynolds number, ratio of boundary layer height to step height and incoming turbulence level (Essel and Tachie, 2017; Sherry et al., 2010). Here we show how the change in wind direction affects the streamwise flow separation
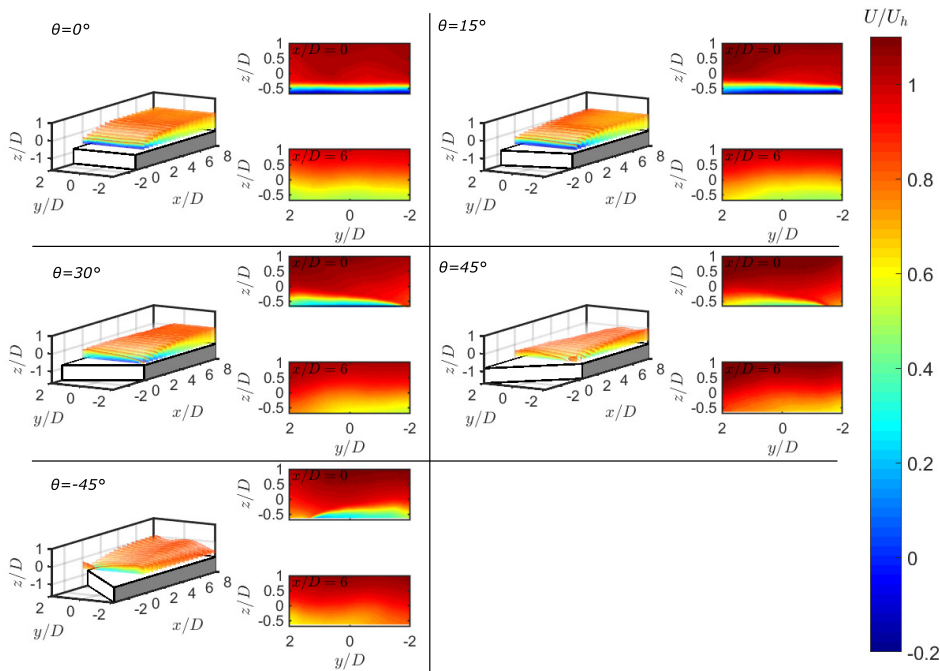
Figure 4.5: Contours of the normalized averaged streamwise velocity in the base flow. The three-dimensional plot shows the development of the shear layer from the cliff leading edge. The three-dimensional contours show steramwise velocity in the range $U/U_h < 0.85$.

from the leading-edge. Figure 4.5 shows the contours of normalized averaged streamwise velocity in the base flow. For $\theta = 0°$, flow separation near the leading edge is observed. The flow reattaches with the surface at about 2 rotor diameters downstream of the leading edge. For $\theta = 15°$, streamwise recirculation (marked by the presence of negative streamwise velocity) is present and stronger near the leading edge in the spanwise direction. A spatial heterogeneity in the spanwise direction also starts to develop in the flow. For wind directions higher than 15°, no streamwise recirculation is observed. The spanwise heterogeneity is also observed to increase with increase in the wind direction. The streamwise velocity is lower on the side of the span closer to the leading edge at larger downstream distances.

To investigate the spanwise flow induced by the FFS leading-edge, we plot contours of the normalized averaged spanwise velocity along with the streamlines of the cross-stream velocity components in figure 4.6. For the wind direction perpendicular to the leading edge, the spanwise velocity is very to close to zero over the FFS, indicating a two-dimensional flow. The streamlines show a vertical velocity, which is induced by the cliff leading edge. With the increase in the wind direction, the yawed leading edge of the step induces a spanwise velocity. This spanwise velocity along with the vertical velocity component leads to the formation of a spanwise recirculation close to the leading edge. The strength of the spanwise recirculation increases with the increase in wind direction. For wind directions above 15°, as the streamwise recirculation disappears, the streamwise velocity advects the spanwise recirculation in the
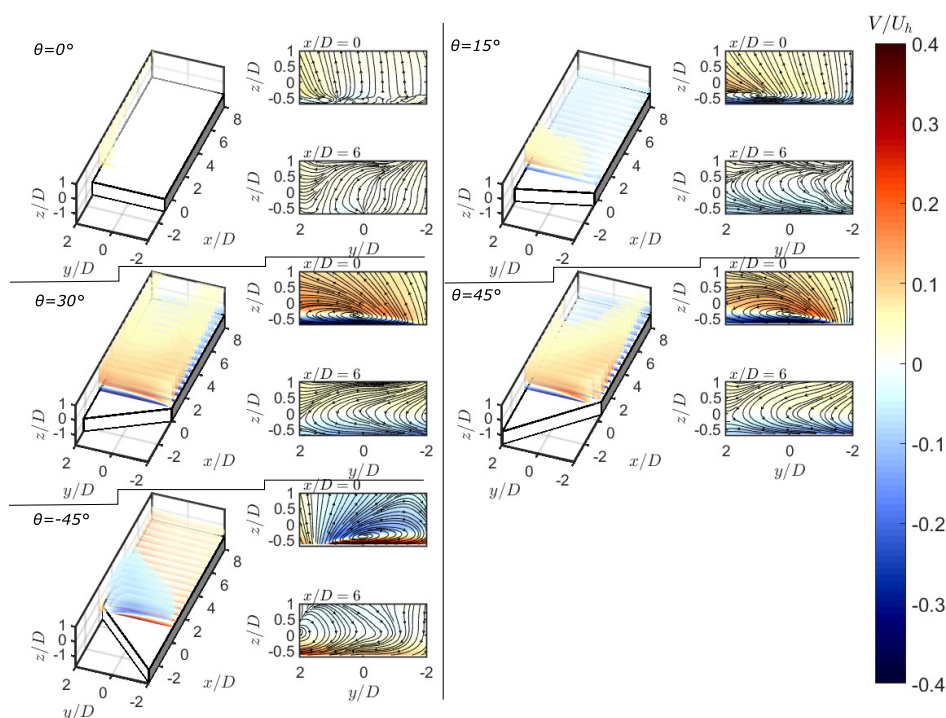
Figure 4.6: Contours of the normalized averaged spanwise velocity in the base flow. Streamlines of the cross-stream velocity profiles are overlaid on the two-dimensional contour plot. The three-dimensional contours show spanwise velocity in the range $-0.04 > V/U_h > 0.04$.

streamwise direction, leading to the helical vortex formation. Further downstream from the leading edge, the spanwise velocity reduces in magnitude, but it still maintains the directional preference dictated by the spanwise recirculation and gives rise to a wind veering effect.

We now focus on turbulence characteristics in the base flow. Figure 4.7 shows the contours of the normalized turbulence kinetic energy $tke = \frac{\overline{u'^2} + \overline{v'^2} + \overline{w'^2}}{2}$, where u', v' and w' are the fluctuating components of the streamwise, spanwise and vertical velocity, respectively. The turbulence kinetic energy over the FFS is contributed by that in the incoming flow and that generated by the shear induced by the separating flow from the leading edge. The second mechanism usually contributes more than the first one as high shear close to the leading edge generates most of the turbulence over the FFS. For the wind direction perpendicular to the leading edge of the FFS, high tke is observed close to the edge which decreases further downstream due to the expansion of the shear layer developed from the leading edge. Interestingly, the normalized tke increases in magnitude for $\theta = 15°$ compared to $\theta = 0°$. However, for wind directions greater than 15°, a decrease in the magnitude of normalized tke is found. A similar observation was made by Rowcroft et al. (2016), who found that the turbulence intensity gain over the FFS maximized at $\theta = 20°$; no explanation was, however, provided in their work. In the following, we provide a physical explanation for the tke trend.

To understand the tke trends observed in figure 4.7, we look into the primary mechanism

responsible for turbulence generation. In a turbulent flow, the turbulence kinetic energy is extracted from the mean flow. Figure 4.8 shows contours of the normalized turbulence production via shear in the mean flow. Total production due to all cross-stream gradients is included, as well as the individual contribution of shear in averaged streamwise velocity and vertical shear in averaged spanwise velocity are shown. It is to be noted that the contribution of streamwise gradients is excluded due to relatively longer distance between consecutive measurement planes. However, this exclusion does not affect our discussion, as streamwise gradients are relatively less important compared to the cross-stream gradients (Rolin and Porté-Agel, 2018).

The normalized total production of tke shows a similar trend to that of tke, with a decrease in magnitude for $\theta > 15°$ (figure 4.8 (a)). The contribution of shear in averaged streamwise velocity also shows a similar trend in figure 4.8 (b). The decrease in the contribution of shear in averaged streamwise velocity can be associated with the streamwise recirculation in the flow. As shown earlier, the streamwise recirculation is observed for $\theta = \{0°, 15°\}$, whereas it disappears for higher wind directions. As the streamwise recirculation disappears, the shear in the averaged streamwise velocity decreases which eventually leads to lesser turbulence production. With increasing wind direction, however, a spanwise recirculation is induced. To understand its role in turbulence production, we plot contours of the normalized turbulence production due to vertical shear in averaged spanwise velocity in figure 4.8 (c). As expected, the contribution from this term to turbulence production increases with increasing wind direction. However, the magnitude of this term is almost three times less than that of the turbulence production due to averaged streamwise velocity. Therefore, the increase in the contribution of vertical shear in spanwise velocity towards turbulence production cannot compensate for the decrease in turbulence production due to shear in streamwise velocity, and an overall decrease in turbulence production is observed for wind directions above 15°. It is to be noted, however, that for wind directions above 15°, recirculation in spanwise velocity still plays a major role in overall turbulence production.

4.3.2   Wake flow

We now turn our attention to the wake of a wind turbine sited on a cliff under different incoming wind directions. Our primary focus is to understand how the complicated base flow generated by the cliff interacts with the wake of the wind turbine and affect its characteristics.

Time-averaged flow characteristics

Figure 4.9 shows the contours of the normalized averaged streamwise velocity in the turbine wake for different incoming wind directions. For wind direction $\theta = 0°$, the normalized averaged streamwise velocity is observed to be symmetrical in the spanwise direction across the centerline of the turbine. With the increase in the wind direction, the shape of the wake is observed to change due to the interaction with the base flow. For $\theta = 15°$, the streamwise
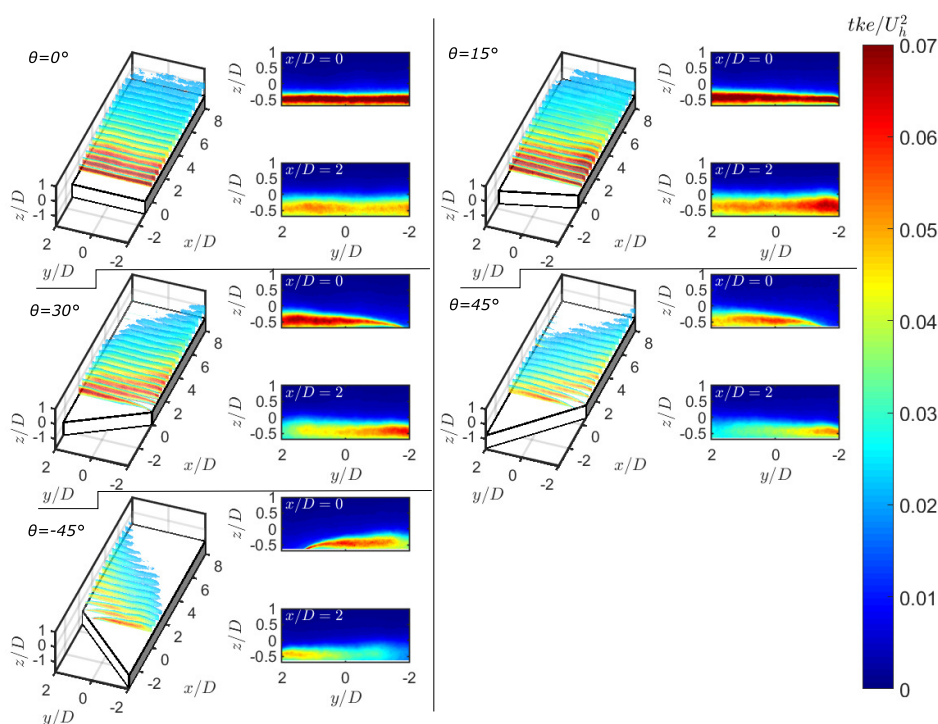
Figure 4.7: Contours of the normalized turbulence kinetic energy in the base flow. The three-dimensional contours show turbulence kinetic energy in the range $tke/U_h^2 > 0.02$.

velocity shows an asymmetrical distribution, with a low-speed region on the right and a high-speed one on the left of the rotor projected area. This asymmetry in the streamwise velocity is observed to increase with the streamwise distance and can be observed in the far wake as well. For $\theta = 30°$, a similar asymmetrical distribution is observed in the near wake, with low and high speed regions on the right and left of the turbine, respectively. In the far wake, however, the streamwise velocity shows a relatively symmetrical profile. Within the rotor projected area in the near wake, the streamwise velocity minimum is observed to be shifted away from the rotor center position. The low speed region outside the rotor projected area also appears to be merged with the turbine wake for $\theta = \{15°, 30°\}$, whereas for $\theta = 0°$, the wake and base flow do not merge together. For $\theta = 45°$, the wake shape within the rotor projected area is observed to be affected significantly by the base flow, where it is shifted away from the rotor centerline close to the surface. For $\theta = -45°$, a similar behavior is observed with an opposite orientation. This shows that the relative rotation of the wake and spanwise recirculation does not have a significant impact on the spatial distribution of the streamwise velocity in the turbine wake.

The magnitude of the normalized averaged streamwise velocity is also observed to be affected by the incoming wind direction (see figure 4.9). The wind direction perpendicular to the cliff leading edge shows lowest normalized averaged streamwise velocity in the turbine wake, where the values of U/U_h are observed to increase with the increase in the wind direction. This can be related to the normalized averaged streamwise velocity in the base flow, which
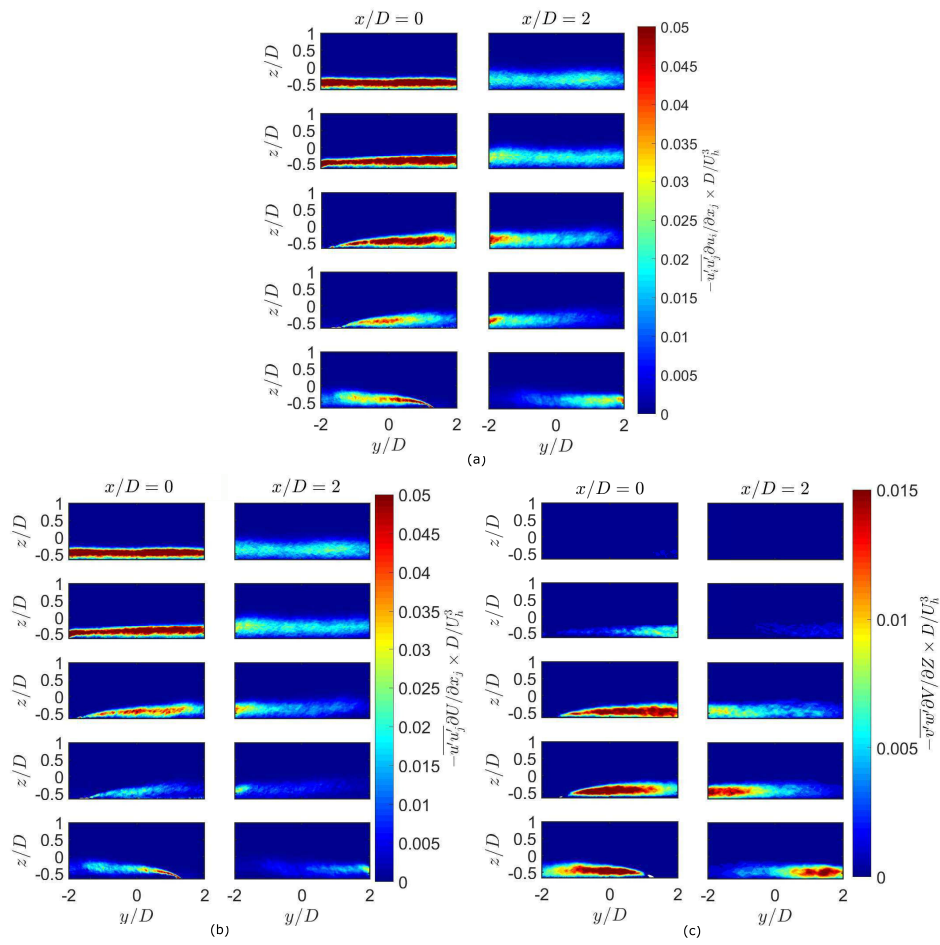
Figure 4.8: Contours of the normalized turbulence production via shear: (a) total production, (b) production due to shear in averaged streamwise velocity and (c) production due to vertical shear in averaged spanwise velocity. From top to bottom: 0°, 15°, 30°, 45° and -45°.
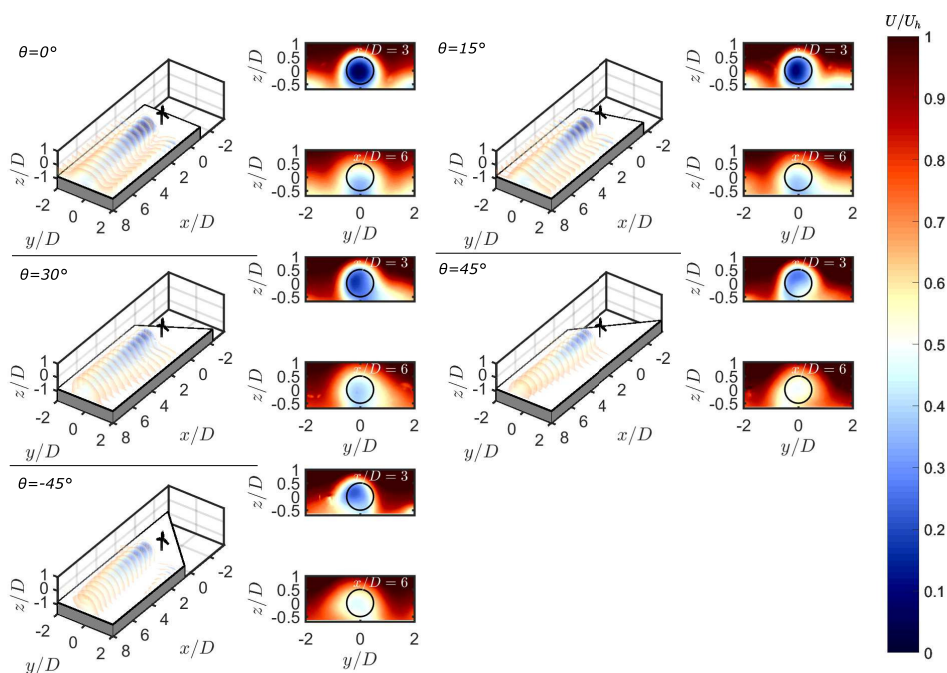
Figure 4.9: Contours of the normalized averaged streamwise velocity in the turbine wake. The three-dimensional plot shows streamwise velocity in the range of $U/U_h < 0.7$. The black circles in two-dimensional contours show the rotor projected area.

shows a similar trend with wind direction. The increase in the magnitude of U/U_h with the wind direction can be due to the decrease in the shear in the averaged streamwise velocity caused by the disappearance of the streamwise recirculation in the base flow.

The spanwise recirculation in the base flow is believed to play a role in determining the streamwise velocity distribution in the wake. Figure 4.10 shows the contours of the normalized averaged spanwise velocity in the turbine wake. For $\theta = 0°$, the normalized averaged spanwise velocity is the smallest out of all the cases and contributed solely by the turbine wake due to an almost zero spanwise velocity in the base flow. With the increase in the wind direction, the normalized averaged spanwise velocity outside the rotor projected area gets stronger. For $\theta = 15°$, the negative spanwise velocity close to the surface in the base flow is relatively small. For wind directions $\theta > 15°$, however, a very strong negative spanwise velocity can be observed close to the surface on the right of the rotor projected area. This strong spanwise velocity is responsible for the change in streamwise velocity distribution from a skewed shape towards right of the rotor in $\theta = 15°$ to a relatively symmetric one in $\theta = 30°$ to the one shifted towards the left of the rotor in $\theta = 45°$ in the far wake. The origin of this spanwise velocity and its role in determining the wake shape will be discussed in detail later.

To characterize the difference in the turbine wake compared to the base flow and to isolate the influence of the turbine on the wake flow, we compute the averaged streamwise velocity deficit $\Delta U(x,y,z) = U_b(x,y,z) - U_w(x,y,z)$, where U_b is the averaged streamwise velocity in
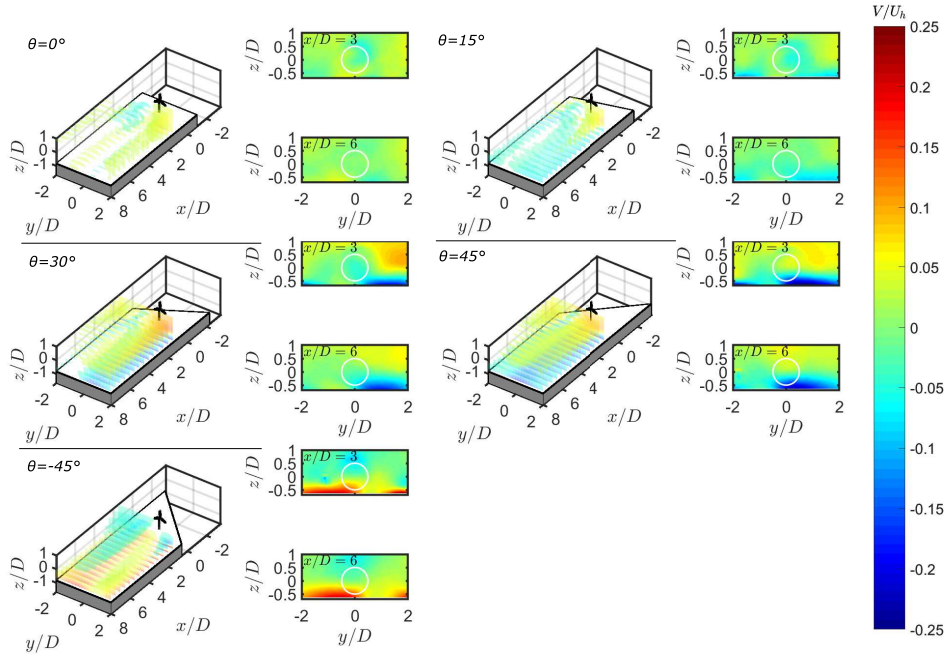
Figure 4.10: Contours of the normalized averaged spanwise velocity in the turbine wake. The three-dimensional plot shows spanwise velocity in the range of $-0.025 > V/U_h > 0.025$. The white circles in two-dimensional contours show the rotor projected area.

the base flow and U_w is the averaged streamwise velocity in the wake flow. Figure 4.11 shows the contours of the normalized averaged streamwise velocity deficit in the turbine wake for different wind directions. A black contour representing $0.5\Delta U_{max}(x)/U_h$ is also included to distinguish the shape of the wake between different cases. Similar to the streamwise velocity contours, the shape of the wake velocity deficit is observed to be affected by the wind direction, with a symmetric distribution in the cross-stream plane across the turbine centerline for $\theta = 0°$. For the higher wind directions, two factors play a key role in determining the wake shape: the lateral velocity component that develops in the base flow, and the flow speed up at the spanwise boundary of the wake close to the surface. For $\theta = 0°$, the flow speed-up close to the surface outside the wake deficit is also symmetric. As explained by Dar and Porté-Agel (2022b), this speed-up occurs as the presence of the turbine suppresses the development of the separated flow from the cliff leading edge, and therefore, reduces the shear in the surrounding flow which leads to the speed-up observed here. For higher wind directions, on the other hand, the speed-up is only observed on one side of the rotor, the magnitude of which is much higher than that for $\theta = 0°$. The expansion of the wake velocity deficit in the cross-stream plane is also observed to be affected by the wind direction, which leads to a difference in the recovery of the maximum streamwise velocity deficit due to momentum conservation, which will be discussed in detail later in the article.

For now, we turn our focus towards understanding the differences in the shape of the wake for different incoming wind directions. At the moment, two questions remain: how does
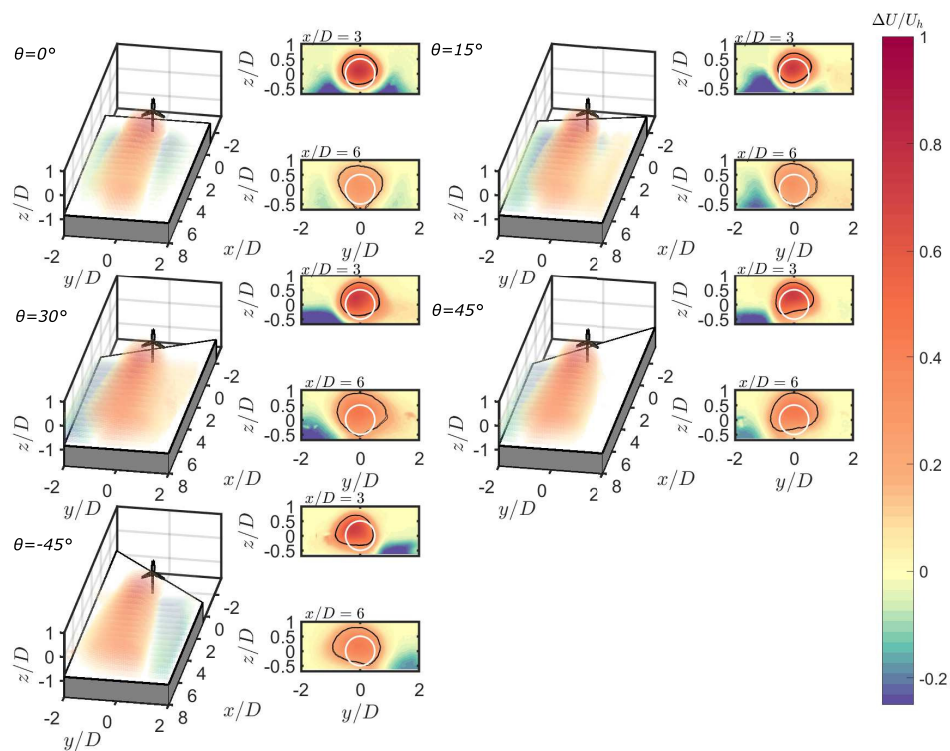
Figure 4.11: Contours of the normalized averaged streamwise velocity deficit in the turbine wake. The three-dimensional plot shows streamwise velocity deficit in the range of $-0.04 > \Delta U/U_h > 0.04$. The black contour lines and the white circles in two-dimensional contours show $0.5\Delta U_{max}(x)/U_h$ and the rotor projected area, respectively.
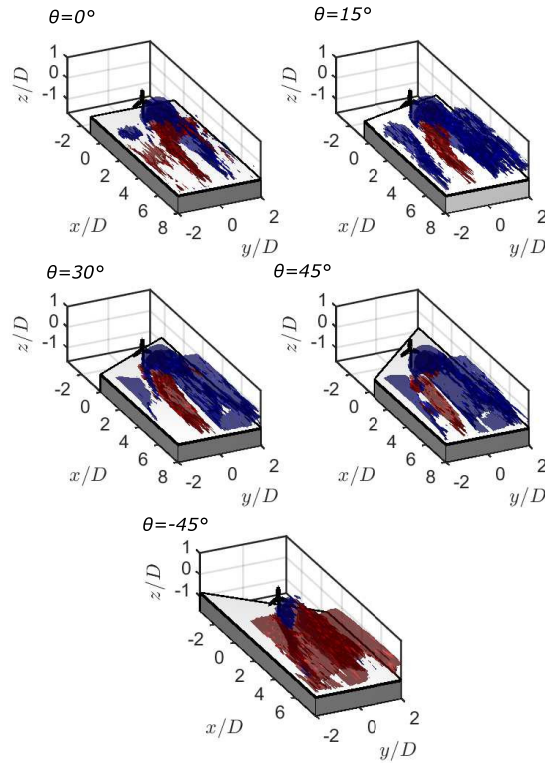
Figure 4.12: Isosurface plots of the normalized averaged streamwise vorticity in the turbine wake. The blue isosurface represents $\omega_x D/U_h = -0.15$ and the red isosurface represents $\omega_x D/U_h = 0.15$.

the spanwise recirculation for higher wind directions interact with the wind turbine wake, and what gives rise to the flow speed-up observed on one side of the rotor for higher wind directions? To answer the first question, we plot the isosurfaces of the normalized averaged streamwise vorticity in the flow in figure 4.12. For $\theta = 0°$, the vorticity in the near wake is dominated by the tip and hub vortices shed by the turbine, whereas in the far wake a counter-rotating vortex pair (CVP) is observed to develop close to the surface. As explained by Dar and Porté-Agel (2022b), the vertical velocity experienced by the turbine from the cliff leading edge leads to the formation of the CVP with a mechanism similar to how the lateral velocity induced by a yawed turbine gives rise a CVP in the wake. With the increase in the wind direction, one leg of the CVP is observed to grow stronger compared to the other and dominates the flow. The spanwise recirculation in the base flow is believed to be responsible for the increase in the vorticity, and the leg of the CVP dominating the flow is found to be dependent on the direction of the spanwise recirculation. One possible reason for the increasing strength of one leg of the CVP for higher wind directions could be the development of high shear around the rotor periphery in the near wake which restricts the base flow spanwise velocity on one side of the rotor.

To investigate the vorticity in the flow in more detail and to answer the second question, we plot the two-dimensional contours of the normalized averaged streamwise vorticity along

with streamlines of the cross-stream velocity components in figure 4.13. The streamlines in the cross-stream planes show some interesting flow structures, the most notable of which is the formation of a saddle point on one side of the rotor in the near wake of the turbine. This saddle point divides the wake flow from the outer base flow, creating two distinct regions of flow and leads to the flow speed up observed on the side of the rotor. The vertical position of the saddle point is observed to get close to the surface with the increase in the wind direction, which restricts the vertical extent of the flow speed up close to the surface. The formation of the saddle point is found to be dependent on the wind direction, as it appears on the left of the turbine center for the positive wind directions and on the right for the negative one. For $\theta = 0°$, the saddle point is replaced by a stable node at the rotor center in the turbine far wake. The formation of this stable node leads to an enhanced entrainment of flow from outside into the wake and to the development of the CVP in the far wake of the turbine, as discussed by Dar and Porté-Agel (2022b).

For higher wind directions, the cross-stream flow structures are rather complex and dependent on the strength of the spanwise recirculation in the base flow. For $\theta = 15°$, a spanwise velocity is induced by the yawed cliff edge, however the spanwise recirculation is relatively small. In the turbine near wake, a small vortex is observed outside the wake on the right side of the rotor. This vortex does not merge with the tip and hub vortices developed from the rotor tips and hub. Further downstream, as the vortices shed by the turbine break down, the spanwise velocity in the base flow sweeps through the rotor projected area. The presence of a saddle point on the other side of the rotor, however, restricts further movement of the spanwise flow velocity in the spanwise direction, which in turn results in the roll up of the vortices and formation of a CVP with an orientation that is $90°$ rotated compared to one for $\theta = 0°$. The saddle point is also observed to move up and away from the turbine center with increase in the streamwise distance, which could be related to the expansion of the wake in the cross-stream directions. As the saddle point exists throughout the far wake, the flow speed-up observed on the right of the rotor does too, which leads to a stronger speed-up in the far wake compared to $\theta = 0°$.

For wind directions above $15°$, the spanwise recirculation in the base flow is strong enough to interact with the vortices shed by the turbine itself. For $\theta = 30°$, in the near wake, the vortex on the right side of the rotor limits the development of the hub vortex and induces a high vertical velocity within the rotor projected area at the interface of the hub vortex and the base flow vortex. This vortex is also responsible for the shift in the position of the maximum streamwise velocity deficit away from the turbine center. Further downstream, it dominates the flow and the positive leg of the CVP observed in $\theta = 15°$ diminishes in size for $\theta = 30°$. The spanwise velocity observed in the turbine wake is induced by this vortex.

For $\theta = 45°$, a similar observation is made, where the base flow vortex is even stronger than that for $\theta = 30°$. The strong base flow vortex affects the hub vortex even more and pushes the wake towards the left side of the rotor near the surface. As the rotation of the hub and base flow vortices are opposite, they do not merge into one in the turbine near wake. In the far wake,
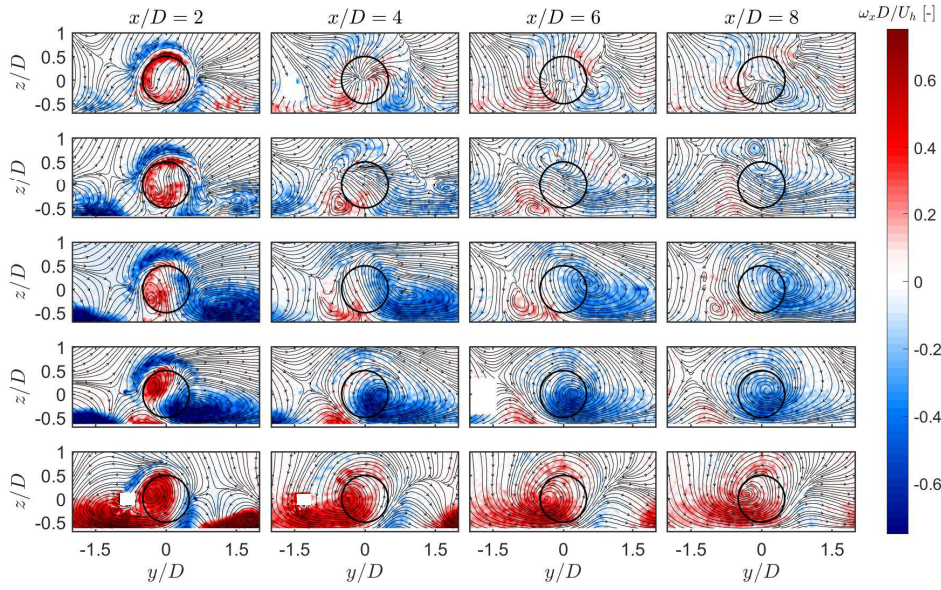
Figure 4.13: Contours of the normalized averaged streamwise vorticity in the turbine wake. Streamlines based on cross-stream velocity components are overlaid. The black circles show the rotor projected area. From top to bottom: $\theta = 0°$, $15°$, $30°$, $45°$, $-45°$.

the hub vortex breaks down, whereas the base flow vortex dominates the flow. For $\theta = -45°$, on the other hand, the hub vortex and the base flow vortex are observed to merge into one, which shifts the wake center slightly towards the left of the turbine center. In the near wake, similar to the positive wind directions, a saddle point is observed. In the far wake, however, this saddle point is replaced by an unstable node, which divides the vortex developed due to the merger of the hub and base flow vortices, and the outer base flow. In general, the shape of the wake and the flow speed-up outside the wake are shown to be affected by the cross-stream flow structures like the saddle point and the CVP in all cases.

Turbulence characteristics

Typically, the turbulence kinetic energy is contributed by the turbulent momentum fluxes and mean flow shear (Wu and Porté-Agel, 2012). For a wind turbine wake in flat terrain, the spatial distribution of turbulence kinetic energy shows a horseshoe shape with a peak around the rotor top tip level. This is due to high mean flow shear and momentum fluxes around the rotor periphery at the top. Moreover, the maximum turbulence kinetic energy and related turbulent momentum fluxes are relatively higher in the turbine wake compared to the surrounding boundary layer flow (Bastankhah and Porté-Agel, 2017c; Wu and Porté-Agel, 2012).

Figure 4.14 shows the contours of the normalized turbulence kinetic energy in the turbine wake on the cliff for different wind directions. For the wind direction $\theta = 0°$, a typical horseshoe shape of high tke is observed, along with some turbulence in the outer flow closer to the cliff leading edge due to high shear. With downstream distance, the magnitude of tke in
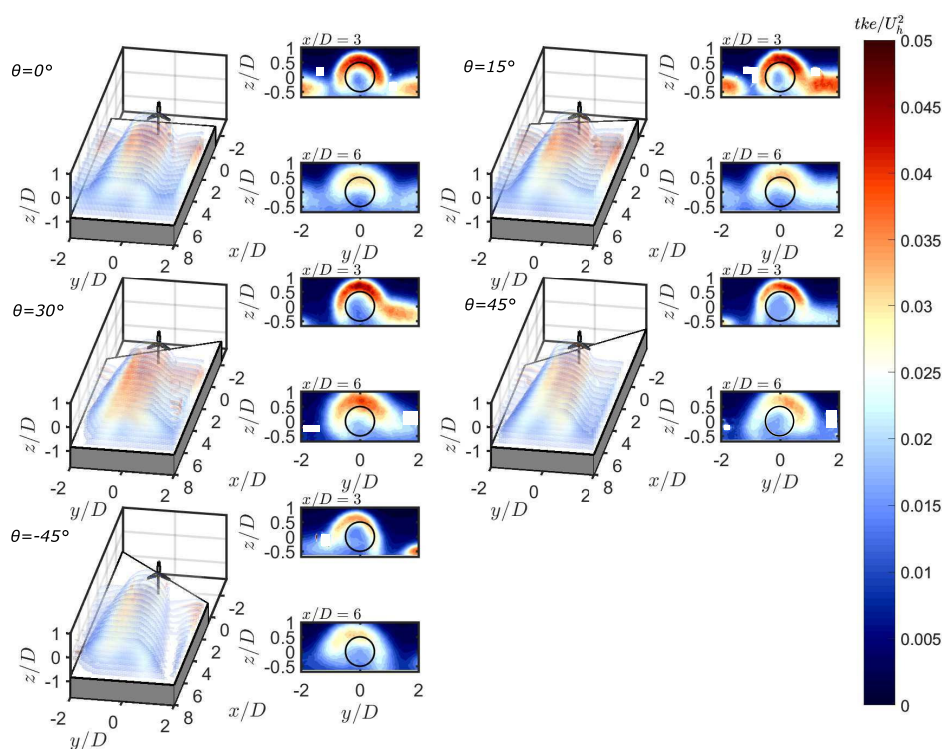
Figure 4.14: Contours of the normalized turbulence kinetic energy in the turbine wake. The three-dimensional plot shows turbulence kinetic energy in the range of $tke/U_h^2 > 0.01$. The black circles in two-dimensional contours show the rotor projected area.

the turbine wake decreases due to decrease in the mean flow shear, although the shape is preserved. As shown earlier, the mean velocity and the wake shape are highly dependent on the wind direction, due to the induction of spanwise recirculation and development of streamwise vorticity in the wake flow. This has an effect on the turbulence kinetic energy in the wake, as it affects both the shear in the mean flow as well as the distribution of the turbulent momentum fluxes. Figure 4.15 shows the contours of the normalized averaged lateral and vertical turbulent momentum fluxes for different incoming wind directions. The influence of the streamwise vorticity on the spatial distribution of these turbulent fluxes can be clearly observed, especially close to the turbine. High turbulence kinetic energy is observed in areas with high mean flow shear, including the rotor top periphery and the surrounding base flow closer to the cliff edge. The shape of the high tke region around the rotor periphery is affected by the shape of the wake, where especially for high wind directions $\theta = \pm 45°$, the peak in the tke is observed to be shifted on one side of the rotor in the far wake. In the base flow, the normalized tke was observed to peak at $\theta = 15°$. In the wake flow, the normalized tke is observed to be highest for $\theta = 30°$, which can be related to the highest magnitude of turbulent momentum fluxes observed for this wind direction compared to the rest of the cases, especially in the far wake (see figure 4.15).
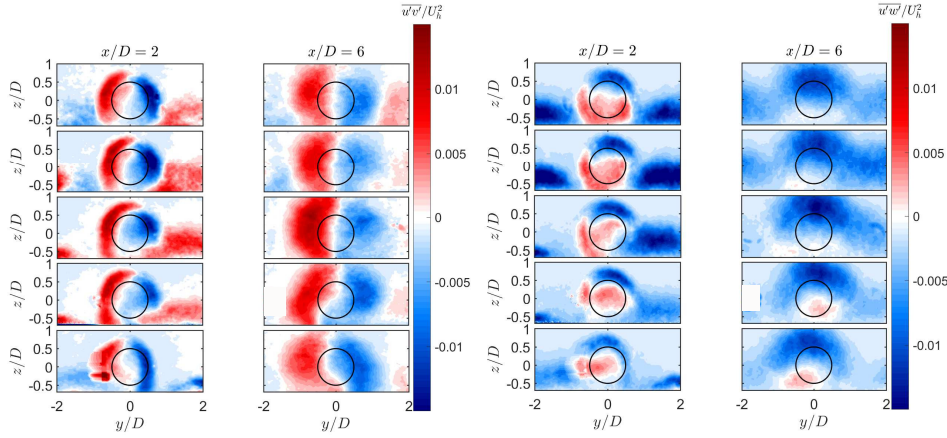
Figure 4.15: Contours of the normalized averaged lateral (left) and vertical (right) momentum flux in the turbine wake for two different streamwise positions. The black circles show the rotor projected area. From top to bottom: $\theta = 0°$, $15°$, $30°$, $45°$, $-45°$.

Volumetric wake characterization

In order to characterize the streamwise wake velocity deficit, we perform a volumetric wake analysis following Brugger et al. (2019). For this purpose, a two-dimensional (2D) Gaussian fit is performed on the streamwise wake velocity deficit in the cross-stream direction at several streamwise positions. The 2D-Gaussian fit is given by:

$$\Delta U(y, z) = C exp(-a(y - y_0)^2 + 2b(y - y_0)(z - z_0) + c(z - z_0)^2), \tag{4.3}$$

where

$$a = \frac{cos^2(\alpha - 90)}{2\sigma_y^2} + \frac{sin^2(\alpha - 90)}{2\sigma_z^2}, \tag{4.4}$$

$$b = \frac{sin(2(\alpha - 90))}{4\sigma_y^2} + \frac{cos(2(\alpha - 90))}{4\sigma_z^2}, \tag{4.5}$$

$$c = \frac{sin^2(\alpha - 90)}{2\sigma_y^2} + \frac{cos^2(\alpha - 90)}{2\sigma_z^2}. \tag{4.6}$$

The maximum velocity deficit is represented by C; σ_y and σ_z are the standard deviations representing wake widths along the principal axes of the 2D-Gaussian fit; y_0 and z_0 represent
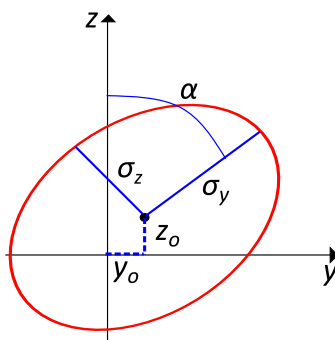
Figure 4.16: Schematic of the 2D-Gaussian fit.

the wake center deviation from the rotor center position and α represents the tilt angle of the wake in the 2D-Gaussian fit. Figure 4.16 shows a schematic of the 2D-Gaussian fit and different fitting parameters. The fit is performed with a weighted non-linear least squares regression, where only the positive velocity deficit is used for fitting. To initialize the fit at $x/D = 2$, starting values corresponding to $C = 4 \ ms^{-1}$, $\sigma_y = \sigma_z = 0.05 \ m$, $y_0 = z_0 = 0 \ m$ and $\alpha = 0°$ are used. For each subsequent streamwise position, the fitted parameters from the previous position are used for initialization.

Figure 4.17 shows contours of the normalized averaged streamwise velocity deficit obtained from the experiments overlaid with the line contours of the 2D-Gaussian fit for different streamwise positions. Overall, the 2D-Gaussian is observed to fit reasonably well to the experimental data, where an R^2 in the range of 0.93-0.96 is obtained between the 2D-Gaussian fits and the experimental data for all cases. From the 2D-Gaussian fit, the wake is observed to have a zero tilt at all streamwise positions for $\theta = 0°$. With the increase in the wind direction, the tilt angle increases, especially in the far wake when the development of the cross-stream velocity alters the wake shape. For $\theta = \{15°, 30°\}$, the wake tilts in the counter-clockwise direction, whereas for $\theta = 45°(-45°)$, the tilt is in the (counter-)clockwise direction. The trend in the tilt angle of the wake observed here for different cases is consistent with how the wake shape is altered by the cross-stream flow development.

Some key wake characteristics are plotted and compared for different wind directions as a function of the streamwise distance in figure 4.18. The recovery of the wake center velocity deficit is quantified via the evolution of the maximum normalized averaged streamwise velocity deficit in figure 4.18 (a). Closer to the turbine, the wind direction perpendicular to the cliff edge shows the highest value of $\Delta U_{max}/U_h$ among all the cases, with values decreasing slightly with the increase in the wind direction. This can be related to the difference in the thrust coefficient observed between different wind directions shown in figure 4.3 (b), and to the effect of the pressure gradient induced by the cliff leading edge on the turbine near wake. As discussed by Dar and Porté-Agel (2022b), although the streamwise velocity deficit in the turbine wake is contributed solely by the turbine thrust in a flat terrain, in a complex terrain, there is an additional contribution resulting from the terrain-induced
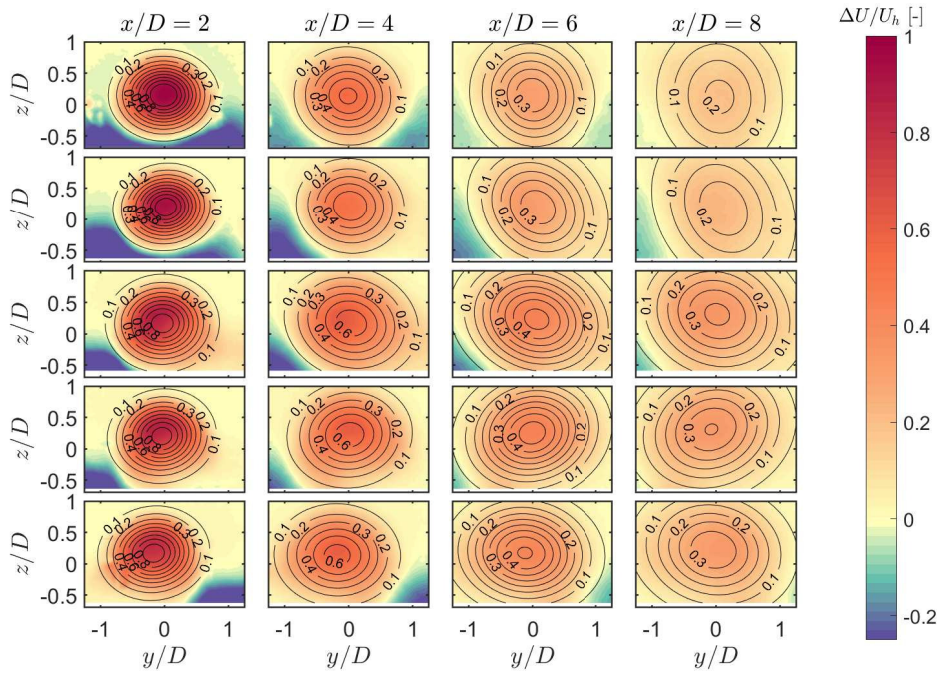
Figure 4.17: Contours of the normalized averaged streamwise velocity deficit in the turbine wake. The black contour lines represent the 2D-Gaussian fit. From top to bottom: $\theta = 0°$, $15°$, $30°$, $45°$, $-45°$.

pressure gradient. As a cliff induces an adverse pressure gradient, this additional contribution results in a higher velocity deficit than without the effect of the induced pressure gradient. As shown by Bastankhah and Porté-Agel (2016), the maximum normalized averaged streamwise velocity deficit in the near wake is around 0.8 for a similar thrust coefficient in a flat terrain for the miniature turbine used in this study. However, in this study, the maximum normalized averaged streamwise velocity deficit in the near wake of the turbine is higher than 0.8 for all wind directions, indicating the effect of the cliff-induced pressure gradient. As discussed by Dar and Porté-Agel (2022b), the cliff induces an adverse pressure gradient on the flow, which leads to a higher velocity deficit in the turbine wake compared to a flat case. This cliff-induced adverse pressure gradient decreases with the increase in the wind direction, as well as, with the increase in the distance from the cliff edge, which results in a decrease in $\Delta U_{max}/U_h$ at $x/D = 2$ for higher wind directions.

Further downstream, the rate of recovery of the wake center velocity deficit is also found to be dependent on the wind direction. The wind directions $\theta = \{0°, 15°\}$ show the highest recovery rate among all the cases. For wind directions $\theta > 15°$, on the other hand, the recovery rate is observed to significantly slow down compared to the first two cases. This observation is consistent with the base flow normalized turbulence kinetic energy, which is observed to decrease for $\theta > 15°$. In addition, the induction of a spanwise velocity in the base flow also results in veering in the vertical direction and leads to the formation of complex vortical structures as illustrated earlier (see figure 4.13). This cross-stream flow development affects

the expansion of the wake, which in turn can affect the recovery of the wake center velocity deficit due to momentum conservation. Figure 4.18 (b) shows the normalized equivalent wake width computed as the geometrical mean of the wake widths along the principal axes of the 2D-Gaussian fit ($\sigma_{eq} = \sqrt{\sigma_y \sigma_z}$). All cases show an approximately linear trend in the normalized equivalent wake width, which is consistent with earlier studies (Dar and Porté-Agel, 2022b; Porté-Agel et al., 2020). The normalized equivalent wake width is generally found to be higher for the wind directions $\theta > 15°$ than for $\theta \leq 15°$, which is consistent with the slower recovery rate of the wake deficit in the former cases. For $\theta = 15°$, the normalized equivalent wake width is observed to be similar to that for $\theta = 0°$ at $x/D \leq 4$, whereas it shows a higher σ_{eq}/D at $x/D > 4$. This could be related to the formation of the CVP aligned with the saddle point as shown in figure 4.13, which stretches the wake in the vertical direction leading to a higher equivalent wake width.

The deflection of the wake center relative to the rotor center in the spanwise and vertical directions is also shown in figure 4.18. For $\theta = 0°$, the spanwise deflection is found to be approximately zero. For positive wind directions, the spanwise deflection is predominantly positive with overall values ranging between $-0.1 < y_0/D < 0.1$. This is consistent with the velocity speed-up on one side of the wake, which results in a lateral shift in the wake center towards the opposite side. For $\theta = 15°$ the deflection is the highest, which can be attributed to the strongest velocity speed-up on one side of the rotor. For $\theta = -45°$, on the other hand, a significant wake center deflection closer to the turbine can be observed, which reduces with the increase in the streamwise distance but shows a higher magnitude than majority of the cases. This spanwise wake center deflection in the $\theta = -45°$ can be attributed to the merger of the hub vortex with the base flow vortex, as discussed in section 4.3.2. As the two vortices (hub vortex and base flow vortex) rotate in the same direction, they merge into one in the near wake, resulting in a shift in the wake center. For positive wind directions, these vortices rotate in opposite directions leading to separate vorticity regions in the near wake and relatively less spanwise deflection.

The vertical deflection in the wake center is shown in figure 4.18 (d). All cases show a positive deflection of the wake above the rotor center, which is related to the positive vertical velocity experienced by the turbine from the cliff leading edge. For $\theta = 0°$, the vertical deflection is the smallest of all the cases, whereas $\theta = 45°$ shows the highest vertical deflection. For smaller wind directions, $\theta = 0°, 15°$, the vertical deflection is almost constant with the streamwise distance, whereas for $\theta > 15°$, it increases with the increase in the streamwise distance.

Streamwise momentum analysis

To further understand the mechanisms behind the recovery of the streamwise momentum in the turbine wake for different wind directions, we examine different terms of the streamwise Reynolds Averaged Navier Stokes (x-RANS) equation. In doing so, we neglect the viscous terms due to high Reynolds number, and no body forces are present in the turbine wake. The RANS
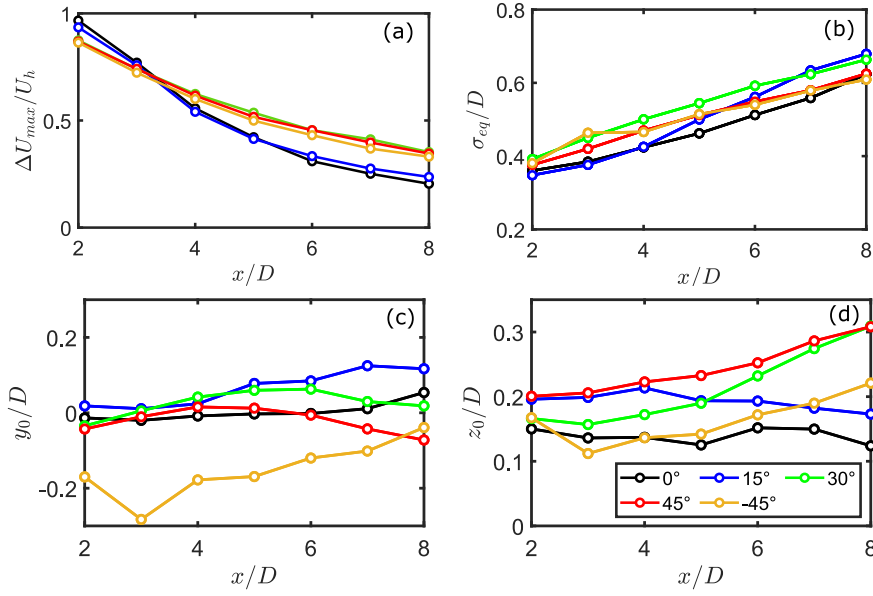
Figure 4.18: (a) Maximum normalized averaged streamwise velocity deficit, (b) normalized equivalent wake width, wake center deflection in the (c) spanwise and (d) vertical direction as a function of streamwise distance.

equation in the streamwise direction can then be written as (Pope, 2000):

$$U_w\frac{\partial U_w}{\partial x} + V_w\frac{\partial U_w}{\partial y} + W_w\frac{\partial U_w}{\partial z} = -\frac{1}{\rho}\frac{\partial P}{\partial x} - \frac{\partial \overline{u'u'}}{\partial x} - \frac{\partial \overline{u'v'}}{\partial y} - \frac{\partial \overline{u'w'}}{\partial z},\tag{4.7}$$

where U_w, V_w and W_w are the time-averaged streamwise, spanwise and vertical velocity components in the turbine wake, respectively. Similarly, u', v' and w' are the fluctuating components of the streamwise, spanwise and vertical velocity, respectively. Analysis of x-RANS equation has been used in the literature to understand the recovery of streamwise momentum, and flow structures in the wake of yawed or tilted turbines (Bastankhah and Porté-Agel, 2016; Bossuyt et al., 2021).

Following Shamsoddin and Porté-Agel (2018a), equation 4.7 can be written in terms of the streamwise velocity deficit by adding $U_w dU_b/dx$ on both sides. Moreover, the pressure gradient induced by the base flow can be approximated by the streamwise gradient of base flow velocity $U_b dU_b/dx$ (Shamsoddin and Porté-Agel, 2018a). After making the above-mentioned substitutions and rearrangement, the following equation is yielded:

$$\underbrace{U_w\frac{\partial(U_b - U_w)}{\partial x}}_{(I)} + \underbrace{V_w\frac{\partial(U_b - U_w)}{\partial y}}_{(II)} + \underbrace{W_w\frac{\partial(U_b - U_w)}{\partial z}}_{(III)} = \underbrace{-(U_b - U_w)\frac{dU_b}{dx}}_{(IV)} + \underbrace{\frac{\partial \overline{u'u'}}{\partial x}}_{(V)} + \underbrace{\frac{\partial \overline{u'v'}}{\partial y}}_{(VI)} + \underbrace{\frac{\partial \overline{u'w'}}{\partial z}}_{(VII)}.\tag{4.8}$$

72

Figure 4.19 shows the normalized contours of different terms of equation 4.8 at $x/D = 4$ for different wind directions. In general, the terms related to the advection of the streamwise momentum are observed to be affected by the change in the wind direction. Specifically, the induction of a spanwise velocity and development of strong vortices in the wake are responsible for the changes in the advection of the streamwise momentum.

The term $U_w \partial(U_b - U_w)/\partial x$ represents the streamwise advection of the streamwise momentum deficit. This term shows a negative region inside the wake and a positive region on the outer periphery of the wake. As the averaged streamwise velocity is positive, a positive streamwise advection is related to $\partial(U_b - U_w)/\partial x > 0$ indicating a slow down of the flow due to the cross-stream expansion of the wake with the increase in the streamwise distance. Similarly, a negative streamwise advection can be associated with $\partial(U_b - U_w)/\partial x < 0$, corresponding to the recovery of the streamwise momentum deficit in the wake. Comparing different wind direction cases, the negative region in the core of the wake is strongest for $\theta = \{0°, 15°\}$, the magnitude of which reduces for $\theta > 15°$. This indicates a faster recovery of the streamwise momentum deficit for wind directions $\theta \leq 15°$ compared to $\theta > 15°$. This is consistent with the recovery of the wake center streamwise velocity deficit observed in the previous section, where two different recovery rates for $\theta \leq 15°$ and $\theta > 15°$ were shown. The positive region surrounding the negative one gets stronger with increasing wind direction, which can be related to a higher wake width in higher wind directions.

The spanwise and vertical advection terms ($V_w \frac{\partial(U_b - U_w)}{\partial y}$ and $W_w \frac{\partial(U_b - U_w)}{\partial z}$, respectively) are observed to be significantly affected by the development of streamwise vorticity in the wake. The magnitude of these terms is comparatively smaller than that of the streamwise advection, which is due to the smaller magnitude of the cross-stream velocity components when compared with the streamwise velocity. For $\theta = \{0°, 15°\}$, the cross-stream advection terms are mostly positive, indicating that these terms play a role in bringing higher momentum flow from outside into the wake, thus, contributing to its recovery. For wind directions higher than 15°, negative regions start to appear, which could play a role in the slow recovery of the momentum deficit in the wake. For $\theta = \pm 45°$ a quadrupole shape is observed for the cross-stream advection terms, where the spanwise and vertical advection terms show opposite sign. The net effect of the cross-stream advection terms would then depend on the relative magnitude of the individual contributors.

The pressure gradient term is observed to be relatively small, although a positive region in the wake center is observed for most cases. This indicates that the pressure gradient tends to slow down the recovery of the streamwise momentum deficit. This is understandable, as the cliff induces an adverse pressure gradient on the flow, which is known to slow down the recovery of the turbine wake (Porté-Agel et al., 2020). The $\partial \overline{u'u'}/\partial x$ term shows the smallest magnitude out of all the terms of the x-RANS equation, and thus, has the smallest contribution to the streamwise momentum in the wake. The observations regarding the pressure gradient term and the streamwise normal Reynolds stress are consistent with previous studies (e.g., Bossuyt et al. (2021)). The gradients of the shear stresses, on the other hand, contribute significantly to
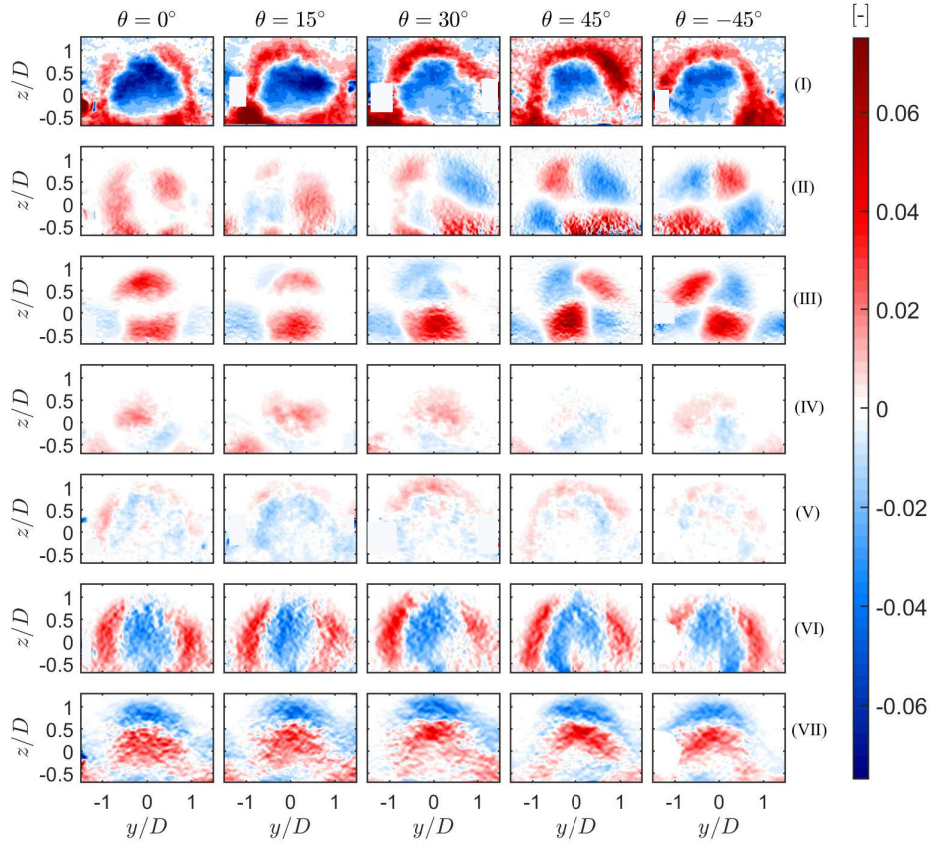
Figure 4.19: Contours of the terms of the streamwise momentum equation (eq. 4.8) computed from measurements at $x/D = 4$. All quantities are normalized by D/U_h^2.

the momentum recovery in the wake for all wind directions. The gradients of the Reynolds stresses are relatively similar among all cases, both in terms of the spatial distribution and overall magnitude. This further indicates that the differences in the recovery of the streamwise momentum are not related to the gradient of the Reynolds stresses, but to the advection terms.

4.4   Summary

Onshore wind energy is currently one of the cheapest available sources of energy. In an onshore environment, terrain complexity plays an important role in determining the performance of a wind farm. Wind turbines are often sited close to cliffs, however, the interaction of flow with the cliff under different wind directions and its influence on a wind turbine wake are not well understood. In this study, we performed comprehensive wind tunnel experiments investigating the flow over a cliff under different incoming wind directions. Moreover, the interaction of this flow with the wake of a wind turbine was also investigated. Five different wind directions were tested: $\theta = \{0°, 15°, 30°, 45°, -45°\}$, where $0°$ is defined as the wind direction perpendicular to the cliff leading edge.

For flow over the cliff without the turbine, known as the base flow, the flow was observed to become heterogeneous in the spanwise direction with the increase in the wind direction. The streamwise flow recirculation was absent for wind directions above 15°, where a spanwise recirculation was induced with the increase in the wind direction. The strength of the streamwise vorticity was observed to be directly proportional to the wind direction. The normalized turbulence kinetic energy was observed to peak at $\theta = 15°$, which was related to the absence of the streamwise flow recirculation for $\theta > 15°$.

The wake of the wind turbine sited on the cliff was observed to be significantly affected by the change in the wind direction. The development of the spanwise recirculation in the base flow had an effect on the streamwise velocity in the wake: it was symmetric in the spanwise direction for the wind direction perpendicular to the leading-edge of the cliff, but became asymmetric with the increase in wind direction. Two important observations made in this regard were the flow speed-up on one side of the rotor and the role of the spanwise velocity on the other side of the rotor in pushing the wake in one direction or the other. These features were investigated further by looking at the normalized streamwise vorticity and cross-stream velocity streamlines. The flow speed-up on one side of the rotor was observed to be a result of the formation of a saddle point, which bifurcates the outer base flow from the wake flow and led to a region of high speed flow. A counter-rotating vortex pair close to the surface was observed to develop in the far wake for the wind direction perpendicular to the cliff. With the increase in the wind direction, one leg of the CVP grew stronger and dominated the flow, which played a major role in changing the spatial distribution of the streamwise velocity in the wake.

The streamwise wake velocity deficit was quantified using a 2D Gaussian fit. The recovery of the normalized streamwise velocity deficit maximum was observed to slow down for wind directions $\theta > 15°$, which was found to be consistent with the decrease in the base flow turbulence. The wake width was observed to be higher for $\theta > 15°$ compared to $\theta = 0°$, which could be related to the increased veering effect caused by the spanwise component of the velocity. The mean wake center in the spanwise and vertical directions was also affected by the wind direction, where the vertical deflection increased with the increase in the positive wind direction. The spanwise wake center position was relatively close to 0 for positive wind directions, but showed a high negative deflection for $\theta = -45°$, which was related to the merging of the hub vortex with the base flow vortex in the mentioned case.

A term-by-term analysis of the streamwise Reynolds Averaged Navier Stokes (x-RANS) equation was performed. This analysis revealed differences in the mechanisms of the recovery of the streamwise momentum between different cases. The advection terms in the x-RANS equation showed significant differences between different wind directions. The gradients of Reynolds stresses were largely unaffected by the wind directions. This pointed out that the differences in the recovery of the wake arise from the advection of the streamwise momentum and not from the gradients of the Reynolds stresses.

Part - II: Wakes under pressure gradient

5 An analytical model for wind turbine wakes under pressure pradient[I]

Abstract

In this study, we present an analytical modeling framework for wind turbine wakes under an arbitrary pressure gradient imposed by the base flow. The model is based on the conservation of the streamwise momentum and self-similarity of the wake velocity deficit. It builds on the model proposed by Shamsoddin and Porté-Agel, (*J. Fluid Mech.*, vol. 837, 2018, R3) which only accounted for the imposed pressure gradient in the far wake. The effect of the imposed pressure gradient on the near wake velocity is estimated by using Bernoulli's equation. Using the estimated near wake velocity as the starting point, the model then solves an ordinary differential equation to compute the streamwise evolution of the maximum velocity deficit in the turbine far wake. The model is validated against experimental data of wind turbine wakes on escarpments of varying geometries. In addition, a comparison is performed with a pressure gradient model which only accounts for the imposed pressure gradient in the far wake, and with a model that does not account for any imposed pressure gradient. The new model is observed to agree well with the experimental data, and it outperforms the other two models tested in the study for all escarpment cases.

5.1   Introduction

Wind turbine wakes can result in significant power losses within a wind farm, as they reduce the power available to the downwind turbines, as well as enhance the fluctuating loads experienced by these turbines (Porté-Agel et al., 2020). Understanding and predicting these wakes is crucial, especially during the planning and layout optimization phase of a wind farm. Computationally inexpensive analytical tools are widely popular in the wind energy community for this purpose, as they offer fast and reasonably accurate estimations of wind turbine wakes, which enables testing different layout configurations and wind conditions in a relatively short time. Given their paramount importance, a number of analytical models for wind turbine wakes have been proposed over the years.

Most attempts to analytically model wind turbine wakes assume an underlying flat homogeneous terrain, which implies a zero pressure gradient situation. Early attempts at analytical modeling of wind turbine wakes started with Jensen (1983), who applied mass conservation downwind of the turbine and assumed a top-hat distribution of the velocity deficit. Later, Frandsen et al. (2006) used mass and momentum conservation around a wind turbine to estimate the velocity deficit in the wake. Similar to Jensen (1983), they also assumed a top-hat distribution of the velocity deficit across the rotor cross-section. Based on the empirical evidence of a self-similar Gaussian distribution of velocity deficit in the turbine wake, Bastankhah and Porté-Agel (2014) proposed an analytical model for the wake velocity deficit derived from streamwise mass and momentum conservation. Their model has since been adapted to different scenarios, such as wakes of turbines under yawed conditions (Bastankhah and Porté-Agel, 2016), or the ones experiencing wind veer effects (Abkar et al., 2018). Recent advances in the analytical modeling of wakes include the so-called super-Gaussian model, which transitions from a top-hat profile in the turbine near wake to a Gaussian profile in the far wake (Shapiro et al., 2019), a model for the wake velocity and added turbulence intensity based on a combination of analytical and numerical studies Ishihara and Qian (2018), analytical models for yawed turbine wakes (Lopez et al., 2019) and for added streamwise turbulence intensity in the wake (Li et al., 2022).

It is highly likely that wind turbines sited in complex flow conditions, such as heterogeneous surface roughness conditions or topographies, experience a pressure gradient imposed by the base flow. This pressure gradient can significantly affect the evolution of the turbine wake, such as the recovery of the wake center velocity deficit and the expansion of the wake. Most conventional wake modeling approaches, however, assume zero pressure gradient and a homogeneous base flow velocity. A practical approach to model wakes in topography, for instance, is to superpose the velocity deficit in the flat terrain on top of the topography. Although simple, this approach has been shown to work only for terrains with very gentle slopes (Crespo et al., 1993; Hyvärinen and Segalini, 2017b). Brogna et al. (2020) proposed a modified form of the Gaussian model (Bastankhah and Porté-Agel, 2014) to be used for their wind farm optimization study in topography. More recently, Farrell et al. (2021) presented a wind farm wake model for varying base flow velocity field. They also based their wake model

on the Gaussian model (Bastankhah and Porté-Agel, 2014), while keeping the reference base flow velocity spatially variable. Hu et al. (2022) presented a genetic algorithm based approach for siting wind turbines in complex terrain. To account for wake effects, they used an adapted Jensen model and Gaussian model based on the Brogna et al. (2020) formulation. These approaches, however, do not explicitly account for the imposed pressure gradient, as the underlying models are derived under the assumption of a flat terrain. Recent years have seen an increased interest in data-driven approaches to the estimation of wake effects in wind farms on flat terrain (see e.g., Hwangbo et al. (2018), Nai-Zhi et al. (2022), and Zehtabiyan-Rezaie et al. (2022)). On complex terrain, the problem complexity increases further due to the dependence of the flow characteristics (such as the imposed pressure gradients) on site-specific terrain characteristics. This hinders the applicability of data-driven modeling to complex terrains due to limitations related to available data for training purposes.

The only existing models that account for the effect of an imposed pressure gradient on wakes are the ones proposed by Shamsoddin and Porté-Agel (2017a, 2018a) and in turn successfully applied by them to study the wake of a wind turbine sited upstream of a hill (Shamsoddin and Porté-Agel, 2018b). These models solve an ordinary differential equation (ODE) for the streamwise evolution of the maximum velocity deficit under pressure gradient, which is derived by applying streamwise momentum conservation in a control volume. A self-similar Gaussian profile of the wake velocity deficit is assumed, which has recently been verified by Dar et al. (2019) and Dar and Porté-Agel (2022b) in different topographies. The invariance of the ratio between the maximum velocity deficit and wake width to the pressure gradient is used to close the system of equations, and to obtain the wake width under the pressure gradient situation. In order to obtain a numerical solution, a boundary condition is required to solve the ordinary differential equation for the streamwise evolution of the maximum velocity deficit. In their original work (Shamsoddin and Porté-Agel, 2017a, 2018a, 2018b), the surrounding base flow imposes a zero pressure gradient at the turbine location and becomes non-zero from a certain location downstream of the turbine. Therefore, the maximum velocity deficit at the first streamwise position is assumed to be the same with or without the imposed pressure gradient. While true for the above-described scenario or for the situations where the imposed pressure gradient at the turbine location is small enough, the assumption may not be valid for situations where there is significant imposed pressure gradient at the turbine location. One such example is a wind turbine sited close to the edge of an escarpment, where the pressure gradient induced by the escarpment is high closer to the edge and vanishes as we move further away from it. Dar and Porté-Agel (2022b) applied the model of Shamsoddin and Porté-Agel (2018a) to predict the wake velocity deficit of a turbine sited close to the edge of an escarpment. They observed that the model worked well for the escarpments with a sloped or a smooth leading-edge, but its performance degraded with the increase in the sharpness of the escarpment's leading-edge.

The objective of the current work is to develop an analytical modeling framework that can be applied in situations where the turbine experiences an arbitrary pressure gradient imposed by the base flow. The new model develops on the one proposed by Shamsoddin and Porté-Agel

(2018a), where Bernoulli's equation is used to estimate a theoretical near-wake velocity under a non-zero imposed pressure gradient. This near-wake velocity is then used to obtain maximum wake velocity deficit at the start of the turbine far wake, where an ordinary differential equation is solved. The model is validated against the experimental data and compared with the results from two existing models (Bastankhah and Porté-Agel, 2014; Shamsoddin and Porté-Agel, 2018a). The rest of the article is structured as follows: the analytical modeling framework is detailed in Section 5.2; validation of the model against experimental data and comparison with other models is performed in Section 5.3; finally, a summary of the work and concluding remarks are given in Section 5.4.

5.2 Analytical Modeling Framework

5.2.1 Problem Formulation

The mean streamwise velocity deficit in a wind turbine wake is known to show a self-similar Gaussian shape in the far wake in flat terrain (Bastankhah and Porté-Agel, 2014), as well as in topography (Dar and Porté-Agel, 2022b; Dar et al., 2019), and can therefore be expressed as:

$$\frac{U_b(x) - U_w(x,r)}{U_b(x)} = C(x) e^{-(\frac{r^2}{2\sigma(x)^2})}, \tag{5.1}$$

where $U_b(x)$ is the velocity in the base flow (flow without turbine), $U_w(x,r)$ is the velocity in the wake flow, $C(x)$ is the normalized maximum velocity deficit at a certain streamwise location, $\sigma(x)$ is the wake width, x is the streamwise distance, and r is the radial distance from the wake center. For the sake of brevity, the term velocity is used to refer to mean streamwise velocity throughout the article, unless otherwise stated. Here, the wake velocity deficit is assumed to be axisymmetric around the wind turbine center. In situations where the velocity deficit is not perfectly axisymmetric, as stated by Shamsoddin and Porté-Agel (2018a), the problem is solved for an equivalent wake width expressed as a geometric mean of the lateral and vertical wake widths.

The base flow velocity $U_b(x)$ is only represented as a function of the streamwise distance, although in some situations it can also vary in other directions. For instance, in the case of two dimensional topography it can vary in both streamwise and vertical directions. Following Shamsoddin and Porté-Agel (2018b), the base flow velocity in the streamwise direction at the hub height of the turbine can be used as an approximation for $U_b(x)$. Alternatively, in the case of highly sheared or three-dimensional base flow, an averaged velocity within the rotor's projected area can be chosen to represent the base flow, although this approach would require more information on the base flow. The imposed pressure gradient is represented by the streamwise gradient of the base flow velocity, where $dU_b/dx = 0$ corresponds to the zero pressure gradient (ZPG), $dU_b/dx > 0$ indicates a favorable pressure gradient (FPG), and $dU_b/dx < 0$ represents an adverse pressure gradient (APG).

The objective of the current study is to present an analytical modeling framework that can predict the evolution of a wind turbine wake under an arbitrarily imposed pressure gradient, provided that the wake evolution under zero pressure gradient and the base flow under pressure gradient are known. The inputs for the zero pressure gradient wake evolution are the same as those required by the Gaussian model developed by Bastankhah and Porté-Agel (2014), i.e., the turbine thrust coefficient and wake width.

5.2.2 Model Derivation

Following Shamsoddin and Porté-Agel (2018a), the integral form of the streamwise momentum equation for an axisymmetric wind turbine wake under pressure gradient can be written as:

$$\frac{d}{dx}\int_0^\infty U_w(U_b - U_w)2\pi r\,dr + \int_0^\infty \frac{dU_b}{dx}(U_b - U_w)2\pi r\,dr = 0, \tag{5.2}$$

where the first term on the left-hand side represents the contribution of the turbine thrust, and the second term accounts for the effect of pressure gradient on the turbine wake. The term $(U_b - U_w)$ vanishes far from the wake center in a plane normal to the streamwise direction. In deriving the above equation, the continuity equation is used, and viscous effects are neglected. Moreover, the mean pressure gradient is represented by $U_b(dU_b/dx)$. Substituting equation (5.1) into equation (5.2) and replacing $\int_0^\infty exp(-r^2/2\sigma^2)2\pi r\,dr$ with $2\pi\sigma^2$ under the assumption of axisymmetry yields the following:

$$\frac{d}{dx}\left[2\pi U_b^2(x)\sigma^2(x)\left(C(x) - \frac{C^2(x)}{2}\right)\right] + \pi\frac{dU_b^2(x)}{dx}\sigma^2(x)C(x) = 0. \tag{5.3}$$

In the case of zero pressure gradient, the second term on the left-hand side of equation (5.3) vanishes, and the following solution is obtained (see Bastankhah and Porté-Agel (2016)):

$$C_0(x) = \frac{\Delta U_{max}(x)}{U_{b0}} = 1 - \sqrt{1 - \frac{C_T}{8(\frac{\sigma_0(x)}{D})^2}}, \tag{5.4}$$

where $C_0(x)$ is the normalized maximum velocity deficit under ZPG, ΔU_{max} is the maximum velocity deficit, U_{b0} is the reference base flow velocity under ZPG, C_T is the turbine thrust coefficient, $\sigma_0(x)$ is the wake width under ZPG, and D is the turbine rotor diameter. Once $C_0(x)$ is obtained, we can compute the invariant ratio between the maximum velocity deficit and wake width such as:

$$\lambda_0(x) = \lambda(x) = \frac{C_0(x)U_{b0}}{\sigma_0(x)}, \tag{5.5}$$

where λ_0 and λ are the ratios under zero and non-zero pressure gradients, respectively. The assumption of the invariance has been verified for different pressure gradient situa-

tions(Shamsoddin and Porté-Agel, 2017a, 2018a; Thomas and Liu, 2004) and is used here to obtain the wake width under pressure gradient:

$$\sigma(x) = \frac{C(x)U_b(x)}{\lambda_0(x)},$$
(5.6)

and to eventually solve equation (5.3), which yields the following ordinary differential equation for $C(x)$ (as obtained by Shamsoddin and Porté-Agel (2018a)):

$$\frac{dC(x)}{dx} = \frac{-1}{\left(\frac{U_b^4(x)}{\lambda_0^2(x)}\right)(3C^2(x) - 2C^3(x))} \left[\frac{1}{4}\frac{dU_b^4(x)}{dx}\frac{C^3(x)}{\lambda_0^2(x)} + \left(C^3(x) - \frac{C^4(x)}{2}\right)\frac{d}{dx}\left(\frac{U_b^4(x)}{\lambda_0^2(x)}\right)\right].$$
(5.7)

In order to obtain a numerical solution for $C(x)$ from equation (5.7), a boundary condition is needed. In their original work, Shamsoddin and Porté-Agel (2018a) defined the boundary condition as:

$$C(x_i) = C_0(x_i),$$
(5.8)

which implies that at the starting point of the model (x_i), regarded as the start of the far wake (or alternatively the end of the near wake), the maximum velocity deficit is the same under a zero or non-zero pressure gradient. This assumption is valid in situations where the imposed pressure gradient is zero at the turbine location and becomes non-zero from a certain location in the far wake of the turbine. In fact, in their validation study (Shamsoddin and Porté-Agel, 2018a) and application of the model to wake flows over hills (Shamsoddin and Porté-Agel, 2018b), the pressure gradient by the terrain was imposed in the far wake, which resulted in the aforementioned boundary condition. However, if we consider a situation where the imposed pressure gradient at the turbine location or in its near wake is non-zero, the above-stated boundary condition does not hold. Examples of such situations can be easily found, for instance, the wake of a turbine sited close to the edge of an escarpment and on top of a hill or a building.

In the following, we present a simplified theoretical estimation of the near wake velocity under a non-zero pressure gradient. Prior to that, it is useful to review some basic characteristics of the wind turbine's near wake. The flow in the near wake is greatly influenced by the turbine characteristics, and a common approach is to assume a gradual transition from a top-hat velocity distribution behind the rotor to a Gaussian distribution at the end of the near wake. This is due to the growth of the shear layer behind the rotor periphery, which expands radially with the increase in the streamwise distance, as the outer flow mixes with the wake flow. The wake center velocity is assumed to be theoretically constant in the near wake region, as the shear layer does not grow enough to re-energize the wake center in this region. Bernoulli's equation has been applied to the regions upstream and downstream of the turbine to estimate the near wake velocity for a wind turbine under uniform inflow and zero pressure gradient

(Bastankhah and Porté-Agel, 2016; Manwell et al., 2010). This theoretical near wake velocity has been used to estimate the end of the near wake and to provide a limit for the maximum velocity deficit obtained from an analytical model in various challenging scenarios, such as wind turbines in yawed conditions or the ones experiencing vertical wind veer (Abkar et al., 2018; Bastankhah and Porté-Agel, 2016). It has also been implemented in different low-fidelity wake modeling utilities to estimate wake velocity at the start of the far wake (see e.g., Farrell et al. (2021)).

A schematic of the turbine wake is shown in figure 5.1, where position 1 corresponds to an upstream location undisturbed by the turbine, position 2 is immediately in front of the rotor, position 3 is immediately behind the rotor, and position 4 corresponds to the location in the wake where the wake pressure becomes equal to the base flow pressure and there is no mixing between the outer (base) flow and wake flow. The conditions defined here for the application of Bernoulli's equation are similar to those used for actuator discs placed in a confined flow with a spatially heterogeneous base flow velocity (Sørensen, 2016; Vogel et al., 2018). Following Bastankhah and Porté-Agel (2016) and Manwell et al. (2010), Bernoulli's equation for the control volumes up- and down-stream of the turbine can be written as:

$$\text{upstream: } P_{b1} + \frac{1}{2}\rho U_{b1}^2 = P_R^+ + \frac{1}{2}\rho U_R^2, \tag{5.9}$$

$$\text{downstream: } P_R^- + \frac{1}{2}\rho U_R^2 = P_{nw} + \frac{1}{2}\rho U_{nw}^2, \tag{5.10}$$

where P_{b1} is the base flow pressure upstream of the turbine (position 1 in Figure 5.1), and U_{b1} is the base flow velocity at the same location, the values of which can be obtained from the base flow information. Furthermore, P_R^+ and P_R^- are pressure values at the front and back sides of the rotor, and the velocities at these positions U_R are assumed to be the same. The wake center velocity in the near wake is U_{nw} (position 4 in Figure 5.1).

Subtracting equations (5.9) and (5.10) result in:

$$[P_{b1} - P_{nw}] + \frac{1}{2}\rho[U_{b1}^2 - U_{nw}^2] - [P_R^+ - P_R^-] = 0, \tag{5.11}$$

where $[P_R^+ - P_R^-] = (1/2)\rho U_{bT}^2 C_T$, U_{bT} is the base flow velocity at the turbine location, and in the case of ZPG, $[P_{b1} - P_{nw}] = 0$. However, in the presence of a pressure gradient in the base flow, the later pressure difference can be obtained by applying Bernoulli's equation on the base flow between positions 1 and 4:

$$[P_{b1} - P_{nw}] = \frac{1}{2}\rho[U_{b4}^2 - U_{b1}^2], \tag{5.12}$$

where U_{b4} is the base flow velocity at position 4. After substituting the base flow pressure difference and pressure difference across the rotor in Equation (5.11), we obtain the following relation for U_{nw}:

$$U_{nw} = \sqrt{U_{b4}^2 - U_{bT}^2 C_T}. \tag{5.13}$$

In the case of ZPG, $U_{b1} = U_{bT} = U_{b4}$, and it can be easily shown that the above equation reduces back to the well known relation: $U_{nw}/U_{bT} = \sqrt{1 - C_T}$. Finally, the maximum velocity deficit for the boundary condition of Equation (5.7) can be written as:

$$C(x_i) = 1 - \frac{U_{nw}}{U_{bxi}}, \tag{5.14}$$

where U_{bxi} is the base flow velocity at the end of the near wake. In the case of a zero pressure gradient imposed by the base flow at the turbine location, the above equation reduces back to Equation (5.8).

5.3 Model Validation

Following the derivation, we aim to validate the model with experimental data. For this purpose, we use the experimental data from Dar and Porté-Agel (2022b). In their experiments, a miniature wind turbine (WiRE-01) is placed one rotor diameter downstream of the edge of an escarpment, where the shape of the escarpment is varied between a forward-facing step with different edge curvatures and a ramp-shaped escarpment. Figure 5.2 shows the geometrical details of the escarpments used in the experiments, and the normalized base flow velocity at the turbine hub height. As can be seen, the variation in the base flow velocity is high closer to the turbine ($x/D = 0$, where D is the rotor diameter), and reaches almost a constant value about five rotor diameters downstream of the turbine. Different escarpment shapes also show differences in their base flow velocities, which indicates a difference in the imposed pressure gradient. The chosen experiments are well-suited to test the new model, as the imposed pressure gradient is higher closer to the edge of the escarpment (i.e., at the turbine location) and differs between the escarpments, which enables us to test the model under different pressure gradients. Table 5.1 presents a description of the escarpments.

In order to apply the pressure gradient model, we need two main inputs: the base flow velocity under the pressure gradient and the characteristics of the turbine wake under the zero pressure gradient ($C_0(x)$ and $\sigma_0(x)$). For the maximum velocity deficit under ZPG $C_0(x)$, we use Equation (5.4), which requires the turbine thrust coefficient C_T and wake width $\sigma_0(x)$. From experiments (Dar and Porté-Agel, 2022b), the thrust coefficient of 0.8 is used, which does not change between the flat and escarpment cases (Bastankhah and Porté-Agel, 2016; Dar and Porté-Agel, 2022b). To obtain the ZPG wake width, we use the linear growth of wake

width in the far wake region (Porté-Agel et al., 2020):

$$\frac{\sigma_0(x)}{D} = k_0 \frac{x}{D} + \epsilon, \tag{5.15}$$

where k_0 is the wake growth rate in ZPG, and ϵ is the initial wake width. The wake growth rate k_0 can be related to the streamwise turbulence intensity (TI) in the flow, where several linear relations between the streamwise turbulence intensity and the wake growth have been proposed in the literature (Brugger et al., 2019; Niayifar and Porté-Agel, 2016). Here, we use the relation proposed by Brugger et al. (2019), which states $k_0 = 0.30 \times TI$, as it fits the wake growth rate found experimentally for the miniature wind turbine in flat terrain by Bastankhah and Porté-Agel (2016). As the pressure gradient model does not explicitly relate the turbulence intensity change in ZPG and PG conditions, we take the rotor-averaged turbulence intensity in the base flow at the turbine location to compute the wake growth rate for the ZPG wake. This is performed in order to account for the change in the turbulence intensity between the zero and non-zero pressure gradient situations. The theoretical normalized wake width ϵ value of $1/\sqrt{8}$ is used at the end of the near wake (Bastankhah and Porté-Agel, 2016). Following (Bastankhah and Porté-Agel, 2016; Vermeulen, 1980), the end of the near wake is assumed to be the position where the theoretical and experimental velocity deficit maximum on the escarpments become equal. The near wake length obtained by this criterion is very similar to the one obtained from theoretical relations derived for flat terrain (Bastankhah and Porté-Agel, 2016; Vahidi and Porté-Agel, 2022b).

In order to use Equation (5.13), we need to define position 4 in Figure 5.1. Mathematically speaking, this position should be chosen such that Equation (5.13) yields a real value. A choice of position 4 where Equation (5.13) results in an imaginary number would indicate a breakdown of the theory, which could be similar to the situation of actuator discs with thrust coefficients above 1 in the classical one-dimensional momentum theory (Hansen, 2015). Following Sørensen (2016) and Vogel et al. (2018), from a physical perspective, position 4 should correspond to a location where the pressure in the wake flow becomes equal to that in the base flow, and there is no mixing between the (outer) base and wake flow. Figure 5.3 shows the contours of the normalized turbulence kinetic energy in the turbine wake for different escarpment cases. Behind the turbine top tip level, a region of high turbulence kinetic energy can be observed, which is relatively thin closer to the turbine but starts to expand in the vertical direction from a certain position downstream, corresponding to the position where tip vortices start to breakdown and the outer flow starts to mix with the wake flow. Therefore, position 4 should be chosen before the region of high turbulence kinetic energy starts to expand in the vertical direction. However, it should not be picked too close to the turbine to avoid the influence of the pressure drop across the rotor.

A common approach in the literature (Crespo et al., 1999; Frandsen et al., 2006; Sanderse, 2009) is to assume one rotor diameter downstream of the turbine as the distance where pressure in the wake and base flow equalizes. This position also lies within the region where the turbulence kinetic energy does not start to grow for all the cases. Therefore, we choose one
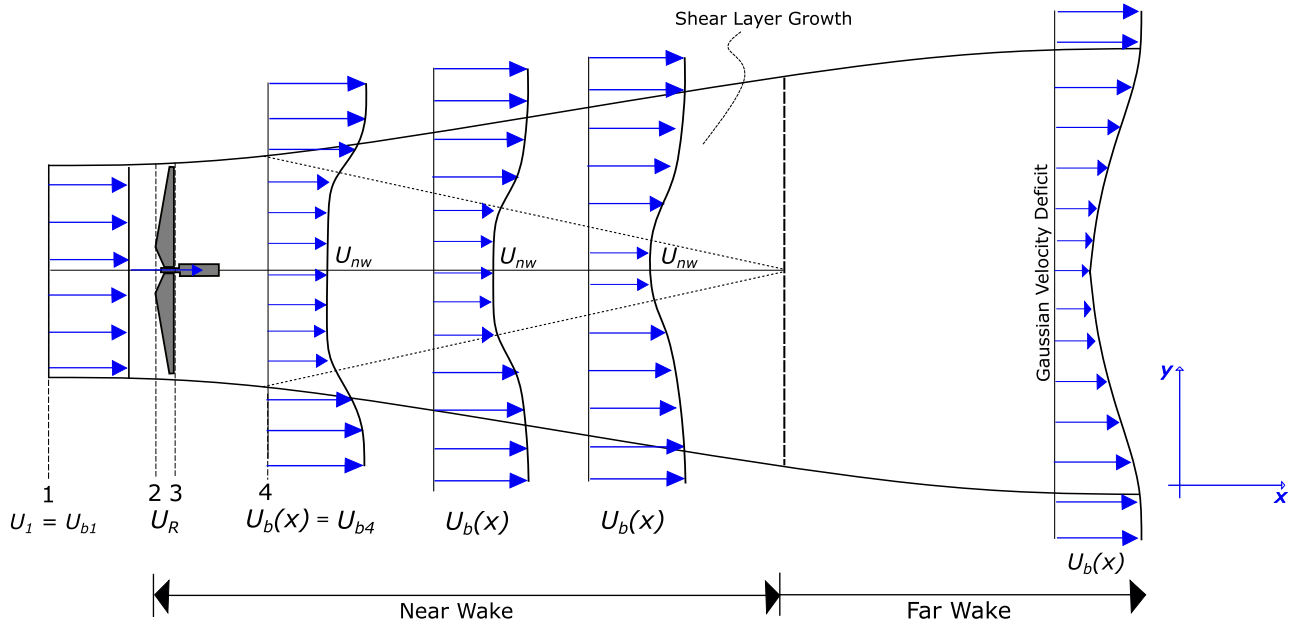
Figure 5.1: Schematic of a wind turbine wake.
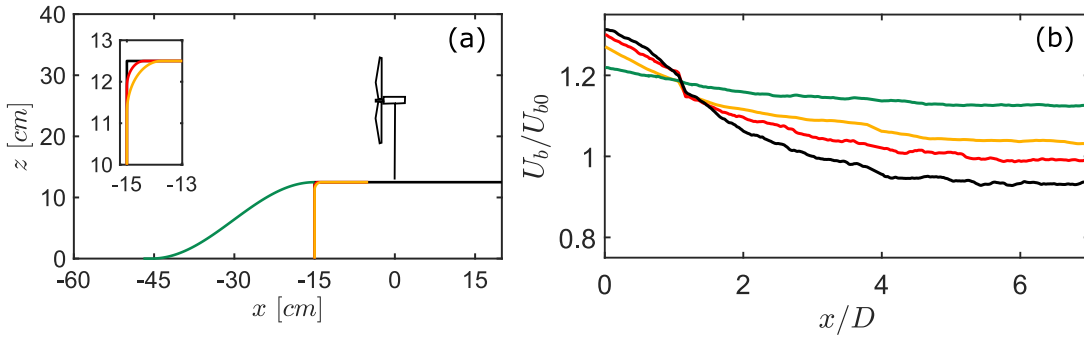
Figure 5.2: Side view of the escarpment geometry (a) and normalized base flow velocity at the hub height on top of the escarpments (b). Colors represent the respective escarpment shapes. The figure is adapted Dar and Porté-Agel (2022b).

Table 5.1: Description of different validation cases and some key parameters.

Case	Description	U_h [ms^{-1}]	$k_0 = 0.3TI$	C_T	U_{b0} [ms^{-1}]
FFS-I	Sharp 90° Edge	4.7	0.0380	4*0.8	4*3.55
FFS-II	5% radius of curvature with respect to height	4.6	0.0290		
FFS-III	10% radius of curvature with respect to height	4.52	0.0231		
Ramp	33° maximum slope	4.34	0.0155		

rotor diameter downstream of the turbine as a common assumption for position 4 in all cases. It is to be noted that the choice of position 4 used here might not be universal, and future work should investigate this. The above discussion comes from the one-dimensional momentum theory for actuator discs, and in reality, the structure of the turbine near wake is much more complex. As shown by Bastankhah and Porté-Agel (2016), the measured near-wake velocity deficit for the miniature turbine is higher than the theoretical one and varies instead of being a constant. This difference is attributed to several factors, including the wake of the nacelle and rotation of the wake. Although a simplified approximation, the theoretical near wake velocity provides useful information on the wake flow, such as the end of the near wake and a theoretical estimation for the velocity at the start of the far wake (Bastankhah and Porté-Agel, 2016; Farrell et al., 2021; Vermeulen, 1980).

Once all the required inputs for the pressure gradient model have been obtained, we compute the maximum velocity deficit under pressure gradient using Equation (5.7) with the new boundary condition given by Equation (5.14) and wake width using Equation (5.6). In addition to the new model, we also test the pressure gradient model by Shamsoddin and Porté-Agel (2018a), and the Gaussian model by Bastankhah and Porté-Agel (2014).

A comparison of the maximum velocity deficit normalized by the hub height velocity between the experiments and the analytical models is shown in Figure 5.4 (left panels). The new pressure gradient model is represented by 'PG-New', whereas the pressure gradient model by Shamsoddin and Porté-Agel (2018a) is named 'PG-SPA', and the zero pressure gradient model (Gaussian model) by Bastankhah and Porté-Agel (2014) is named 'ZPG'. The imposed pressure gradient depends on two factors: the shape of the escarpment, as a sharper edge would induce a higher pressure gradient, and the distance from the escarpment leading edge, as the pressure gradient would reduce with the increase in the distance from the escarpment edge. As a result, the differences between the different models compared here are also dependent on the same two factors. In general, the new pressure gradient model predicts the maximum velocity deficit reasonably well for all escarpments, as it accounts for the imposed pressure gradient at the turbine location. The PG-SPA model performs well for the ramp-shaped escarpment, as the imposed pressured gradient at the turbine location is lowest in this case. For the forward facing step cases, however, its performance degrades with the increase in the sharpness of the escarpment edge, where it works for the FFS-III case at distances greater than five rotor diameters, but underestimates the maximum velocity deficit for the other two FFS escarpments. This is due to the fact that the imposed pressure gradient is higher at the turbine location than in the far wake, and the PG-SPA model does not account for it, thereby underestimating the maximum velocity deficit. The zero pressure gradient model also underestimates the maximum velocity deficit for almost all the cases as it cannot account for the contribution of the pressure gradient to the velocity deficit.

The escarpments impose an adverse pressure gradient on the flow, which is known to slow down the recovery of the turbine wake compared to that under the zero pressure gradient (Shamsoddin and Porté-Agel, 2018a; Thomas and Liu, 2004). This explains why the models

that do not account for the imposed pressure gradient at the turbine location underestimate the maximum velocity deficit. It can also be noted that for the two forward-facing step escarpments with relatively sharper edges (FFS-I and FFS-II), the PG-SPA and ZPG models show very similar values of the maximum velocity deficit. This is due to the fact that in the mentioned cases, the base flow velocity at the start of the far wake is almost the same with and without the escarpment. In other words, these escarpments not only induce the highest pressure gradient closer to the escarpment edge, but they also show the fastest decay in the induced pressure gradient with downstream distance. Therefore, at around four rotor diameters downstream of the turbine (five rotor diameters from the escarpment edge), the pressure gradient induced by the escarpments in the FFS-I and FFS-II cases is almost zero; as the PG-SPA model does not account for the imposed pressure gradient at the turbine location, it yields values similar to the ZPG model.

Following the maximum velocity deficit, the equivalent wake width obtained from the analytical models is compared with the experimentally obtained one in Figure 5.4 (right panels). The ZPG wake width is smaller than the experimental equivalent wake width. This is to be expected, as an adverse pressure gradient results in a larger wake width compared to the zero pressure gradient one (Shamsoddin and Porté-Agel, 2018a; Thomas and Liu, 2004). The PG-SPA underestimates the wake width for the FFS-I and FFS-II cases, but works well for the rest of the cases. The wake width obtained from the new pressure gradient model is observed to agree well with the experimental data for all the cases.

A comparison of the normalized velocity deficit profiles between the analytical models and experiments is shown in Figure 5.5. The velocity deficit profiles obtained from the new pressure gradient model agree well with the experimentally obtained profiles for all escarpment cases. As shown by Dar and Porté-Agel (2022b), the wake width in the lateral and vertical directions can vary depending on the escarpment shape. However, as mentioned earlier, in the current modeling approach, we solved the problem for an equivalent wake width ($\sigma = \sqrt{\sigma_y \sigma_z}$). Comparing the experimental and (new) analytical velocity deficit profiles in the lateral and vertical direction shows that this approach works well. The PG-SPA and ZPG models, on the other hand, yield underestimated velocity deficit profiles for the most part. The PG-SPA model underestimates the velocity deficit profiles for the FFS-I and FFS-II cases, whereas it shows reasonable agreement for FFS-III case for downstream distances greater than five rotor diameters. For the ramp-shaped escarpment, it shows good agreement for all downstream distances. The ZPG model gives reasonable results at a downstream distance greater than five rotor diameters in the case of the ramp-shaped escarpment, which can be related to the fact that the effect of the pressure gradient is lowest for the ramp-shaped escarpment at high downstream distances. In general, we can say that the new pressure gradient model can successfully predict the velocity deficit in the turbine wake for all escarpment cases and outperforms the other two models tested in the study.
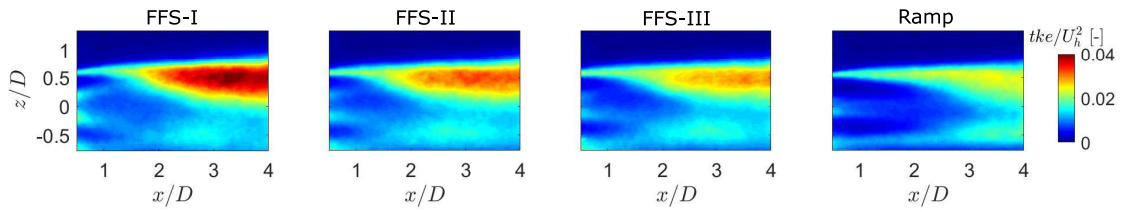
Figure 5.3: Contours of the normalized turbulence kinetic energy in the turbine wake.
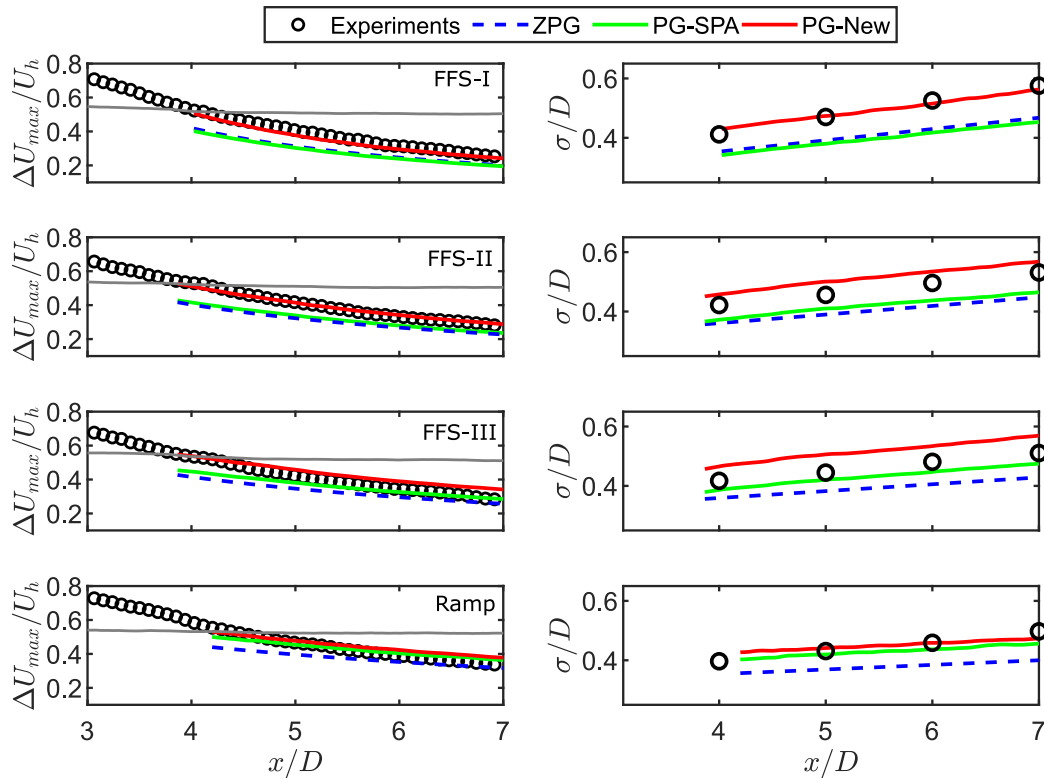
Figure 5.4: Comparison of the maximum normalized velocity deficit (left) and equivalent wake width (right) between the experiments and the analytical models. The solid gray line shows the theoretical maximum velocity deficit assuming a fixed near wake velocity.
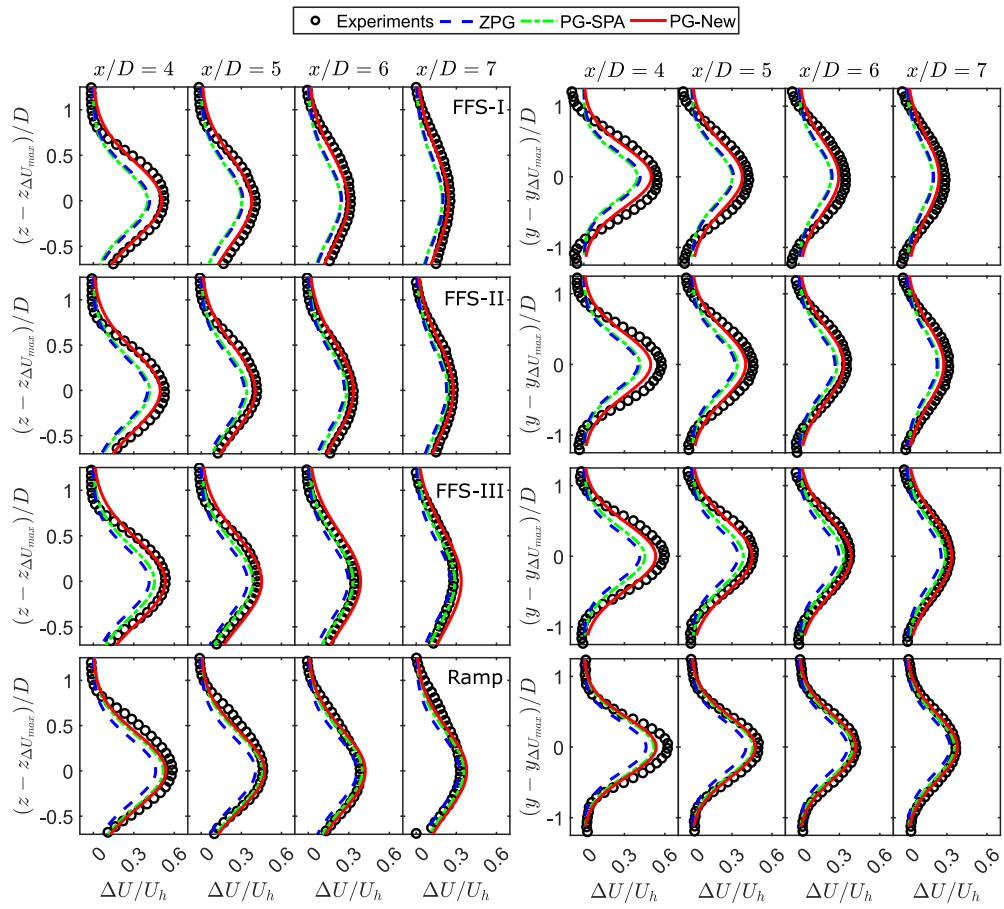
Figure 5.5: Comparison of the normalized vertical (left) and lateral (right) velocity deficit profiles between the experiments and the analytical models for different escarpments.

5.4 Summary

Wind turbines sited in heterogeneous terrain experience varying levels of pressure gradient. In the current work, we have developed an analytical modeling framework that can predict the velocity deficit downstream of a wind turbine under an arbitrary imposed pressure gradient. The model is based on the cross-stream integration of the streamwise momentum conservation equation, and the self-similarity of the wind turbine wake velocity deficit. It solves an ordinary differential equation to estimate the maximum velocity deficit in the far wake, where a theoretical estimate of the near wake velocity under pressure gradient is used as a boundary condition. The current model builds on a previously proposed one, which only accounted for the effect of imposed pressure gradient in the turbine far wake. With the new model, we can also account for the effect of an imposed pressure gradient at the turbine location, which increases the number of applications the model can be used for. The pressure gradient model requires the base flow velocity under the pressure gradient, and the wake characteristics (maximum velocity deficit and wake growth rate) under a zero pressure gradient as input parameters.

A validation of the new model against experimental data is performed. The experimental study involves a wind turbine placed close to the edge of escarpments of varying shapes. The turbine experiences varying levels of pressure gradient depending on the shape of the escarpment. The maximum velocity deficit and equivalent wake width obtained from the new model agree well with the experimental data for all cases. The velocity deficit profiles obtained analytically also show good agreement with both lateral and vertical velocity deficit profiles obtained experimentally. A comparison with another pressure gradient model and a model without any pressure gradient effects is also included. The new pressure gradient model is observed to outperform the other two models tested in the study for all cases. The other pressure gradient model worked for certain cases with relatively small imposed pressure gradients at the turbine location; however, its performance degraded for the cases with high imposed pressure gradients at the turbine location. Finally, the zero pressure gradient model only worked in the far wake of the escarpment with a smooth slope ahead of the turbine. Therefore, with the new modeling approach, we have extended the capability of analytical models to predict the wake velocity deficits of turbines experiencing an arbitrary imposed pressure gradient.

6 An experimental and analytical study of wind turbine wakes under pressure gradient[I] [II]

Abstract

This work is dedicated to the systematic investigation of wind turbine wakes under the effect of pressure gradient. Wind tunnel experiments are carried out with a wind turbine positioned on straight ramps of increasing angle such that it experiences an approximately linear flow speed-up/slow-down from the induction region into the far wake. Fifteen ramp angles are studied: 7 favorable (FPG), 7 adverse (APG) and 1 zero pressure gradient (ZPG). The wake center is shown to follow the base flow streamline originating from a virtual turbine hub height. A quasi-linear relationship between the pressure gradient and near wake length is demonstrated. Far wake characteristics such as the recovery of the wake center velocity deficit and wake growth rate are observed to vary systematically with the pressure gradient. The wake recovery rate increases (decreases) with the increase in the FPG (APG) and the wake growth rate shows a linear increase from most favorable to most adverse pressure gradient. The turbine power coefficient decreases significantly with increasing APG, to a greater degree than the increase in power coefficient under FPG. The engineering approach of superposing the wake deficit predicted by the standard Gaussian model on the modified base flow is shown to work for very moderate pressure gradients. In light of this, a threshold in terms of flow speed-up/slow-down along the wake trajectory is established, below which the engineering approach can be reasonably employed. Finally, a physics-based model for wakes under pressure gradient is tested. A new theoretical relation for near wake length under pressure gradient is proposed. Using the theoretical near wake length, the pressure gradient model predicts the turbine wakes for all cases with good accuracy and shows a significant improvement from the engineering approach.

6.1   Introduction

Global wind energy capacity has grown exponentially over the last few decades, with a cumulative installed capacity of 837 GW at the end of 2021 (GWEC, 2022). Despite this growth, it is estimated that to achieve the goal of net zero emissions by 2050, the yearly new wind energy installations need to be tripled by 2030 compared to those in 2020 (GWEC, 2022). Although wind energy has grown significantly - making it one of the cheapest available energy sources today (IRENA, 2021), even bigger challenges lie ahead if we are to achieve the ambitious goals set to tackle climate change. According to Veers et al. (2019), we need to address three grand challenges in the science of wind energy to access its full potential. The first of these challenges is to improve our understanding of the complicated physical interactions between atmospheric flows and wind farms, whereas the other two challenges are concerned with the aerodynamics of large wind turbines and grid integration of large wind farms. The fact that within wind farms most wind turbines operate in the wake of others makes things even more challenging. Turbine wakes, characterized by low velocity and high turbulence, depend mainly on the characteristics of the local flow and turbine operating conditions. A large body of literature exists which aims at understanding the interactions between wind turbines and surrounding flows under a range of different flow and turbine operating conditions (Porté-Agel et al., 2020; Stevens and Meneveau, 2017).

For wind turbines installed onshore, the likelihood is high that wind farms are sited in complex terrain or heterogeneous surface roughness conditions (Alfredsson and Segalini, 2017). Changes in terrain elevation or surface roughness have significant consequences for the boundary layer flow developing on top of it, inducing variations in flow shear, generating localized flow features and imposing localized pressure gradient. Understanding how wind turbines interact with such complicated flows, and more importantly, how those interactions differ from the ones in flat terrain is of paramount importance. This is due to the fact that most existing literature deals with wind turbines on flat terrain, and to what extent that knowledge can be extrapolated to a complex one remains to be understood.

Recent years have seen an increased interest in wind turbine wakes and power performance in complex terrain from the wind energy community. Tian et al. (2013) performed an experimental study of a wind farm sited on a two-dimensional gentle hill and showed that the hill top was the ideal location for power production, whereas turbines sited on the up- or downhill slopes produced comparatively less power due to the sheltering effect and wake of the hill, respectively. Hyvärinen and Segalini (2017a) investigated the power and thrust coefficients of wind turbines sited on periodic sinusoidal hills. They showed that the thrust and power coefficients remained comparable between a turbine sited on flat and sinusoidal hills. For two aligned turbines, they observed that the in-wake turbine performed better in the presence of hills than in the flat case. Liu and Stevens (2020a) showed that the power performance of a turbine sited on a two-dimensional hill depends on the relative height of the turbine with respect to the hill. For a wind farm sited across the hill, the turbines located on the leeward side of the hill suffered in terms of power production. Atmospheric stability has also been

shown to have a strong effect on wind turbine power production in complex terrain (de Sá S. et al., 2022; Han et al., 2018; Radünz et al., 2021). More recently, Troldborg et al. (2022) showed that complex terrain can change the power curve of a wind turbine compared to a flat terrain due to a change in the turbine induction.

For wind turbine wakes in complex terrain, several studies have investigated how the terrain affects some important wake characteristics. Recovery of the wake velocity deficit is an important factor in determining optimal inter-turbine spacing within a wind farm. Most studies have shown that turbine wakes recover faster in complex terrain compared to what is normally reported in a flat one (Astolfi et al., 2018; Dar and Porté-Agel, 2022b; Dar et al., 2022; Politis et al., 2012; Tabib et al., 2016; Yang et al., 2022; Zhang et al., 2022). This observation is attributed to the terrain enhanced turbulence production, which leads to higher entrainment of energy into the wake, and thus, faster recovery. An associated characteristic of the wake is its expansion in the cross-stream direction, which has also been shown to be higher in steep terrain (Dar and Porté-Agel, 2022b; Dar et al., 2022; Zhang et al., 2022). The terrain is also known to affect the trajectory of the wake. Menke et al. (2018) found that the wake trajectory is dependent on atmospheric stability in a complex terrain. They showed that the turbine wake follows the terrain in stable conditions, deflects upward in unstable conditions and propagates horizontally in neutral conditions. Barthelmie and Pryor (2019), however, made an opposite observation in the same terrain and associated the discrepancy with the observations of Menke et al., 2018 to the downstream distance over which the wake trajectory was followed. Liu et al. (2021) performed large eddy simulation of wind turbine wake over two- and three- dimensional hills, and evaluated different strategies of superposing a turbine wake on a hill. They found that the strategy of following the flow streamline originating from turbine hub height works best. Dar and Porté-Agel (2022b) showed that for a turbine sited on an escarpment, the vertical velocity imposed by the surrounding flow affects the wake trajectory. They also showed that the meandering of the wake is dependent on the turbulence intensity induced by the terrain (Dar and Porté-Agel, 2020, 2022b). Moreover, atmospheric stability has also been shown to influence the development of turbine wakes in complex terrain (Han et al., 2018; Liu and Stevens, 2021).

Changes in terrain elevation or surface roughness conditions also result in localized pressure gradients. The effect of pressure gradient on the development of wakes is a classical problem of fluid mechanics. Hill et al. (1963) investigated the effect of moderate pressure gradients on the wake of an obstructive rectangular bar. They showed that adverse pressure gradients can cause the wake deficit recovery to slow down and wake width to grow rapidly. Additionally, they developed a simple model to capture these effects. Nakayama (1987) performed a combined study of pressure gradient and streamline curvature on the wake of a two-dimensional airfoil-like thin plate. They showed that both the mean flow and turbulence quantities are affected by the pressure gradient and streamline curvature. Liu et al. (2002) performed experiments to investigate a planar wake exposed to constant adverse and favorable pressure gradients. They showed that even moderate pressure gradients can affect the wake deficit and growth rate. In addition, they found that the wake deficit remains self-similar under pressure gradient.

A follow-up study was performed to investigate the similarities and differences between symmetric and asymmetric wakes under pressure gradient (Thomas and Liu, 2004). Among other things, they showed that the ratio of wake deficit to its width remained insensitive to the imposed pressure gradient. Rogers (2002) performed direct numerical simulations of turbulent planar wakes. They found a universal profile for the mean wake velocity deficit and observed that the response of turbulence quantities to the pressure gradient was smaller than that of the mean flow. More recently, Shamsoddin and Porté-Agel (2017a) proposed an analytical model for planar wakes and validated it with the experimental data of Liu et al. (2002). All of these studies consider turbulent planar wakes, where favorable (adverse) pressure gradients have been shown to enhance (slow-down) the wake deficit recovery and reduce (increase) the wake expansion rate.

Wind turbine wakes, on the other hand, are three-dimensional with a reasonable axisymmetry in the cross-stream plane. The effect of terrain-induced pressure gradient on wind turbine wakes has been explored in some recent studies. Shamsoddin and Porté-Agel (2018a) proposed an analytical model for turbulent axisymmetric wakes and validated it with their large-eddy simulations. They then applied this model to the wake of a wind turbine located upstream of a hill and combined it with the streamline curvature caused by the hill (Shamsoddin and Porté-Agel, 2018b). They also identified two regions of flow over a hill corresponding to adverse and favorable pressure gradients and showed how the recovery of the wake depends on its position relative to the hill. Cai et al. (2021) performed an experimental study of wind turbine wake under pressure gradient. They placed a turbine at the edge of a ramp and varied the imposed pressure gradient by altering the ramp slopes. They tested the model of Shamsoddin and Porté-Agel (2018a) and found good agreement with the data. Furthermore, they investigated the effect of pressure gradient induced change in velocity on the power output of the turbine.

Analytical modeling of wake velocity deficit is one of the most active areas of research in the wind energy community, as it provides computationally cheap estimation of turbine wakes with a reasonable accuracy. Such models are widely used in the industry during layout optimization phase of wind farm planning, as they enable the evaluation of multiple layouts and wind directions in relatively short time. For a detailed review of analytical wake models, the reader is referred to Göçmen et al. (2016), Kaldellis et al. (2021), and Porté-Agel et al. (2020). Some notable mentions in this context are Jensen (1983), Frandsen et al. (2006), and Bastankhah and Porté-Agel, 2014. Most analytical models are derived using mass and/or momentum conservation under the assumption of a zero pressure gradient. The Gaussian model (Bastankhah and Porté-Agel, 2014) derives an algebraic equation for the streamwise evolution of the maximum wake velocity deficit and uses the self-similarity of the wake to produce the velocity deficit profiles. This self-similarity of the turbine wake has been verified experimentally and numerically for flat and complex terrains (Bastankhah and Porté-Agel, 2017a; Dar and Porté-Agel, 2022b; Dar et al., 2019; Xie and Archer, 2017).

For wind turbines in complex terrain, the assumption of a zero pressure gradient does not hold. Nevertheless, several studies have tried to adapt the Gaussian model (Bastankhah and

Porté-Agel, 2014) for application in complex terrain. Brogna et al. (2020) proposed a modified Gaussian model for their layout optimization study. For different turbines, the local base flow (flow without turbine) velocity at a given turbine position was used to account for topography effects. More recently, Farrell et al. (2021) also proposed an adapted formulation of the Gaussian model for application in complex terrain. They made the reference velocity in the Gaussian model spatially variable throughout the wake, thereby, claiming to improve over the approach of Brogna et al. (2020). They, however, acknowledged that the approach of adapting Gaussian model to varying base flow velocity violates the conservation of streamwise momentum, as the underlying model is derived under the assumption of zero pressure gradient. Such approaches of superposing a Gaussian model on a varying base flow can at best be considered engineering approaches and their simplicity makes them suitable for industrial applications. A physics-based model for wind turbine wakes under pressure gradient has been proposed by Shamsoddin and Porté-Agel (2018a). This model accounts for the effect of an arbitrary imposed pressure gradient on the far wake evolution of an axisymmetric wake. More recently, Dar and Porté-Agel (2022a) extended the model of Shamsoddin and Porté-Agel (2018a) to account for the effect of an imposed pressure gradient in the near wake as well.

Current work is inspired by the need for a systematic study of wind turbine wakes under a range of terrain-induced pressure gradients. We have performed wind tunnel experiments with a miniature wind turbine, where the pressure gradients are induced by means of constant slope ramps with different inclination angles. The turbine is placed such that the induction region, near wake and far wake are all exposed to an approximately constant flow acceleration or deceleration caused by the pressure gradient. The objectives of this study are threefold:

1. To understand systematically how some important wake characteristics such as its recovery, expansion, turbulence quantities and near-to-far wake transition change across a range of imposed pressure gradients.

2. To define a threshold imposed pressure gradient beyond which the simplified engineering approach of superposing a wind turbine wake obtained from a zero pressure gradient model on a spatially varying base flow velocity does not work.

3. To demonstrate how a physics-based analytical model designed for wakes under pressure gradient can improve the wake deficit prediction, when the simplified engineering approach fails.

The rest of the article is structured as follows: the experimental setup and results are presented in section 6.2, the analytical modeling approaches are described and compared in section 6.3, and finally a summary of the work along with some concluding remarks are given in section 6.4.

6.2 Experiments

6.2.1 Setup

The experiments are performed in the closed-loop boundary layer wind tunnel at the WiRE laboratory of EPFL. It is a low-speed wind tunnel driven by a 130 kW fan, with an area contraction ratio of 5:1 at the inlet and a test section of dimensions 28 m × 2.56 m × 2 m (length × width × height). The free-stream turbulence intensity in the test section is typically less than 1%. This is achieved by conditioning the flow through a series of honeycomb meshes and mesh screens before the beginning of the contraction. In addition, the area contraction before the inlet further helps to create a laminar and uniform flow at the inlet. A zero pressure gradient boundary layer is developed in the wind tunnel with the adjustment of the ceiling height and width of the walls.

The miniature wind turbine used in this study is a three-bladed horizontal axis turbine developed at the WiRE lab. It is a scaled-down version of the WiRE-01 turbine Bastankhah and Porté-Agel (2017a), where the scaling ratio is 1:1.43 between the scaled-down and original turbine. Dar et al. (2022) characterized the power and thrust coefficients of the scaled-down turbine and showed that scaling-down the turbine does not influence its performance as long as the Reynolds number is comparable between the original and scaled-down turbines. The hub height z_h and rotor diameter d of the miniature turbine are 8.75 cm and 10.5 cm, respectively. The rotor is manufactured through 3D-printing using a liquid photopolymer resin material. The rotor is mounted on a direct current motor (model: DCX10L) and controlled using a servo controller (model: ESCON 36/2 DC).

We use linear ramps, where the slope of the ramps is varied between 0° and 13.1° to impose a range of pressure gradients. In total 15 different pressure gradient cases are studied: one for the zero pressure gradient, and seven each for the favorable and adverse pressure gradients. The ramps are 1.35 m (13d, where d is the rotor diameter) in length, 2.5 m in width, and their heights are: 0 mm (0 d, 0°), 35 mm (1/3 d, 1.5°), 52 mm(1/2 d, 2.2°), 79 mm (3/4 d, 3.3°), 105 mm (1 d, 4.4°), 157 mm (1.5 d, 6.6°), 210 mm (2 d, 8.8°) and 315 mm (3 d, 13.1°). In the favorable pressure gradient (FPG) cases, the ramps have a positive slope and the turbine is placed at a horizontal distance of 2.5d from the front edge of the ramp, whereas in the adverse pressure gradient (APG) cases, the ramps have a negative slope and the turbine is placed at a horizontal distance of 4d from the front of the ramp. The turbine streamwise position is chosen to distance it from the effect of ramp edges, and the turbine and to position the turbine and wake in a region of approximately constant pressure gradient. The ramp edges were smoothed out with tape to reduce the effects of sharp convex corners. In all cases the turbine tower is pitched to align the rotor with the incoming base flow angle at the hub height. This choice was made to avoid effects of a rotor tilted relative to the flow, so to better isolate the effect of pressure gradient.

A two-dimensional two-component (2D2C) particle-image velocimetry (PIV) system is used
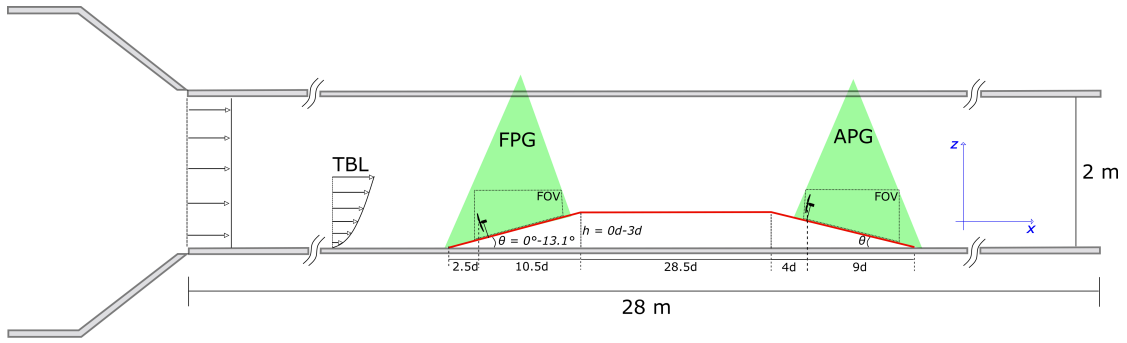
Figure 6.1: Schematic representation of the experimental setup (not to scale).

to capture flow measurements in a vertical (xz) plane passing through the turbine centerline. Flow measurements are taken with and without the turbine to characterize the wake and base (without turbine) flow, respectively. The PIV system is comprised of one sCMOS camera (2560 × 2160 pixels) with a 50 mm lens; a 425 mJ double-pulsed Nd:YAG laser (Litron lasers, Nano TRL 425-10) at a wavelength of 532 nm; and a programmable timing unit (LaVision, PTU-v9). The measurements are captured at a sampling rate of 10 Hz, where 1000 instantaneous fields are used (except for one case, where 750 fields are used) to obtain time averaged flow statistics. The size of the field-of-view (FOV) is $7.5d \times 6.3d$ with a spatial resolution of $0.024d$. The flow is seeded with olive oil droplets of several microns in diameter through a slot near the inlet of the test section. A sketch of the experimental setup is shown in figure 6.1.

A double-pass reducing size interrogation window of 64 × 64 pixels and 32 × 32 pixels with a 75% overlap between consecutive windows is used to perform image post-processing. Bad vectors from the correlation are removed using an outlier detection method, where the maximum uncertainty in the mean flow is estimated to be around 0.06 ms^{-1} based on a correlation statistics approach (Wieneke, 2015).

The power produced by the turbine P is measured by multiplying the shaft torque Q of the turbine by its rotational speed Ω. The shaft torque is estimated by multiplying the torque constant K of the DC motor by the generated current I, and adding to it the frictional torque Q_f. The detailed procedure for power measurements is described by Bastankhah and Porté-Agel (2017a). The power coefficient C_P is estimated using the following relation: $C_P = \frac{P}{1/2\rho A U_r^3}$, where ρ is air density, A is the rotor swept area and U_r is the rotor equivalent velocity at the turbine position.

Although a natural boundary layer can develop on the smooth wind tunnel floor due to its length (Dar and Porté-Agel, 2022b), in the current work we facilitate the development of the boundary layer to further increase its height. We place a picket fence (10 cm in length and 5 cm in height, with spikes of 3 cm in length) at the inlet of the test section and cover the floor of the wind tunnel with double-rolled chains at a streamwise spacing of 40 cm. This is done to increase the boundary layer height such that it is more than twice the height of the ramp in the most extreme case. The inlet velocity of the test section is varied such that the

turbine hub height velocity is similar in all cases. The hub height velocity is in the range of 6.26 - 6.73 ms^{-1}, except for one case where it is 5.96 ms^{-1}. This is done to achieve a comparable Reynolds number ($Re_d = \frac{U_h d}{\nu}$, where ν is the kinematic viscosity of air) in all the cases, which is found to be in the range of 42500-48000 in all the cases. Although the Reynolds number in the wind tunnel experiments is smaller than the one for the utility-scale wind turbines, it is close to the threshold observed by Chamorro et al. (2012) at which the mean wake flow becomes independent of Reynolds number. In addition, it is well established that most of the far wake characteristics are dependent on the turbine thrust coefficient (Porté-Agel et al., 2020). The miniature turbine used in the current study is specifically designed to achieve a thrust coefficient close to the utility-scale turbines, which makes it possible to extend the findings of this study to the utility-scale turbines.

To characterize the incoming turbulent boundary layer, a combination of the 2D2C PIV system described earlier and a laser Doppler velocimetry (LDV) system is used. The LDV system used in the study is previously described by Dar et al. (2022). A combination of the two techniques is employed for two reasons: the PIV field-of-view is not high enough to capture the boundary layer height, whereas for the LDV system, measurements near the ground can not be captured due to the blockage of one of the laser beams close to the ground. Measurements are taken 20 m downstream of the test section inlet, where PIV measurements for different pressure gradient cases are taken. A comparison of the normalized averaged streamwise velocity U/U_h, where U_h is the hub height velocity, the streamwise turbulence intensity ($I_u = \sigma_u/U_h$, where σ_u is the standard deviation of the horizontal velocity), and the normalized averaged vertical momentum flux between the PIV and LDV is shown in figure 6.2. A good degree of agreement is observed in the overlapping region of the two measurement techniques for the normalized averaged streamwise velocity, streamwise turbulence intensity and the normalized averaged vertical momentum flux. From the LDV measurements, the free stream velocity U_∞ is 9.7 ms^{-1}, where by using the criteria of $\delta = 0.99 U_\infty$ the boundary layer height is estimated to be around 58.5 cm. This shows that the boundary layer height is almost twice compared to the height of the tallest ramp. A logarithmic profile is fitted to the PIV data in the surface layer to obtain the aerodynamic surface roughness z_0 and the friction velocity u_*. The logarithmic fit and measured velocity profile are shown in figure 6.2 (d), where a friction velocity u_* value of 0.386 ms^{-1} and aerodynamic surface roughness z_0 of 0.1 mm are obtained.

6.2.2   Results

This section deals with the results from the PIV experiments. We first show the differences in the base flow (flow without the turbine) caused by the increase in the inclination of the ramps, for both the FPG and APG cases. For the turbine, we first show how the power coefficient is affected by the change in the pressure gradient and follow it up with a comprehensive wake flow analysis. For the mean flow, we define U as the time-averaged streamwise velocity, which is defined as $U = \sqrt{U_x^2 + U_z^2}$, where U_x and U_z are horizontal and vertical velocity components, respectively.
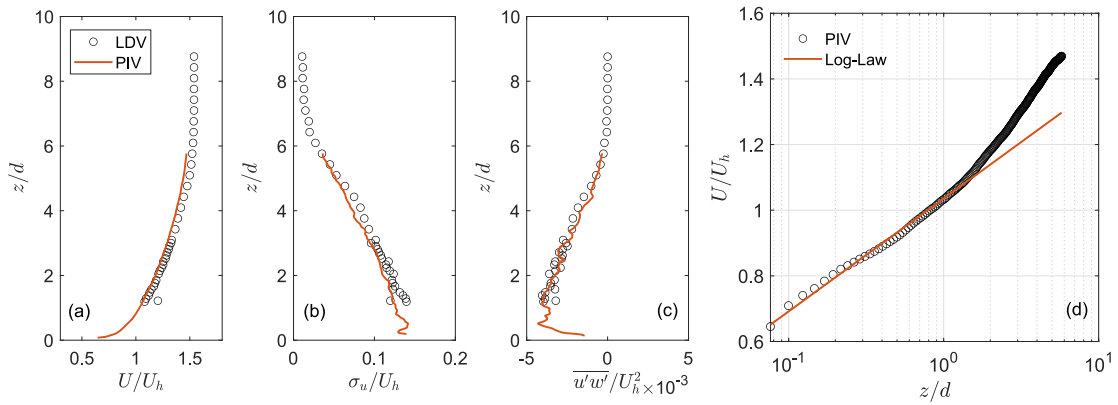
Figure 6.2: Comparison of the (a) normalized averaged streamwise velocity, (b) streamwise turbulence intensity and (c) normalized averaged vertical momentum flux obtained from PIV and LDV. (d) Normalized averaged streamwise velocity obtained in semi-logarithmic coordinates with the logarithmic fit in the brown line.

Base flow contours

We first characterize the base flow under different imposed pressure gradient situations. Figure 6.3 shows contours of the normalized averaged streamwise velocity along with flow streamlines for different pressure gradients. Here, $(x, z) = (0, 0)$ represents the prospective turbine hub position. For ZPG, the streamwise velocity appears to be constant in the streamwise direction with a vertical shear, and the flow streamlines are parallel to the ground. Flow acceleration and deceleration is observed in FPG and APG cases, respectively. In FPG cases, the flow roughly follows the ramp angle at smaller ramp angles, whereas for higher ramp angles, the streamlines tend somewhat into the surface of the ramp, following an angle less than ramp angle. In high inclination APG cases, the flow appears to move away from the ramp surface, rather than following the ramp slope. No flow separation is observed in any of the modeled cases. As a more quantitative comparison between different cases, we plot the normalized averaged streamwise velocity at the local hub height as a function of the horizontal distance in figure 6.4. It can be readily seen that for the captured field-of-view, the flow speed-up and deceleration induced by the ramps is linear in all cases, whereas for ZPG the velocity is constant throughout the horizontal distance captured in this study. A flow speed-up of 1.33 with respect to the streamwise velocity at the hub height of the prospective turbine is observed for the highest FPG cases, whereas a deceleration to a value of 0.47 is seen for the highest APG case at $x/d = 7$. This translates to a flow speed-up of 4.7% per rotor diameter for the highest FPG case and a flow deceleration of 7.5% per rotor diameter for the highest APG case at a fixed local height above the surface with respect to the streamwise velocity at the prospective turbine location.

In Shamsoddin and Porté-Agel (2018a), the imposed pressure gradient is present only in the far wake, and exhibits a non-linear trend in the horizontal direction. The maximum speed-up and deceleration is about 1.55% and 0.67% per rotor diameter for the FPG and APG cases, respectively. For Dar and Porté-Agel (2022a), adverse pressure gradients are induced by the
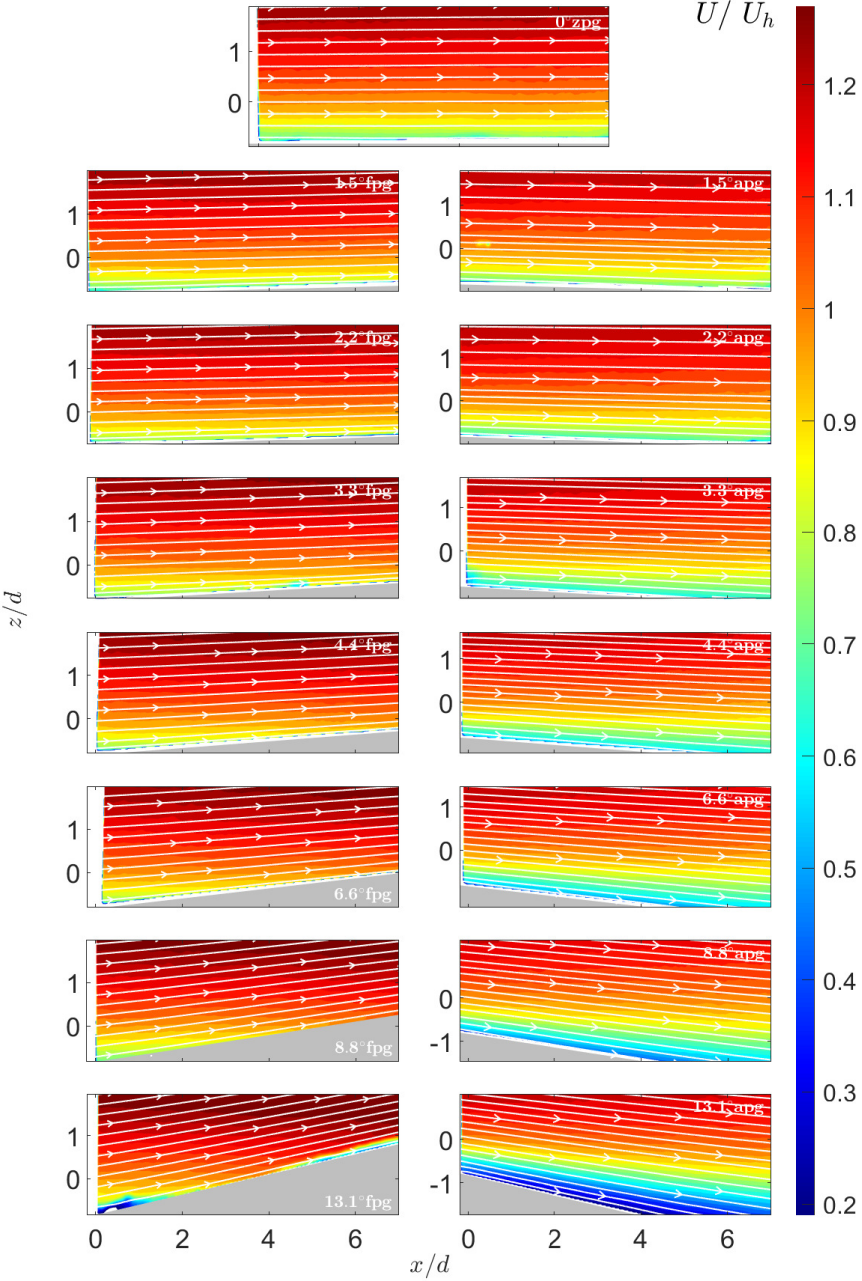
Figure 6.3: Contours of the normalized averaged streamwise velocity in the base flow for different pressure gradient conditions. Mean flow streamlines are overlaid on the contours.
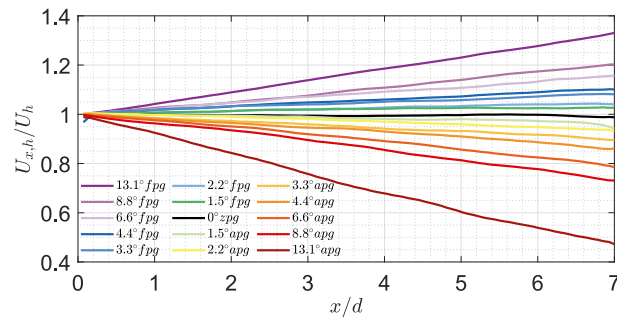
Figure 6.4: Normalized averaged streamwise velocity at the local hub height above the ramp as a function of horizontal distance for different pressure gradient cases.

escarpments with high pressure gradients in the near wake, which diminish in the far wake with a non-linear trend. In Cai et al. (2021), the turbine is located at the edge of a ramp, where the base flow is initially affected by the curvature of the ramp edge. The flow speed-up in the highest FPG case is around 1.67% per rotor diameter and its deceleration is approximately 1.45% per rotor diameter in the highest APG case. Therefore, in the current study, we have created stronger pressure gradients than the ones tested before in the context of wind energy. Another key difference from previous studies is that the flow all the way from the turbine induction region through to its far wake is exposed to an approximately constant pressure gradient.

Figure 6.5 shows the contours of the horizontal turbulence intensity $I_x = \sigma_{U_x}/U_h$ for different pressure gradient situations. For ZPG case, high turbulence intensity near the ground due to high flow shear is observed, which is approximately constant in the horizontal direction. The change in the ramp inclination has a significant influence on the mean flow shear, which results in the change in the turbulence intensity. For FPG cases, as the flow speeds up over the ramp, the mean flow shear near the ground decreases, which results in a decrease in the horizontal turbulence intensity with the increase in the horizontal distance. For the APG cases, on the other hand, as the flow moves away from the surface (shown previously using streamlines), the mean flow shear increases with increase in the horizontal distance and ramp inclination, thereby resulting in an increase in turbulence intensity. The pressure gradient imposed by the terrain is characterized by the streamwise velocity gradient $((-1/\rho)\partial p/\partial x \approx U_b dU_b/dx)$ (Dar and Porté-Agel, 2022a; Shamsoddin and Porté-Agel, 2017a, 2018a), where $dU_b/dx = 0$ corresponds to ZPG, $dU_b/dx > 0$ corresponds to FPG and $dU_b/dx < 0$ corresponds to APG.

Power performance

Several studies have shown that terrain can have a significant influence on the power production of a wind turbine sited on it. Cai et al. (2021) showed that the pressure gradient induced change in velocity can lead to a difference in the turbine power production compared to that in a flat terrain. More recently, Troldborg et al. (2022) showed that the non-homogeneity of the base flow can affect the power coefficient of a wind turbine in a complex terrain compared
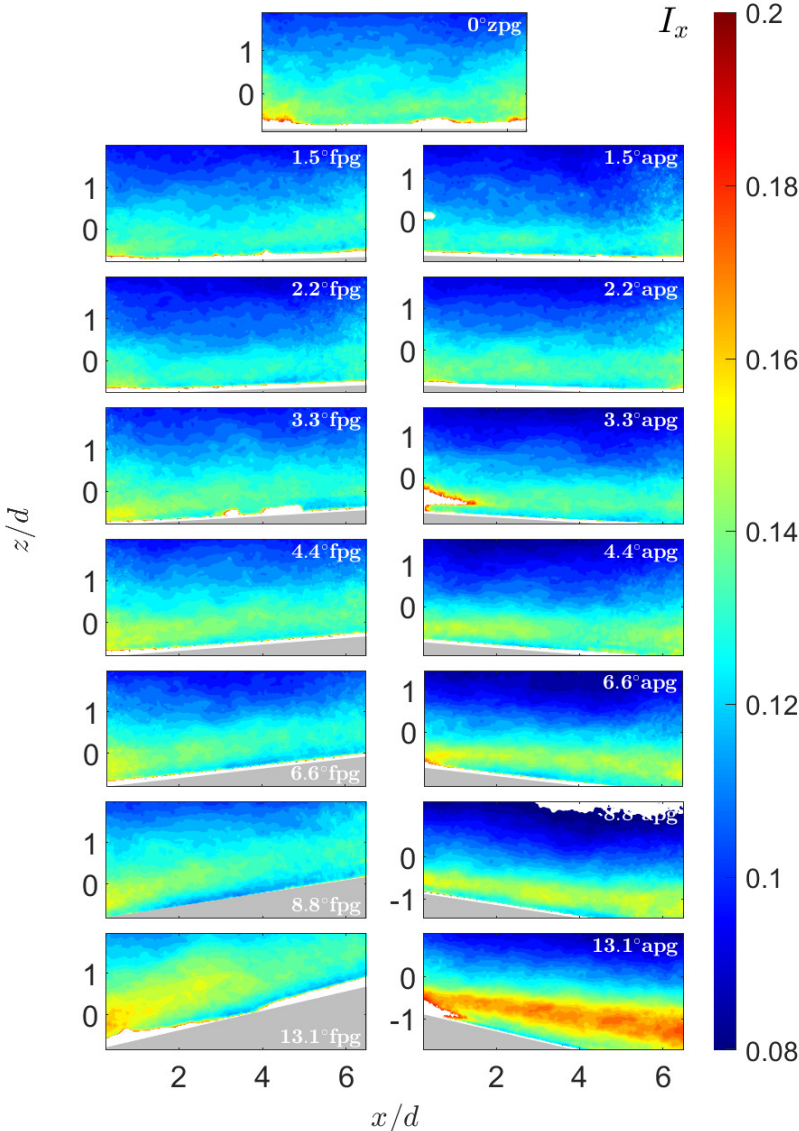
Figure 6.5: Contours of the horizontal streamwise turbulence intensity in the base flow for different pressure gradient conditions.
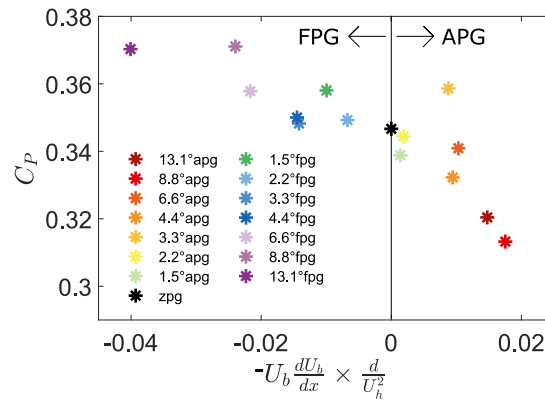
Figure 6.6: Wind turbine power coefficient as a function of normalized imposed pressure gradient.

to a reference power curve obtained in the flat terrain. In this work we are interested in understanding the variation of power coefficient of a turbine under a systematic change in the imposed pressure gradient.

Figure 6.6 shows the variation of the power coefficient as a function of normalized imposed pressure gradient at the turbine position. The pressure gradient is characterized via the streamwise velocity gradient along the wake trajectory, which will be explained later in section 6.2.2. The miniature turbine is always operated at an optimal tip speed ratio for a certain pressure gradient situation. For the ZPG case, a value of 0.347 is observed, which is similar to the one reported by Dar et al. (2022) for the same turbine. This indicates that the power coefficient for the model wind turbine used in the study is insensitive to the turbulence intensity of the incoming flow, as the power curve in Dar et al. (2022) was measured at an incoming turbulence intensity of around 7%.

A general trend is observed, which shows that the power coefficient decreases with the increase in the adverse pressure gradient, whereas it shows an increase with the increase in the favorable pressure gradient. The decrease in the power coefficient with the increase in adverse pressure gradient is observed to be much stronger compared to the increase in the power coefficient with the increase in favorable pressure gradient. Quantitatively, C_P decreases by approximately 9.7% in the highest APG case compared to a 6.7% increase in the highest FPG case. However, the magnitude of pressure gradient in the highest FPG case is twice that in the highest APG case. This indicates that an APG can have more severe consequences for a turbine power coefficient than the benefits obtained in a FPG situation. This can be particularly important for turbines sited on or around hillsides, where depending on the wind direction, a turbine will be operating in a favorable or adverse pressure gradient situation. Apart from the general trend, some anomalies are observed (e.g. 3.3° apg case), which could be related to the uncertainties in the power measurements, as discussed by Bastankhah and Porté-Agel (2017a).

Wake flow contours

The effect of pressure gradient on the turbine wake development is quantified in this section. Figure 6.7 shows the contours of the normalized averaged streamwise velocity in the turbine wake, along with the in-plane streamlines. For the FPG cases, the normalized averaged streamwise velocity shows an increase in magnitude compared to the ZPG case with the increase in favorable pressure gradient, whereas for the APG cases, it decreases with the increase in the adverse pressure gradient. In addition, figure 6.8 shows the contours of the normalized averaged vertical velocity in the turbine wake. For the ZPG case, the normalized averaged vertical velocity is the smallest among all the cases. For the pressure gradient cases, the normalized averaged vertical velocity induced by the inclination of the ramp affects the vertical velocity in the wake flow. For FPG cases, the vertical velocity is mostly positive where an increase in magnitude with the increase in the ramp angle is observed. For the APG cases, a small region of positive vertical velocity is observed close to the turbine, whereas it is mostly negative due to the downward inclination of the ramps. To isolate the effect of the turbine on the wake velocity, we compute the streamwise velocity deficit $\Delta U = U_b - U_w$, where U_b is the time-averaged base flow velocity and U_w is the time-averaged wake flow velocity. Figure 6.9 shows the contours of the normalized averaged streamwise velocity deficit for different pressure gradient situations. Consistent with the previous studies (Cai et al., 2021; Liu et al., 2002; Shamsoddin and Porté-Agel, 2018a), the streamwise velocity deficit is observed to decrease with the increase in the FPG and increase with the increase in APG. This is attributed to the fact that a favorable pressure gradient enhances the wake recovery, whereas an adverse pressure gradient slows it down.

Looking at the wake trajectory, which is identified as the vertical position of the maximum streamwise velocity deficit at each horizontal position, it is observed that the wake does not follow the terrain for higher inclination angles. For the FPG cases, the wake shows a downward trajectory and becomes increasingly attached to the surface with the increase in the FPG, whereas for the APG cases, it moves away from the surface. It is shown that, to a good approximation, the wake trajectory follows the base flow streamlines - rather than travelling horizontally, or following a line of constant height above the surface of the hill. Figure 6.10 shows the normalized averaged streamwise velocity in the base flow along with flow streamlines and turbine wake trajectory. It can be seen that the wake trajectory follows the base flow streamlines originating from the turbine hub position to a good degree of approximation. In situations where wake trajectory is unknown, the base flow streamline originating from the prospective turbine hub position can be employed as a proxy. In most cases, the vertical deviation of the wake trajectory from the hub height streamline is less than $0.05d$ over a horizontal distance of $7d$. In the most extreme APG case, however, a deviation of about $0.2d$ in the vertical direction is observed at a horizontal position of $7d$, which leads to a difference of about 7.5% at $7d$ between the velocity at the wake trajectory and that at the streamline. Following the base flow streamline was in all cases, a significantly better strategy compared to following the projected hub height.
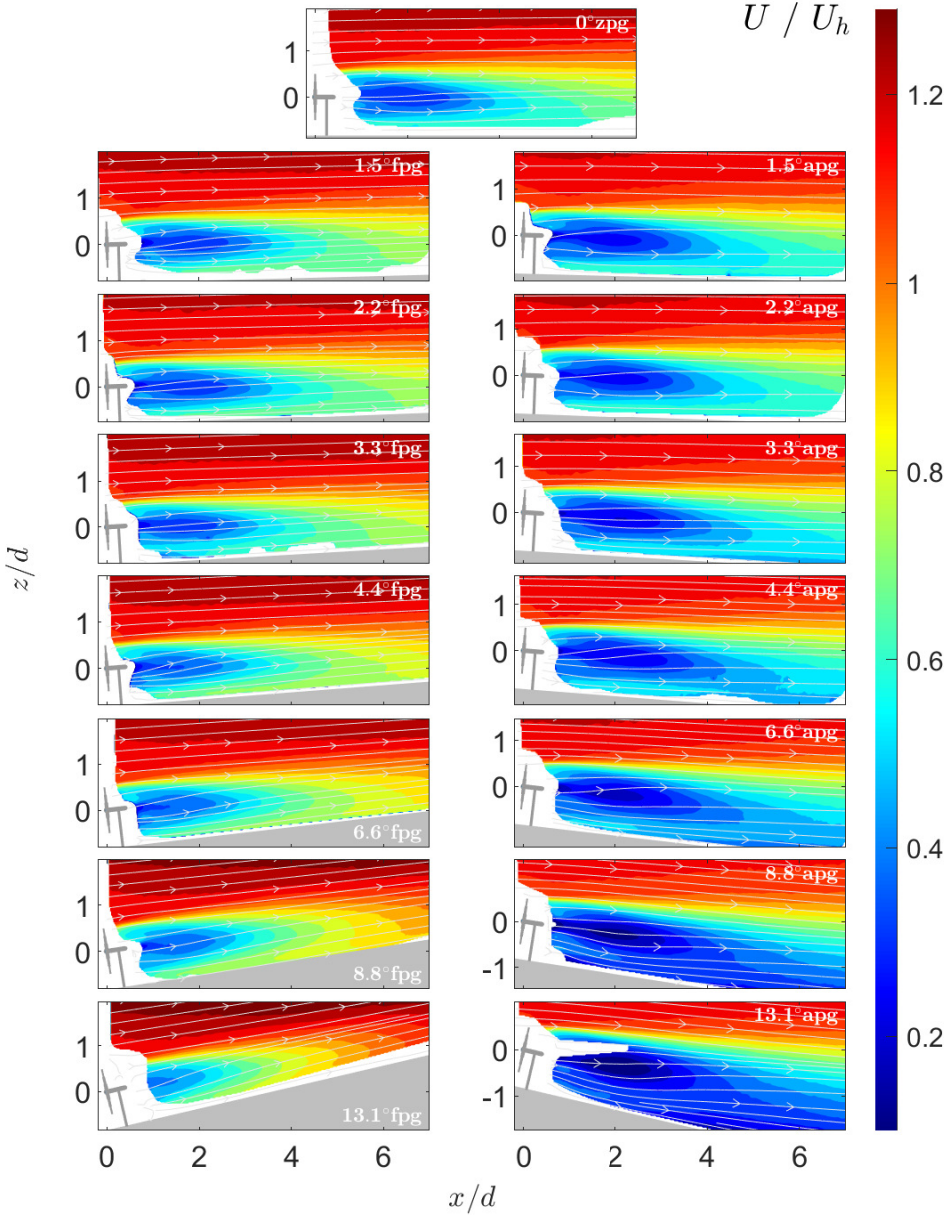
Figure 6.7: Contours of the normalized averaged streamwise velocity in the wake flow for different pressure gradient conditions. Mean flow streamlines are overlaid on the contours.
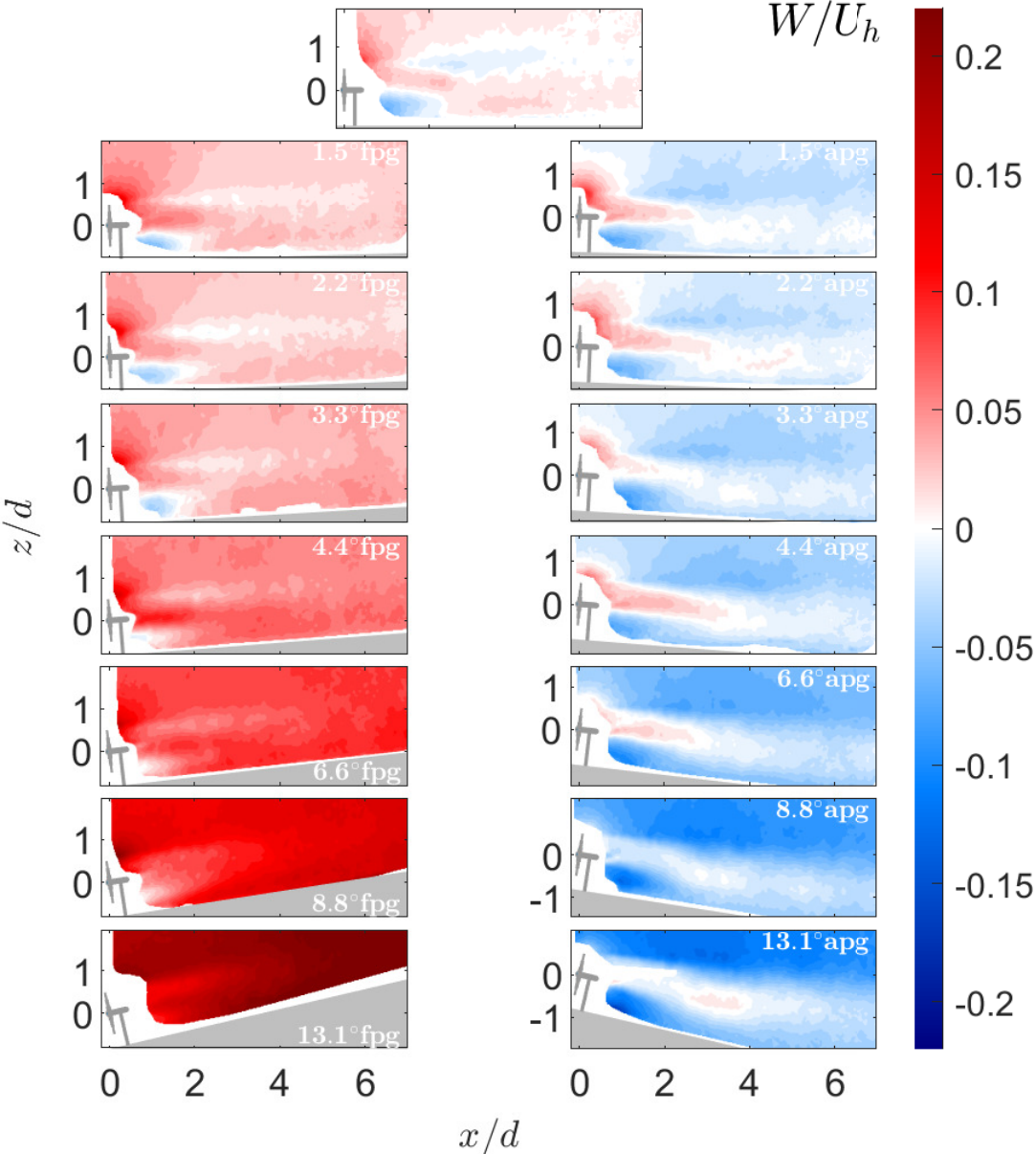
Figure 6.8: Contours of the normalized averaged vertical velocity in the wake flow for different pressure gradient conditions.
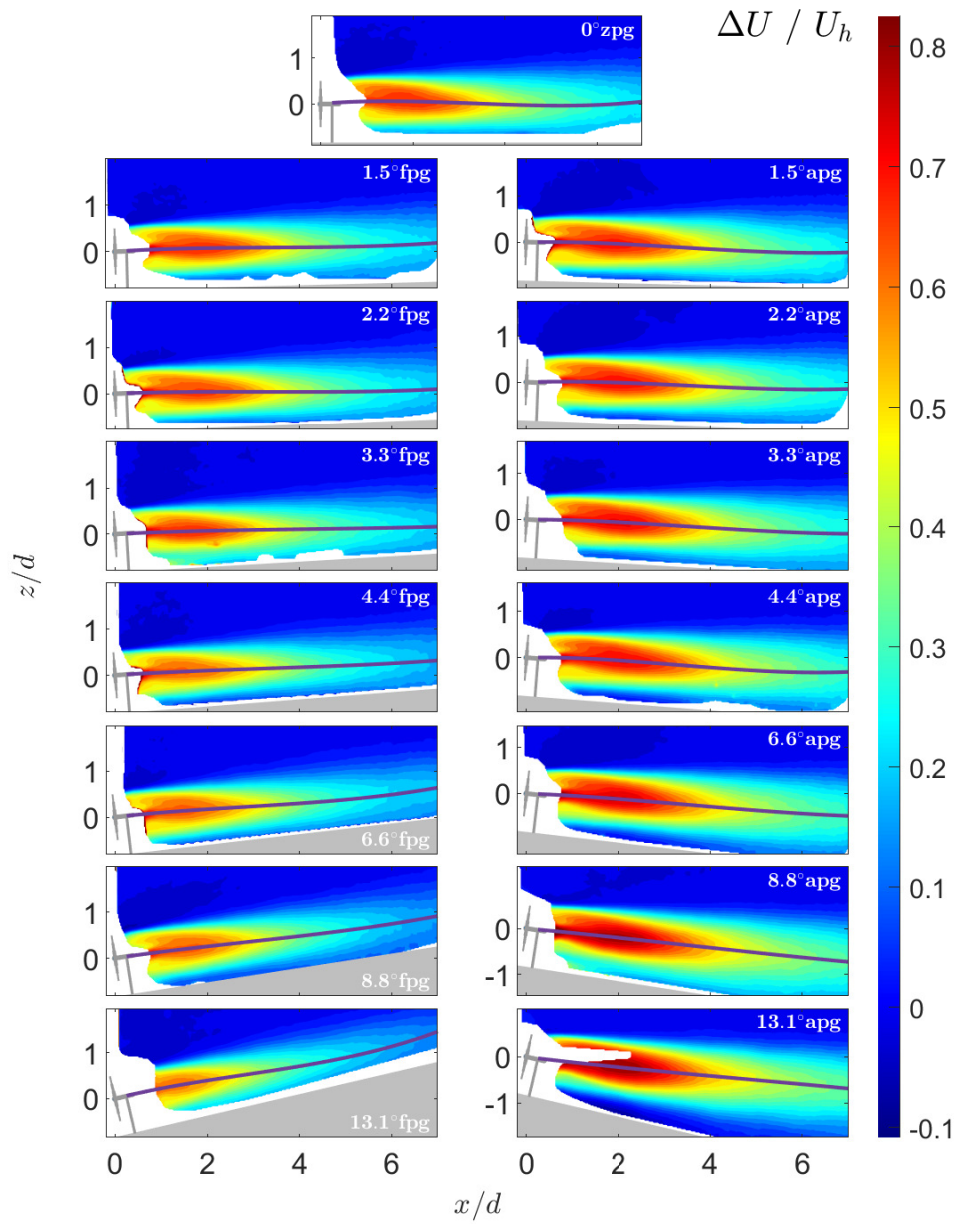
Figure 6.9: Contours of the normalized averaged streamwise velocity deficit in the wake flow for different pressure gradient conditions. The solid line represents the wake trajectory.
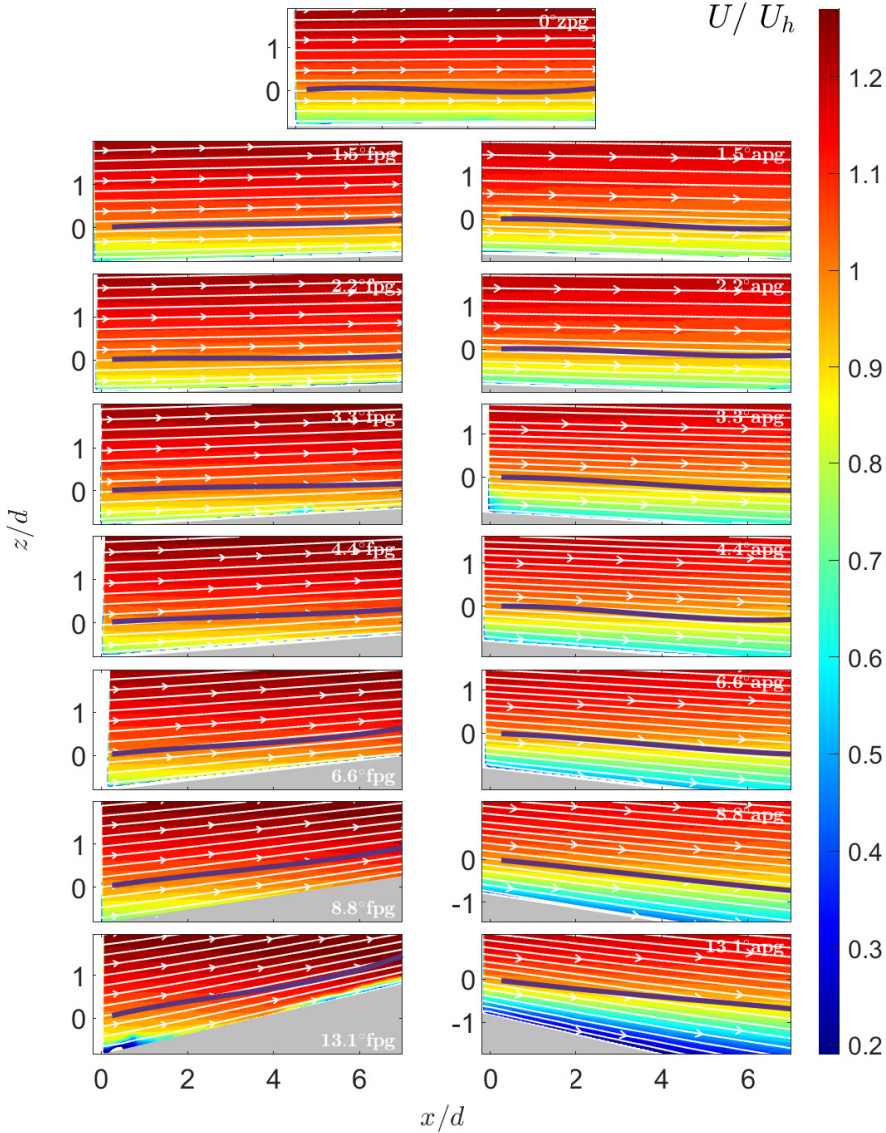
Figure 6.10: Contours of the normalized averaged streamwise velocity in the base flow for different pressure gradient conditions. The streamlines of the horizontal and vertical velocity components are overlaid on the contours. The dark solid lines show the wake trajectory For two column panels, the left one corresponds to FPG and the right one corresponds to APG.

This is consistent with the findings of Liu et al. (2021), who showed that for several two- and three-dimensional hills, the wake follows the flow streamline originating from the turbine hub position. As a turbine wake is advected downstream by the surrounding base flow, it stands to reason that its trajectory is similar to the trajectory of the base flow. Therefore, subsequently, the base flow characteristics along the wake trajectory will be used to quantify the imposed pressure gradient and for wake modeling. In practical situations, where the wake trajectory can be an unknown quantity, the base flow streamline can be used as a proxy.

Figure 6.11 shows the contours of the horizontal turbulence intensity. A peak in turbulence intensity at the upper interface between the wake and the outer base flow is observed, which is commonly attributed to the high shear between the outer base flow and the low velocity wake flow. The magnitude of the turbulence intensity in the peak is observed to be dependent on the imposed pressure gradient. The horizontal turbulence intensity is observed to increase in peak magnitude with the increase in FPG, and decrease with the increase in APG. This may be related to the fact that a fixed hub height mean velocity is used to normalize the standard deviation of the velocity. If an alternate normalization is used, where the standard deviation is normalized with the base flow velocity along the wake trajectory, the FPG cases still show a higher peak in I_x close to the turbine. However in the far wake, the APG cases show a higher peak (for the sake of brevity, the figure is not shown). This is understandable, as the APG slows down the wake recovery, thereby resulting in higher shear in the far wake compared to the FPG cases. As the wake does not follow the ramp, the turbulence intensity peak also moves into or away from the ramp for the FPG and APG cases, respectively.

Pressure gradient and turbulence intensity along wake trajectory

In section 6.2.2 we quantified the flow speed up along the hub height over the ramps, which is useful and relevant from a resource assessment perspective prior to turbine placement. However, as seen in the previous section, the wake does not follow the ramp inclination, especially at high inclination angles. Therefore, here we quantify the velocity and associated pressure gradient along the wake trajectory. Figure 6.12 shows the normalized averaged streamwise velocity and the normalized pressure gradient along the wake trajectory. The flow speed up in the FPG cases is observed to be comparatively similar to that obtained along the hub height over the local surface. This is due to the fact that the downward trajectory of the wake is somewhat limited by the presence of a solid surface in the FPG cases. In the APG cases, on the other hand, the flow deceleration along the wake trajectory is comparatively less than that observed following the hub height over the local surface. This is attributed to the fact that, in APG cases, the wake trajectory is away from the surface into high velocity flow compared to that near the surface. The difference in the flow deceleration along the wake trajectory compared to flow deceleration along the local hub height is greatest for the two steepest APG cases. Somewhat surprisingly, the case with 13.1° inclination angle shows weaker wake deceleration at $x/d > 4$ than does the 8.8° case. This is explained by the fact that the wake trajectory moves away from the surface of the hill most strongly in the 13.1°
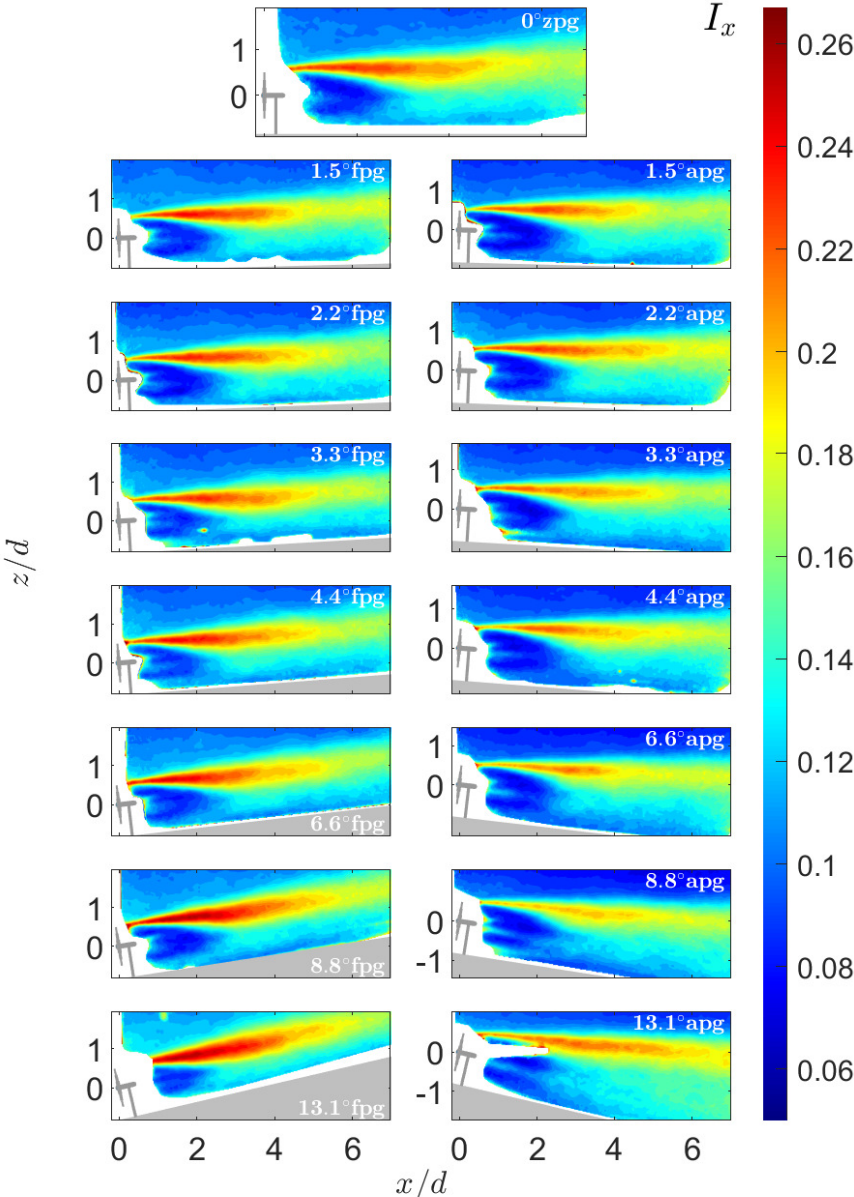
Figure 6.11: Contours of the horizontal turbulence intensity in the wake flow for different pressure gradient conditions.
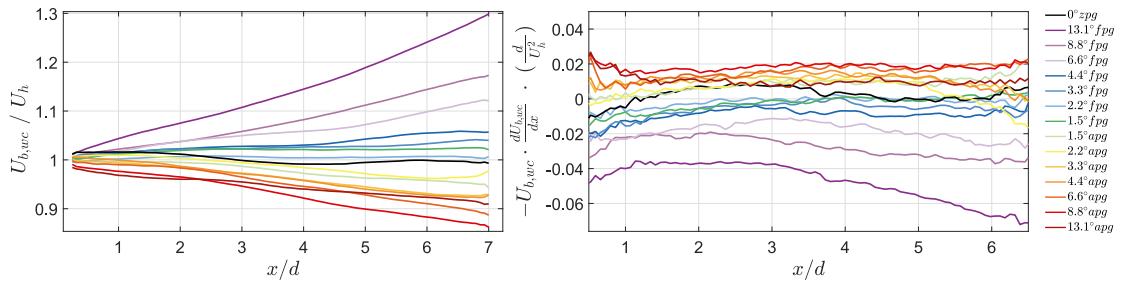
Figure 6.12: Normalized averaged streamwise velocity (left), and normalized pressure gradient (right) in the base flow along the wake trajectory across different ramp angle cases.

case. Over all the cases, the maximum flow speed-up along the wake trajectory is 4.3% per rotor diameter (compared to $4.7\%/d$ along the local hub height), whereas the maximum flow deceleration along the wake trajectory is 2% per rotor diameter (compared to $7.5\%/d$ along the local hub height). The deceleration of 2% per rotor diameter is still higher than those reported in previous studies (Cai et al., 2021; Shamsoddin and Porté-Agel, 2018a).

Figure 6.12 (right) shows the trends in the imposed normalized pressure gradient for all ramp angles. The pressure gradients observed are approximately constant for most of the cases, except the extreme FPG case, where it increases with increase in the distance. In addition, the magnitude of the pressure gradient in the maximum FPG case is more than twice the value in the maximum APG case. In the rest of this section, we will quantify some important wake characteristics as a function of pressure gradient along the wake trajectory.

It is well known that the wake characteristics of a turbine depend on the base flow turbulence intensity. Figure 6.13 shows the rotor averaged turbulence intensity along the wake trajectory for all the cases. It can be seen that for most of the cases, the turbulence intensity lies within a close range of 0.12 - 0.14, and no systematic trend between the rotor averaged turbulence intensity and ramp angle is observed. Therefore, it can be concluded that within the limits of experimental setup, turbulence intensity has minimal effect on the wake of the wind turbine, and pressure gradient is the dominating factor responsible for the systematic differences observed in the turbine wake.

Wake center recovery

Recovery of the wake center velocity deficit is an important wake characteristic, quantified by the evolution of the maximum velocity deficit with distance from the turbine. Figure 6.14 shows the maximum normalized streamwise velocity deficit for different pressure gradients. The maximum normalized streamwise velocity deficit in the turbine wake is observed to be affected by the pressure gradient, with the highest APG case showing the largest deficit and the highest FPG case showing the smallest one. In addition, the maximum deficit near the turbine is also shifted higher (lower) in the APG (FPG) cases compared to that in the ZPG case. This is associated with the effect of the pressure gradient on the turbine induction which
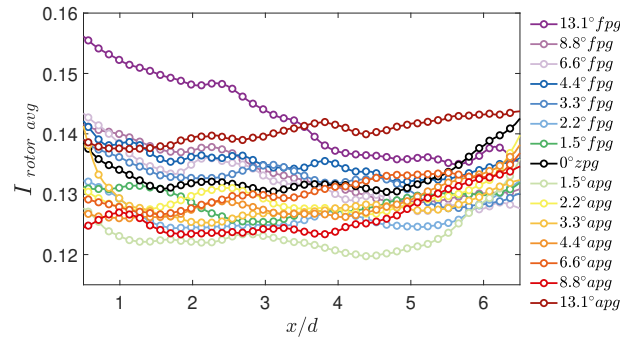
Figure 6.13: Rotor averaged horizontal turbulence intensity along wake trajectory

affects the maximum velocity deficit in the near wake. A similar observation was made by Dar and Porté-Agel (2022b), who found that the maximum velocity deficit in the proximity of the turbine is affected by the adverse pressure gradient imposed by an escarpment. This is due to the fact that in addition to the turbine thrust, pressure gradient also contributes to the streamwise momentum in the turbine wake (Shamsoddin and Porté-Agel, 2017a, 2018a). Depending on the sign of the pressure gradient (favorable or adverse), it either subtracts or adds to the contribution from the turbine thrust. As an adverse pressure gradient slows the wake recovery, it adds to the maximum velocity deficit contribution from the turbine thrust, whereas the favorable pressure gradient subtracts from it.

The effect of pressure gradient can be observed even more clearly in figure 6.14 (right), which subtracts the maximum streamwise velocity deficit in the ZPG case from all the cases. All the APG cases show a positive difference from the ZPG cases, whereas all the FPG cases show a negative one. Interestingly, the difference shows a variation near the turbine, while, in the far wake it reaches a nearly constant value, which depends on the pressure gradient. The variation in the difference with respect to the ZPG velocity deficit maximum close to the turbine can be partly associated with the difference in the near wake length in different cases. The near wake length is shorter (longer) for the FPG (APG) cases compared to that for the ZPG case. A shorter near wake length indicates an earlier re-energization of the wake center velocity deficit compared to that in the ZPG case, which explains why the difference between the FPG and ZPG cases is more pronounced than that between the APG and ZPG cases. The relation between the near wake length and the imposed pressure gradient will be discussed in detail in the remainder of this section.

Near wake length

The near wake of a turbine is characterized as the region close to the turbine where the flow has a 'memory' of the turbine geometry. It is a region of complex flow marked by the tip and hub vortices, rotation of the wake, and wake of the turbine nacelle. A simplified approach is to assume a gradual transition from a top-hot velocity profile at the turbine position to a
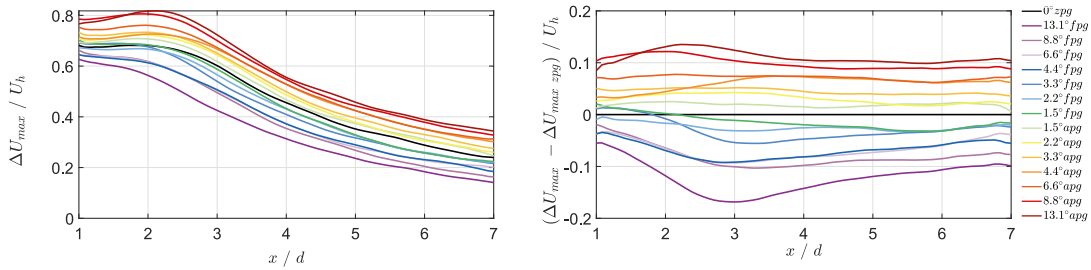
Figure 6.14: Maximum normalized streamwise velocity deficit as a function of streamwise distance for different pressure gradient cases (left), and maximum normalized velocity deficit minus ZPG normalized velocity deficit for different pressure gradient cases (right).

Gaussian velocity profile at the end of the near wake. The length of the near wake, defined as the downstream distance until which the wake flow has a memory of turbine geometry, has been shown to depend on many factors such as the incoming turbulence intensity, the turbine thrust coefficient, and the turbine tip speed ratio (Porté-Agel et al., 2020). Here, we are interested in understanding the dependence of the near wake length on the pressure gradient imposed by the terrain. This is motivated by the fact that the end of the near wake region marks the onset of the far wake, which is of most interest for the wind energy community, especially from the perspective of wind resource assessment, layout optimization and analytical wake modeling.

Several methods are used in the wind energy community to characterize the near wake length. Of these, the most commonly used ones are: the downstream distance at which the streamwise velocity deficit profiles become Gaussian (Porté-Agel et al., 2020), and the downstream distance at which the maximum streamwise velocity deficit becomes equal to the theoretically predicted maximum (Abkar et al., 2018; Bastankhah and Porté-Agel, 2016; Vermeulen, 1980). In the following, we will compare the near wake length obtained from both these criteria and comment on their differences. For the first criterion, which is based on the downstream distance from the turbine at which the streamwise velocity deficit profile becomes Gaussian, we perform a Gaussian fitting on the vertical profiles of the streamwise velocity deficit at each horizontal position. The goodness of the fit, identified by the coefficient of determination ($R^2 > 0.985$), is used to identify the onset of the far wake, and the distance from the turbine at which it is obtained is classified as the near wake length. For the second criterion, we employ the definition of the near wake velocity under pressure gradient using one-dimensional momentum theory given by Dar and Porté-Agel (2022a). The near wake velocity under pressure gradient is defined as: $U_{nw} = \sqrt{U_{nb}^2 - U_h^2 C_T}$, where U_{nw} is the near wake velocity, U_{nb} is the base flow velocity in the near wake, U_h is the hub height velocity and C_T is the turbine thrust coefficient. In the context of Dar and Porté-Agel (2022a), U_{nb} was fixed at a location near the turbine where the wake flow pressure and base flow pressure equalize - to ensure that the defined equation yields a real value, which resulted in a constant near wake

velocity. Here, we generalize this approach by keeping U_{nb} variable with the downstream distance in the near wake. This is done to account for the variation in the near wake velocity deficit maxima due to the pressure gradient in the streamwise direction. Given that the above-defined equation yields real values for all cases, it is possible to evaluate the feasibility of this approach. For analytical modeling in section 6.3, the same approach will be adopted and validated to account for the effect of pressure gradient in the near wake of the turbine.

Figure 6.15 (a) shows the normalized near wake length obtained from the two criteria defined above as a function of the imposed pressure gradient. Overall, both criteria show similar trend between the imposed pressure gradient and the normalized near wake length. In general, the near wake length shortens with the increase in the favorable pressure gradient, and lengthens with the increase in the adverse pressure gradient compared to that in the ZPG case. As FPGs results in base flow acceleration, it leads to an acceleration in the growth of the shear layer surrounding the rotor periphery, thereby bringing higher energy flow into the wake center at an earlier downstream position compared to the ZPG case, which explains the shorter near wake length. The opposite can be said about the adverse pressure gradient, which slows down the growth of the shear layer between the wake and base flow compared to the ZPG case. A bivariate correlation coefficient of 0.89 is measured between the imposed pressure gradient and the normalized near wake length which indicates a strong positive statistically significant correlation.

Although both criteria for near wake length show similar trend, there appears to be an offset between the near wake length values obtained from these criteria. This offset is in the range of 0.9-1.3 rotor diameters for different pressure gradient cases. In the following we attempt to provide a physical explanation for this offset. As noted in previous studies (Bastankhah and Porté-Agel, 2016; Dar and Porté-Agel, 2022b; Dar et al., 2022), the miniature wind turbine used in the study usually shows a higher maximum streamwise velocity deficit in the near wake than what is predicted by the simplified one-dimensional momentum theory. This can be attributed, among other factors, to the wake of the turbine nacelle. As the one-dimensional momentum theory is designed for actuator discs with no nacelle, it does not account for the drag of the nacelle in the near wake of the turbine. It is commonly assumed that as the shear layer grows enough to reach the wake center, the wake deficit profiles become Gaussian. For actuator discs without any nacelle, the maximum velocity deficit at this position will be the same as that predicted by the one-dimensional momentum theory. However, in the current scenario, the maximum velocity deficit at this position is higher than the one obtained from the one-dimensional momentum theory, as the wake still has to recover the deficit caused by the nacelle. Therefore, the maximum velocity deficit at the position where the profiles first show a Gaussian shape is higher than that predicted by the one-dimensional momentum theory. It can be assumed that the offset between the values of near wake length obtained from the two criteria is accounted for by the extra distance it takes to recover the maximum velocity deficit contributed by the turbine nacelle. The fact that the offset lies within a close range for all the cases supports this hypothesis
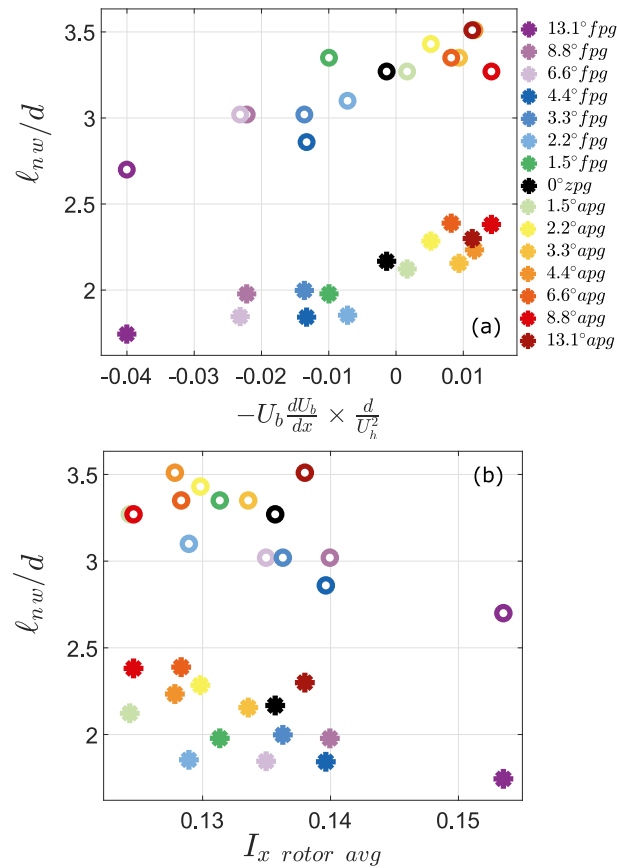
Figure 6.15: Normalized near wake length as a function of imposed pressure gradient in the near wake (a), and as a function of rotor averaged turbulence intensity in the near wake (b). Circles denote the near wake length using the criteria of maximum theoretical streamwise velocity deficit and stars denote the near wake length using the criteria of a Gaussian streamwise velocity deficit profile.

It is well agreed upon in the literature that near wake length depends on the incoming flow turbulence intensity, where higher turbulence leads to a shorter near wake length (Wu and Porté-Agel, 2012). To ensure that the correlations observed here between pressure gradient and near wake length, are not simply a result of correlated turbulence intensity, we correlate normalized near wake length as a function of the rotor averaged horizontal turbulence intensity in the base flow in figure 6.15 (b). It can be seen that the rotor averaged turbulence intensity lies in a relatively tight range of 0.125-0.155 between cases, and that the spread of the data perpendicular to its linear regression line is large relative to its span parallel to the line. The bivariate correlation coefficient in the data is -0.61, indicating a statistically insignificant correlation between near wake length and rotor averaged turbulence intensity.

Wake growth rate

As the wind turbine wake moves downstream, it expands radially in the cross-stream direction. This is due to the growth of the shear layer around the rotor periphery and related mixing of the wake with the outer base flow. The rate at which wake expands in the cross-stream direction with the increase in the streamwise distance is known as the wake growth rate. In the far wake, it is well known that the wake grows linearly in flat (Porté-Agel et al., 2020), as well as complex terrain (Dar and Porté-Agel, 2022b; Dar et al., 2022). To quantify the wake growth rate, the wake width at any downstream distance needs to be quantified. One approach is to characterize the wake width as the standard deviation of a Gaussian fit to the cross-stream profile (either lateral or vertical). The slope at which the standard deviation grows with the increase in the streamwise distance identifies the wake growth rate. This is done according to the following relation: $\frac{\sigma_z}{d} = k\frac{x}{d} + \epsilon$, where σ_z is the wake width in the vertical direction, k is the wake growth rate, and ϵ is the initial wake width.

Here, we are interested in finding a systematic relation between the wake growth rate and the imposed pressure gradient. Figure 6.16 (a) shows the wake growth rate as a function of the imposed pressure gradient. Once again, a clear difference between the FPG and APG cases can be observed, with the ZPG case lying in the middle. The wake growth rate is observed to decrease with the increase in the FPG and increase with the increase in the APG compared to that in the ZPG case. A strong positive (statistically significant) trend is measured between the two parameters, with a bivariate correlation coefficient of 0.92. Moreover, there appears to be a linear relation between the imposed pressure gradient and the wake growth rate. This relation is given as $k = 0.311 \times PG + 0.053$, where PG is the non-dimensional imposed pressure gradient ($-U_b\frac{dU_b}{dx} \times \frac{d}{U_h^2}$). The wake growth rates are obtained based on the vertical profiles of the streamwise velocity deficit only, which could differ from a wake growth rate measure that takes into account the lateral wake width.

Similar to the near wake length, the wake growth rate is also known to be dependent on the ambient turbulence intensity (Porté-Agel et al., 2020). We plot the estimated wake growth rates as a function of rotor averaged horizontal turbulence intensity in figure 6.16 (b). A very wide spread in the wake growth rates is seen when plotted against turbulence intensity. Additionally, the wake growth rates are lower for higher turbulence intensity, which is opposite to what would be expected without the presence of any pressure gradient. It can therefore be said that the differences in the wake growth rates observed here can only be explained by the imposed pressure gradient.

6.3   Analytical modeling

Analytical models provide a reasonably accurate and computationally cheap estimation of the wake velocity deficit behind a turbine. Such models are widely used in the wind energy community to estimate the effects of wakes on power available within a wind farm, and
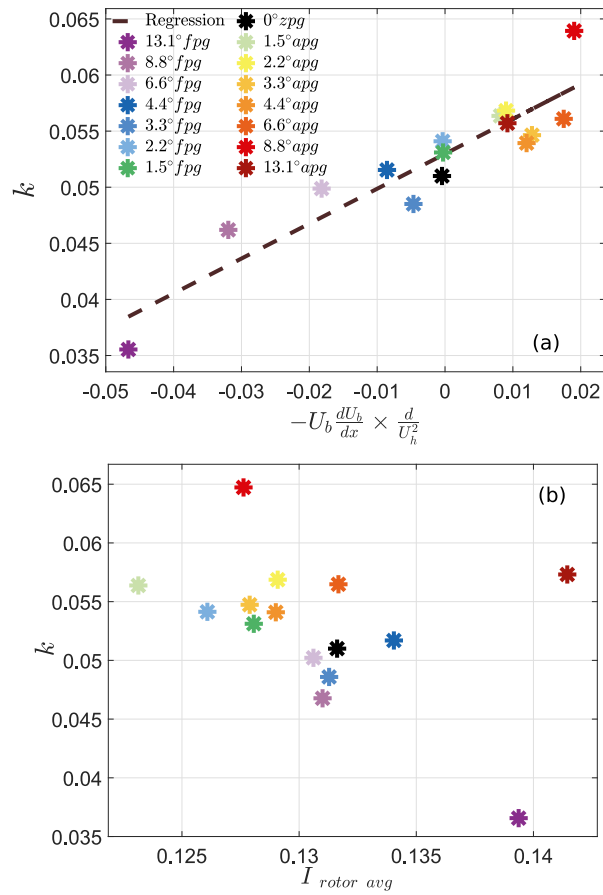
Figure 6.16: Wake growth rate as a function of imposed pressure gradient (a), and as a function of rotor averaged turbulence intensity in the far wake (b). Dashed line shows a linear fit to the data.

facilitate testing multiple layouts and wind directions in a relatively short time. In the following, we provide an assessment of some common analytical modeling approaches available in the literature for wakes under pressure gradient.

Standard Gaussian model

One of the most popular analytical models used today is the Gaussian wake model proposed by Bastankhah & Porté-Agel (Bastankhah and Porté-Agel, 2014, 2016). This model is derived using mass and momentum conservation under an assumption of a zero pressure gradient, and uses the self-similarity of the streamwise wake velocity deficit to produce the velocity deficit profiles. Despite the fact that the model is derived under an assumption of a ZPG, it is a fairly common practice in the wind energy community to use it in complex terrain with a pressure gradient. A common approach to implement the Gaussian model in complex terrain is to superpose the velocity deficit obtained from the model on a varying base flow velocity field. In other words, the reference base flow velocity in the Gaussian model is assumed to be a function of the streamwise distance rather than a fixed value. A few recent examples of such adaptation of the Gaussian model are given in Brogna et al. (2020), Fan et al. (2021), Farrell et al. (2021), and Hu et al. (2022).

In the current work, our objective is to assess the accuracy of this common approach across a range of imposed pressure gradient. We aim to find a threshold in terms of the flow speed-up or deceleration caused by the imposed pressure gradient up to which the simple approach of superposing the standard Gaussian model on varying base flow can yield reasonable results.

The streamwise wake velocity deficit in the far wake is given by:

$$\frac{U_b - U_w}{U_b} = C(x)\, e^{-\left(\frac{r^2}{2\sigma(x)^2}\right)}, \tag{6.1}$$

where $C(x)$ is the maximum normalized streamwise velocity deficit, r is the radial distance from the wake center, and σ is the wake width. The maximum normalized streamwise velocity deficit $C(x)$ is obtained from streamwise momentum balance, and written as a function of the turbine thrust coefficient C_T and the wake width σ in the far wake. Here we use the formulation of the Gaussian model given by Bastankhah and Porté-Agel (2016):

$$C(x) = 1 - \sqrt{1 - \frac{\sigma_0^2 C_0 (2 - C_0)}{\sigma(x)^2}}, \tag{6.2}$$

where σ_0 is the wake width at the start of the far wake taken from the experiments, C_0 is the maximum streamwise velocity deficit at the start of the far wake obtained from the one dimensional momentum theory ($C_0 = 1 - \sqrt{1 - C_T}$, where $C_T = 0.8$), and σ is the wake width in the far wake. The wake growth rate k needed to compute σ is obtained from the relation

between the wake growth rate and base flow streamwise turbulence intensity, given as: $k = 0.3I$ Brugger et al. (2019).

Figure 6.17 shows the comparison of the maximum normalized averaged streamwise velocity deficit obtained from the experiments and from the model equation 6.2. The model prediction agrees well with the experimental data for the ZPG case. However, the difference between the experiments and the model increases with the increase in the pressure gradient. Figure 6.18 shows the comparison of the vertical profiles of the normalized averaged streamwise velocity deficit between the experiments and the model at several downstream positions. For smaller imposed pressure gradients, the streamwise velocity deficit profiles seem to show a reasonable agreement between the Gaussian model and the experiments. However, the error both in the maximum deficit and the wake width, grows with increasing magnitude of the imposed pressure gradient, for both favorable and adverse pressure gradients. Furthermore, the model predicts a slower wake recovery under favorable pressure gradients, and faster under adverse - opposite to the trend actually observed in the experiments. The superposition of the Gaussian model on varying base flow fails to capture the correct qualitative trend for wake velocity deficit under imposed pressure gradients. For the interested reader, this is explainable. This is explainable: take the case for example of favorable pressure gradients. As the base flow speeds up along the streamwise direction, the model subtracts the same ZPG wake velocity from a faster base flow, leading to a greater predicted deficit, and an apparent slowed wake recovery - contrary to what is experimentally observed.

It is of potential importance to the wind community to define a threshold condition above which it becomes inappropriate to use the superimposed Gaussian model. For the APG cases, the Gaussian model yields a reasonable result only up to a ramp inclination of 2.2°, which corresponds to a flow deceleration of $\approx 0.57\%$ per rotor diameter along the wake trajectory. For the 3.3° APG case, which corresponds to a flow deceleration of $\approx 1\%$ per rotor diameter along the wake trajectory, the model shows significant deviation from the experiments. For the FPG cases, on the other hand, an acceptable agreement between the Gaussian model and experiments is observed up to a ramp inclination of 3.3°, which also corresponds to a flow speed-up of $\approx 0.59\%$ per rotor diameter along the wake trajectory. We have shown that the range of pressure gradient conditions over which the simplistic approach of superimposing the Gaussian model predicted deficit on a changing base flow works is relatively small. This indicates that special attention must be paid to the base flow acceleration before using the Gaussian model in complex terrain. In practical situations, where the wake trajectory is unknown, flow acceleration along the base flow streamlines can be used as an alternative, as discussed previously in section 6.2.2.

Pressure gradient model

In this section, we investigate if an analytical model derived for pressure gradient can provide a better prediction than the standard Gaussian model. For this purpose, we use the model initially derived by Shamsoddin and Porté-Agel (2018a) for the effect of an imposed pressure
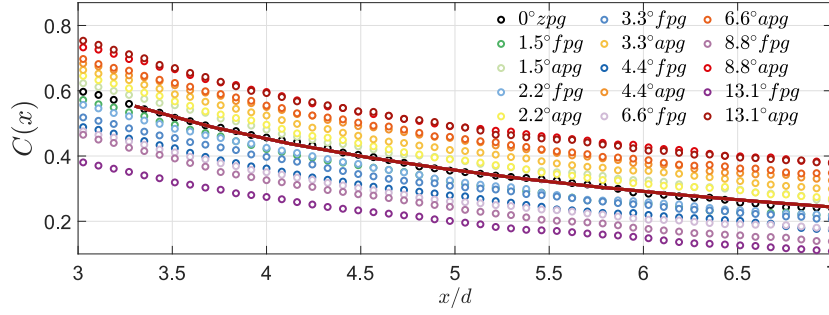
Figure 6.17: Comparison of the normalized maximum streamwise velocity deficit $C(x)$ obtained from the Gaussian model (solid line) and the experiments (circles) for different imposed pressure gradients.

gradient on the far wake, and further extended to account for an imposed pressure gradient in the near wake by Dar and Porté-Agel (2022a). A brief summary of the model along with the procedure followed to obtain the velocity deficit profiles is given below. In addition, we complement the pressure gradient model with a theoretical relation for the estimation of the near wake length.

Similar to the standard Gaussian model, the far wake streamwise velocity deficit is self-similar and has a Gaussian shape function under pressure gradient. Therefore, its functional form is also given by equation 6.1. The streamwise evolution of the maximum velocity deficit, wake width and the onset of the far wake, however, are dependent on the imposed pressure gradient. The base flow velocity along the wake trajectory is used as an input for the model. The normalized maximum streamwise velocity deficit in the far wake is estimated using the following ordinary differential equation:

$$\frac{dC(x)}{dx} = \frac{-1}{\left(\frac{U_b^4(x)}{\lambda_0^2(x)}\right)(3C^2(x) - 2C^3(x))} \left[\frac{1}{4}\frac{dU_b^4(x)}{dx}\frac{C^3(x)}{\lambda_0^2(x)} + \left(C^3(x) - \frac{C^4(x)}{2}\right)\frac{d}{dx}\left(\frac{U_b^4(x)}{\lambda_0^2(x)}\right)\right]. \quad (6.3)$$

where Λ_0 is the ratio of streamwise velocity deficit to wake width, which is known to be invariant to the pressure gradient (Shamsoddin and Porté-Agel, 2018a; Thomas and Liu, 2004). This invariant ratio is defined as:

$$\Lambda_0 = \frac{C_{zpg}U_{zpg}}{\sigma_{zpg}}, \quad (6.4)$$

where C_{zpg}, U_{zpg} and σ_{zpg} are the maximum normalized velocity deficit, base flow velocity and wake width under zero pressure gradient. The wake width under pressure gradient is estimated using the invariant ratio, and is given by:
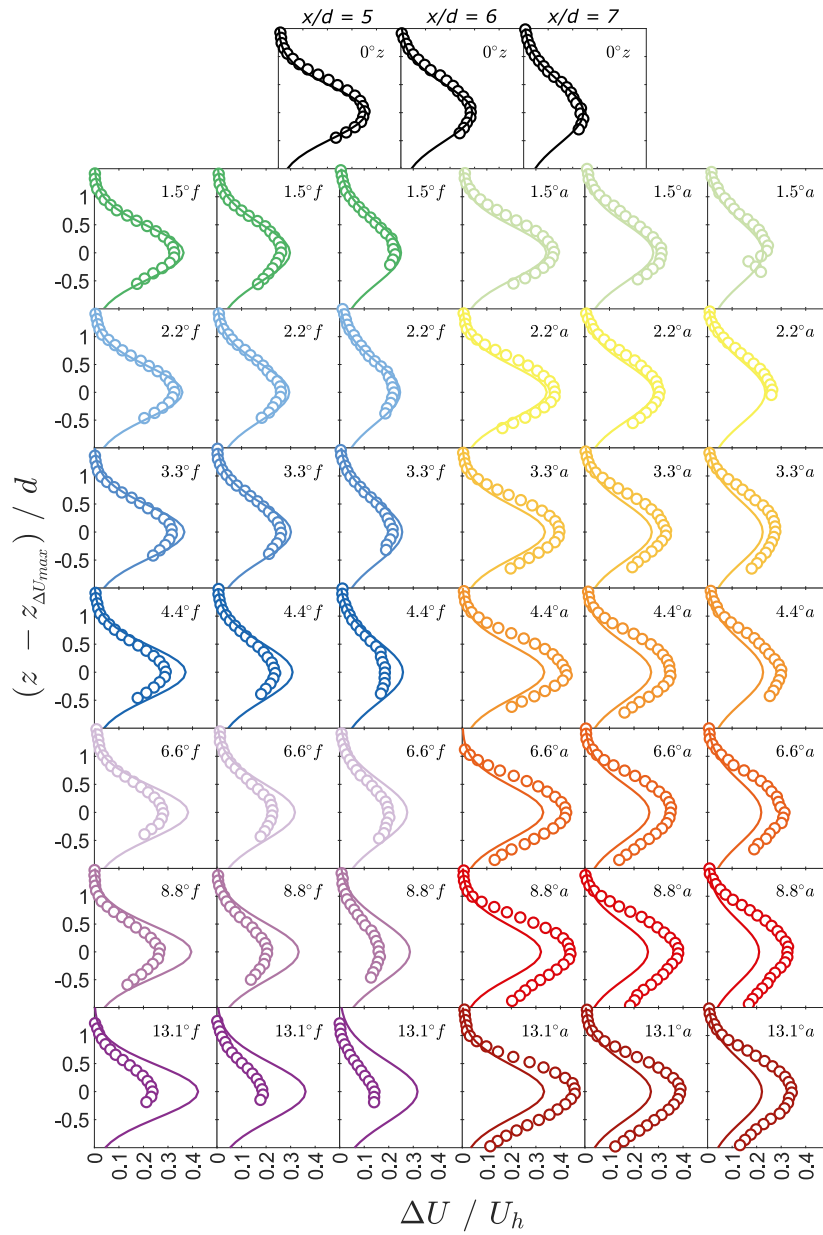
Figure 6.18: Comparison of the vertical profiles of the normalized averaged streamwise velocity deficit between the experiments (circles) and the Gaussian model (solid line) at selected downstream positions.

$$\sigma(x) = \frac{CU_b}{\Lambda_0}. \tag{6.5}$$

Equation 6.3 is valid in the turbine far wake, and it needs the near wake velocity deficit as a boundary condition. Dar and Porté-Agel (2022a) provided an analytical equation for the near wake velocity deficit under pressure gradient:

$$C_{nw}(x) = 1 - \frac{U_{nw}(x)}{U_b(x)}, \tag{6.6}$$

where $C_{nw}(x)$ is the normalized maximum velocity deficit in the near wake and U_{nw} is the near wake velocity, which can be obtained as follows:

$$U_{nw}(x) = \sqrt{U_{nb}(x)^2 - U_h^2 C_T}, \tag{6.7}$$

where U_{nb} is the base flow velocity in the near wake. In the model validation of Dar and Porté-Agel (2022a), the near wake velocity was assumed to be a constant and obtained at the position where the base and wake flow pressure equalize. This distance was fixed at 1 rotor diameter downstream of the turbine. Here, we generalize this approach by keeping the near wake velocity variable. Contrary to Dar and Porté-Agel (2022a), equation 6.7 yields real values throughout the near wake due to a linear speed-up/slow down of the base flow in the current study, enabling us to test this approach.

In addition to the analytical relations for near and far wake velocity deficit, an estimation of the near wake length is needed to switch the model from near to far wake solution. Currently, no analytical relations for the length of near wake under a pressure gradient exist. In the following, we derive a theoretical relation for near wake length under an imposed pressure gradient.

The near wake of a turbine is characterized by the growth of a shear layer behind the rotor periphery. This shear layer expands radially as the wake is advected downstream due to the mixing between the low energy wake flow and the high energy base flow outside the wake. Following Bastankhah and Porté-Agel (2016), the near wake length can be characterized as the distance downstream of the turbine where the shear layer width reaches the wake center, thus energizing the wake center. In their study, Bastankhah and Porté-Agel (2016) generalized the model for the growth of a shear layer originally proposed by Lee and Chu (2012) to account for the effects of turbulence intensity and velocity difference between the wake and outer flow on the development of a shear layer. However, their derivation was meant for the growth of a free shear layer under a zero pressure gradient. Here, we will further generalize their model for an arbitrary pressure gradient.

According to Bastankhah and Porté-Agel (2016), the variation of a free shear layer width can

be expressed as:

$$\frac{1}{U_\infty} \frac{ds}{dt} = \frac{U_s}{U_\infty} \frac{ds}{dx} = \alpha I + \beta \frac{U_e}{U_\infty}, \tag{6.8}$$

where U_∞ is a constant velocity of the flow outside the wake, s is the width of the shear layer, t is the time, U_s is the characteristic velocity of the shear layer defined as $0.5(U_\infty + U_{nw})$, U_e is the relative velocity in the shear layer given by $0.5(U_\infty - U_{nw})$; finally, α and β are model constants. Under the assumption of a zero pressure gradient, all the velocities in equation 6.8 are constant, which simplifies the model. For the development of a free shear layer under an imposed pressure gradient, equation 6.8 can be interpreted as a local relation and re-written as follows:

$$\frac{1}{U_b(x)} \frac{ds}{dt} = \frac{U_s(x)}{U_b(x)} \frac{ds}{dx} = \alpha I + \beta \frac{U_e(x)}{U_b(x)}, \tag{6.9}$$

where $U_b(x)$ is the local base flow velocity, $U_s(x)$ is the local shear layer characteristic velocity defined as $0.5(U_b(x) + U_{nw}(x))$ and $U_s(x)$ is the local relative velocity estimated by $0.5(U_b(x) - U_{nw}(x))$. The integral form of equation 6.9 can be written as follows:

$$\int_0^{\sigma_{nw}} ds = \int_0^{l_{nw}} \frac{U_b(x)}{U_s(x)} \left[\alpha I + \beta \frac{U_e(x)}{U_b(x)} \right] dx. \tag{6.10}$$

Inserting expressions for different velocities in the above equation yields:

$$\sigma_{nw} = (2\alpha I + \beta) \int_0^{l_{nw}} \frac{1}{1 + \frac{U_{nw}(x)}{U_b(x)}} dx - \beta \int_0^{l_{nw}} \frac{1}{1 + \frac{U_b(x)}{U_{nw}(x)}} dx. \tag{6.11}$$

Equation 6.11 is a general equation which can be solved for any form of base flow $U_b(x)$ to estimate the near wake length. Here, we will solve equation 6.11 in the context of the current work. For this purpose, we assume the base flow to be linear and express it as $U_b(x) = (\gamma x + U_h)$, where γ is the flow speed-up factor, which will be positive for FPG and negative for APG. Inserting the functional form of $U_b(x)$ and $U_{nw}(x)$ in equation 6.11 yields:

$$\sigma_{nw} = (2\alpha I + \beta) \int_0^{l_{nw}} \frac{1}{1 + \sqrt{1 - \frac{U_h^2 C_T}{(\gamma x + U_h)^2}}} dx - \beta \int_0^{l_{nw}} \frac{1}{1 + \frac{1}{\sqrt{1 - \frac{U_h^2 C_T}{(\gamma x + U_h)^2}}}} dx, \tag{6.12}$$

the above equation is solved analytically using MATLAB to obtain the near wake length l_{nw}. To solve for l_{nw} we need to specify the wake width σ_{nw}. Here, we take the σ_{nw} for zero pressure gradient from the experiments, whereas the wake width for different pressure gradient situations is obtained using the invariant ratio. While solving equation 6.12, all the velocities are normalized by U_h in the respective cases and all the distances are normalized by the rotor diameter d. This is done to account for the difference in the reference velocity U_h between different cases while computing the invariant ratio. Finally, the values for model constants (α and β) need to be specified. Here we choose $\alpha = 0.58$ and $\beta = 0.077$, which are the same
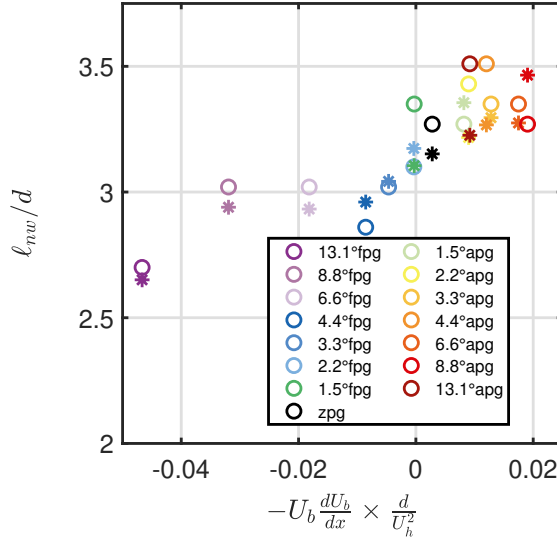
Figure 6.19: Comparison of near wake length obtained from the experiments (circles) and the theoretical model (asterisks).

values as suggested by Bastankhah and Porté-Agel (2016). However, the α and β values chosen here may not be universal and further research is needed to find universal values for these constants.

Figure 6.19 shows a comparison of the near wake length obtained from the experiments and the model. Overall, it can be observed that the model can predict the trend between the near wake length and imposed pressure gradient with a very good accuracy. The predicted values are also very close to the experimental ones. Thus, we have derived and validated a theoretical model to estimate the near wake length under an imposed pressure gradient. For the prediction of wake velocity deficit under pressure gradient, we will use this newly derived theoretical near wake length to transition from the near wake solution to the far wake one.

In previous studies (Shamsoddin and Porté-Agel, 2018a; Thomas and Liu, 2004), the invariant ratio $\Lambda = \frac{CU_b}{\sigma}$ has been verified under the conditions where the far wake is exposed to a pressure gradient. Here we check its validity under the condition when the turbine experiences a pressure gradient from the induction region to the far wake. Figure 6.20 (a) shows the invariant ratio obtained experimentally for different pressure gradients as a function of downstream distance normalized by the rotor diameter. It is observed that the invariant ratio shows a spread between different pressure gradient cases for $x/d < 4$, beyond which it converges to similar values for all the cases. The spread in the invariant ratio for $x/d < 4$ can be attributed to the difference in the near wake length between different pressure gradient cases. In fact, it can be seen in figure 6.20 (b) that normalizing the downstream distance with the near wake length leads to a near-perfect collapse of the invariant ratio in the far wake. We may therefore state that the invariant ratio holds when properly accounting for the difference in near wake
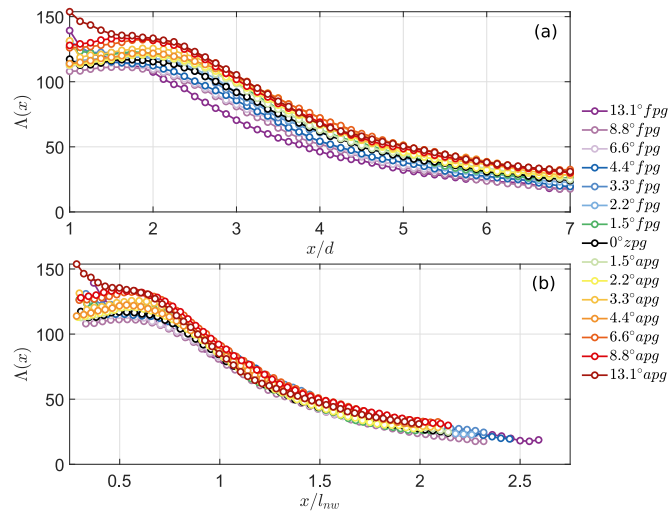
Figure 6.20: Comparison of the experimentally obtained invariant ratio with the downstream distance normalized by the rotor diameter (a) and the near wake length (b).

length caused by the pressure gradient. A similar idea has been recently proposed by Vahidi and Porté-Agel (2022a), who showed that turbine wake deficit in flat terrain under different turbulence intensities collapses on a single profile when scaled with respect to the near wake length.

For the pressure gradient model, the invariant ratio under ZPG Λ_0 is obtained from the standard Gaussian model. The invariant ratio in the far wake is used as an input for the estimation of the far wake maximum normalized averaged velocity deficit and wake width for different pressure gradient cases. Figure 6.21 shows a comparison of the experimentally obtained $C(x)$ and $\sigma(x)/d$ with that obtained from the pressure gradient model. A remarkable improvement over the standard Gaussian model is observed, demonstrating the importance of a physics-based analytical model for wakes under pressure gradient. Overall, the maximum normalized averaged velocity deficit and normalized wake width show a good agreement between the experiments and the pressure gradient model for all the cases. In a few cases, $C(x)$ at the starting point of the pressure gradient model is slightly shifted from the experimental value. This is due to the difference in the experimental and theoretical near wake length estimation. This difference is also observed to decrease with the increase in the downstream distance, as further downstream the model is less sensitive to the chosen near wake length. In fact, if the model is run with the experimental near wake length as an input, the differences between the model and the experiments disappear (figure not shown for the sake of brevity). However, the theoretical near wake length is more useful for practical applications, and it can be stated that the model yields reasonable results for both $C(x)$ and $\sigma(x)/d$.

Finally, figure 6.22 compares the vertical profiles of the normalized averaged streamwise velocity deficit between the experiments, the standard Gaussian model and the pressure gradient model at several downstream distances. It can be seen that the pressure gradient
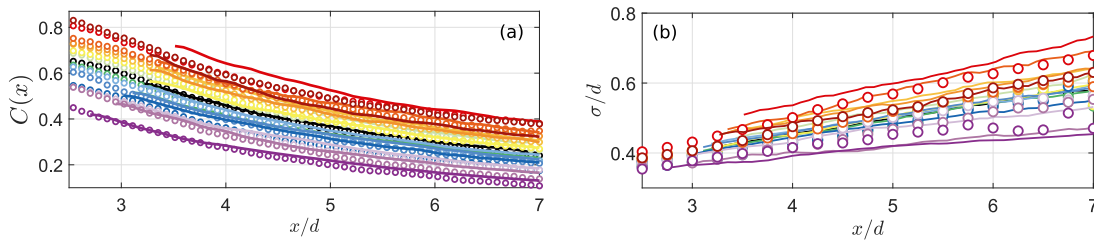
Figure 6.21: Comparison of the (a) normalized averaged maximum streamwise velocity deficit $C(x)$ and (b) the normalized wake width obtained from the pressure gradient model (solid lines) and the experiments (circles) for different imposed pressure gradients. The color scheme is the same as figure 6.17.

model predicts well the experimental results, and offers a significant improvement over the standard Gaussian model, which over (under)-predicts the streamwise velocity deficit for FPG (APG) cases at moderate and high inclination angles. Therefore, we have demonstrated that the pressure gradient model is the better option to analytically model wakes under pressure gradient compared to the engineering approach of superposing the standard Gaussian model on a varying base flow.

6.4 Summary and concluding remarks

Changes in terrain elevation or surface roughness can impose a pressure gradient on the flow, which has a significant effect on the evolution of wind turbine wakes. In this study, we performed a systematic investigation of a wind turbine under an imposed pressure gradient. Wind tunnel experiments were carried out, where flow measurements were made using a planar PIV setup. The pressure gradient was imposed by means of ramps, where the slope of the ramp was varied to impose different pressure gradients. The turbine was placed sufficiently away from the ramp edges such that it experiences an approximately linear flow speed-up/slow-down from its induction region to the far wake. The ramp angle was varied at 15 different inclinations to produce a range of pressure gradients. Seven adverse pressure gradients were produced with inclinations from $-13.1°$ to $-1.5°$, seven favorable from $1.5°$ to $13.1°$, and one zero pressure gradient case at $0.0°$. In the following, we briefly re-address the research questions set out at the beginning of the article.

The experimental results showed a clear systematic relation between the imposed pressure gradient and both the wind turbine performance and wake characteristics. The power co-efficient showed a non-linear dependence on the pressure gradient, with a decrease of up to 9.7% for the strongest adverse pressure gradient, whereas a gain of 6.7% was observed for the strongest favorable pressure gradient. The wake velocity deficit was strongly correlated with pressure gradient - its recovery slowed down with increase in adverse pressure gradient, and was enhanced by increase in favorable pressure gradient. A difference between the wake recovery under pressure gradient and zero pressure gradient was computed, which showed
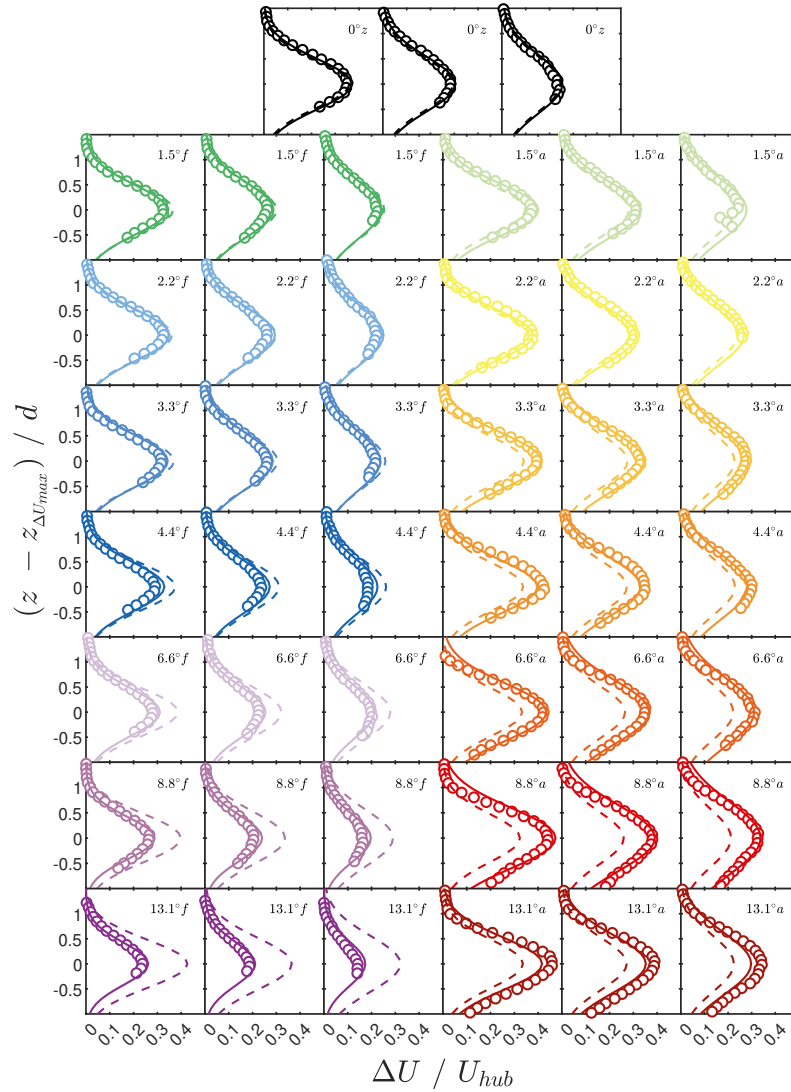
Figure 6.22: Comparison of the normalized averaged streamwise velocity deficit profiles obtained from the experiments (circles), the standard Gaussian model (dashed lines) and the pressure gradient model (solid lines) for different imposed pressure gradients. The profiles are shown for $x/d = 5, 6, 7$.

some variation in the near wake before reaching a constant value in the far wake. This was related to the difference in the near wake length for different pressure gradient situations. The effect of pressure gradient on near-to-far wake transition has remained unanswered in the literature. In the current work, we showed that the near wake length is approximately linearly dependent on the imposed pressure gradient, with a decrease (increase) in the near wake length for favorable (adverse) pressure gradient compared to the zero pressure gradient situation. This was related to the fact that an accelerating base flow results in a faster growth of the shear layer, leading to a shorter near wake length and vice versa. We also showed that the rate of cross-stream expansion of the wake varied linearly as a function of the imposed pressure gradients in our study.

The experimental data was then used to assess different analytical modeling approaches for prediction of wake velocity deficit. In this context, we first assessed the engineering approach of superposing the streamwise velocity deficit obtained from a zero pressure gradient model on the base flow obtained under pressure gradient. This approach is currently the most popular one for practical applications. However, we showed that such approach has serious limitations, as it only worked for moderate pressure gradient situations. We established a threshold in terms of the flow speed-up/slow-down along the wake trajectory up to which the approach yielded acceptable results. This threshold was found to be a speed-up/slow-down of the base flow by 0.57%-0.59% per rotor diameter along the wake center trajectory. We recommend that this threshold must be monitored before applying the standard Gaussian model to pressure gradient situations.

Finally, we showed that a physics-based model developed for wind turbine wakes under pressure gradient can provide accurate wake deficit prediction. Existing physics-based models provide relations for near/far-wake maximum wake velocity deficit and wake width under pressure gradient situations. However, analytical relations for near wake length under pressure gradient were lacking. In this context, we derived an analytical relation for the near wake length based on the growth of a shear layer around the rotor periphery. The analytical relation was validated with the experimental data, and integrated in the physics-based model to predict the wake velocity deficit under pressure gradient. The approach was shown to yield excellent results, and significantly outperform the engineering approach described earlier. We therefore strongly recommend the use of a physics-based analytical model for practical applications involving even moderate pressure gradients, instead of the common engineering approach.

7 Wind turbine wake superposition under pressure gradient[I]

Abstract

We investigate the effect of pressure gradient on the cumulative wake of multiple turbines in wind tunnel experiments spanning across a range of adverse (APG), zero (ZPG), and favorable (FPG) pressure gradients. Compared to the upstream-most turbine, the in-wake turbines exhibit lower (higher) wake velocity in APG (FPG) than in the ZPG. The maximum velocity deficit shows lesser difference for the in-wake turbine between different cases compared to the upstream-most one. This is linked to the effect of the wake of the upstream turbine. Conversely, the wake width varies more for the in-wake turbines. A new analytical approach to model the cumulative wake velocity deficit is proposed. This approach extends the application of the analytical pressure gradient model to multiple turbine wakes. Specifically, the new approach explicitly accounts for the effect of the pressure gradient induced by the wake of the upstream turbine on the wake of the downstream one. It also eliminates the need for superimposing individual wake velocity deficits. The new method is compared to the linear summation approach and experimental data. It agrees well with the experiments and outperforms the linear summation approach.

[I]The contents of this chapter are under review for publication in *Physics of Fluids.*

7.1 Introduction

Onshore wind energy constitutes about 93% of the installed global wind energy capacity (GWEC, 2022). The continuous decrease in the levelized cost of electricity (LCOE) of onshore wind projects (IRENA, 2021) and a push towards renewable energy sources have resulted in the rapid growth of onshore wind energy. Wind turbines are often installed in clusters, known as wind farms, where depending on the wind farm layout and wind direction certain wind turbines operate in the wake of others. Turbine wakes, marked by lower velocity and higher turbulence, compared to the undisturbed flow, are responsible for lower available power and higher fluctuating loads on the in-wake turbines. While most of the existing literature on wind turbine wakes assumes a flat terrain Porté-Agel et al. (2020) and Stevens and Meneveau (2017), wind turbines are often sited on non-flat topography in onshore conditions.

Flow over topography is inherently complex and depends significantly on the changes in surface elevation and roughness. The interaction of wind turbine wakes with the flow in complex terrain has been investigated in several wind-tunnel (Dar and Porté-Agel, 2020, 2022b; Hyvärinen and Segalini, 2017a; Tian et al., 2013), numerical (Dar et al., 2019; Liu and Stevens, 2020a; Politis et al., 2012; Troldborg et al., 2022; Zhang et al., 2022) and field (Han et al., 2018; Menke et al., 2018; Radünz et al., 2021) studies. These studies have shown that the turbine power performance and wake characteristics such as its recovery, trajectory, expansion, and turbulence quantities are significantly affected by the flow in complex terrain.

One key feature of flow in topography is the streamwise variation in velocity which imposes a pressure gradient on the flow. The effect of pressure gradient on the development of planar wakes has been explored in several studies (Hill et al., 1963; Liu et al., 2002; Rogers, 2002; Shamsoddin and Porté-Agel, 2017a; Thomas and Liu, 2004). These studies showed that a pressure gradient can affect the recovery of the mean wake center velocity, where an adverse pressure gradient (APG) tends to slow it down and a favorable pressure gradient (FPG) tends to speed it up compared to a zero pressure gradient (ZPG) situation. In addition, the expansion of the wake in the cross-stream direction is also affected by the pressure gradient, with a higher wake width under an APG and a lower wake width under an FPG compared to that under a ZPG. The mean wake velocity deficit profiles were shown to be self-similar under pressure gradient situations, and the turbulence quantities were comparatively less affected by the pressure gradient.

The effect of pressure gradient imposed by the flow on wind turbine wakes has been recently investigated in several studies. Shamsoddin and Porté-Agel (2018a) proposed an analytical model for the far wake of a wind turbine under an imposed pressure gradient. In addition, they simulated a wind turbine wake using large-eddy simulation (LES), and extended some of the findings of planar wakes under pressure gradient to the axisymmetric ones. Shamsoddin and Porté-Agel (2018b) also performed a combined LES and analytical study of wind turbine wake flow over a two-dimensional hill. They used their analytical model (Shamsoddin and Porté-Agel, 2018a) together with the model of Hunt et al. (1988) to model the wake of a wind

turbine sited upstream of a hill with moderate slope. The LES results were used to validate the analytical framework. Using the LES, they also simulated several turbine positions across the hill, and divided the flow over the hill into two regions of faster and slower wake recovery rate compared to a turbine in flat terrain. They associated this behavior with the pressure gradient experienced by the turbine wake. Cai et al. (2021) conducted wind tunnel experiments to investigate the effect of pressure gradient imposed by linear ramps on the turbine wake and power production. They also validated the model of Shamsoddin and Porté-Agel (2018a) with their experimental data. More recently, Dar et al. (2023) performed a systematic study of wind turbines exposed to pressure gradient imposed by a flow linearly speeding up/slowing down from its induction region to the far wake. They showed that the wake deficit varies systematically with the change in pressure gradient, and the near wake length and wake growth rate showed linear relationship with the pressure gradient. They also showed that compared to ZPG, the power coefficient of the turbine increased with the increase in the FPG, whereas it decreased with the increase in the APG.

As wind turbine wakes can lead to significant power losses in a wind farm (especially when the turbines in a row are fully aligned), it is of great interest to estimate these wake losses during the planning and layout optimization phase of a wind farm. For this purpose, simplified engineering wake models are extremely popular, as they offer reasonably accurate and computationally inexpensive estimation of mean wake velocity behind turbines. There are two categories: models for stand-alone wind turbine wakes, and models which superpose multiple wakes to provide estimation of cumulative wake velocity behind a row of turbines. For stand-alone wind turbine wakes, several models have been proposed to estimate the mean wake velocity deficit in flat (Abkar et al., 2018; Bastankhah and Porté-Agel, 2014; Bempedelis and Steiros, 2022; Frandsen et al., 2006; Ishihara and Qian, 2018; Jensen, 1983) and complex (Brogna et al., 2020; Dar and Porté-Agel, 2022a; Dar et al., 2023; Shamsoddin and Porté-Agel, 2018a; Sun et al., 2019) terrain. As for the wake superposition models, several strategies have been proposed in the literature. The most popular of these are the linear summation principle (Lissaman, 1979; Niayifar and Porté-Agel, 2016) and the sum of squares approach (Katic et al., 1986; Voutsinas et al., 1990). These superposition models are, however, for the most part empirical, and more recently some physics-based approaches have been proposed by Zong and Porté-Agel (2020b) and Bastankhah et al. (2021). Although, these superposition methods are designed for wind farms in flat terrain, they have been applied for wake superposition in complex terrain as well (see e.g., Brogna et al. (2020) and Sun et al. (2019)). Lanzilao and Meyers (2022) also proposed a wake superposition method for a varying base flow velocity field with application to offshore wind farms close to coastlines.

In this work, we perform a combined experimental and analytical study of multiple wind turbines exposed to a base flow pressure gradient. As the existing literature isolating the effect of pressure gradient on wind turbine wakes focuses on single turbine cases, we look to provide useful physical insights into the case of multiple turbine wakes exposed to a quasi-linear surrounding base flow. In addition, we propose two different strategies of modeling the cumulative wake behind multiple turbines in flat, as well as, compelex terrain. The first

approach is a modified version of the linear sum approach proposed by Niayifar and Porté-Agel (2016) adapted for streamwise variation in the base flow. The second approach is to use the pressure gradient model (Dar et al. (2023) and Shamsoddin and Porté-Agel (2018a)), which accounts for the effect of the upstream turbine(s) in the base flow term. This approach eliminates the need for any superposition method to combine stand-alone wakes of the turbines and can model the cumulative wakes, both in flat and complex terrain. The rest of the article is organized as follows: section 7.2 presents a description of the experimental setup and results from the experiments; section 7.3 details the modeling approaches and compares them; and section 7.4 provides a summary of the work and some concluding remarks.

7.2 Experiments

7.2.1 Setup

The measurements are carried out in the boundary layer wind tunnel facility at the WiRE laboratory of EPFL. The wind tunnel is a closed-loop type with a test section of dimensions 28 m × 2.56 m × 2 m (length × width × height), and a contraction with an area ratio of 5:1 is present at the inlet of the test section. The flow is conditioned through a series of honeycomb meshes and screens before the contraction. This ensures a low free-stream turbulence intensity (< 1%) and a uniform flow at the inlet of the test section. The flow in the wind tunnel is driven by a 130 kW fan, which is capable of generating wind speeds up to 25 ms^{-1} in the test section.

A three-bladed horizontal axis miniature wind turbine with a rotor diameter D of 10.5 cm and hub height z_h of 8.75 cm is used in this work. The turbine rotor is a scaled-down version of the WiRE-01 turbine Bastankhah and Porté-Agel (2017a), where a scaling of 1:1.43 is kept between the original and the scaled-down rotor models. The power and thrust characteristics of the scaled-down turbine are characterized by Dar et al. (2022), which showed that the turbine performance is unaffected by scaling it down as long as the Reynolds number is comparable between the original and the scaled-down models. The rotor is 3D printed using a liquid photopolymer resin, and is mounted on a direct current (DC) motor manufactured by Maxon Motors (model: DCX10L). The DC motor is connected to a servo controller in order to acquire data and control the operation of the turbine. For all the experiments, turbines are operated at the tip speed ratio corresponding to maximum power extraction. The power extracted by the turbine P is quantified by multiplying the shaft torque Q of the turbine by its rotational speed Ω. A frictional toque Q_f is added to the torque estimated by multiplying the generated current I with the torque constant K in order to estimate the total shaft torque. The details of the power measurement procedure are given in Bastankhah and Porté-Agel (2017a).

Seven different pressure gradient situations are tested in this study, including one zero pressure gradient (ZPG) case corresponding to flat terrain. For non-zero pressure gradients, linear ramps are used to generate terrain-induced pressure gradients. The ramps used in this study are the same as the ones used by Dar et al. (2023). The ramps are 13 rotor diameters

long, and their height h is varied to change the slope. Three different ramp angles are used, corresponding to 13.1°, 8.8° and 4.4°, where a positive slope leads to a favorable pressure gradient (FPG), and a negative one induces an adverse pressure gradient (APG). The cases are labeled as 'ZPG' for the zero pressure gradient one, 'APG-I', 'APG-II' and 'APG-III' for APG cases with 4.4°, 8.8° and 13.1° angles, respectively, and 'FPG-I', 'FPG-II' and 'FPG-III' for FPG cases with 4.4°, 8.8° and 13.1° angles, respectively. In the ZPG case, three wind turbines are placed in a fully aligned configuration, with an inter-turbine spacing of 5 rotor diameters. In the FPG and APG cases, however, two turbines are placed on the ramp with a spacing of 5 rotor diameters. This is due to the limitation of the ramp length, which can only allow for two turbines to be placed. The first turbine is placed 3 rotor diameters from the upstream edge of the ramp. This is done to ensure that the base flow (flow without the turbine) experienced by the turbine is unaffected by the ramp edge. The choice of ramps is made in order to generate a quasi-linear base flow increase or decrease with streamwise distance under different pressure gradient situations. The turbines are placed such that their axis of rotation is parallel to the ramp surface. As the turbine motor has a current limitation for optimal operation, the inflow velocity is adjusted between different cases such that all turbines can be controlled at their optimal tip speed ratio.

Velocity measurements are performed using a two-dimensional two-component (2D2C) particle-image velocimetry (PIV) setup also known as a planar PIV setup. The measurements are performed in a vertical plane normal to the rotor plane and passing through the turbine centerline. The flow without any turbines, termed the base flow, and the flow with the turbines, termed the wake flow, are captured in the current study. The PIV system used in the study comprises a sCMOS camera (2560×2160 pixels) with a 50 mm lens, a dual pulse Nd:YAG laser (model: Litron lasers, Nano TRL 425-10), and a programmable timing unit (model: LaVision, PTU-v9). The size of the field-of-view (FOV) is 6D × 5D, with a spatial resolution of 0.0189D, with an overlap of approximately 1D in the x direction between consecutive FOVs. The image pairs are captured at a sampling rate of 10 Hz, and 1000 instantaneous flow fields are used to obtain time-averaged flow statistics. Olive oil droplets of diameter on the order of several micrometers are used as seeding particles for flow measurements.

Image processing is performed using the DaVis software developed by LaVision. Reducing size interrogation windows of 64×64 pixels and 32×32 pixels are used for image cross-correlation. An overlap of 75% is kept between consecutive windows and the correlation is obtained after two passes through each window size. Bad velocity vectors are removed from the data using a universal outlier detection method, and replaced using interpolation based on surrounding vectors. The maximum uncertainty in mean velocity is estimated using the correlation statistics approach (Wieneke, 2015), which gives a value of 0.06 ms^{-1} in the regions of high flow shear.

The floor of the tunnel is covered by double-rolled chains with an inter-chain spacing of 40 cm. In addition, a picket fence of dimensions 10 cm in length, and 5 cm in height with spikes of 3 cm in length is placed at the inlet of the test section. This is done to facilitate the growth of a
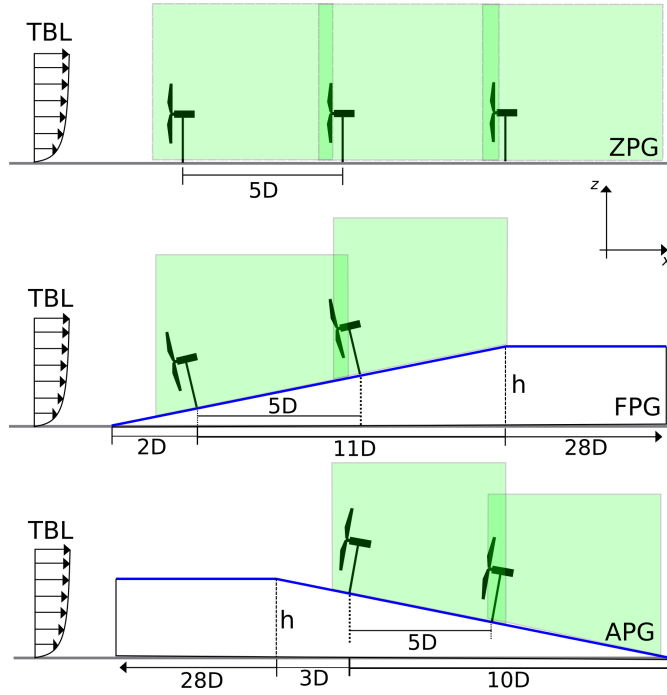
Figure 7.1: Schematic of the experimental setup (not to scale). The shaded green rectangles show the particle-image velocimetry field-of-views.

turbulent boundary layer (TBL) in the tunnel. Figure 7.2 characterizes the incoming turbulent boundary layer using the 2D2C PIV setup described above. The hub height velocity U_h is used for normalization with a high gradient in the normalized averaged streamwise velocity close to the wall. The boundary layer height is more than 5 rotor diameters and is similar to the one developed in Dar et al. (2023). The streamwise turbulence intensity $I_u = \sigma_U / U_h$, where σ_U is the standard deviation in the streamwsie velocity, shows an almost linear decrease with height. The streamwise turbulence intensity at the hub height of a prospective turbine is 0.135. A logarithmic fit is performed on the velocity data in the surface layer ($\approx 20\%$ of the boundary layer height). The result of the fit is shown in figure 7.2 (c). The aerodynamic surface roughness z_0 and friction velocity u_* are found to be 0.24 mm and 0.44 ms^{-1}, respectively. It is to be noted that the height coordinate z in figure 7.2 is set on the tunnel floor, while it is set on the first turbine hub position in the rest of the article.

7.2.2 Results

Here we present the results from the wind tunnel experiments. The results are sub-divided into two categories: we first report the results related to the flow without any turbines, which is followed by the results related to the turbine wake flow. For mean flow statistics, we define the mean streamwise velocity as $U = \sqrt{U_x^2 + U_z^2}$, where U_x and U_z are the mean horizontal and vertical velocity components, respectively. It is to be noted that $(x, z) = (0, 0)$ represents the hub location of the first turbine in each case.
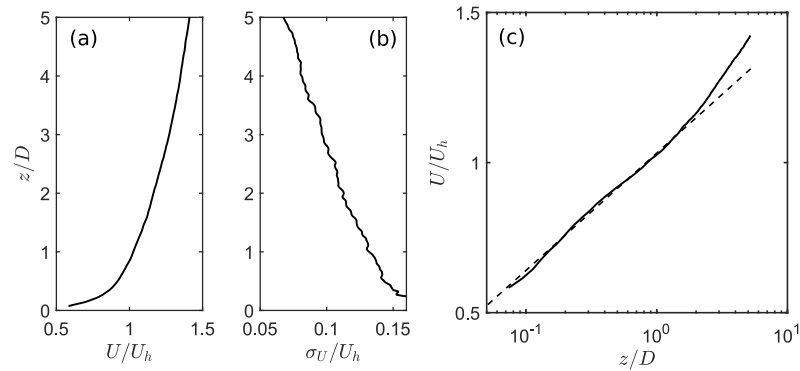
Figure 7.2: Vertical profiles of the normalized averaged streamwise velocity (a), streamwise turbulence intensity (b), and normalized averaged streamwise velocity with the height coordinate in log scale. The solid black line shows the experimental data and the dashed black line shows the logarithmic fit.

Base flow

Figure 7.3 shows the base flow contours of the normalized averaged streamwise velocity, together with the streamlines of the in-plane velocity vector field. The flow is homogeneous in the streamwise direction for the ZPG case, but shows an acceleration and deceleration for the FPG and APG cases, respectively. The flow acceleration/deceleration increases with the increase in the ramp angle for the pressure gradient situations. The flow streamlines are approximately parallel to the surface for the ZPG and smallest ramp angles ('APG-I' and 'FPG-I'), whereas they move away from the surface in the APG situation, and move towards it in the FPG situation, with the increase in the ramp angle.

Figure 7.4 (a) shows the normalized averaged streamwise velocity along the streamline originating from the hub position of a prospective turbine, and along the local hub height for different pressure gradient situations. For most of the cases, the two velocities are comparable. However, the difference between them is significant for the APG-III case. This shows that the deviation of the flow streamlines from the ramp slope is marginal for the majority of the cases. For the APG-III case, the streamlines move away from the surface into a higher velocity flow, which causes an increase in the velocity compared to that at the local hub height. It can also be observed that the increase or decrease in velocity with the increase in streamwise distance is approximately linear for all the cases, with the speed-up or slow-down in velocity increasing with increasing ramp slope.

Following previous works (Dar et al., 2022; Shamsoddin and Porté-Agel, 2017a, 2018a), the streamwise pressure gradient is approximated by UdU/dx. A zero pressure gradient corresponds to $UdU/dx = 0$, a favorable pressure gradient corresponds to $UdU/dx > 0$, and an adverse pressure gradient corresponds to $UdU/dx < 0$. Figure 7.4 (b) shows the normalized averaged pressure gradient along the velocity profiles shown in figure 7.4 (a). For the favorable pressure gradient cases, a clear increase in the pressure gradient with the increase in the

139

Figure 7.3: Contours of the normalized averaged streamwise velocity in the base flow. The streamlines of the in-plane velocity vectors are overlaid on the contours.

ramp angle can be observed for both velocities i.e., the one along the streamline and the one along the local hub height. For the adverse pressure gradient cases, a clear increase in the pressure gradient can be observed for the velocity along the local hub height, however, the values get closer for the velocity along the streamline. The development of a shear layer along the ramp length in the adverse pressure gradient cases causes the streamlines to move away from the surface. As the shear layer is stronger in the APG-III case compared to the APG-II case, the deflection of the streamline is also larger, which leads to a decrease in the pressure gradient compared to that along the local hub height. As shown previously by Dar et al. (2023), a stand-alone wind turbine wake follows the base flow streamline originating from the virtual hub height position, therefore, the velocity and pressure gradient profiles along the base flow streamline are more relevant for characterizing the wake flow.

The contours of the turbulence intensity based on the horizontal component of the velocity are shown in figure 7.5. High levels of turbulence intensity close to the surface are observed in the ZPG case. For the pressure gradient cases, the turbulence intensity also shows a significant change with the streamwise distance. For the APG cases, the turbulence intensity close to the surface increases with the streamwise distance from the ramp edge. Due to the negative slope of the ramp, the flow close to the surface of the ramp is sheltered from the upstream flow, which creates a shear layer with high mean velocity gradient, and thereby, high turbulence
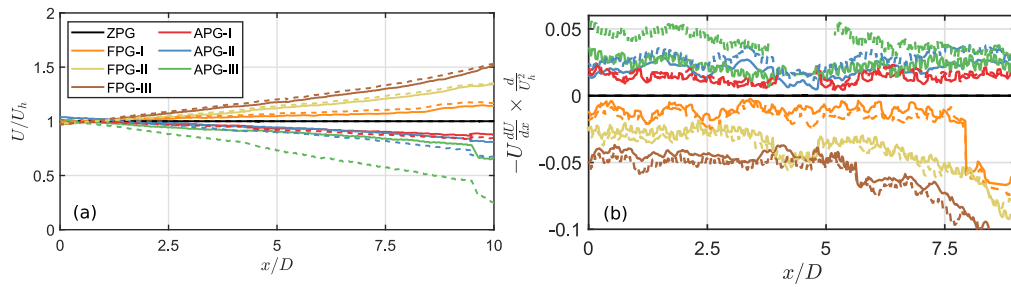
Figure 7.4: Normalized averaged streamwise velocity (a) and normalized pressure gradient (b) in the base flow along streamline originating at $(x, z) = (0, 0)$ (solid lines), and along local hub height (dashed lines) for different pressure gradient situations.
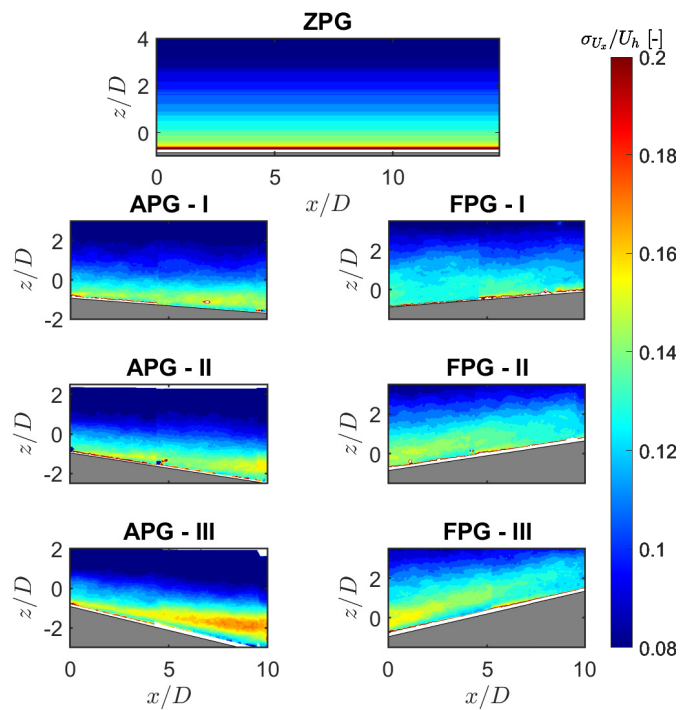
Figure 7.5: Contours of the horizontal turbulence intensity in the base flow.

intensity. For the FPG cases, on the other hand, the turbulence intensity close to the surface is observed to decrease with the increase in the streamwise distance. This can be related to the decrease in the mean flow shear close to the surface as the flow speeds up on the ramp. Figure 7.6 shows the turbulence intensity along the hub streamline in the base flow and the local hub height for all the cases. For all the cases, the turbulence intensity ranges between 0.12 and 0.155 along the streamline, with values increasing with distance for the APG cases, and decreasing for the FPG cases.

141
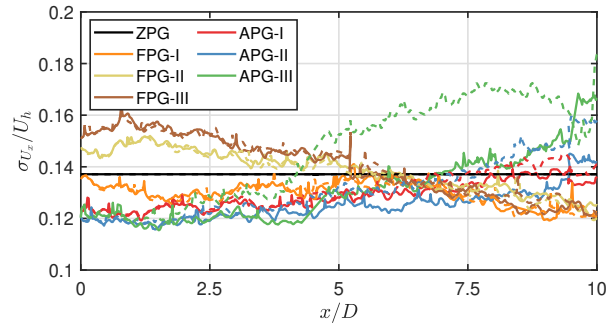
Figure 7.6: Horizontal turbulence intensity in the base flow along streamline originating at $(x, z) = (0, 0)$ (solid lines), and along local hub height (dashed lines) for different pressure gradient situations.
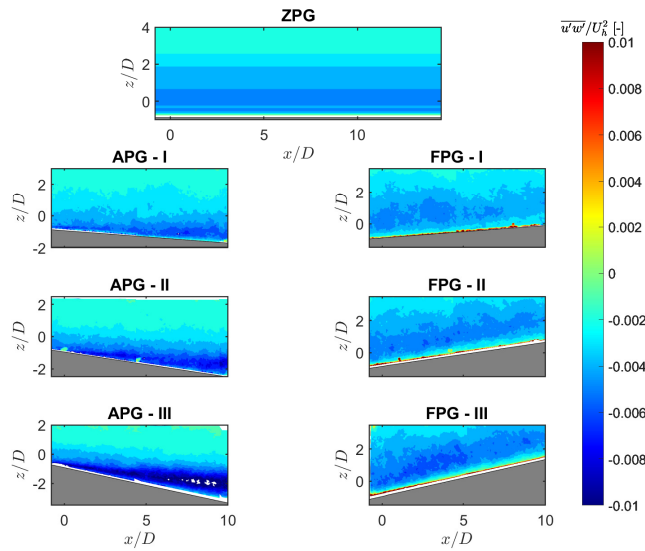
Figure 7.7: Contours of the normalized averaged vertical momentum flux in the base flow.

The vertical momentum flux along with the mean flow shear is responsible for the production of turbulence in turbulent boundary layers. The vertical momentum flux can be associated with the coherent motions that are responsible for energy transfer from the mean flow to the turbulent flow (Deshpande and Marusic, 2021). Figure 7.7 shows the contours of the normalized averaged vertical momentum flux in the base flow for all the cases. The normalized averaged momentum flux shows the highest magnitude in the APG cases in the shear layer, which corresponds to high turbulence intensity. For the FPG cases, the magnitude of the normalized averaged momentum flux is lower than for the APG ones, and it is distributed over a larger vertical extent. In general, the trends in the normalized averaged vertical momentum flux are consistent with those in the turbulence intensity.
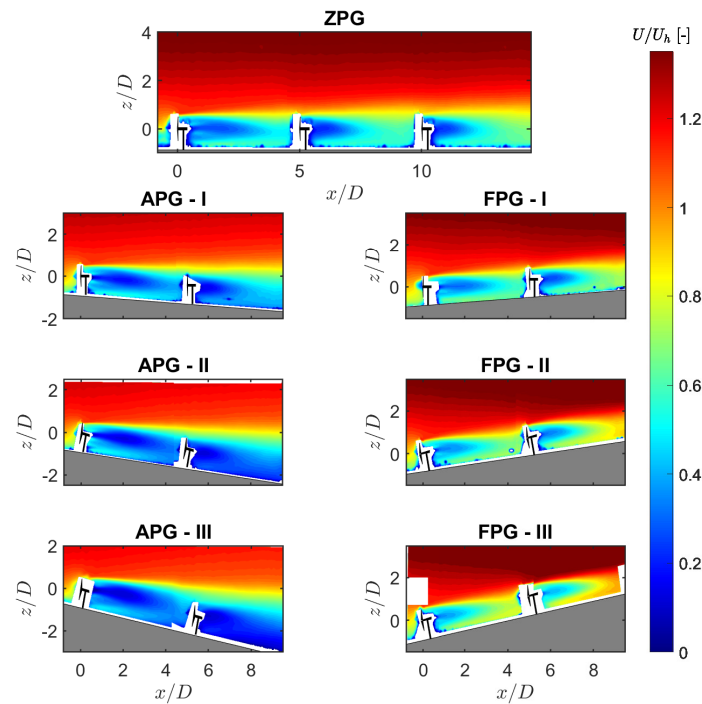
Figure 7.8: Contours of the normalized averaged streamwise velocity in the base flow.

Wake flow

In this section, we present results related to the wake of multiple fully aligned wind turbines (3 in the case of ZPG and 2 in the pressure gradient cases). Figure 7.8 shows the contours of the normalized averaged streamwise velocity in the wake flow for different pressure gradient situations. Previous studies (Cai et al., 2021; Dar et al., 2023; Shamsoddin and Porté-Agel, 2018a) have focused on stand-alone turbine wakes under base flow pressure gradient. Here we can observe that the normalized averaged streamwise velocity behind the second turbine is also affected by the ramp angle. In general, it is observed that the mean wake velocity decreases with the increase in the APG and increases with the increase in FPG, compared to the ZPG case, which is consistent with the previous studies (Cai et al., 2021; Dar et al., 2023; Shamsoddin and Porté-Agel, 2018a). For the ZPG case, the in-wake turbines have a lower velocity close to the turbine, but a higher velocity further downstream compared to the turbine in the free flow. This is due to the turbine-added turbulence intensity, which enhances the wake recovery. For the APG-I case, a similar observation to the ZPG case is made. For the APG-II and APG-III cases, however, the wake velocity is observed to be lower for the second turbine compared to the first one. This can be related to the lower velocity in the base flow for the second turbine. For the FPG cases, an opposite trend is observed where the second turbine shows a higher wake velocity compared to the first turbine due to an increase in the base flow velocity with the increase in the streamwise distance.
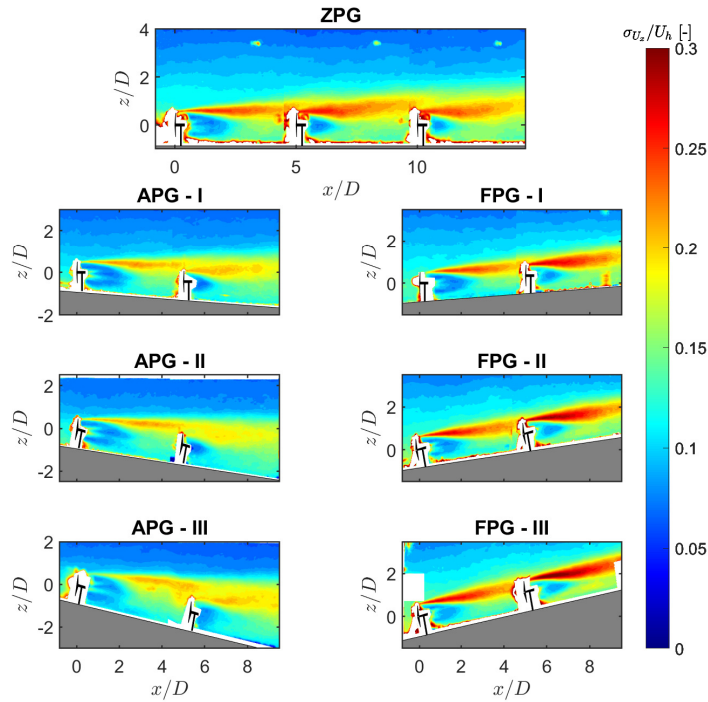
Figure 7.9: Contours of the horizontal turbulence intensity in the wake flow.

The horizontal turbulence intensity in the wake flow is shown in figure 7.9. A peak of turbulence intensity behind the rotor top tip can be seen in all the cases, which is associated with high mean flow shear around that region (Wu and Porté-Agel, 2012). For the ZPG case, the turbulence intensity increases behind the second and third turbines compared to that behind the first one. This is associated with the turbulence intensity added by the upstream turbine(s). For the FPG cases, a higher turbulence intensity is observed compared to the ZPG one, which increases with the increase in the FPG, and in the wake of the second turbine compared to the first one. For the APG cases, on the other hand, the peak of the turbulence intensity is lower than the FPG cases, and there seems to be no significant increase in the turbulence intensity behind the second turbine compared to the first one. As can be seen in figure 7.9, for the FPG cases, the peak region of turbulence intensity behind the two turbines is approximately aligned, resulting in an overall increase in the turbulence intensity behind the second one. In the APG cases, as the wake moves away from the surface, the peak regions behind the two turbines are not completely aligned, which results in a turbulence intensity distribution downstream of the second turbine with a peak value similar to that behind the first turbine, and a larger vertical spread compared to the FPG cases.

Vertical momentum flux acts as a mechanism to re-energize the wake by bringing high momentum flow from the outside into the wake. The inclination of the terrain also has an effect on the vertical momentum flux in the wake flow. Figure 7.10 shows the contours of the nor-
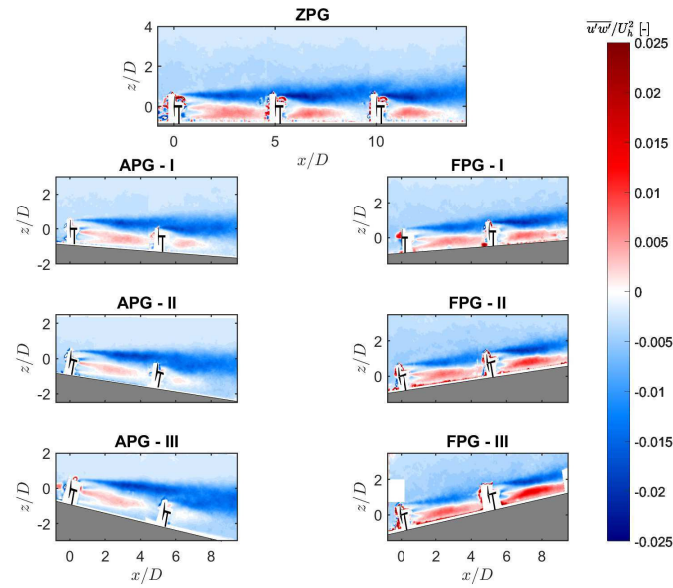
Figure 7.10: Contours of the normalized averaged vertical momentum flux in the wake flow.

malized averaged vertical momentum flux in the wake for different cases. For the ZPG case, the normalized averaged vertical momentum flux shows a negative value around the upper wake edge and a positive value around the lower wake edge, indicating the entrainment of energy from above and below into the wake. For the APG cases, the negative region behind the rotor top tip grows stronger in magnitude and shows high expansion in the vertical direction, similar to the expansion of the horizontal turbulence intensity profile. This is consistent with the expansion of the wake velocity profiles, which in the APG cases have a larger width (Dar et al., 2023). The magnitude of the normalized averaged vertical momentum flux gets stronger with the increase in the ramp angle. For the FPG cases, the negative region of the vertical momentum flux behind the rotor top tip is smaller compared to the ZPG and APG cases, whereas the positive region behind the rotor bottom tip gets larger with the increase in the positive ramp angle. This indicates that the ramp inclination has an influence on the distribution of momentum flux in the wake.

We now focus on characterizing the wake velocity deficit behind the turbines for different ramp cases. Here, the streamwise velocity deficit ΔU is defined as the difference between the base and wake flow velocities such that $\Delta U(x,z) = U_b(x,z) - U_w(x,z)$, where U_b and U_w are the base and wake flow velocities, respectively. The mean wake trajectories identified by the position of the maximum averaged wake velocity deficit are also shown. Following Shamsoddin and Porté-Agel (2018b), we plot contours of the averaged streamwise velocity deficit normalized by the base flow velocity at the hub position of the first turbine (figure 7.11 (a)), and normalized by the base flow velocity along the wake trajectory (figure 7.11 (b)). For the ZPG case and for the first turbine in the pressure gradient cases, both normalizations show similar trends. The normalized averaged wake deficit is higher in the APG cases and
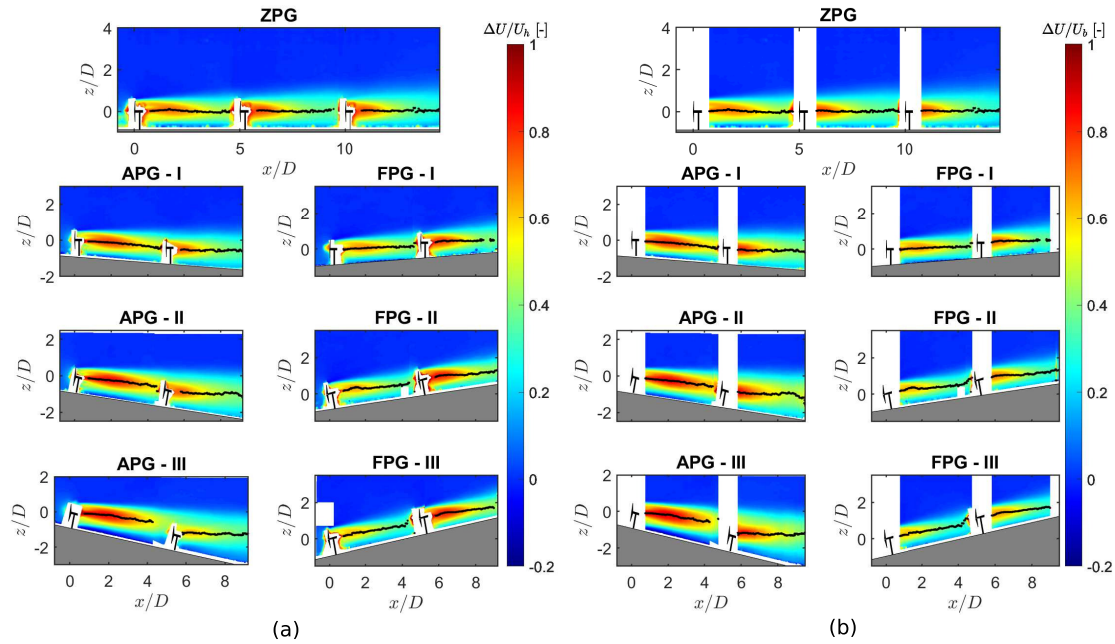
Figure 7.11: Contours of the averaged streamwise velocity deficit in the wake flow normalized by the base flow velocity at the hub position of the first turbine (a), and by the base flow velocity along the mean wake trajectory (b) along with the mean wake trajectories (black dots).

lower in the FPG cases, compared to the ZPG one behind the first turbine, which is consistent with the previous studies (Cai et al., 2021; Dar et al., 2023). For the in-wake turbine, when normalized by U_h, the APG cases show a lower velocity deficit compared to the FPG ones, whereas when normalized by the base flow velocity along the wake trajectory, it shows a higher value for the APG cases than the FPG ones. In this case, it makes more sense to use the base flow velocity along the wake trajectory as a reference, as it yields trends that are consistent with those for the first turbine wake deficit. It must be noted, however, that for the second turbine, the streamwise pressure gradient is due to the streamwise variation of the wake velocity of the upstream turbine(s), which can be approximated from the evolution of the wake center velocity of the first turbine in the absence of the second one.

To further characterize the wake velocity deficit, we show the evolution of the wake center velocity deficit in figure 7.12. It can be observed that the difference in the wake center velocity deficit between different cases is higher behind the first turbine compared to the second one, no matter what normalization is used. This is an important finding and can be related to the effect of the wake of the first turbine on the second turbine. As all wakes recover with the increase in the downstream distance, they impose a favorable pressure gradient on the downstream turbine(s), which together with the enhanced wake turbulence leads to a faster recovery of the downstream turbine compared to the upstream one.

Figure 7.13 shows the normalized wake width for different cases. The wake width is obtained by fitting a Gaussian function to the vertical profile of the wake velocity deficit at each downstream
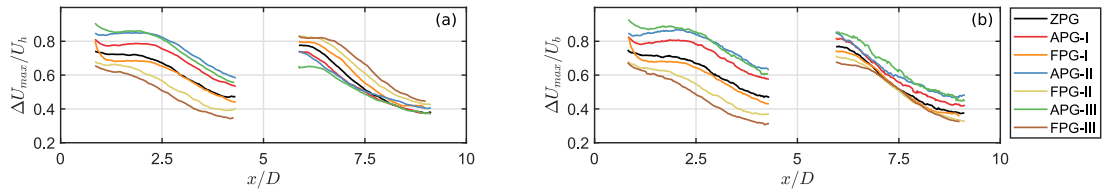
Figure 7.12: Wake center velocity deficit normalized by the hub position base flow velocity (a), and by the base flow velocity along the wake center (b).
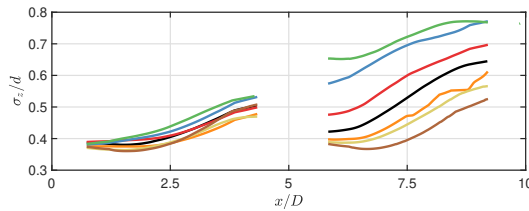
Figure 7.13: Comparison of the normalized wake width between different pressure gradient cases.

distance. Consistent with previous studies (Cai et al., 2021; Dar et al., 2023; Shamsoddin and Porté-Agel, 2018a), the wake width behind the first turbine is higher for APG cases and decreases for the ZPG and FPG cases, respectively. In the wake of the second turbine, the same trend holds but the difference between different cases increases compared to that in the first turbine's wake. In addition, the difference is higher between the ZPG and APG cases than that between the ZPG and FPG cases. This is likely due to the fact that the wake moves away from the surface in the APG cases giving it more space to expand with the streamwise distance, whereas it moves towards the surface in the FPG cases, which limits the expansion of the wake.

Some recent studies have shown that a wind turbine wake follows the base flow streamline originating from the hub position (Dar et al., 2023; Liu et al., 2021). Here we investigate the trajectory of the cumulative wake of multiple turbines to see if it follows the wake trajectory of the upstream-most turbine or deviates from it. For this purpose, we show the mean wake center trajectory overlaid on the base flow velocity and streamlines in figure 7.14. For majority of the cases, we can see that the wake trajectory for different turbines is approximately aligned with the base flow streamline originating from the hub position of the free flow turbine. One exception is the APG-III case, where for the in-wake turbine the trajectory is almost horizontal and does not necessarily follow either the upstream turbine or the base flow streamlines. Overall, for most cases, following the base flow streamline from the hub position of the first turbine seems to be a reasonable approximation for the wake trajectory of the cumulative wake of multiple turbines under pressure gradient.
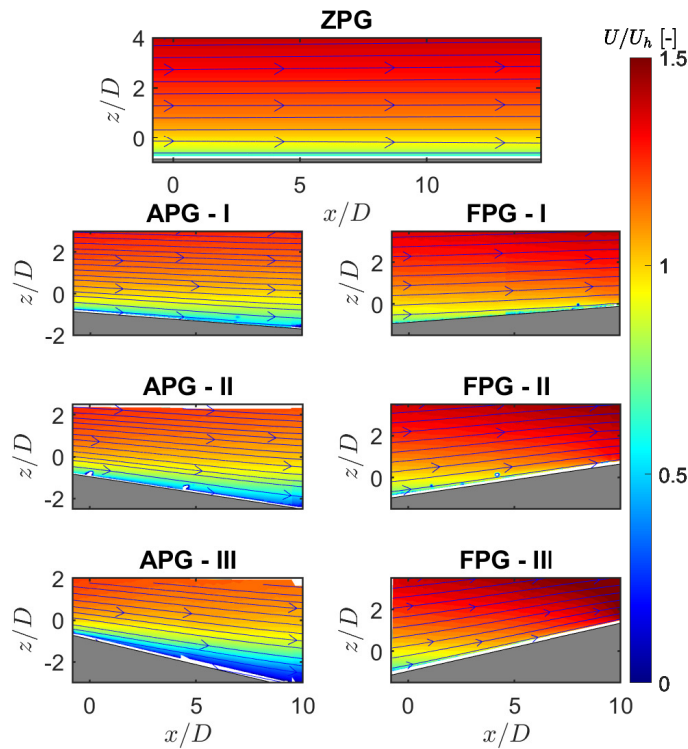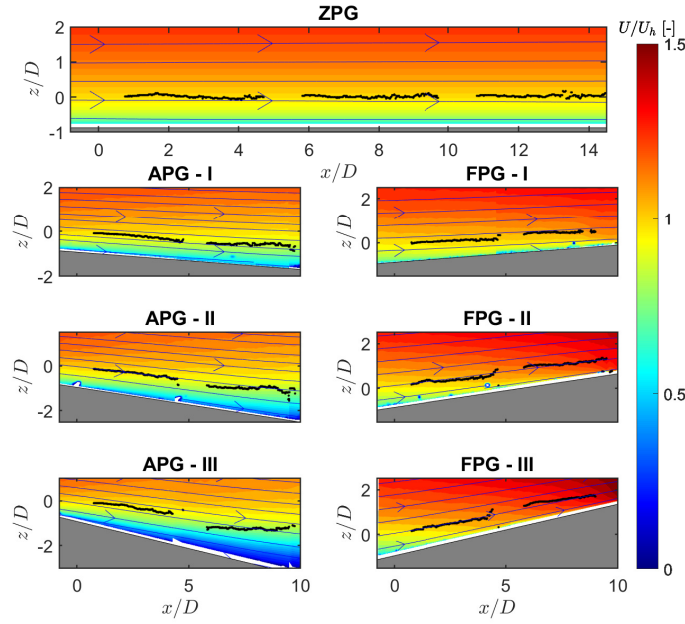
Figure 7.14: Contours of the normalized averaged streamwise velocity in the base flow along with the streamlines of the in-plane velocity vectors(arrow lines) and the mean wake trajectories (black dots).

7.3   Analytical modeling

In this section, we focus on analytically modeling the cumulative wake velocity deficit of multiple turbines under a pressure gradient. For this purpose, we test two different strategies. The first strategy is based on an adapted version of the linear summation approach proposed by Niayifar and Porté-Agel (2016), whereas the second one is based on the pressure gradient model proposed by Dar et al. (2023) and Shamsoddin and Porté-Agel (2018a). In the following, we will provide details of the two strategies and compare the results obtained from them. For both approaches, the wake velocity deficit in the far wake is assumed to follow a Gaussian distribution given by:

$$\frac{U_b - U_w}{U_b} = C(x) e^{-\left(\frac{r^2}{2\sigma(x)^2}\right)}, \tag{7.1}$$

where U_b is the base flow velocity, U_w is the wake flow velocity, $C(x)$ is the normalized maximum velocity deficit, r is the radial distance from wake center and $\sigma(x)$ is the wake width.

148

7.3.1   Adapted linear summation approach

The linear summation approach for wake superposition proposed by Niayifar and Porté-Agel (2016) states:

$$U_w(x, y, z) = U_\infty - \sum_i (u_0^i - U_{w,s}^i(x, y, z)), \tag{7.2}$$

where U_w is the cumulative mean wake velocity, U_∞ is the mean base flow velocity, u_0^i is the mean velocity perceived by the *ith* turbine, and $U_{w,s}^i$ is the mean wake velocity of the *ith* wind turbine in stand-alone conditions. In order to adapt the superposition method for a streamwise varying base flow, two changes are made: the base flow velocity U_∞, and the turbine perceived velocity u_0 are expressed as a function of x as $U_b(x)$ and $u_0(x)$, respectively, to account for the variation in the perceived velocity along the wake. The adapted model is then written as:

$$U_w(x, y, z) = U_b(x) - \sum_i (u_0^i(x) - U_{w,s}^i(x, y, z)). \tag{7.3}$$

To model the stand-alone turbine wake, we use the Gaussian model proposed by Bastankhah and Porté-Agel (2014, 2016). The normalized maximum wake velocity deficit $C(x)$ is modeled as:

$$C(x) = 1 - \sqrt{1 - \frac{\sigma_0^2 C_0(2 - C_0)}{\sigma(x)^2}}. \tag{7.4}$$

In the above equation, C_0 is the maximum wake velocity deficit at the start of the far wake obtained from 1-D momentum theory ($C_0 = 1 - \sqrt{1 - C_T}$, where $C_T = 0.8$). The start of the far wake is estimated by the near wake length model proposed by Bastankhah and Porté-Agel (2016). The wake width in the far wake σ is assumed to grow linearly with a growth rate k, which is a function of the horizontal turbulence intensity ($k = 0.3 TI$ Dar et al. (2023)). The wake width at the start of the far wake σ_0 is obtained from experiments. The horizontal turbulence intensity is taken from the base flow information for the free-flow turbine, whereas for the in-wake turbines, the added turbulence intensity of upstream turbines is accounted for, where the total turbulence intensity is then $TI = \sqrt{I_0^2 + I_a^2}$, with I_0 the base flow turbulence intensity and I_a the added turbulence intensity. The added turbulence intensity is modeled using the Frandsen model (Frandsen, 2007):

$$I_a = \frac{1}{1.5 + \frac{0.8}{\sqrt{C_T}} \frac{x}{d}}. \tag{7.5}$$

7.3.2 Pressure gradient model approach

The pressure gradient model proposed initially by Shamsoddin and Porté-Agel (2018a) and further developed by Dar and Porté-Agel, 2022a; Dar et al., 2023 accounts for the effect of a base flow streamwise pressure gradient on the evolution of a wind turbine wake. So far this model has only been applied for stand-alone wind turbine wakes (Cai et al., 2021; Dar et al., 2022; Shamsoddin and Porté-Agel, 2018b; Zhang et al., 2022). Here we look to apply the model for the case of multiple turbines in an aligned condition. The idea behind this is the following: for the first wind turbine, the pressure gradient is solely due to the streamwise variation of the base flow, whereas for the turbines in the wake of upstream ones, the pressure gradient is due to the streamwise variation of the wake flow of the upstream turbines - which already includes the effect of the base flow pressure gradient. In this approach, the effect of the upstream turbine wake(s) is modeled into the base flow term for the downstream turbine wake, which eliminates the need for a subsequent superposition of wakes. In the following, we describe the procedure for applying the model to a multiple turbine case.

The first step is to model the wake of a turbine exposed only to the pressure gradient imposed by the base flow i.e., the turbine in no-wake condition. For this purpose, we solve the ordinary differential equation for maximum velocity deficit:

$$\frac{dC}{dx} = \frac{-1}{(\frac{U_b^4}{\Lambda_0^2})(3C^2 - 2C^3)} \left[\frac{1}{4} \frac{dU_b^4}{dx} \frac{C^3}{\Lambda_0^2} + (C^3 - \frac{C^4}{2}) \frac{d}{dx}(\frac{U_b^4}{\Lambda_0^2}) \right],$$

(7.6)

where U_b is taken as the base flow along the wake trajectory and Λ_0 is the invariant ratio defined as:

$$\Lambda_0 = \frac{C_{zpg}U_h}{\sigma_{zpg}},$$

(7.7)

where U_h is the hub height velocity at the turbine location, C_{zpg} is the maximum velocity deficit under zero pressure gradient condition, and σ_{zpg} is the wake width under zero pressure gradient. In order to solve equation 7.6, an estimation of the maximum velocity deficit at the start of the far wake is needed in the form of a boundary condition. This is defined as:

$$C_{nw}(x) = 1 - \frac{U_{nw}(x)}{U_b(x)},$$

(7.8)

where $C_{nw}(x)$ is the normalized maximum velocity deficit in the near wake and U_{nw} is the near wake velocity, which can be obtained as follows:

$$U_{nw}(x) = \sqrt{U_{nb}(x)^2 - U_h^2 C_T},$$

(7.9)

where U_{nb} is the base flow velocity in the near wake. The estimation of near wake length is

made by solving the following equation (Dar et al., 2023):

$$\sigma_{nw} = (2\alpha I + \beta) \int_0^{l_{nw}} \frac{1}{1 + \sqrt{1 - \frac{U_h^2 C_T}{U_b^2}}} dx - \beta \int_0^{l_{nw}} \frac{1}{1 + \frac{1}{\sqrt{1 - \frac{U_h^2 C_T}{U_b^2}}}} dx, \tag{7.10}$$

where l_{nw} is the near wake length, σ_{nw} is the wake width at the end of the near wake, α and β are model constants taken as 0.58 and 0.077, respectively.

Finally, the wake width under pressure gradient can be obtained from the invariant ratio:

$$\sigma(x) = \frac{C U_b}{\Lambda_0}. \tag{7.11}$$

For an in-wake turbine, the wake flow of the upstream turbine(s) becomes the new base flow. In this work, we approximate that base flow from the modeled minimum wake velocity of the upstream turbine and plug it in equation 7.6, where now $U_b = U_{w,min}^{i-1}$. We also need to estimate the invariant ratio for the in-wake turbine using equation 7.7. Here, U_h is now the wake velocity of the *i-1th* wind turbine at the hub location of the *ith* turbine in its absence. In order to obtain C_{zpg} and σ_{zpg}, we once again need the wake growth rate k, which in this case depends on the base flow turbulence intensity and wake added turbulence intensity, and similar to the linear sum approach can be written as $k = 0.3\sqrt{I_0^2 + I_a^2}$. The added turbulence intensity is estimated using the Frandsen model. The process is repeated in an iterative manner, where for each downstream turbine, the base flow velocity and invariant ratio are updated based on the cumulative wake velocity of the upstream turbines.

Due to the lack of experimental data for U_w^{i-1} in the overlapping region of *i-1th* and *ith* turbine wakes, an additional step is needed in order to perform a comparison between the model and the experimental data. This involves re-scaling $C(x)$ and $\sigma(x)$ for the *ith* turbine with respect to the base flow in the absence of any upstream turbines. The maximum deficit C obtained for the *ith* turbine can be written as:

$$C^i(x) = \left[\frac{U_w^{i-1} - U_w^i}{U_w^{i-1}} \right]_{max}, \tag{7.12}$$

which can be used to get the minimum U_w^i, and eventually compute the maximum deficit with respect to the base flow without any turbine:

$$C(x) = \left[\frac{U_b - U_w^i}{U_b} \right]_{max}. \tag{7.13}$$

151

In order to compute the wake width, the invariant ratio is computed as:

$$\Lambda_0^i = \frac{C_{zpg}^i U_{b,x_i}}{\sigma_{zpg}^i},$$
(7.14)

where U_{b,x_i} is the base flow velocity at the position of the *ith* turbine. This eventually gives the wake width:

$$\sigma(x) = \frac{C U_b}{\Lambda_0^i}.$$
(7.15)

Finally, the wake deficit profiles with respect to the base flow can be computed using equation 7.1. Alternatively, we could use equation 7.1 such that we get U_w^i and then subtract it from the global base flow U_b. Both methods of computing global wake deficit yield equivalent results.

7.3.3   Comparison between experiments and models

We now compare the results from the two modeling approaches described above with the experimental data. Figure 7.15 compares the normalized maximum velocity deficit in the wake between the experiments and different models. Both approaches yield reasonable results for the ZPG case. By definition, the normalized maximum velocity deficit is the same for all the cases in the linear summation approach, whereas it changes for the pressure gradient model, as it accounts for the effect of the change in the base flow in the computation of the normalized maximum deficit. This is why the result of the pressure gradient model (red line) is observed to change depending on the case, whereas the linear summation (green line) remains the same. For the APG cases, the pressure gradient model is able to predict the normalized maximum velocity deficit well in the far wake of both turbines, whereas the linear summation approach under-predicts it. The under-prediction of the normalized maximum deficit is higher in the wake of the first turbine compared to that in the wake of the second. This is explained by the fact that the difference between the ZPG and pressure gradient wake deficit is higher in the first turbine wake than in the second turbine one. Similarly, for the FPG cases, the pressure gradient model can predict the normalized maximum velocity deficit well for the FPG-I and FPG-II cases; however, it under-predicts in the FPG-III case. This could be related to the fact that the normalized maximum velocity deficit in the second turbine's wake is comparable between different FPG cases, however, the wake velocity of the first turbine varies. While the experimental data shows a comparable maximum velocity deficit, the one predicted by the model decreases due to the higher FPG of the upstream turbine. As the turbine wake has a downward trajectory into a low momentum region close to the surface with the increase in the ramp angle for FPG cases, this could result in an apparent slowdown of the wake recovery observed in the second turbine wake. It is to be noted that, in the near wake of the turbines, the experimental normalized maximum velocity deficit is higher than the modeled one. This can be associated with the effects of the turbine hub drag and the rotation of the wake, which are not included in the simplified theoretical estimation of the near wake velocity deficit
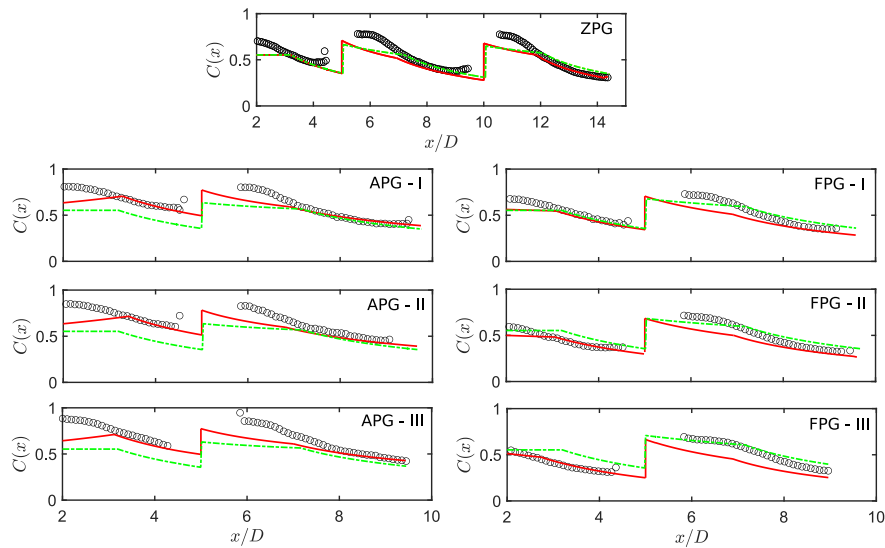
Figure 7.15: Comparison of the normalized maximum velocity deficit in the wake between the experiments (circles), linear superposition approach (green line), and pressure gradient model (red line).

(Bastankhah and Porté-Agel, 2016; Dar and Porté-Agel, 2022a; Zong and Porté-Agel, 2020b). In addition, the Gaussian-based models are applicable in the far wake region and do not conserve momentum in the near wake region. A region of increased normalized maximum velocity deficit can also be observed upstream of the in-wake turbines in the measurements, which is associated with the induction of the turbines. This increase in the normalized maximum velocity deficit in the induction region is most pronounced in the ZPG case and is relatively less significant in the pressure gradient cases. However, this effect is not captured by the analytical wake models.

Figure 7.16 compares the vertical profiles of the normalized streamwise velocity deficit in the wake for different pressure gradient cases. For the ZPG case, the pressure gradient model is able to predict the velocity deficit profiles behind all three wind turbines with reasonably good accuracy. As a reference, the linear summation approach for wake superposition is also shown to predict the velocity deficit profiles well. This shows that the pressure gradient model can actually be used for predicting the velocity deficit profiles in a wind farm in flat terrain without the need for any subsequent superposition of wakes. For the APG cases, the pressure gradient model predicts the velocity deficit profiles well for all the cases. The linear summation approach, on the other hand, does not yield satisfactory results. Behind the first turbine, there is a significant underestimation of the velocity deficit profiles compared to the experimental data, both in terms of the maximum deficit and wake width. For the second turbine, the prediction of maximum velocity deficit improves, whereas the wake width is still significantly underestimated compared to the experimental velocity deficit profiles. For the FPG cases, the pressure gradient model agrees reasonably well with the experiments for all cases except the second turbine in the FPG-III case. The linear summation approach results
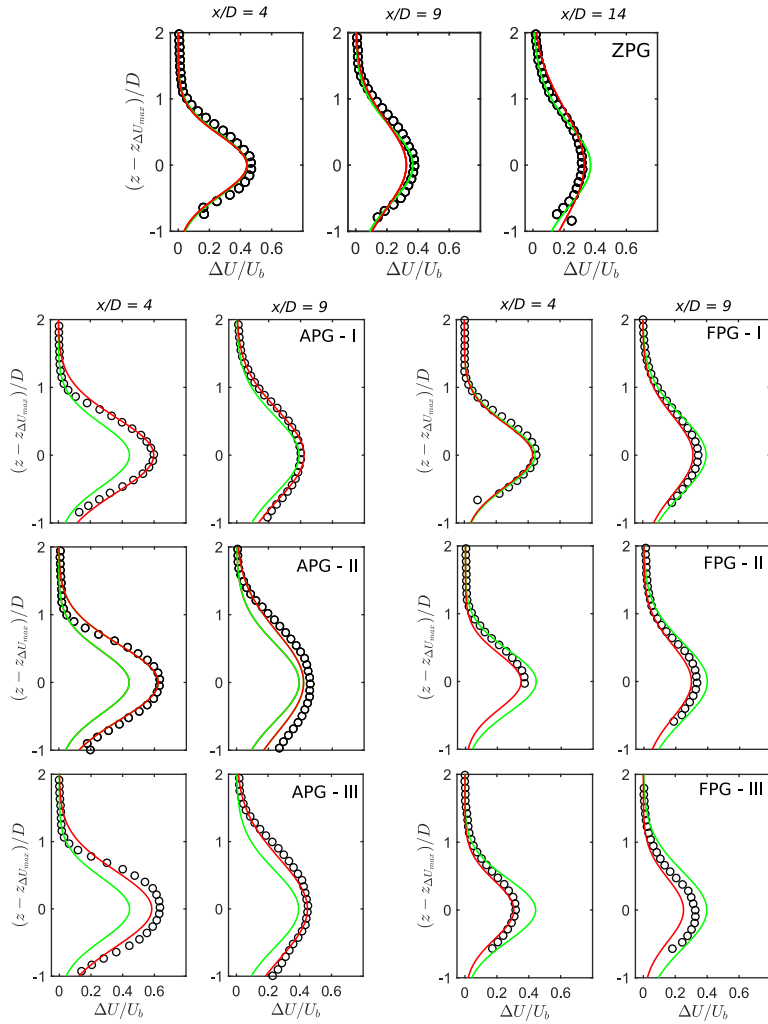
Figure 7.16: Comparison of the vertical profiles of the normalized averaged velocity deficit in the wake between the experiments (circles), linear superposition approach (green line), and pressure gradient model (red line).

in an overestimation of the maximum velocity deficit for all the cases, except the first turbine in the FPG-I case.

Through this comparison, the pressure gradient model approach to estimate the cumulative wake of multiple turbines in flat and non-flat terrain is validated. The model conserves momentum in the far wake and eliminates the need for any empirical approach to superpose individual wakes. The linear summation approach, on the other hand, does not yield good results for non-flat cases. This can be related to the fact that while it can approximately conserve momentum in the flat case (Zong and Porté-Agel, 2020b), it cannot account for the pressure gradient imposed by the base flow in non-flat cases.

7.4   Summary

Wind turbines in complex terrain can experience pressure gradients due to the change in surface elevation or roughness characteristics. In this study, we systematically investigated the wake of multiple turbines under a range of terrain-induced pressure gradients using wind tunnel experiments. The pressure gradients were imposed by means of linear ramps, where in total 7 different pressure gradient cases were investigated. The flow speed-up/slow-down was linear in all cases, and two turbines were sited on the ramps at an inter-turbine spacing of 5 rotor diameters, and three turbines were used in the zero pressure gradient case. The focus of the study was to understand the effect of pressure gradient on the cumulative wake of multiple turbines.

The normalized averaged streamwise velocity was shown to decrease behind the in-wake turbine with the increase in the APG compared to that behind the turbine exposed to the free flow. For the ZPG and FPG cases, on the other hand, the normalized streamwise velocity behind the in-wake turbine increased with increasing pressure gradient magnitude. This was related to the turbine-added turbulence and the flow speed-up in the FPG cases. The horizontal turbulence intensity showed a peak at the rotor top tip level due to high mean flow shear. The magnitude of the turbulence intensity peak was observed to increase in the cumulative wake of multiple turbines in the ZPG and FPG cases, compared to the upstream-most turbine, whereas no considerable increase in the magnitude was observed for the APG cases. This behavior was associated with the wake trajectory and overlapping of the peak turbulence intensity region of the two turbine wakes. The vertical momentum flux was also observed to change with the ramp slope, which was likely associated with the inclination of the ramp. The vertical momentum flux showed a higher magnitude around the rotor top tip level in APG cases, whereas in the FPG cases, it was stronger near the bottom tip of the turbine.

The wake velocity deficit was also characterized. The velocity deficit behind the first turbine showed a higher difference between different pressure gradient cases than behind the second turbine. This was related to the change in the pressure gradient due to the wake of the upstream turbine. The normalized wake width, on the other hand, showed a higher difference between different cases behind the second turbine than behind the first one. This is likely due to the larger distance traveled by the cumulative wake, leading to a larger cross-stream expansion of the wake.

We proposed a new approach to model the cumulative wake velocity deficit of multiple wind turbines. In this approach, we use the pressure gradient model proposed previously to model stand-alone wind turbine wakes in topography. This is the first instance of the application of the model to a case with multiple wind turbines. To model the wake velocity deficit behind an in-wake turbine, the wake velocity minimum of the upstream turbine(s) wake flow is used as a base flow to estimate the maximum wake velocity deficit, and the invariant ratio is used to obtain the wake width. This eliminates the need for any subsequent superposition to model the cumulative wake. The new approach is tested against the linear summation approach

to superpose the wake velocity deficit of stand-alone turbines and against the experimental data. For the wind farm in flat terrain, both methods of modeling the velocity deficit yield reasonable results. For the two turbine cases under pressure gradient, the new approach is found to agree well with the experiments for most of the cases and outperforms the approach based on the linear summation superposition. Therefore, with the new approach, we can model wind farm wakes in flat and complex terrain without the need for any superposition principle.

Part - III: Wind turbines in urban environment

8 An experimental investigation of a roof-mounted horizontal-axis wind turbine in an idealized urban environment[I] [II]

Abstract

Wind-tunnel experiments are performed to investigate the effect of minor modifications to the roof edge shape on the power performance and wake characteristics of a horizontal-axis wind turbine sited on a cube-shaped building. Three roof edge shapes are considered: a sharp edge, a rounded edge, and a solid fence. The power performance of the turbine is dependent on its streamwise position, and on the roof edge shape due to the difference in the flow shear induced by different roof edges. The sharp edge and solid fence cases show high variation in power with the turbine position, which is reduced significantly in the rounded-edge case. The turbine shows the worst power performance regardless of its position in the fence case. The roof edge shape is also found to affect the wind turbine wake. Specifically, the wake recovery and expansion rates are found to be greatest for the fence case, and they decrease with the increasing smoothness of the roof edges. This is related to the difference in the base flow turbulence induced by different roof edge shapes. Compared to the base flow, turbulence intensity in the wake is reduced on the building, except at the rotor top tip level.

8.1   Introduction

Our world has undergone intense urbanization, with the global population living in urban areas increasing from 30% in 1950 to 55% in 2016 (Division, 2001; Ritchie and Roser, 2018). In the developed world, these numbers are even higher, with more than 80% of the population living in urban areas (Ritchie and Roser, 2018). This rapid urbanization has also resulted in an overall increase in the global energy demands. Although most of the world energy needs are currently provided by fossil fuels; renewable energy sources have emerged as a promising alternative to decarbonize the energy market, and potentially mitigate the harmful impact of fossil fuels on the environment. In this context, it is also relevant to highlight the sustainable development goals (SDGs) promoted by the United Nations (Desa et al., 2016), two of which concern the promotion of renewable energy sources and the development of sustainable cities. Localized micro-generation of energy within urban environments via renewable sources can play a crucial role in achieving the above-mentioned SDGs. While wind energy is traditionally harvested from wind farms sited away from urban settlements, wind energy generation within the urban environment has been highlighted as an under-explored potential for clean energy generation closer to the end consumer (Rezaeiha et al., 2020).

Several studies have explored the potential and challenges associated with urban wind energy. Stathopoulos et al. (2018) reviewed recent developments in the field of urban wind energy. They stressed on the need to further explore the influence of building aerodynamics on the potential wind energy generation and wind resource assessment. Micallef and Van Bussel (2018) also presented a review of urban wind energy research with a special focus on urban aerodynamics. They highlighted that urban wind energy research suffers from a lack of synergistic efforts between different areas of research, which is crucial for the success of urban wind energy. Walker (2011) reviewed the methods used for urban wind resource assessment, and showed that the most common approach of combining a wind turbine power curve with the wind rose information gives inaccurate estimation of potential urban wind energy yield. This was associated with the complexity of flow in an urban environment including the influence of the shape of the buildings. Concerns regarding the noise generation and public acceptance of urban wind energy also present a challenge (Evans et al., 2011; Micallef and Van Bussel, 2018). Despite these challenges, the assessment of urban wind energy on a national or regional scale shows that it can play a significant role in providing decentralized renewable energy. Mithraratne (2009) performed an assessment of urban wind energy generation using roof-mounted wind turbines in New Zealand. They showed that, while urban wind energy cannot act as an alternative for the large-scale wind energy generation, it has the potential to reduce the carbon footprint of New Zealand's electricity generation. Drew et al. (2013) assessed the potential of wind energy generation within the Greater London area in the UK. They found that most areas with high wind energy potential were located towards the outskirts of the city, although some areas closer to the city center also had high potential for wind energy generation. Grieser et al. (2015) studied the economic feasibility of small wind turbines in urban environments in Germany. They showed that optimized positioning of wind turbines

in an urban environment based on flow conditions is crucial. In addition, combining a wind energy generation system with an energy storage system was observed to enhance the economic feasibility of urban wind energy generation. More recently, Rezaeiha et al. (2020) developed a framework to assess wind energy potential of roof-mounted wind turbines. When applied to the Netherlands, they found that across existing high rise buildings in 12 cities of the Netherlands, an annual energy production of 150.1 GWh can be achieved.

Assessment of wind resources in an urban environment is, however, a challenging task due to the complex nature of urban flow and its strong dependence on building aerodynamics. Different studies have been reported in the literature that assess the potential energy yield of wind turbines in an urban environment. Bayoumi et al. (2013) developed a tool to optimize the integration of a vertical axis wind turbine in the building design in order to achieve a certain energy yield. Their model relied on some pre-computed computational fluid dynamics results of flow around the buildings, and was able to provide an estimation of the optimal number, position and size of the turbines required to generate the target energy yield. Abohela et al. (2013) investigated the effect of wind direction, turbine position and roof shapes (such as flat, dome-shaped, pyramid-shaped and vaulted) on the energy yield of wind turbines. They concluded that an informed decision based on the understanding of flow around the building and optimal placement of wind turbines can result in an increase in the potential energy yield. Al-Quraan et al. (2016) compared wind tunnel measurements of flow around buildings with field data to assess the accuracy of wind tunnel measurements. They concluded that, while wind tunnel data showed good agreement with the field data for an initial assessment of wind energy potential, the agreement between the two decreased with the increase in the inhomogeneity of the surrounding terrain. Emejeamara and Tomlin (2020) proposed a new method for estimating power production of vertical axis wind turbines, which could also account for unsteady power performance of the turbine due to turbulent nature of the flow. Rezaeiha et al. (2020) developed a framework to assess the wind energy potential using the information of building aerodynamics, wind speed at building height, turbine characteristics and number of turbines. They demonstrated the use of the framework by computing the annual energy production using roof-mounted turbines across the Netherlands. Ruiz et al. (2021) presented an optimization of ducted openings in high rise buildings for wind energy harvesting. They optimized the design of the ducted opening by changing the fillet radius and diameter of the duct, and showed that aerodynamic design of the buildings can significantly enhance wind energy production. Li et al. (2021) showed that an array of vertical axis turbines optimized for the roof shape can lead to enhanced power performance. More recently, Higgins and Stathopoulos (2021) took an artificial intelligence (AI) approach to assess the potential of urban wind energy. They developed artificial neural network (ANN) and tested its performance for different city configurations against wind tunnel data. They concluded that AI modeling can prove to be a useful tool for identification and assessment of potential turbine locations in an urban environment.

While the potential of urban wind energy has been readily reported in the literature, the interaction of wind turbines with the atmospheric boundary layer in an urban environment

is relatively under-explored. For the large-scale wind energy, this has been the focus of research over the past few decades (Porté-Agel et al., 2020; Stevens and Meneveau, 2017). The general working principles of horizontal axis wind turbines, their aerodynamics and momentum theory are covered in detail in (Hansen, 2015; Sørensen, 2016). The wake of a turbine, characterized by its low velocity and turbulent nature, is responsible for reduction in power available for downstream turbines. Accounting for the turbine wake effects is, therefore, important for clustering of wind turbines in an urban environment. In addition, these wakes can also alter the fatigue load distribution on downstream turbines, as well as on any built structures downstream of the turbine. It is, therefore, of great interest to understand how turbine wakes evolve in urban environments. Due to their potential impact on the success of any wind energy project, several studies investigating wind turbine wakes in an urban environment have recently emerged. Ge et al. (2020) investigated the effect of the wake of a turbine on an urban district model located downstream, where the turbine hub height and diameter were twice the height of the buildings. They found that the urban district resulted in a faster recovery of the turbine wake and modified its trajectory. The turbine wake also reduced the wind speed in the streamwise streets of the urban district. Ge et al. (2021) also performed large-eddy simulation of single and multiple wind turbines located downstream of a cube-shaped building. They showed that the building resulted in a decrease in power and increase in power fluctuations of the first turbine located downstream. The turbine wake also showed faster recovery due to higher turbulence and secondary mean flow induced by the building. A second turbine placed downstream of the first one showed higher power output in the presence of the building than in its absence. Fan et al. (2021) studied the effect of buildings and trees on the performance of roof-mounted wind turbines. Their results showed that trees higher than buildings caused a decrease in the power output of the turbines compared to the case with trees lower than the building height. The wake of the turbine was asymmetric and had a downward trajectory. Xu et al. (2021a, 2021b) studied vertical axis wind turbines located on the side of and between buildings. For wind turbines on the side of the buildings, different flow scenarios and arrangements of turbines were simulated. From these simulations, they deduced that for a stand-alone turbine, tailwind position performed best, whereas for multiple turbines a combination of crosswind and tailwind arrangement proved best. For wind turbines installed between the buildings, counter-rotating turbine arrangement performed better than the co-rotating arrangement. They also placed five arrays of wind turbines between the buildings, and showed that their performance was rather complex and dependent on the flow conditions. The effect of wind direction was also investigated, revealing best performance at 15° incoming wind direction. All of the above-mentioned studies utilize numerical tools, and there is an obvious lack of experimental work investigating the interaction of wind turbines with an urban environment.

Urban wind energy can also benefit from recent advances in the field of wind energy in complex terrain. Several studies have shown that local changes in terrain elevation can have significant effects on wind resources available for wind turbines (Dai et al., 2017; Nedjari et al., 2017). In addition, atmospheric stability has also been shown to have significant effect on

available power for wind turbines in complex terrain, with higher spatial variability during stable conditions (Radünz et al., 2020). Especially, the studies focused on wind turbines located on escarpments can be relevant for urban wind energy, as an escarpment can be considered as a building with infinite length and width. Lange et al. (2017) showed that the edge of the escarpment can have a significant effect on the flow over it, and consequently on the power available for turbines. Qian and Ishihara (2019) showed that the ratio of escarpment height to the turbine height can have an effect on the turbine wake deflection. More recently, Dar and Porté-Agel (2020, 2022b) showed that the shape of the escarpment leading-edge significantly affects the wake of a wind turbine sited on it.

In the current study, we have performed wind tunnel measurements on a roof-mounted wind turbine in an idealized urban environment, where the building is represented by a cube-shaped block. Of particular interest is the shape of the roof edges, where minor modifications, such as slight curvature or addition of a boundary fence, are introduced in addition to a sharp-edged roof. The sensitivity of the turbine power output to the roof edge shape and streamwise position of the turbine on the building is first investigated. The wake of the turbine placed at the position corresponding to maximum power output is then compared between different roof edge shapes. To the best of the authors' knowledge, this is the first wind tunnel study investigating the effect of seemingly minor modifications of the roof edge shapes and turbine position on the power performance and wake characteristics of a roof-mounted wind turbine. The rest of the article is structured as follows: section 8.2 documents the experimental setup and the urban boundary layer developed; results from the study are reported and discussed in section 8.3; finally, a summary of the work and conclusions are presented in section 8.4.

8.2   Experimental Setup

The experiments are conducted in the closed-loop boundary layer wind tunnel at the WiRE laboratory of EPFL. The wind tunnel has a test section of 28 m length, 2.6 m width and 2 m height, with a contraction of 5:1 area ratio before the inlet. A 130 kW fan drives the flow in the wind tunnel.

A miniature three-bladed horizontal axis wind turbine is used in this study. The miniature turbine is a scaled-down version of the WiRE-01 miniature turbine developed at WiRE, EPFL (Bastankhah and Porté-Agel, 2017a; Bastankhah and Porté-Agel, 2017c). A scaling ratio of 1:1.43 is established between the scaled-down and original turbine models. This scaling results in a rotor diameter d of 10.5 cm and a hub height z_h of 8.75 cm for the scaled-down turbine. The blade profile has a circular arc shape with a sharp leading-edge, where the chord length varies from 8.4 mm at the blade root to 5.88 mm at the tip. The rotor is built from a liquid photopolymer resin by 3D printing. The rotor is mounted on a direct current (DC) motor manufactured by Maxon motors (model: DCX10L), which has a diameter of 10 mm (leading to a rotor to nacelle diameter ratio of 10.5) and length of 25 mm. The DC motor is controlled by a servo controller (model: ESCON 36/2 DC) via a digital encoder (model: ENX10).

The performance of the scaled-down turbine is first characterized and compared with the original turbine model. For this purpose, power and thrust measurements are made in a flat terrain. The power produced by the turbine P is measured by multiplying the shaft torque Q with the rotational speed Ω of the turbine. For more details on power measurements procedure, the reader is referred to Bastankhah and Porté-Agel (2017a). The power coefficient C_p is then calculated by the following relation:

$$C_p = \frac{P}{\frac{1}{2}\rho A \overline{u}_h^3} = \frac{Q\Omega}{\frac{1}{2}\rho A \overline{u}_h^3}, \tag{8.1}$$

where ρ is the air density, A is the rotor swept area and $\overline{u}_h$ is the mean streamwise velocity at the hub height. In order to measure the thrust force T, the turbine is mounted on a multi-axis strain gauge sensor (model: ATI-nano-17Ti). Similar to the power coefficient, the thrust coefficient C_T is calculated by:

$$C_T = \frac{T}{\frac{1}{2}\rho A \overline{u}_h^2}, \tag{8.2}$$

where T is the total thrust force measured by the strain gauge sensor. The averaged streamwise velocity at the hub height $\overline{u}_h$ (measured by a pitot static tube) is kept at 6.7 ms^{-1} for these measurements. The velocity $\overline{u}_h$ is chosen to establish a dynamic similarity in terms of the Reynolds number Re_d (based on $\overline{u}_h$ and rotor diameter d) between the original and scaled-down turbine models. For the original WiRE-01 turbine, the power and thrust coefficient data is obtained from Bastankhah and Porté-Agel (2016), which has approximately the same Re_d (~ 47000) as in the current experiments. Figure 8.1 shows the comparison of the power and thrust coefficients as a function of tip speed ratio λ between the scale-down and original turbine models. Here, it should be noted that the tip speed ratio is varied by varying the rotational speed of the turbine, while keeping the incoming velocity constant. Both turbines show very similar trends and values of the power and thrust coefficients. The maximum power coefficient is 0.34 and 0.35 for the scaled-down and original turbines, respectively, at a tip speed ratio of around 3.8. The thrust coefficient at λ corresponding to maximum C_p is about 0.8 and 0.82 for the scaled-down and original turbine models, respectively. This comparison shows that scaling down the turbine does not affect its performance characteristics. For subsequent measurements in the urban boundary layer, the turbine is operated at the λ corresponding to maximum C_p for each case.

A two-component frequency-shifted laser Doppler velocimetry (LDV) system developed by TSI is used to measure the streamwise and vertical velocity components in the flow. The LDV probe containing the transmitter and receiver optics is mounted on a 3 degrees-of-freedom (DOF) traversing system outside the test section of the wind tunnel. In order to increase the focal length of the transmitter, a beam expander is fitted in front of the LDV probe. The total focal length of the LDV transmitter is 2.29 m. The flow is seeded with olive oil droplets, which
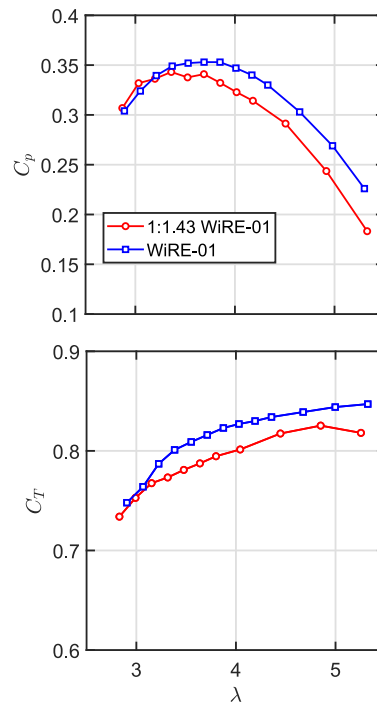
Figure 8.1: Comparison of the power (top) and thrust (bottom) coefficients as a function of tip speed ratio between the original and scaled-down turbine models.

have a diameter on the order of several micrometers. Flow seeding is done through a slot in the tunnel floor at the inlet of the test section. This ensures that the seeding method does not influence the flow in the test section, especially, around the building. Data is acquired using the FlowSizer-64 software (also developed by TSI). The velocity statistics are weighted by the transit time (also known as the gate time) of the tracer particles to compensate for high velocity bias, which occurs because the particles with higher velocity travel further and, thus, have a higher probability of getting sampled.

An idealized urban canopy model is set up inside the test section to simulate an urban boundary layer. The idea is to have a relatively taller building surrounded by a set of smaller ones. The small buildings are represented by square base prisms, with the base dimensions of 8 cm × 8 cm and height of 10 cm. The square base prisms are arranged in a staggered configuration, with a spanwise and streamwise spacing of two and four times their length, respectively. Similar arrangements have been used in the past to investigate flows within and above urban canopies. Castro et al. (2006) performed wind tunnel measurements using a staggered configuration of cubic blocks to understand urban boundary layer flows. Similarly, Cheng and Porté-Agel (2015) compared the staggered and aligned configurations of cubic arrays using large-eddy simulation to investigate the adjustment of boundary layer to urban surfaces. A picket fence of 2.5 m width with a total height of 13 cm, including saw-tooth shaped spikes of width and height equal to 3 cm, is also placed at the inlet of the test section to enhance turbulence production.

The taller buildings used for mounting a turbine are cube-shaped, with a height of 40 cm. This yields a ratio of 4 between the height of the tall building and surrounding urban canopy. The ratio between the building height and turbine hub height is 4.5, showing that the turbine is considerably smaller than the building it is placed on. Minor modifications to the roof edges inspired from roof shapes found in reality are made. Three different roof edge shapes are used, which are described in detail below:

1. Roof with sharp 90° edges (labeled: Cube).

2. Roof with a curved edge shape, where radius of curvature is 5% with respect to the building height (labeled: Round).

3. Roof with a solid boundary fence, where fence height is also 5% with respect to the building height (labeled: Fence).

A schematic representation of the experimental setup, along with a picture of the cubic buildings used for mounting the turbine, is shown in figure 8.2.

Measurements can be sub-divided into two parts: power measurements and velocity measurements. All measurements are performed with the turbine placed in the center of the building span. For power measurements, the turbine is placed at different streamwise locations to investigate the effect of its distance from the building leading edge on power performance. Once the streamwise position corresponding to maximum power is identified, that position is chosen to place the turbine for velocity measurements, which are carried out with and without the turbine. In the vertical direction, measurements are taken with a spatial resolution of 1 cm, which yields 10 points across the rotor. Above the building, measurements are taken until a height of $2d$; whereas behind the building, measurements are taken from $1d$ below the building height to $2d$ above it. This results in 21 and 33 measurement points in each vertical profile on and behind the building, respectively. Vertical profiles of mean and turbulence quantities at several representative streamwise locations are measured (8 in the base flow and 6 in the wake flow). In total, 204 measurements points for the base flow, and 162 measurement points for the wake flow are considered in each case, where 15000 instantaneous velocity samples are taken at each measurement point to ensure statistical convergence.

The turbulent boundary layer 1 m upstream of the cubic tall building is measured using LDV with a spatial resolution of 2 cm. Figure 8.3 shows the vertical profiles of the normalized averaged streamwise velocity, streamwise turbulence intensity and normalized averaged vertical momentum flux. In this figure, $z/d = 0$ represents the test section floor; whereas in the rest of the article, it represents the building roof. The streamwise velocity at the projected height of the turbine center on the building $z_{h,up} = 48.75$ cm in the upstream flow $\overline{u}_{h,up} = 6$ ms^{-1} is used for normalization in figure 8.3. The normalized averaged streamwise velocity shows higher shear closer to the surface and increases with height. A power law fit according to $\overline{u} = \overline{u}_{h,up}(\frac{z}{z_{h,up}})^n$ is also shown with a blue line in figure 8.3 (a). The shear exponent n of the
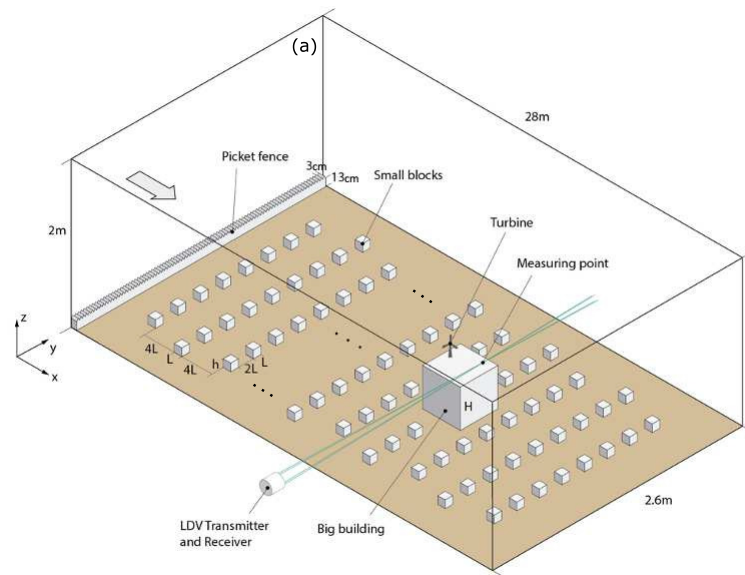
Figure 8.2: (a) Sketch of the experimental setup inside the test section; L = 8 cm, h = 10 cm and H = 40 cm. (b) A picture of the cubic tall buildings with modified roof edges.
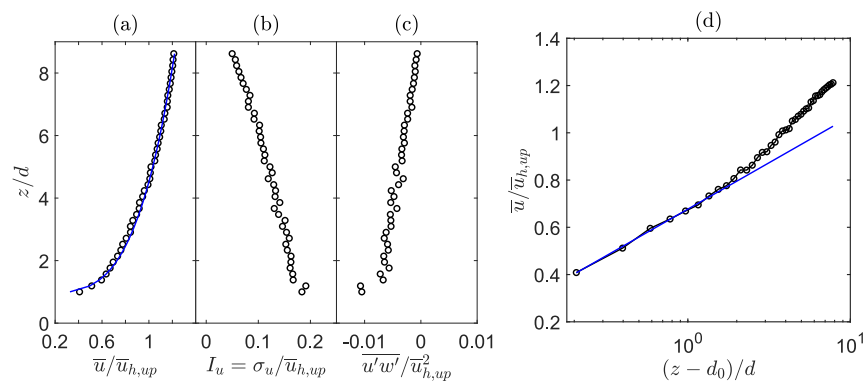
Figure 8.3: Vertical profiles of the normalized averaged streamwise velocity with power law fit in blue line (a), streamwise turbulence intensity (b) and normalized averaged vertical momentum flux (c). The normalized averaged streamwise velocity is also plotted in a semi-logarithmic scale with a logarithmic law fit in blue color (d).

power law fit is 0.26, which indicates high shear in the flow. The velocity at the maximum height of the boundary layer is 7.29 ms^{-1}. Due to the limitation of optical access, measurements above this height (i.e. 90.5 cm from the test section floor) cannot be taken. Therefore, the boundary layer height is assumed to be equal to 90.5 cm. This assumption is reasonable since the velocity only increases by 1.5% between $z/d = 8$ and $z/d = 8.6$. It is important to note that the boundary layer height is more than twice the height of the cubic building, which means that both the turbine and the building are fully immersed in the boundary layer. Considering that a logarithmic layer constitutes the lowest 10-15% of the boundary layer height, a logarithmic fit is done on the lowest 12.5% of the boundary layer. Following Stull (1988), the logarithmic fit is done using the following relation:

$$\overline{u} = \frac{u_*}{\kappa} ln\left(\frac{z - d_0}{z_0}\right),$$ (8.3)

where u_* is the friction velocity, κ is the von Karman constant taken as 0.41, z_0 is the aerodynamic roughness length, and d_0 is the displacement height. The displacement height is implemented to account for the effect of the urban canopy height on the development of the boundary layer. The normalized averaged streamwise velocity together with the logarithmic fit is shown in figure 8.3 (d). The values of friction velocity u_*, aerodynamic roughness length z_0, and displacement height d_0 obtained from the logarithmic fit are 0.41 ms^{-1}, 0.2 cm, and 8.34 cm, respectively. The streamwise turbulence intensity is around 0.2 at the bottom of the boundary layer and decreases almost linearly with height. The decrease in streamwise turbulence intensity with height is related to the decrease in the mean flow shear with height. At the projected height of the turbine center on the building, the streamwise turbulence intensity is 0.12 in the upstream boundary layer. The normalized averaged vertical momentum flux also shows highest values closer to the surface, due to high shear in the flow. Table 8.1 summarizes key flow parameters in the upstream boundary layer.

$\overline{u}_{h,up}$ (ms^{-1})	$\overline{u}_\infty$ (ms^{-1})	n	u_* (ms^{-1})	z_o (cm)	d_0 (cm)	δ (cm)
6	7.29	0.26	0.41	0.2	8.34	90.5

Table 8.1: Key flow parameters in the upstream boundary layer.

8.3 Results

8.3.1 Base Flow

We first investigate the flow development across the mid span of the building without the turbine, termed as the base flow. Figure 8.4 shows a comparison of the vertical profiles of the normalized averaged streamwise velocity in the base flow for different roof edge shapes. For the building with sharp 90° edges (named as 'Cube'), a region of high shear and reverse flow is observed near the building leading edge, close to the surface. With the increase in the

streamwise distance, the flow velocity close to the surface increases, along with the height of the high shear region. This is related to the growth of the shear layer that develops across the building roof due to the interaction of the separated flow closer to the surface and the free flow away from the surface. Immediately behind the building at $x/d = 4.5$, there is a sharp transition between the flow under the building height and that above it. This is due to the wake of the building, which has not mixed with the flow above at the given streamwise location. With the increase in the streamwise distance, the building wake grows and mixes with the flow above it, leading to a smoother velocity profile.

For the curved roof shape (named as 'Round'), rounding the roof edges leads to higher velocity and lesser shear across the building roof compared to the Cube case. This is because rounding the roof edges leads to a reduction in the adverse pressure gradient induced by the building, and no flow separation is observed in this case. Behind the building, an even stronger transition between the flow under the building height and that above it is observed compared to the Cube case.

The addition of the solid boundary fence ('Fence' case) results in a stronger separation, with the position of maximum shear located higher than that for the Cube case, which is likely caused by the blockage induced by the boundary fence. Across the building, the Fence case shows highest shear and lowest velocity compared to the rest of the cases. Behind the building, the Fence case also shows highest shear and lowest velocity compared to the other cases, where the differences between different cases reduce with the increase in the downstream distance. It is to be noted that, from here on, $x/d = 0$ represents the building leading edge and $z/d = 0$ represents the building roof surface. The averaged hub height streamwise velocity at the turbine position on the building $\overline{u}_h$ in each respective case is used to normalize all the flow quantities. The choice of the turbine position on the building will be discussed later in section 8.3.2. The normalization velocity $\overline{u}_h$ is 6.5 ms^{-1}, 6.54 ms^{-1} and 6.38 ms^{-1} for Cube, Round and Fence cases, respectively.

Figure 8.5 shows the development of the normalized averaged vertical velocity for the three cases. As can be seen, high vertical velocity values are observed closer to the building leading edge. As expected, the Fence case shows highest vertical velocity, with the values decreasing gradually for the Cube and Round cases. For streamwise positions $x/d \geq 2.5$, the vertical velocity is very close to zero above the building height for all cases. Below the building height, positive and negative velocities are observed at $x/d = 4.5$ and $x/d = 6.5$, respectively. This can be related to the flow recirculation that develops behind the building. A turbine would experience high vertical velocity across the rotor if it is located close to the leading edge of the building, and the vertical velocity magnitude would be highest in the Fence case and lowest in the Round case.

In order to characterize the evolution of turbulence across the building, we compute the streamwise turbulence intensity $I_u = \frac{\sigma_u}{\overline{u}_h}$, where σ_u is the standard deviation of the streamwise velocity. Figure 8.6 shows a comparison of the streamwise turbulence intensity between the
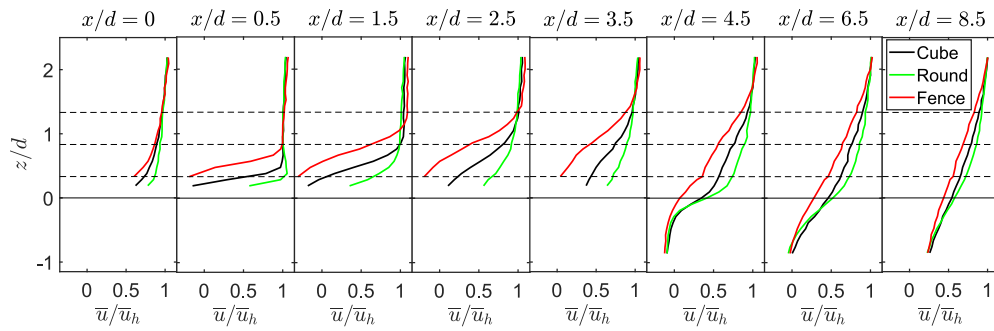
Figure 8.4: Vertical profiles of the normalized averaged streamwise velocity in the base flow across the building. The horizontal black solid line traces the height of the building, whereas the black dashed lines trace the prospective rotor bottom tip, hub and top tip locations.

three building cases. High streamwise turbulence intensity values are observed for all cases, where values close to 0.1 are observed in the free stream flow for all cases. The streamwise turbulence intensity is highest in the shear layer developed from the roof leading edge. Peak streamwise turbulence intensity values of around 0.45 are observed for the Fence case at $x/d = 1.5, 2.5$, and for the Cube case at $x/d = 1.5$. The streamwise turbulence intensity showed highest values and stronger variation in the vertical direction for the Fence case, and lowest values for the Round case, with the Cube case showing values somewhere in between. The trends observed in the evolution of streamwise turbulence intensity are consistent with the shear observed in the mean flow, as higher shear in the Fence case would lead to higher turbulence production compared to the other cases.

The vertical position of the maximum streamwise turbulence intensity also changes with the roof shape. Following Kiya and Sasaki (1983), the peak location of the streamwise turbulence intensity can be used to characterize the center of the shear layer that grows from the building roof edge. Figure 8.7 shows the growth of the shear layer center for different roof shapes. The shear layer center initially moves vertically up with streamwise distance from the leading edge, but reaches an almost constant value for each case, which is consistent with the observations of Kiya and Sasaki (1983). The center of the shear layer is observed to be highest for the Fence case, coinciding with the turbine hub height at $x/d > 1.5$. For the Round case, it is below the turbine bottom tip height for all locations, except the last one; whereas it is slightly above the bottom tip height for the Cube case. The vertical position of the shear layer center with respect to the rotor is important, as it determines the turbulence profile experienced by the turbine and can have an effect on the fatigue loads on the rotor.

8.3.2   Power Performance

We now focus on the power extracted by the turbine from the base flow. More specifically, we want to understand how the power production is affected by the turbine position on the building, as well as by the roof edge shape. For this purpose, we first plot the maximum
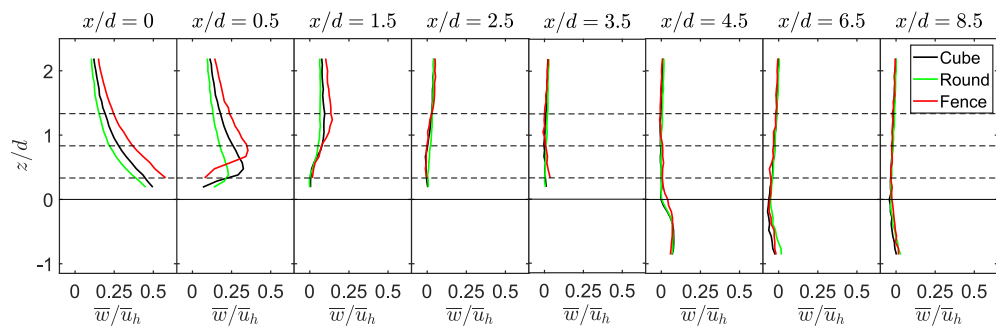
Figure 8.5: Vertical profiles of the normalized averaged vertical velocity in the base flow across the building. The horizontal black solid line traces the height of the building, whereas the black dashed lines trace the prospective rotor bottom tip, hub and top tip locations.

Figure 8.6: Vertical profiles of the streamwise turbulence intensity in the base flow across the building. The horizontal black solid line traces the height of the building, whereas the black dashed lines trace the prospective rotor bottom tip, hub and top tip locations.

171
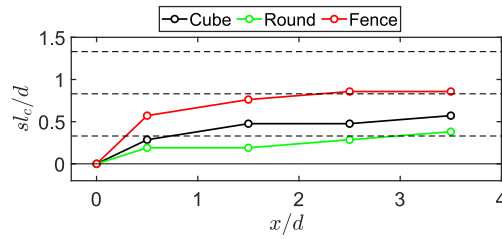
Figure 8.7: Growth of the shear layer center as a function of downstream distance. The horizontal black solid line traces the height of the building, whereas the black dashed lines trace the prospective rotor bottom tip, hub and top tip locations.

mean power produced by the turbine at different streamwise positions for the three cases in figure 8.8(a). The Cube case shows highest power production among all cases at a streamwise position of $x/d = 0.5$, with the maximum mean power dropping for $x/d > 0.5$, where values less than half compared to the peak are observed at $x/d \geq 2.5$. Adding a solid boundary fence leads to not only a decrease in the maximum mean power, but also to a higher variability in the maximum mean power with the streamwise position. Mean power values of approximately 10% compared to the peak value are observed at $x/d \geq 2.5$. Rounding the roof edges leads to a slightly lower peak value compared to the Cube case at $x/d = 0.5$, but it shows the least amount of variation in power with the streamwise position among all the cases. As the wind direction can change in the real world, the variation in mean power production with streamwise distance from the building leading edge is important, and roof shapes with least amount of variability should be preferred for urban wind energy installation.

Another important factor in consideration to the power performance of a turbine is the fluctuations in power. Figure 8.8(b) shows the standard deviation in power production normalized by maximum mean power extracted by the turbine at a certain position. Closer to the roof leading edge, all cases show similar values of normalized standard deviation in power of around 0.3, which in itself is a high number and can be attributed to high turbulence in the upstream boundary layer. Cube and Round cases initially show comparable values closer to the roof edge, where the difference between the two grows for $x/d > 1$. The Fence case, on the other hand, shows a significant increase in normalized standard deviation, with the values reaching as high as 1.29 at $x/d = 3$. In addition to the flow separation from the roof leading edge, the poor performance of the turbine on the back end of the roof in the Fence case can also be related to the additional blockage caused by the fence at the back end of the building.

To understand the effect of the turbine rotational speed on the power production, figure 8.9 shows the power production of the turbine at two different streamwise positions for different roof shapes. These positions correspond to the maximum and minimum values of P_{max} across the streamwise extent of the building, as observed in figure 8.8(a). The range of the turbine rotational speed differs in different cases to ensure that the tip speed ratio remains the same. Similar to the trend of power coefficient seen in figure 8.1 for flat terrain, the extracted power for a certain case first increases with the increase in rotor speed before
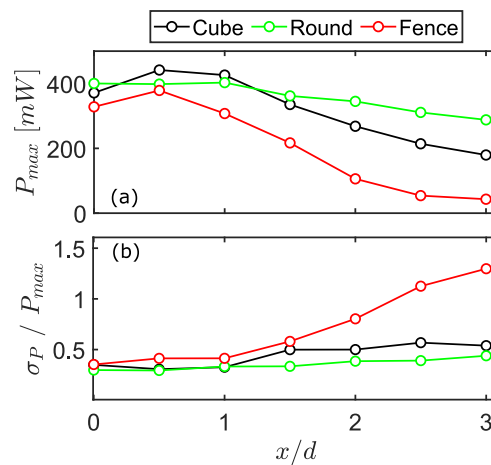
Figure 8.8: (a) Maximum mean power produced by the turbine and (b) normalized standard deviation in power as a function of streamwise distance.

reaching a maximum value beyond which, a decrease in power is observed with an increase in the rotational speed. The effect of roof shape is observed for the whole range of rotational speed, where the difference in power between different cases is smaller at $x/d = 0.5$, but grows significantly at $x/d = 3$.

To explain the variation in power production with the turbine position and roof edge shape, we plot the vertical profiles of averaged streamwise velocity and its standard deviation for several streamwise positions in figure 8.10. Power available for a turbine scales with the cube of velocity, therefore higher velocity across the rotor would mean that more power is available for the turbine. As can be seen in figure 8.10, at $x/d = 0.5$ the Cube and Round shape cases show similar velocity profiles, whereas the Fence case shows high shear in the bottom half of the rotor. For each case, this is the streamwise location where maximum velocity is observed across the rotor, thereby resulting in maximum power produced by the turbine. The relatively
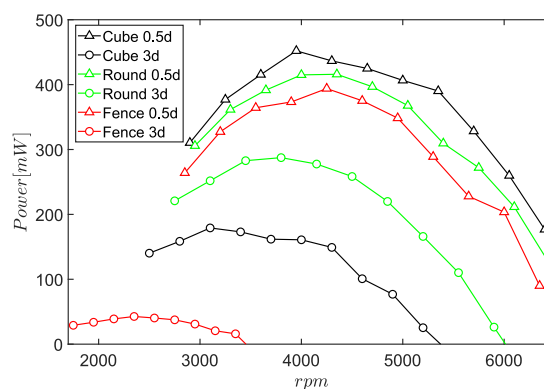
Figure 8.9: Mean power produced by the turbine as a function of turbine rotational speed for different streamwise positions.
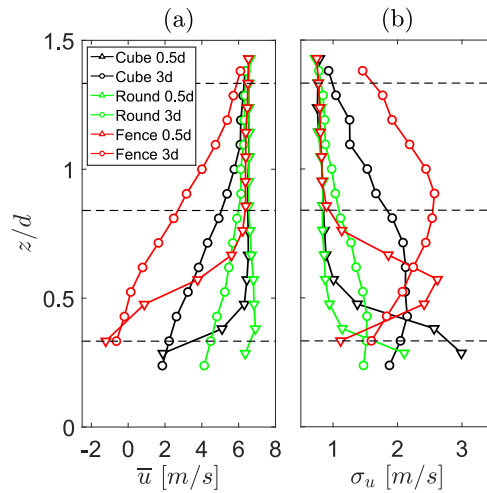
Figure 8.10: (a) Vertical profiles of averaged streamwise velocity and (b) standard deviation of streamwise velocity across the rotor for different streamwise positions. The dashed horizontal lines trace the rotor bottom tip, hub and top tip locations.

lower velocity encountered across the rotor at $x/d = 3$ results in the low power production obtained at this location, where the Fence case shows lowest values across the whole rotor compared to the other cases. The differences between the velocity profiles at 0.5 and 3 rotor diameters for each case appear to be consistent with the differences in the power production observed between these positions. For the fluctuations in power observed in figure 8.8(b), the standard deviation in the streamwise velocity profiles provides useful insights. Highest standard deviation values across the rotor, with a peak around the turbine hub height are observed for the Fence case at $x/d = 3$, which is consistent with the highest fluctuations in power observed at this location. The peak value of standard deviation at $x/d = 0.5$ is similar to that at $x/d = 3$ for the Fence case, although the location of peak is in the lower half of the rotor, with relatively smaller values in the upper half of the rotor, thereby resulting in lesser fluctuations in power. The Round case shows smaller standard deviation values compared to the other cases, which explains lower power fluctuations in this case. The Cube case shows standard deviation higher than the Round case, but smaller than the Fence one, resulting in power fluctuations more comparable to the Round case than the Fence one.

The dependency of the power produced by the turbine on its streamwise position, as well as on the roof edge shape is clearly shown. Building with curved roof edges is found to perform best and in a practical scenario, such building should be preferred for wind turbine siting. For the wake flow analysis in the following section, the turbine is placed at the streamwise position of $x/d = 0.5$, as it performs best in terms of power at this streamwise position. This is in accordance with how a turbine siting would be done in reality, where turbines are commonly placed at positions corresponding to the highest available resources.

Figure 8.11: Vertical profiles of the normalized averaged streamwise velocity in the turbine wake across the building. The base flow profiles are added for reference. The horizontal black solid line traces the height of the building, whereas the horizontal black dashed lines trace the prospective rotor bottom tip, hub and top tip locations.

8.3.3 Wake Flow

We now investigate the wake of the turbine; specifically, we are interested in the comparison of the turbine wake for different roof edge shapes. Figure 8.11 shows vertical profiles of the normalized averaged streamwise velocity in the turbine wake for different roof shapes. The profiles of normalized averaged streamwise velocity in the base flow are also included as a reference in this figure. The normalized averaged streamwise velocity in the wake is found to be highly dependent on the roof shape, where its magnitude is highest for the Round case and lowest for the Fence case. The symmetry of the velocity profile, especially on top of the building, is also observed to be affected by the roof shape, with relatively more symmetric profiles for the Round case. For the Cube and Fence cases, the profiles become asymmetric, with the Fence case showing highest asymmetry. Both the magnitude of the velocity and symmetry of the velocity profiles in the wake are consistent with the base flow velocity profiles, which showed least (highest) shear and highest (lowest) velocity for the round (Fence) case. The Fence case is particularly interesting, as it shows negative velocities in the wake below the hub height on top of the building. This can be related to the relatively strong flow separation from the leading edge, as well as to the blockage and formation of a vortex in front of the back fence on the building. Behind the building, an enhanced expansion of the wake is observed, where the velocity differences between different cases follow the same trend as that on the building. Below the building height, the differences between the turbine wake and base flow increase with the increase in the distance, which could be associated with the downward trajectory of the turbine wake and its interaction with the building wake.

To quantify the differences in the wake flow with respect to the base flow, we compute the streamwise velocity deficit $\Delta \overline{u} = \overline{u}_b - \overline{u}_w$, where $\overline{u}_b$ and $\overline{u}_w$ are the averaged streamwise velocities in the base and wake flow, respectively, at the same physical location. Figure 8.12 shows the comparison of vertical profiles of the normalized averaged streamwise velocity deficit between different cases. Compared to the streamwise velocity profiles, the streamwise
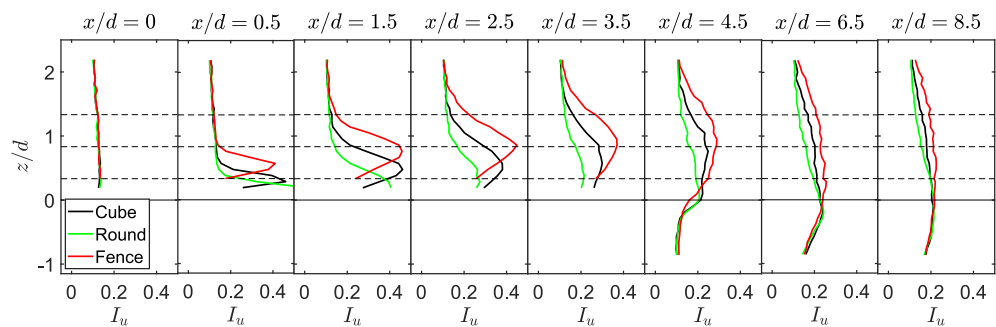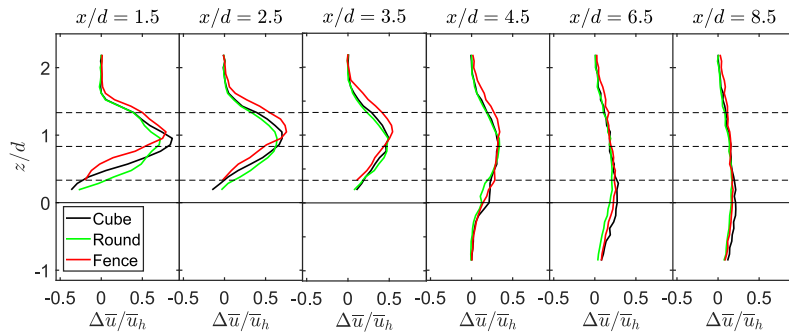
Figure 8.12: Vertical profiles of the normalized averaged streamwise velocity deficit in the turbine wake across the building. The horizontal black solid line traces the height of the building, whereas the horizontal black dashed lines trace the prospective rotor bottom tip, hub and top tip locations.
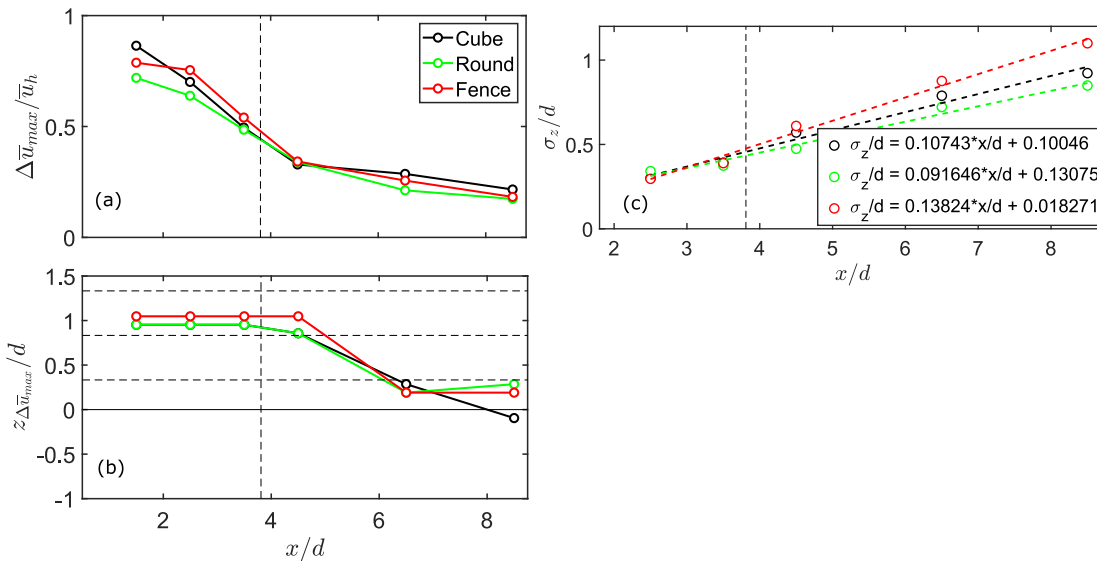

Figure 8.13: (a) Maximum normalized velocity deficit, (b) vertical position of the maximum velocity deficit and (c) normalized standard deviation of the streamwise velocity deficit as a function of downstream distance. The horizontal black solid line in (b) traces the height of the building, whereas the black horizontal dashed lines trace the rotor bottom tip, hub and top tip locations. The vertical dashed black line marks the end of the building.

velocity deficit profiles show less difference between different cases. On top of the building the profiles appear to be fairly symmetric for all cases, whereas behind the building they show a relatively wider profile. A region of negative streamwise velocity deficit is observed close to the building leading edge for all cases. This is a result of flow speed up near the surface, as the turbine hinders the development of the separated flow from the building leading edge. To further characterize the streamwise wake velocity deficit, we plot the normalized maximum wake velocity deficit, the vertical position of the maximum wake velocity deficit and the normalized wake width as a function of downstream distance in figure 8.13.

The normalized maximum velocity deficit is used to characterize the recovery of the turbine wake center (figure 8.13 (a)). On top of the building, the normalized maximum velocity deficit is observed to be highest for the Fence case, with values decreasing for the Cube and Round case, respectively. As discussed by Dar and Porté-Agel (2022b), the normalized maximum velocity deficit is affected by the pressure gradient induced by the topography. Here the Fence case induces the highest pressure gradient on the wake, resulting in the highest value of the wake velocity deficit. The recovery of the velocity deficit is observed to be remarkably fast on top of the building, which could be related to the high turbulence intensity in the base flow. Behind the building, however, the recovery of the wake center slows down significantly for all cases. This can be related to the fact that, as the wake undergoes enhanced expansion due to the sudden absence of a surface, the recovery of the maximum velocity deficit has to slow down in order to conserve momentum.

To characterize the trajectory of the wake, we plot the normalized vertical position of the maximum velocity deficit (also called the wake center) in figure 8.13 (b). On top of the building, the wake center is observed to be above the hub height of the turbine for all cases, which can be related to the high vertical velocity experienced by the turbine in the base flow. The wake trajectory is also observed to be almost constant for all cases above the building. The Round and Cube cases show very similar wake trajectory above the building, whereas the Fence case shows a slightly higher location of the wake center compared to the rest. The presence of the fence above the building roof results in a high vertical velocity, which can explain the upward shift in the wake trajectory in this case. Behind the building the wake center moves down for all the cases, which indicates toward a downward movement of the turbine wake.

As the turbine wake moves downstream, it undergoes an expansion due to the shear layer developed from the rotor edge, which plays a role in the transport of energy in the wake from the outer flow. Wind turbine wakes are known to expand linearly as a function of downstream distance in the far wake in flat, as well as complex terrain (Dar and Porté-Agel, 2022b; Porté-Agel et al., 2020). As a result, the wake growth rate k in the far wake can be estimated by the slope of a linear fit to the wake width such that:

$$\frac{\sigma_z}{d} = k\frac{x}{d} + \epsilon, \tag{8.4}$$

where σ_z is the wake width estimated by the standard deviation of a Gaussian curve fitted to the vertical profile of the streamwise velocity deficit at each downstream position and ϵ is the initial wake width. Figure 8.13 (c) shows the normalized wake width as a function of downstream distance, along with the linear fit according to equation 8.4 for the three cases. The wake growth rate is found to be highest for the Fence case, and decreases for the Cube and Round cases. It is also found to be significantly higher than the values typically reported in flat terrain (see, e.g. Cheng and Porté-Agel, 2018) or those reported for a turbine sited on escarpments (Dar and Porté-Agel, 2022b). This is consistent with the relatively high streamwise turbulence intensity across the building compared to the flat terrain or escarpment studies. In

addition, the sharp changes in the streamwise pressure gradient induced by the building could also play a role in different rate of expansion compared to flat terrain. The streamwise velocity deficit profiles are found to be Gaussian at $x/d = 2.5$ for all cases. This indicates that the near wake length is shorter than 2 rotor diameters, which is consistent with the high turbulence intensity in the base flow, as higher turbulence usually leads to a shorter near wake length.

Focusing on turbulence characteristics in the wake, we first plot the normalized averaged vertical momentum flux in figure 8.14. The vertical momentum flux is a key factor in determining the exchange of momentum between outer and wake flow, and plays a role in production of turbulence together with the mean flow shear. In the near wake ($x/d = 1.5$), all three cases show similar values of normalized averaged vertical momentum flux. However, in the far wake, the Fence case shows significantly higher values than the rest of the cases, with a peak around the rotor top tip height at $x/d = 3.5$. In previous studies on flat (Bastankhah and Porté-Agel, 2017c) and complex terrain (Dar and Porté-Agel, 2022b), the vertical momentum flux is observed to be negative in the upper half of the rotor and positive in the lower half, especially for downstream distances shorter than 8 rotor diameters. In the current study, only the Round case depicts the behavior described above, whereas the Cube and Fence cases show predominantly a negative vertical momentum flux across the whole rotor, with relatively smaller values in the lower half of the rotor. Relatively high vertical momentum flux in the shear layer developed from the building leading edge in the base flow is believed to play a role in the above described behavior. The fact that the peak of the vertical momentum flux in the base flow on top of the building is located closer to the surface and found to be significantly higher than that in the wake flow helps explain the observed trend. Behind the building, the vertical momentum flux in the turbine wake is found to be comparable to that in the base flow, with slightly higher values in the turbine wake than the base flow.

The streamwise turbulence intensity in the turbine wake is shown in figure 8.15. Consistent with the vertical momentum flux, the streamwise turbulence intensity is observed to be highest in the Fence case, with values decreasing for the Cube and Round case. On top of the building, the streamwise turbulence intensity shows a peak around the rotor top tip height. Wu and Porté-Agel (2012) performed a kinetic energy budget analysis to show that even though momentum fluxes are high across the whole rotor projected area, the peak in turbulence intensity at the rotor top tip height appears due to high mean flow shear around that height. A similar reasoning can be used here to explain the peak around the rotor top tip height. In addition, the peak value of streamwise turbulence intensity in the wake is observed to be smaller than that in the base flow. This will be discussed in detail below. Behind the building, the streamwise turbulence intensity profile flattens out, mainly because the mean flow shear becomes almost constant (see figure 8.11).

The streamwise turbulence intensity in the turbine wake is contributed by two sources: the one in the base flow and the one added or subtracted by the turbine. To quantify the streamwise turbulence intensity contributed by the turbine, we compute the added streamwise turbulence intensity I_{add}:
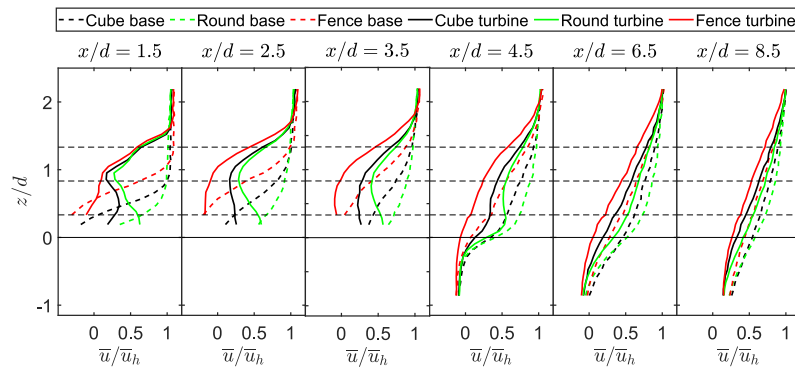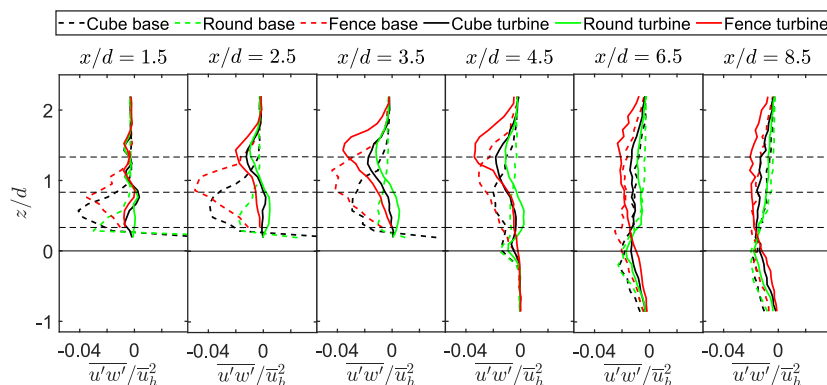
Figure 8.14: Vertical profiles of the normalized averaged vertical momentum flux in the turbine wake across the building. The base flow profiles are added for reference. The horizontal black solid line traces the height of the building, whereas the horizontal black dashed lines trace the prospective rotor bottom tip, hub and top tip locations.
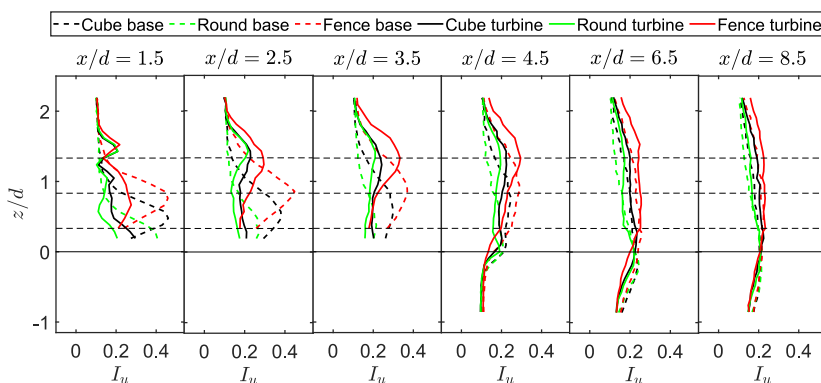

Figure 8.15: Vertical profiles of the normalized averaged streamwise turbulence intensity in the turbine wake across the building. The base flow profiles are added for reference. The horizontal black solid line traces the height of the building, whereas the horizontal black dashed lines trace the prospective rotor bottom tip, hub and top tip locations.

$$I_{add} = \begin{cases} +\sqrt{I_{u,w}^2 - I_{u,b}^2}, & I_{u,w} \geq I_{u,b}, \\ -\sqrt{I_{u,b}^2 - I_{u,w}^2}, & I_{u,w} < I_{u,b}, \end{cases}$$

where $I_{u,w}$ and $I_{u,b}$ are the streamwise turbulence intensities in the turbine wake and base flow, respectively. Figure 8.16 shows the vertical profiles of the added streamwise turbulence intensity. The peak of the positive added streamwise turbulence intensity around the rotor top tip is found to be the same in all three cases. This indicates that the difference in the peak of streamwise turbulence intensity between different cases in the turbine wake comes from the difference in the base flow turbulence intensity, whereas the turbine contribution remains constant.

179
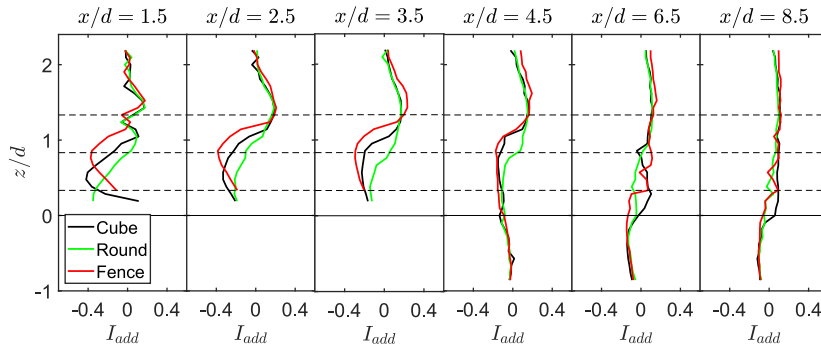
Figure 8.16: Vertical profiles of the added streamwise turbulence intensity in the turbine wake across the building. The horizontal black solid line traces the height of the building, whereas the horizontal black dashed lines trace the prospective rotor bottom tip, hub and top tip locations.

A region of negative added streamwise turbulence intensity above the building is observed in all cases. The negative added streamwise turbulence intensity means that the turbine suppresses turbulence in the wake compared to that in the base flow. Dar and Porté-Agel (2022b) explained that this negative added streamwise turbulence intensity appears because the turbine suppresses the development of the shear layer from the escarpment (in the current work, the building) leading edge in its wake. As the mean flow shear in the turbine wake close to the surface is lower than that in the base flow, the turbulence production is suppressed. While the positive added streamwise turbulence intensity is insensitive to the roof shape, the negative added streamwise turbulence intensity depends on the roof shape. The Fence case shows highest suppression of the streamwise turbulence intensity. In the Fence case, apart from the region around the rotor top tip, the profile is predominantly negative, with the magnitude of the peak value higher than that for the positive added streamwise turbulence intensity. The peak position and magnitude of the negative added streamwise turbulence intensity decrease for the Cube case, which further decrease for the Round case. Behind the building, all three cases show similar profiles, with approximately constant values at $x/d \geq 6.5$.

8.4   Summary

In this study, we performed wind tunnel experiments on a roof-mounted horizontal-axis wind turbine placed in an urban environment. Of particular interest was the effect of roof edge shape on power performance and wake characteristics of a turbine sited on top of a tall cubic building. In addition, the effect of streamwise position of the turbine on its power performance was also investigated. The roof edge shapes were inspired from the ones observed in reality: a roof with sharp 90° edges (Cube case), a roof with slightly curved roof edges (Round case) and a roof with a solid boundary fence (Fence case). The modifications in the roof edge shapes could easily be deemed minor in a conventional resource assessment study, however, our results showed that such small modifications can significantly affect both the power performance

and the wake of a turbine sited on top of the building.

The flow velocity, shear and streamwise turbulence intensity in the base flow were observed to be highly dependent on the roof edge shape. This was related to the growth of the shear layer due to flow separation from the building leading edge. This shear layer was found to be strongest in the Fence case, followed by the Cube and Round cases, respectively. As a result, the power available for a turbine was also dependent on the roof edge shape. All cases showed maximum mean power production at a streamwise distance of about half rotor diameter from the leading edge of the building. The Round case showed least variation in the maximum mean power production with the streamwise position and least amount of normalized standard deviation in power production. For the Cube case, maximum mean power production decreased after $x/d = 0.5$, where an increase in the normalized standard deviation was also observed. The Fence case showed highest drop in maximum mean power production, with values reaching approximately 10% at the back end of the building compared to those at the front end. The normalized standard deviation in power was also observed to be highest at the back end of the building for the Fence case, with values greater than 1 at $x/d \geq 2.5$.

For wake flow measurements, the turbine was placed at $x/d = 0.5$, as it corresponded to the position with highest power production. For all cases, the wake characteristics on top of the building and those behind the building showed significant differences, which were related to the sudden absence of a surface after the building edge. On top of the building, the normalized averaged streamwise velocity profiles in the wake showed differences between different cases, with higher velocity and relatively symmetric profiles for the Round case. The wake velocity was observed to be smaller and have more asymmetric profiles for the Cube and Fence cases, which was related to the separation induced by the leading edge in the base flow. The Fence case showed the highest normalized streamwise velocity deficit above the building, with values decreasing for the Cube and Round case, respectively. The recovery of the wake center velocity deficit was found to be faster on top of the building, whereas it slowed down behind the building due to the sudden expansion of the wake. The wake growth rate was found to be highest in the Fence case, with values decreasing for the Cube and Round cases. The wake growth rate was also observed to be higher than the values typically reported in flat or complex terrain, which was associated with high base flow turbulence intensity across the building. The Fence case also showed relatively higher turbulence in the wake compared to the rest of the cases, whereas the turbulence added by the turbine was found to be the same around the rotor top tip height in all cases. The turbine also suppressed the turbulence production near the surface, as it suppressed the growth of the shear layer due to flow separation from the building leading edge. This negative added turbulence was found to be dependent on the case with the highest magnitude in the Fence case and lowest in the Round case.

In conclusion, the sensitivity of both the power production and wake characteristics to the roof edge shape is clearly shown. Ideally, building shapes with least variation in power with position should be chosen to account for wind direction changes. The flow separation and

shear layer development from the building edge are found to be the differentiating factors for the power and wake characteristics of a turbine. For the numerical modeling and resource assessment community, these results emphasize the importance of accurate building modeling, as seemingly minor differences in the roof edge shape can result in huge differences in the estimation of power production and wake effects of a roof mounted turbine.

9 Effect of roof fence shape on flow over a building and its impact on wind turbine performance[I] [II]

Abstract

We investigate the effect of roof boundary fence shape on the flow over a cubic building and on the power and thrust performance of a roof-mounted wind turbine via wind-tunnel experiments. The effect of fence height, porosity, angle, and curvature is investigated, with the turbine placed at several streamwise positions along the mid-span of the building. For the flow without the turbine, the flow separation and shear layer growth from the roof leading edge are significantly affected by the fence shape. Vertical fences result in a decrease in the mean power and thrust with the increase in the fence height and streamwise distance from the roof leading edge. Increasing the fence porosity improves the turbine performance for streamwise distance greater than one rotor diameter. Inward-angled fences improved the turbine performance, with the 60° inward angle leading to a power performance similar to a case with no fence. Rounding the fence outward also led to a smoother flow, which resulted in higher mean power and thrust compared to inward-curved fences. The power and thrust coefficients were computed using rotor equivalent and hub height velocity magnitude as reference velocity, where the former one yielded physically feasible results for all the cases.

[I]The contents of this chapter are to be submitted for publication.

[II]Author contributions: A.S.D., F.W. and F.P-A. conceived the research plan, A.S.D. led the experimental campaign with assistance from F.W. A.S.D., F.W. and F.P-A. laid out the plan for formal analysis. F.W. and A.S.D. analyzed the experimental data. The manuscript was written by A.S.D. with input from F.P-A. and F.W.

9.1 Introduction

Wind energy has emerged as a major player in the transition towards renewable energy sources. Approximately 7.6% of the global electricity was generated by wind energy in 2022 (EMBER, 2023), with its contribution expected to grow in the coming years. While wind farms are typically installed in remote areas, wind resources in urban environments offer the potential for electricity generation using small-scale wind turbines (Rezaeiha et al., 2020). Some of the benefits associated with urban wind energy are the generation of electricity closer to the consumer, which significantly reduces transportation costs and transmission losses, and the contribution towards the development of sustainable cities. High-rise buildings offer ideal locations for wind turbine installation due to high wind resources on rooftops. The variability of wind resources due to urban morphology, high turbulence levels in urban flows, and public acceptance are some of the challenges in the development of urban wind energy (Micallef and Van Bussel, 2018; Toja-Silva et al., 2013).

The impact of building shape or urban morphology on available wind resources for roof-mounted wind turbines has been investigated in several studies. Ledo et al. (2011) compared flow over flat, pitched, and pyramidial roofs. They concluded that flat roofs offered the best wind conditions for wind turbine installation. Abohela et al. (2013) investigated the effect of roof shape and wind direction on available power for a roof-mounted wind turbine. They showed that, for each roof shape, the optimal position of the turbine is different, and vaulted roofs offer the highest potential for wind energy production. Yang et al. (2016) performed a combined field and simulation study to investigate wind resources in a real urban site. They showed that surrounding high-rise buildings can have a blockage effect on a potential site, and rounding the building edges can result in higher available power. Toja-Silva et al. (2015) investigated the effect of different roof shapes and roof edge shapes on wind energy potential. They showed that curved roof shapes such as vaulted or spherical ones and curved edge shapes are favorable for wind energy deployment. Toja-Silva et al. (2016) developed a tool for optimizing building and roof geometry for wind energy exploitation. Using this tool they showed that cylindrical buildings with a spherical roof offer highest available wind resources. Zhou et al. (2017) showed that a composite prism diffuser geometry is ideal for wind energy installation in low-rise buildings. Juan et al. (2021) investigated the effect of urban morphology on wind energy potential on high-rise buildings. They showed that reducing plan area density can reduce turbulence levels and rounded building corners improved power density. In addition, they showed that staggered building layouts offered low wind energy potential compared to aligned layouts. In another study, Juan et al. (2022) showed that for building layout of 2×2, a smaller spanwise gap between buildings offered higher wind potential between upstream buildings and a larger gap showed high available power between downstream buildings. Comparing different turbine types, they showed that horizontal axis wind turbines outperformed vertical axis ones.

Several studies have also explored the performance of wind turbines in urban environments. Kooiman and Tullis (2010) investigated the performance of a vertical axis wind turbine in an

urban environment and concluded that the turbine performance was affected for turbulence intensity above 15%. Pagnini et al. (2015) compared the performance of horizontal and vertical axis wind turbines in an urban environment. They showed that the horizontal axis wind turbine produced higher power but was more susceptible to wind gusts and wind direction changes compared to the vertical axis one. They also observed that the power curves of both turbines were below the reference power curves provided by the manufacturer. Cooney et al. (2017) tested the performance of a large-scale horizontal axis wind turbine in an urban environment. They observed that the measured power curve correlated well with the one provided by the manufacturer. This correlation can in part be due to the scale of the turbine compared to that of the surrounding buildings. Longo et al. (2020) carried out numerical simulations to study the effect of surrounding buildings on the performance of a vertical axis wind turbine. They concluded that the turbine's performance can be severely affected by surrounding buildings, and careful investigations must be performed to assess the feasibility of installing wind turbines in urban environments. Pellegrini et al. (2021) investigated the performance of a small-scale horizontal axis wind turbine in an urban environment, and showed that the project was not economically feasible. Most of these studies are field or simulation based, with turbines located in complex urban environments. There is currently a need to isolate the effects of certain parameters on the performance of wind turbines sited on buildings. To this end, some wind-tunnel studies have been performed on roof-mounted wind turbines recently. Jooss et al. (2022a) conducted an experimental study on a vertical axis wind turbine sited on several locations on two aligned cubic buildings. They showed that the turbine had a significant impact on the flow over the buildings, which eventually affected its own power performance as well. In a separate study, Jooss et al. (2022b) studied the effect of turbine position and wind direction on the power curve of a vertical axis wind turbine. For the sake of simplicity, they chose the streamwise velocity upstream of the building as a reference for computing the power coefficient. They showed that the maximum power coefficient is significantly affected by the turbine position and wind direction, where a gain of up to 41.1 % and a loss of up to 87.5 % was observed for certain wind directions and turbine positions.

Dar et al. (2022) performed a wind-tunnel study on a roof-mounted horizontal axis wind turbine. By changing the roof edge shapes between a sharp edge, a rounded edge and an edge with a boundary fence, they showed that the turbine performance and wake characteristics are affected by the roof edge shapes. The turbine on the building with boundary fence showed worst performance, both in terms of mean power and power fluctuations. However, boundary fences are integral to the buildings from a safety perspective. Due to their significance, some recent studies have explored their effect on the flow over a building. Zou et al. (2021) performed wind tunnel experiments to investigate the effect of a building with a boundary wall on the incoming flow. They showed that the flow close to the surface of the building was significantly affected by the boundary wall, whereas the effect of the building on the flow decreased with the increase in the measurement height. More recently, Dai et al. (2022) showed that the effect of boundary fence height on flow over a building depends on the location on the roof and wind direction.

For the success of roof-mounted wind turbines, it is important to understand how boundary fences affect the flow over a building, and what impact they can have on the performance of a wind turbine. It is also of interest to identify fence shapes that can benefit wind turbine performance while preserving the safety feature of the fence. In this study, wind tunnel experiments are performed, where a horizontal axis wind turbine is mounted on top of a cubic building. We investigate a variety of boundary fence geometries to quantify the impact of different fence shapes on turbine performance characteristics, and to identify optimal fence shapes. The effect of several fence characteristics such as height, porosity, curvature and angle is investigated. The rest of the article is organized as follows: section 9.2 provides details of the experimental setup, building and fence geometries, wind turbine, and measurement techniques; results from the study are presented and discussed in section 9.3; and section 9.4 provides some concluding remarks.

9.2 Experimental Setup

The experiments are performed in the closed-loop boundary layer wind tunnel at the WiRE laboratory of EPFL. The wind tunnel has a test section of 28 m length, 2 m height and 2.6 m width. A 130 kW fan drives the flow in the wind tunnel and a contraction of 5:1 area ratio is present at the inlet of the test section. A three-bladed horizontal axis wind turbine model is used in the experiments. The turbine model is the same as the one used by Dar et al. (2022). It is a scaled-down version of the WiRE-01 turbine model, where the scaling ratio between the scaled-down and original rotor is 1:1.43. The hub height z_h and rotor diameter d are 8.75 cm and 10.5 cm, respectively. The rotor is manufactured by additive manufacturing using a liquid photopolymer resin. The rotor is mounted on a direct current motor (model: DCX10L) to measure the power extracted by it. The motor is controlled by a servo controller (model model: ESCON 36/2 DC). The details on the rotor geometry can be found in Bastankhah and Porté-Agel (2017a).

Flow measurements on the roof of the cubic building are performed using a two-dimensional two-component (2D2C) particle-image velocimetry (PIV) system. The measurements are performed in a vertical plane passing through the middle of the span of the building model. Horizontal and vertical velocity components are measured by this setup. The PIV system comprises of an sCMOS camera (2560 × 2160 pixels), a 50 mm objective, a 532 nm Nd:YAG dual-pulsed laser with energy of 425 mJ and a programmable timing unit. The flow is seeded with olive oil droplets of diameter on the order of several micrometers. Image post-processing is performed using the DaVis software developed by LaVision. The cross-correlation is performed using a double-pass strategy using reducing size interrogation windows, where the window size in the final pass is 32 × 32 pixels and an overlap of 75% is kept between neighboring windows. Bad vectors are removed using a universal outlier detection algorithm, and subsequently replaced by interpolation. The captured field of view is $6d \times 5d$ in size with a spatial resolution of 0.0187d. In order to obtain flow statistics, 1000 instantaneous images are acquired at a sampling rate of 10 Hz. Figure 9.1 shows a schematic of the experimental setup.

An urban canopy model similar to Dar et al. (2022) is set-up inside the test section. The model comprises of square base prisms of base dimensions 8 cm × 8 cm ($L \times W$) and height of 10 cm arranged in a staggered fashion. The streamwise and spanwise spacing between consecutive prisms is four and two times their length, respectively. A picket fence of 2.5 m width, 13 cm height with spikes of 3 cm height and width is placed at the inlet of the test section to facilitate the development of a turbulent boundary layer. The building used for mounting the turbine has a cubic shape with a height H of 40 cm, leading to $H/d = 3.8$. It is placed approximately 20 m downstream from the inlet of the test section surrounded by the urban canopy model. Different fence geometries are mounted on the cubic building. These can be sub-divided into five categories:

1. Cube with no fence, used as a reference base case

2. Fences of different vertical heights:

    (a) 1 cm vertical height, leading to fence to a building height ratio of 0.025
    (b) 2 cm vertical height, leading to fence to a building height ratio of 0.05
    (c) 3 cm vertical height, leading to fence to a building height ratio of 0.075

3. Fences of 2 cm height with varying porosity:

    (a) circular holes with 7% porosity
    (b) circular holes with 20% porosity
    (c) circular holes with 40% porosity

4. Fences of 2 cm height with different angles from the vertical:

    (a) 30° inward angle
    (b) 30° outward angle
    (c) 60° inward angle
    (d) 60° outward angle

5. Fences with circular arc shapes:

    (a) inward curvature with a radius of curvature of 1 cm
    (b) outward curvature with a radius of curvature of 1 cm
    (c) inward curvature with a radius of curvature of 2 cm
    (d) outward curvature with a radius of curvature of 2 cm

Figure 9.2 shows the geometric sketches of different fence shapes with labels used to represent different cases throughout the rest of the article.

Turbine performance is characterized as a function of the fence shape and streamwise distance from the roof leading edge. For each fence shape, the turbine is placed at seven streamwise
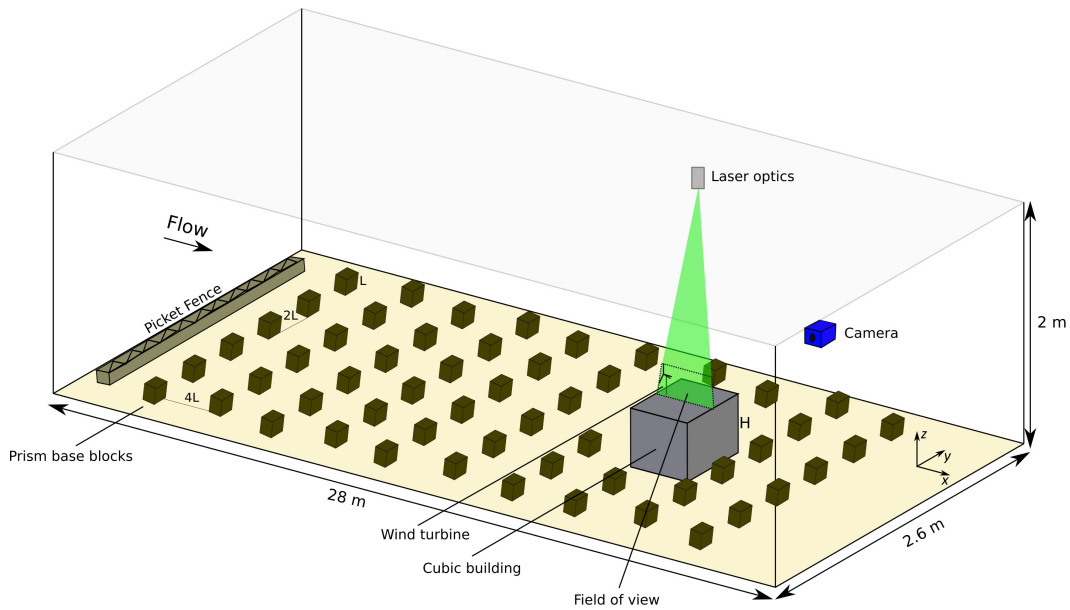
Figure 9.1: Schematic of the experimental setup (not to scale).

positions along the middle of the span of the building. These positions correspond to 0d, 0.5d, 1d, 1.5d, 2d, 2.5d and 3d from the leading edge of the roof. Power and thrust measurements are performed to characterize the performance of the turbine. For power measurements, the current generated by the turbine I is multiplied by the torque constant of the motor k, which gives the electrical torque. The frictional torque Q_f estimated using the relation given in Bastankhah and Porté-Agel (2017a) is then added to the electrical torque to obtain the total mechanical torque. The mechanical torque is multiplied by the rotational speed of the rotor to obtain the power P produced by the turbine. More details on power measurements can be found in Bastankhah and Porté-Agel (2017a). The thrust force T is measured using a multi-axis strain gauge sensor with a resolution of 1.5×10^{-3} N. The turbine is operated at the optimal tip speed ratio for each fence shape and streamwise position. Power and thrust measurements are recorded for 100 seconds at 1 kHz sampling rate.

A two-component laser Doppler velocimetry (LDV) system is used to characterize the turbulent boundary layer developed above the urban canopy model. More details on the LDV system are provided in Dar et al. (2022). The boundary layer measurements are performed 1 m (2.5 times the height of the building) upstream of the cubic building. Figure 9.3 shows some key characteristics of the turbulent boundary layer. It is to be noted that in figure 9.3, $z/d = 0$ represents the surface of test section floor, whereas in the rest of the article, it represents the roof surface of the cubic building. Figure 9.3 (a) shows the normalized averaged streamwise velocity as a function of height. A power law fit according to $U = U_{ref}(z/z_{ref})^n$ is also shown in the plot. The power law exponent is found to be 0.23, which indicates high shear in the flow. The reference velocity $U_{ref} = 6.22 ms^{-1}$ is the streamwise velocity in the upstream boundary layer at a reference height z_{ref} equal to the combined height of the building and turbine
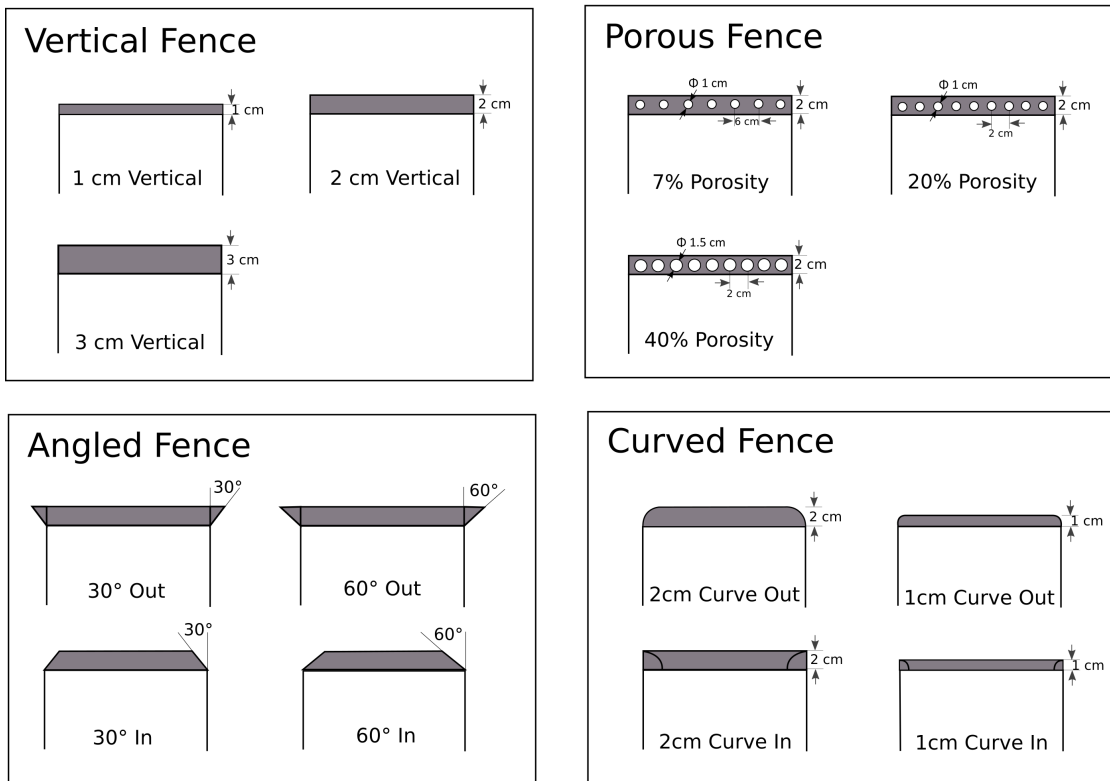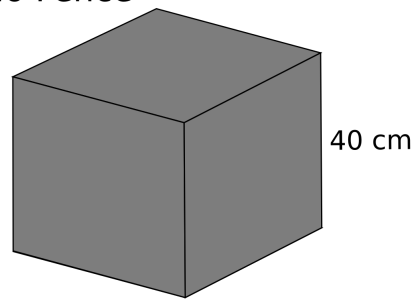
Figure 9.2: Sketches of different fence geometries (side view, not to scale).
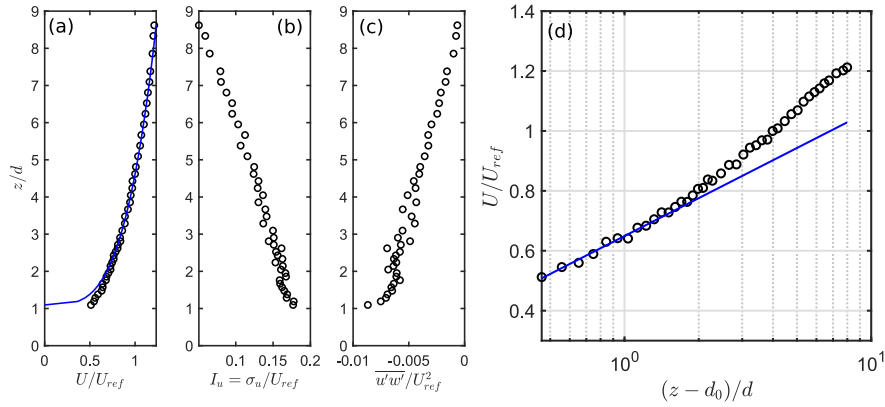
Figure 9.3: Vertical profiles of the normalized averaged streamwise velocity with power law fit in blue line (a), streamwise turbulence intensity (b), normalized averaged vertical momentum flux (c), and normalized averaged streamwise velocity with the height coordinate in log scale with logarithmic fit in blue line (d).

hub. The same reference velocity is used throughout the article. The streamwise turbulence intensity $I_u = \sigma_u / U_{ref}$, where σ_u is the standard deviation in the streamwise velocity, is shown in figure 9.3 (b). High shear in the flow results in high turbulence intensity close to the height of the urban canopy, which decreases with height. The normalized averaged momentum flux is also plotted in figure 9.3 (c), which shows a higher magnitude close to the surface and decreases in magnitude with the increase in height - showing similar trend to the streamwise turbulence intensity. Figure 9.3 (d) shows the normalized averaged streamwise velocity with the height in log coordinates. A logarithmic fit according to $U = \frac{u_*}{\kappa} log(\frac{z-d_0}{z_0})$ is also performed on the lowest 15% of the boundary layer. Here, u_* is the friction velocity, κ is the von Karman constant, d_0 is the displacement height and z_0 is the aerodynamic roughness length. The von Karman constant is chosen to be 0.41, and the friction velocity, displacement height and aerodynamic roughness length are 0.4 ms^{-1}, 6.65 cm and 0.3 cm, respectively.

9.3   Results

This section presents results from the experimental study. In particular, we look at how flow over the building without the turbine changes with the change in the fence shape, and its effect on the power and thrust characteristics of a roof-mounted wind turbine. We also compare two different methods of computing power and thrust coefficients of a turbine in an urban environment.

9.3.1   Parametric study

Based on different categories of fence shapes described in section 9.2, the effect of fence height, porosity, curvature and angle on the flow over the roof without any turbine, and on

the performance of a turbine are investigated. The case with no boundary fence is taken as a reference case for comparison.

Effect of fence height

The fence height causes an additional blockage to the incoming flow. Figure 9.4 (a) shows the contours of the normalized averaged streamwise velocity magnitude ($U_{mag} = \sqrt{U^2 + W^2}$, with U and W the horizontal and vertical velocity components, respectively) along with the streamlines of the flow for different fence heights. For the building with no fence, a flow separation close to the leading edge of the roof is observed which leads to the growth of a shear layer between the low-velocity flow near the surface and the high-velocity one away from it. The strength and size of the separation bubble are observed to increase with the increase in the fence height. A bigger separation bubble leads to higher shear and lower horizontal velocity at a given streamwise position. This is evident in the comparison of the vertical profiles of the normalized averaged horizontal velocity (as shown in figure 9.4 (b)). At the roof leading edge, the location of the maximum flow shear is shifted vertically upwards with the increase in the fence height. Further downstream, the negative velocities in the separation region have a higher magnitude with the increase in the fence height, which results in higher shear and lower velocity in the prospective rotor area. The normalized averaged vertical velocity shows an increase in magnitude and the point of maximum velocity is shifted vertically upwards with the increase in the fence height. This indicates that a turbine will have a lower available power, and will face high flow inclination angle with the increase in the fence height. A higher inclination angle can lead to a reduction in the power performance of the turbine (Bianchi et al., 2014).

The effect of the fence height on the horizontal turbulence intensity is shown in figure 9.5. High turbulence intensity is observed in the flow separation and high shear regions. Close to the roof leading edge, the case with no fence shows the highest turbulence intensity. In the center of the roof, the peak magnitude of the turbulence intensity is comparable between different cases, whereas it is higher for the taller fence at the back end of the roof. This can be related to the evolution of the mean flow shear with distance from the roof leading edge. The position of the peak turbulence intensity is also shifted vertically due to the shift in the shear layer center. Following Kiya and Sasaki (1983), the shear layer center sl_c is quantified by the vertical position of the peak location of the horizontal turbulence intensity at each streamwise position. Figure 9.6 compares the normalized shear layer center between different fence heights. As expected, the shear layer center is observed to get higher with the increase in the fence height. For the no fence case, the shear layer center stays within the lower half of the rotor. For the higher fence cases (2 cm and 3 cm Vertical), the shear layer center reaches or goes higher than the turbine hub height for downstream distances greater than 1 rotor diameter. Higher shear and turbulence intensity variation across the rotor results in a highly fluctuating flow, which can eventually affect its power performance and induce high fatigue loads.

Figure 9.4: (a) Contours of the normalized averaged streamwise velocity magnitude on the building roof for different fence heights along with the streamlines of the in-plane velocity vectors. Comparison of the vertical profiles of normalized averaged streamwise velocity (b) and vertical velocity (c) between cases with different fence heights. The horizontal dashed lines show the turbine top tip, hub level, and bottom tip heights.

(a)

(b)

Figure 9.5: (a) Contours of the horizontal turbulence intensity on the building roof for different fence heights. Comparison of the vertical profiles of the horizontal turbulence intensity (b) between cases with different fence heights. The horizontal dashed lines show the turbine top tip, hub level and bottom tip heights.
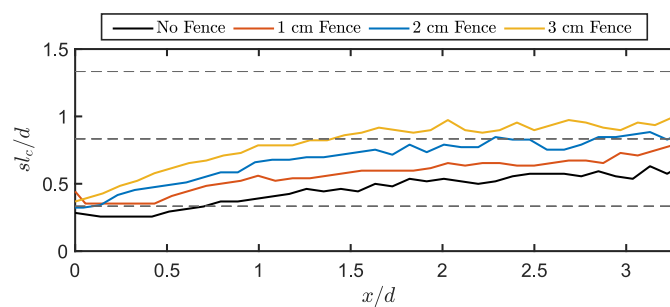
Figure 9.6: Comparison of the shear layer center between cases with varying fence heights. The horizontal dashed lines show the turbine top tip, hub level and bottom tip heights.
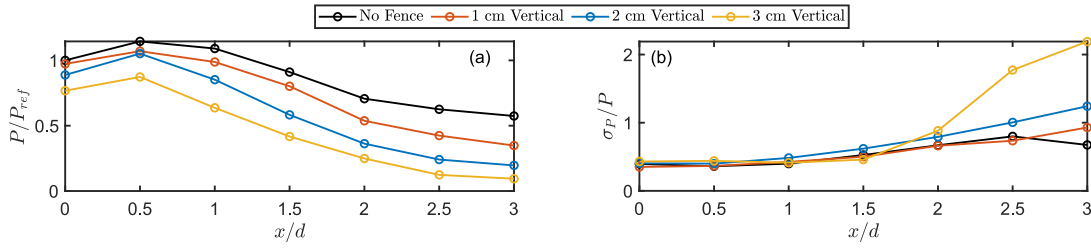
Figure 9.7: Comparison of the normalized mean power (a) and normalized standard deviation in power (b) between cases with different fence heights.

Focusing on the wind turbine performance, figure 9.7 (a) shows the normalized mean power of a turbine placed at different streamwise positions on the roof for different fence heights. Here, the reference power P_{ref} is the mean power at $x/d = 0$ in the No Fence case. All cases show similar trends, where the normalized mean power increases from $x/d = 0$ to $x/d = 0.5$, followed by a gradual decrease. Increasing the fence height results in a systematic decrease in the normalized mean power due to a decrease in the available power to the turbine. Understanding the effect of streamwise position is important to account for a 180° change in the wind direction. High turbulence intensity in the flow can also have an impact on the fluctuations in the power. This is quantified by the standard deviation in power normalized by the mean power at a given position (see figure 9.7 (b)). For all cases, the normalized standard deviation in power is approximately constant and comparable between cases up to $x/d = 1.5$. For $x/d > 1.5$, the normalized standard deviation increases with the increase in the streamwise distance. In addition, the 2 cm Vertical and 3 cm Vertical cases show a higher normalized standard deviation in power than the other two cases, with the 3cm Vertical case showing values more than twice the mean power. As the peak in the turbulence intensity moves upwards with the increase in the fence height, the upper part of the rotor (where the velocity is higher) experiences high turbulence, which results in an increase in power fluctuations.

Figure 9.8 shows the normalized total mean thrust force as a function of streamwise distance. The total mean thrust force is computed as $T_{tot} = \sqrt{T_x^2 + T_y^2 + T_z^2}$, where T_x, T_y and T_z are the thrust components in x, y and z directions, respectively. The normalized total mean thrust force shows a trend similar to the mean power, i.e. a decrease in the normalized thrust force with the increase in the fence height. The values for the normalized thrust are closer between different cases compared to those for the normalized power. This is due to the fact that power has a cubic relation with the flow velocity, whereas thrust has a quadratic one, making power results more sensitive to the changes in flow velocity compared to thrust force with the change in fence height.

Effect of fence porosity

For a given fence height, its porosity can affect the flow over the roof. To investigate the effect of fence porosity, we fix the fence height to 2 cm (0.05 fence to building height ratio) and
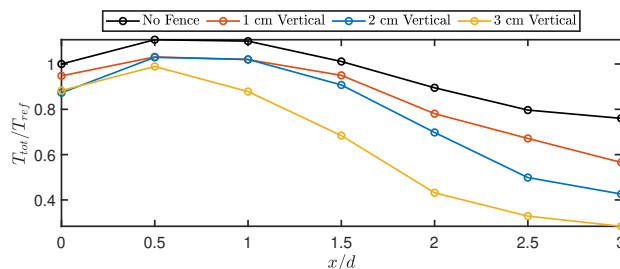
Figure 9.8: Comparison of the normalized mean thrust force between cases with different fence heights.

vary the porosity between 0% and 40%. Figure 9.9 (a) shows the contours of the normalized averaged velocity magnitude along with the velocity streamlines. The flow separation and shear layer development from the building leading edge are not considerably affected by the fence porosity for cases with porosity in the range of 0-20%. For the case with 40% porosity, the separation bubble is observed to be smaller than the rest of the cases. Similarly, comparing the vertical profiles of the horizontal velocity (figure 9.9 (b)), we can observe that the porosity only causes a noticeable increase in the velocity for the 40% porosity case. However, the normalized horizontal velocity is considerably smaller than the No Fence case for all porosity cases. Close to the roof leading edge, the vertical velocity decreases with the increase in the fence porosity (see figure 9.9 (c)). This can be related to the fact that more flow can go throw the porous frontal area of the fence with the increase in the porosity, which decreases the blockage and, therefore, the vertical deflection of the flow. In general, it can be stated that increasing fence porosity above 20% have a favorable effect on the available wind resources on a building roof.

Figure 9.10 shows the contours and vertical profiles of the horizontal turbulence intensity. The horizontal turbulence intensity is affected by the fence porosity. Compared to the No Fence case, a lesser turbulence intensity is observed close to the roof leading edge for all fence cases, whereas a higher turbulence intensity is observed at the back end of the roof. Increasing the porosity decreases the turbulence intensity magnitude, with the 7% porosity case showing similar values to the case with zero porosity. For 20% and 40% porosity cases, a gradual decrease in the turbulence intensity magnitude is observed. This is due to the fact that higher porosity leads to lesser blockage to the incoming flow, which reduces the flow shear, eventually leading to lesser turbulence production. The vertical position of the peak turbulence intensity is used to quantify the shear layer center in figure 9.11. Consistent with earlier discussion, the shear layer center is observed to be similar for cases with the porosity in the range of 0%-20%. The 40% porosity case shows a lower shear layer center than the other fence cases. However, it is still significantly higher than the no fence case.

We now focus on comparing the performance of a turbine located on buildings with different roof fence porosity. Figure 9.12 (a) shows the comparison of the normalized mean power for different cases. The values for the No Fence case are shown as a reference. For streamwise
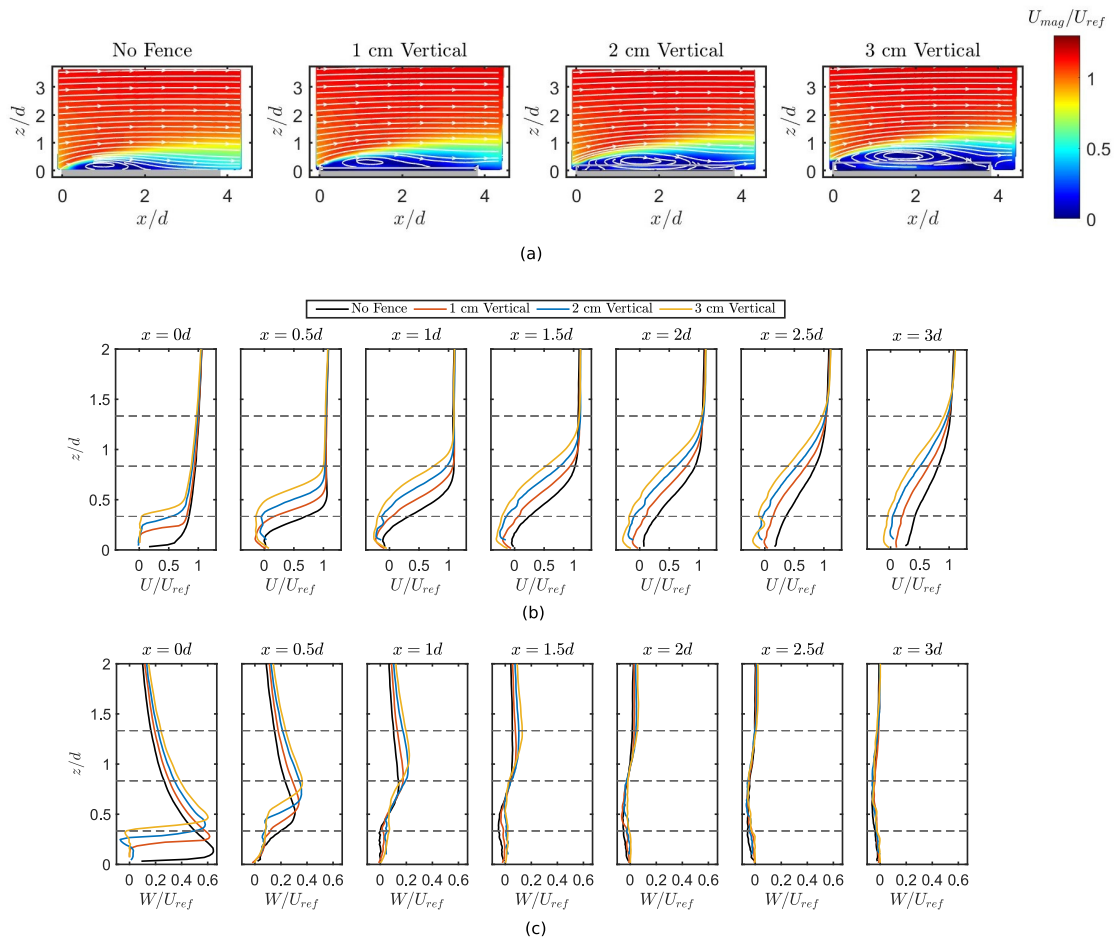
Figure 9.9: (a) Contours of the normalized averaged streamwise velocity magnitude on the building roof for different fence porosity along with the streamlines of the in-plane velocity vectors. Comparison of the vertical profiles of normalized averaged streamwise velocity (b) and vertical velocity (c) between cases with different porosity. The horizontal dashed lines show the turbine top tip, hub level and bottom tip heights.
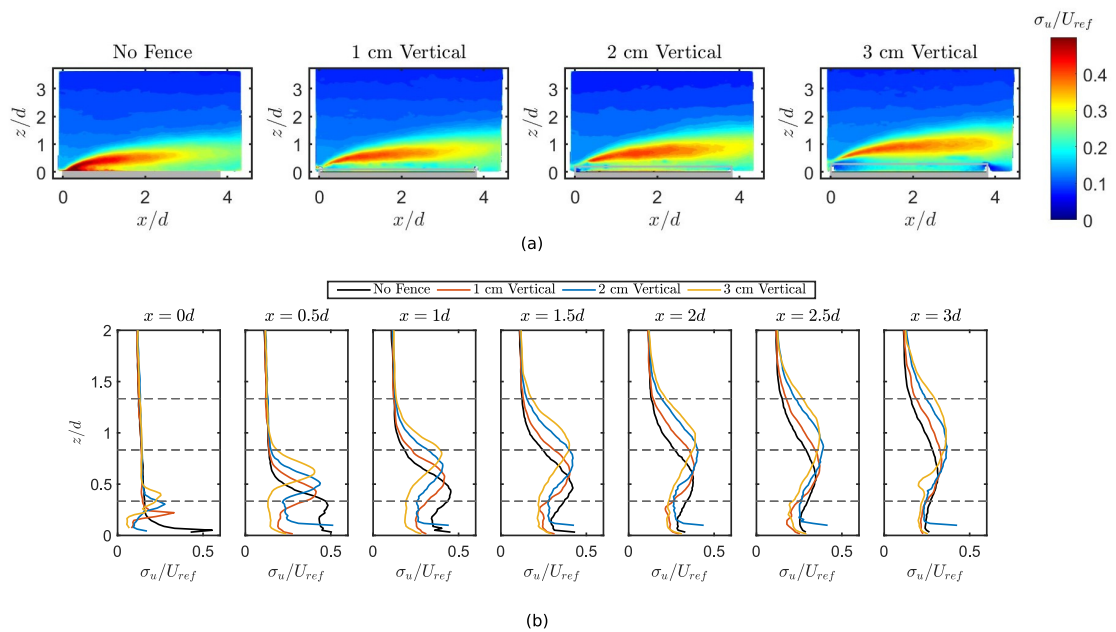
(a)

(b)

Figure 9.10: (a) Contours of the horizontal turbulence intensity on the building roof for different fence porosity. Comparison of the vertical profiles of the horizontal turbulence intensity (b) between cases with different porosity. The horizontal dashed lines show the turbine top tip, hub level and bottom tip heights.

Figure 9.11: Comparison of the shear layer center between cases with different fence porosity. The horizontal dashed lines show the turbine top tip, hub level and bottom tip heights.

Figure 9.12: Comparison of the normalized mean power (a) and normalized standard deviation in power (b) between cases with different fence porosity.

Figure 9.13: Comparison of the normalized mean thrust force between cases with different fence porosity.

positions close to the roof leading edge ($x/d \leq 0.5$), all fence cases show similar mean power. At further downstream positions, increasing porosity leads to higher power production. It is interesting to note that even though the difference in the mean velocity was very small for fence porosity in the range of 0%-20%, an improvement in power production is still observed. This is because of the cubic relation between the power and velocity. In addition, it could be due to the reduction in the flow inclination angle, which can also contribute to a better turbine performance (Bianchi et al., 2014). Fence porosity reduces power fluctuations, as shown in figure 9.12 (b). For porous fences, the normalized fluctuations are similar to the No Fence case at $x/d \leq 1.5$. At higher streamwise distances, 7% and 20% porous fences show an increase in the power fluctuations. The 40% porous fence shows values similar to the No Fence case for all distances, except the last one. This shows that even a very small porosity can have positive effect on both the mean power and power fluctuations compared to the case with a solid fence.

The effect of fence porosity on the normalized thrust force is shown in figure 9.13. Fence porosity has a less significant impact on the normalized thrust force. The case with 40% porous fence shows a higher thrust at $x/D \geq 2$ than the other porous cases. This is because compared to the power results, the thrust force is less sensitive to velocity, and as the velocity difference between various porosity cases is not very high, the thrust force is comparable.

Effect of fence angle

For a given fence height, its angle can affect the development of the separation bubble and the subsequent shear layer. In order to understand the effect of fence angle on the flow over the building, we try four different geometries: with fence angles of 30° and 60° pointing inward and outward of the building. Once again, the 2 cm Vertical fence case is chosen as the reference case.

Figure 9.14 (a) compares the contours of the normalized averaged velocity magnitude along with the flow streamlines for different fence angle cases. It can be clearly observed that the fence angle has a significant impact on the flow separation from the building leading edge. For the 30° fence, an inward angle shows very similar flow behavior compared to the 2 cm Vertical fence, whereas the outward angle results in a smaller reattachment length but a higher separation bubble. For the 60° fence, an inward angle leads to a more attached flow with a smaller separation bubble and shorter reattachment length. An outward angle in this case leads to a shorter reattachment length but a higher separation bubble. The height of the separation bubble and its reattachment length affect the shear in the flow. Figure 9.14 (b) compares the vertical profiles of the normalized averaged horizontal velocity between different cases. Close to the roof leading edge, the outward-angled fences show lesser velocity than the 2 cm Vertical fence. This is due to the larger separation bubble height in the outward-angled fences compared to the vertical one. Further downstream the 60° outward fence shows a higher velocity compared to the vertical one, and the 30° one shows a horizontal velocity similar to the vertical one. For the 30° inward-angled fence, the horizontal velocity is slightly larger than the for vertical fence at some streamwise positions. For the 60° inward fence, the velocity profile is much closer to the one for the No Fence case than to the vertical fence one, indicating a higher available power in this case. Finally, the normalized averaged vertical velocity is compared in figure 9.14 (c). The magnitude of the normalized averaged vertical velocity close to the roof leading edge depends on the fence angle, where the 60° fences show a lower vertical velocity magnitude than the 30° one. The position of the peak vertical velocity is lower for the inward-angled fences than for the outward-angled ones. The difference in the vertical velocity magnitude between different cases lasts for downstream distances up to 1.5 rotor diameters, beyond which all cases show similar vertical velocity magnitude.

The horizontal turbulence intensity is compared between different cases in figure 9.15. In general, an inward fence angle leads to a smaller horizontal turbulence intensity compared to a vertical fence, whereas an outward fence angle leads to a larger one. Comparing the vertical profiles of horizontal turbulence intensity, an outward fence angle leads to a higher horizontal turbulence intensity close to the roof leading edge compared to a vertical fence, whereas further downstream the values get closer to the ones in the vertical fence case. For the 30° inward fence angle, the horizontal turbulence intensity is smaller than the vertical fence close to the roof leading edge, but the difference between the two reduces with the increase in the streamwise distance. The most interesting case is that of the inward 60° angle, which shows the smallest magnitude of horizontal turbulence intensity, with peak values smaller

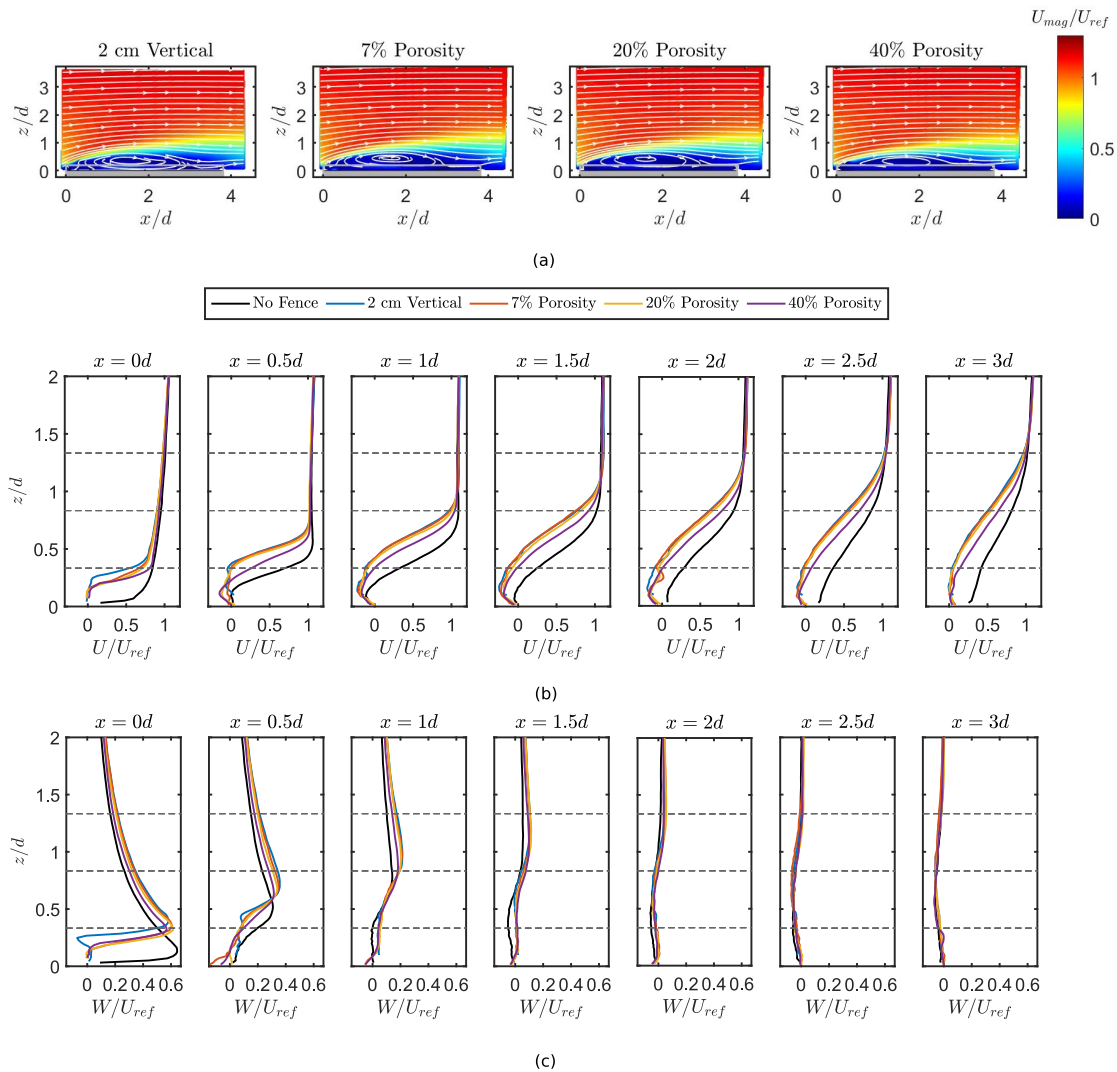Figure 9.14: (a) Contours of the normalized averaged streamwise velocity magnitude on the building roof for different fence angles along with the streamlines of the in-plane velocity vectors. Comparison of the vertical profiles of normalized averaged streamwise velocity (b) and vertical velocity (c) between cases with different fence angles. The horizontal dashed lines show the turbine top tip, hub level and bottom tip heights.
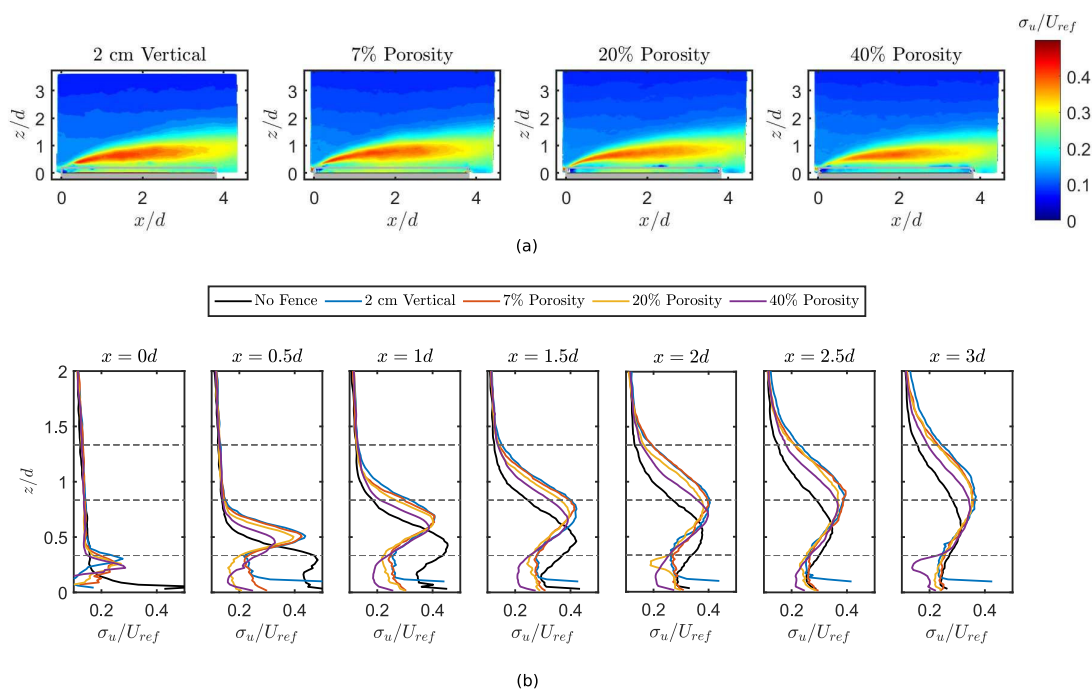
Figure 9.15: (a) Contours of the horizontal turbulence intensity on the building roof for different fence angles. Comparison of the vertical profiles of the horizontal turbulence intensity (b) between cases with different fence angles. The horizontal dashed lines show the turbine top tip, hub level and bottom tip heights.
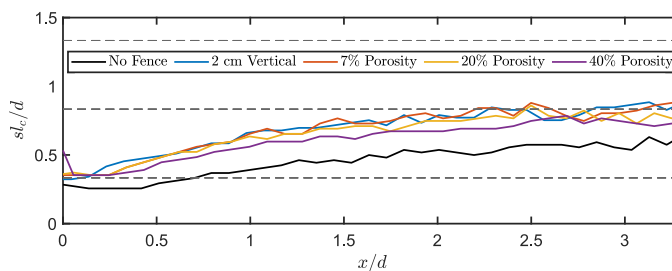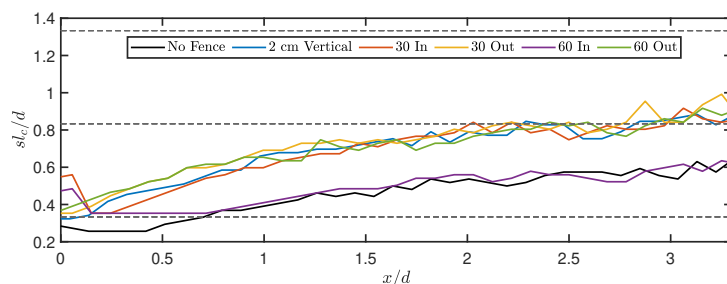

Figure 9.16: Comparison of the shear layer center between cases with different fence angles. The horizontal dashed lines show the turbine top tip, hub level and bottom tip heights.

than or equal to the No Fence case at all streamwise positions. This can be related to the fact that the flow separation in this case is similar to the No Fence case.

Comparing the shear layer center positions in figure 9.16, it is observed that all angled fences except the 60° inward fence show similar shear layer center positions. The 60° inward fence, on the other hand, shows a shear layer center position closer to the No Fence case. This can have a significant impact on the power fluctuations as will be discussed in the following.

Coming to the turbine performance, we first show the turbine power characteristics in figure 9.17. The outward-angled fences show normalized mean power values similar to the vertical fence case for all streamwise positions. The 30° inward fence shows a better power
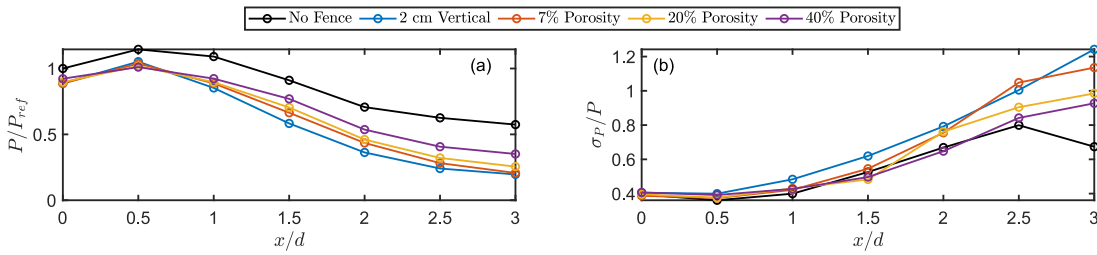
Figure 9.17: Comparison of the normalized mean power (a) and normalized standard deviation in power (b) between cases with different fence angles.
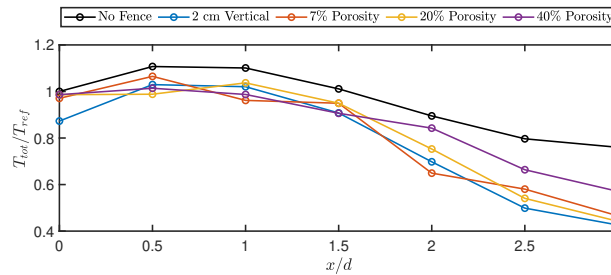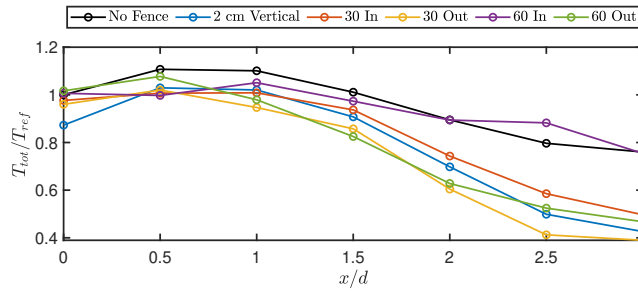

Figure 9.18: Comparison of the normalized mean thrust force between cases with different fence angles.

performance than the outward fence cases, whereas the 60° inward fence case shows the best power performance among all the fences compared. It even shows normalized mean power comparable to the No Fence case for $x/d \geq 1$. In terms of the normalized fluctuations in power, the outward fence cases show higher fluctuations than the vertical fence for $x/d > 1$. Both inward fence shapes show lower power fluctuations than the vertical fence for all streamwise positions, where the 30° inward case shows values greater than the No Fence case for $x/d > 2$ and the 60° inward fence shows values lower than or equal to the No Fence case for all streamwise positions. This makes 60° inward case an ideal fence angle in terms of power performance, as it provides performance comparable to the No Fence case while keeping the safety feature of the boundary fence.

Figure 9.18 compares the normalized total thrust force for different fence angles. Away from the roof leading edge, the outward fence angles show a lower normalized thrust compared to the vertical fence case. The inward fence angle cases have a higher thrust, with the 60° inward fence case showing values comparable to the No Fence case at $x/d \geq 1$.

Effect of fence curvature

As shown by Dar et al. (2022), a rounded roof shape is favorable for a roof-mounted wind turbine. Here, we attempt to incorporate a similar rounded design into the shape of the fence and investigate its effect on the flow over the building and on the turbine performance. The

fence height, radius, and direction of curvature are the variable parameters.

Figure 9.19 (a) shows the contours of the normalized averaged velocity magnitude along with flow streamlines for different fence curvatures. An outward curvature leads to a smaller separation bubble with a shorter reattachment length for the same radius of curvature. This is because an outward curvature provides a smoother path for the incoming flow, thereby reducing the flow separation. A comparison of the vertical profiles of the normalized averaged horizontal velocity is shown in figure 9.19 (b). The profiles of the No Fence, 2 cm Vertical, and 1 cm Vertical cases are also shown as a reference. The inward curvature cases showed profiles similar to the vertical fence cases for the respective fence heights. This indicates that inward curvature would lead to no significant benefit in available power to the turbine. An outward curvature, on the other hand, leads to a significant increase in the velocity compared to the vertical fence. The 2 cm outward curvature case shows higher velocity than both the 1 cm Vertical and 1 cm inward curvature cases. This means that, if a higher fence height is necessary, outward curvature can help achieve similar turbine performance as a smaller vertical fence. For the 1 cm outward curvature case, the velocity profiles in the rotor limits are very similar to the No Fence case for $x/d \leq 2$, whereas a slight decrease in the velocity is observed at higher downstream distances. Figure 9.19 (c) compares the profiles of the normalized averaged vertical velocity between different cases. The vertical position and magnitude of the maximum vertical velocity near the roof leading edge are affected by the fence curvature. Among the fenced cases, the outward curvature ones show the smallest magnitude with the maximum located close to the roof surface, whereas the 2 cm Vertical and inward curved cases show the highest vertical position and magnitude of the vertical velocity. Higher vertical velocity leads to higher inclination of the flow, which can be detrimental to the turbine performance (Bianchi et al., 2014).

Figure 9.20 (a) shows the contours of the horizontal turbulence intensity for different fence curvatures. An outward fence curvature results in a lower turbulence intensity, with peak turbulence intensity located close to the surface. A comparison of the vertical profiles of the horizontal turbulence intensity is also shown in figure 9.20 (b). Close to the roof leading edge, the No Fence case has the highest peak turbulence intensity, followed by the 2 cm Vertical case, whereas the rest of the cases show a comparable peak value. Towards the back end of the roof, the No Fence and 2 cm Vertical cases have the lowest and highest peak values, respectively. The 2 cm inward curved case shows a similar profile to the 2 cm Vertical one, whereas the 1 cm inward curved case shows a profile similar to the 1 cm Vertical one. The 2 cm outward curvature shows a lower turbulence intensity than the 1 cm Vertical and 1 cm inward curved case, whereas the 1 cm outward curvature case shows a profile similar to the No Fence case at the back end of the roof. Similar trends can be observed for the shear layer center location shown in figure 9.21.

Focusing on the turbine performance, we first discuss the power performance of the turbine for different fence curvatures in figure 9.22. In general, all fence curvature cases show higher normalized mean power than the 2 cm vertical fence with no curvature. At the position
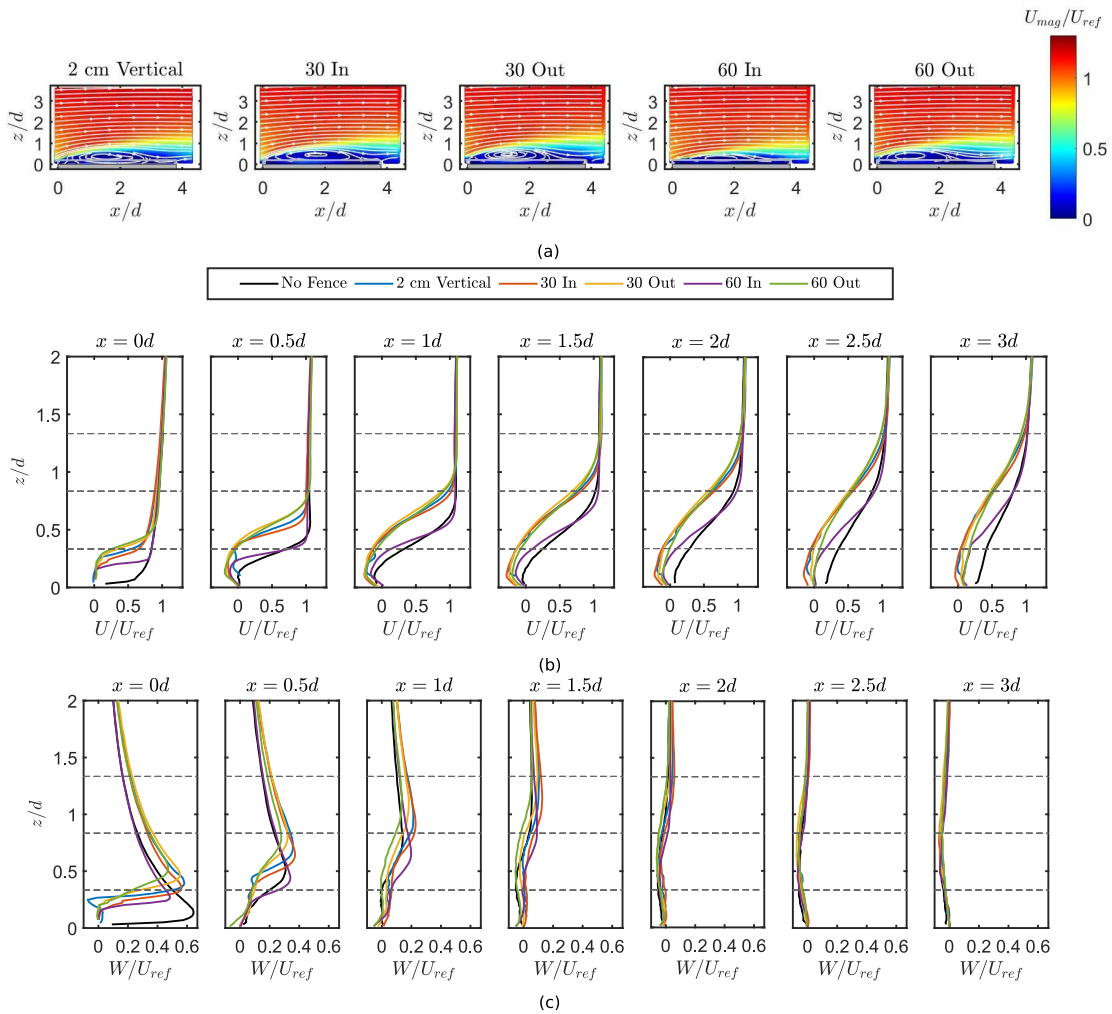
(a)

(b)

(c)
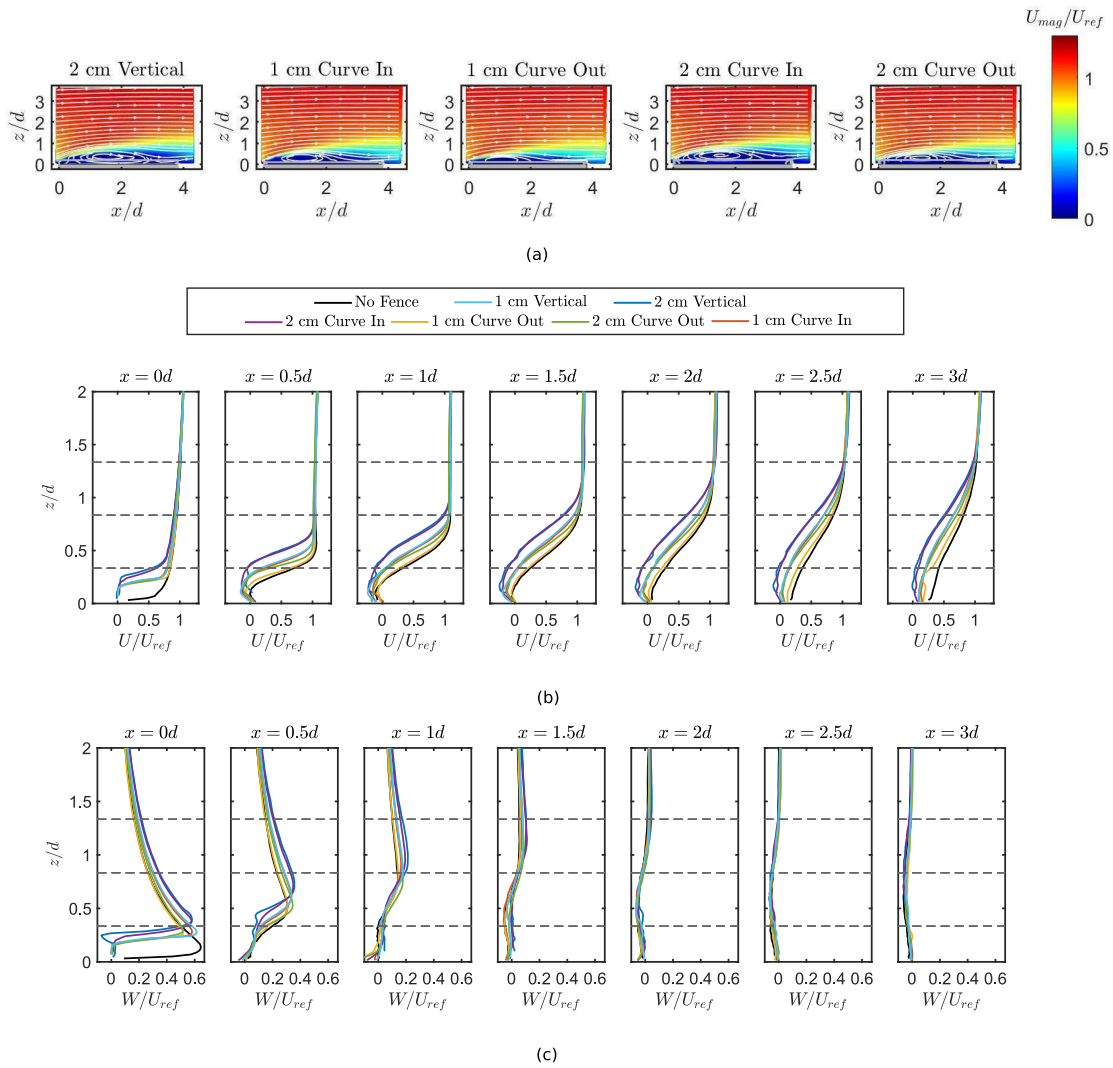
Figure 9.19: (a) Contours of the normalized averaged streamwise velocity magnitude on the building roof for different fence curvatures along with the streamlines of the in-plane velocity vectors. Comparison of the vertical profiles of normalized averaged streamwise velocity (b) and vertical velocity (c) between cases with different fence curvatures. The horizontal dashed lines show the turbine top tip, hub level, and bottom tip heights.
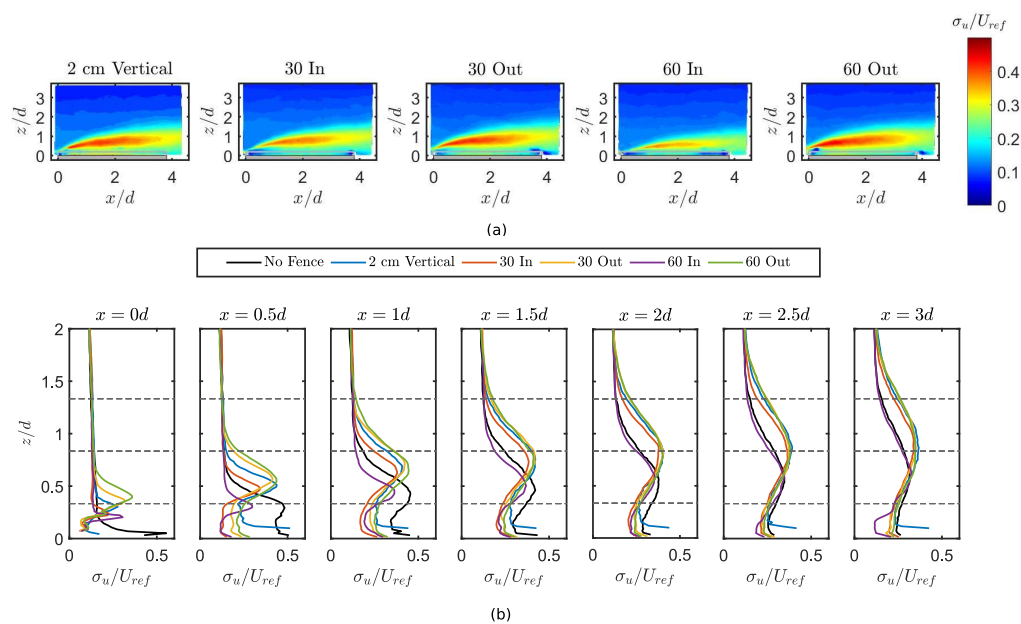
(a)

(b)
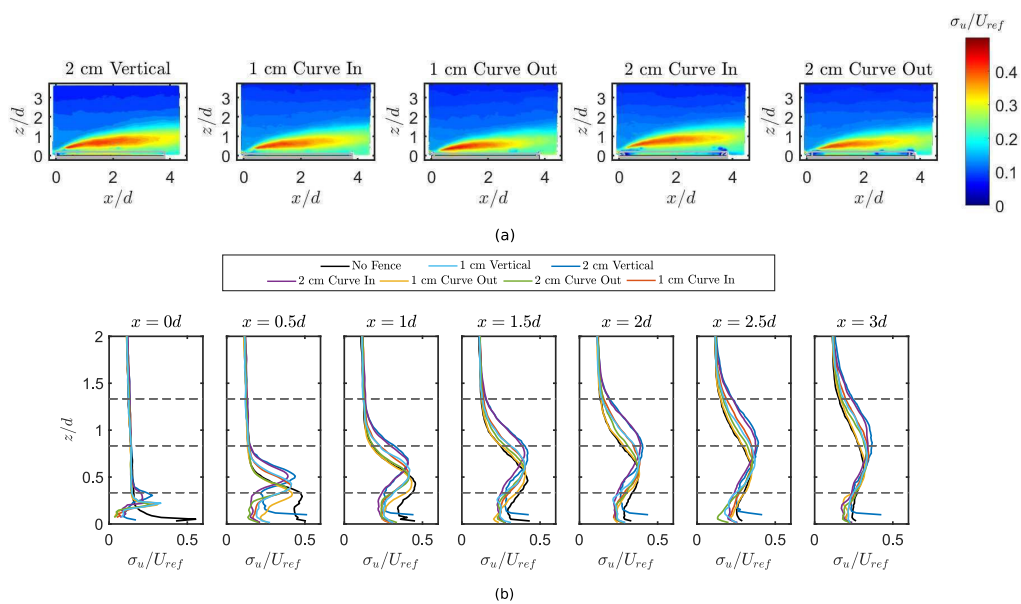
Figure 9.20: (a) Contours of the horizontal turbulence intensity on the building roof for different fence curvatures. Comparison of the vertical profiles of the horizontal turbulence intensity (b) between cases with different fence curvatures. The horizontal dashed lines show the turbine top tip, hub level, and bottom tip heights.
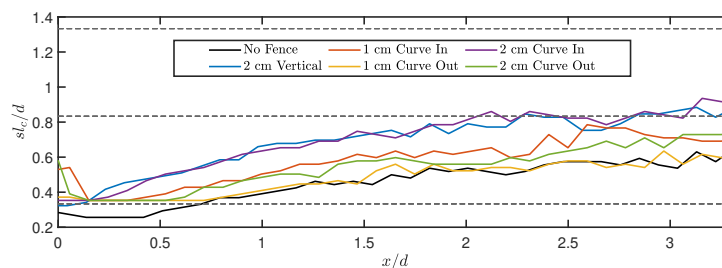
Figure 9.21: Comparison of the shear layer center between cases with different fence curvatures. The horizontal dashed lines show the turbine top tip, hub level, and bottom tip heights.
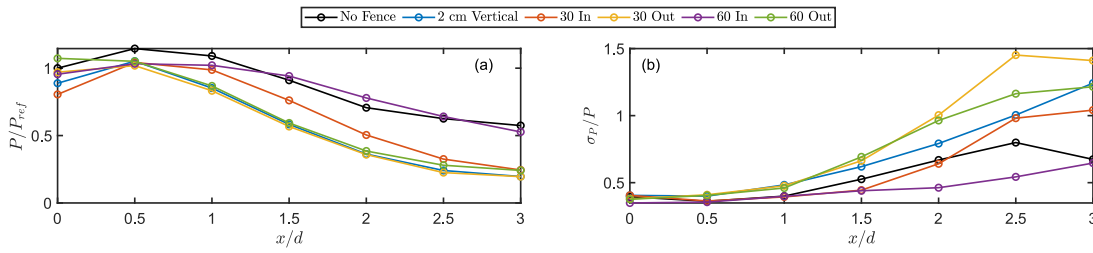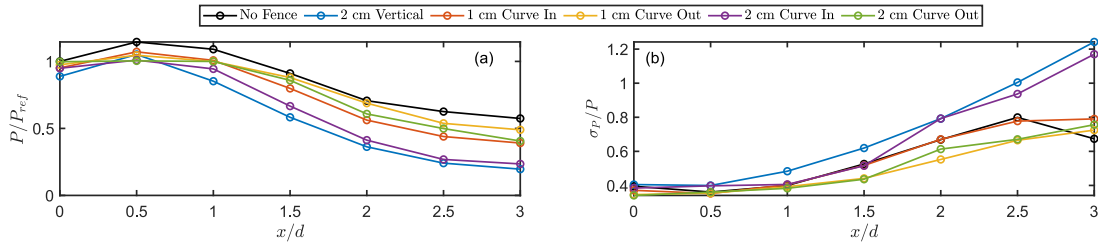
Figure 9.22: Comparison of the normalized mean power (a) and normalized standard deviation in power (b) between cases with different fence curvatures.

corresponding to the maximum normalized mean power, the difference between different fence cases is the smallest. Further downstream, the 2 cm inward curved fence shows a slight improvement in power, whereas a significant improvement in power is observed for the 2 cm outward curvature compared to the 2 cm Vertical case. At $x/d > 1$, the 2 cm outward curved fence produces more power than the 1 cm inward curved. The 1 cm outward curved fence shows the power production close to the No Fence case for $x/d > 1$. However, it is interesting to note that the improvement in power between the inward and outward curved fences for a fixed radius of curvature is higher for the 2 cm case than for the 1 cm one. Fence curvature has a significant impact on the distribution of turbulence intensity in the flow, which affects the fluctuations in power production. Figure 9.22 (b) shows the normalized power fluctuations for different fence curvatures. The two outward curved fences show lower power fluctuations than the No Fence case, whereas the 1 cm inward fence shows the same normalized standard deviation, and the 2 cm inward fence shows a higher normalized standard deviation at the majority of the turbine positions compared to the No Fence case. Overall, curved fences are shown to be effective in improving the mean power and reducing power fluctuations compared to vertical fences.

The normalized total thrust force on the turbine is compared between different fence curvatures in figure 9.23. As the thrust forces are less sensitive to changes in velocity than the power production, a much tighter spread in the normalized mean thrust force is observed. Close to the roof leading edge, at $x/d \leq 1$, thrust force values are very close to each other for different fence curvatures. At $x/d > 1$, the two outward curved fences show a higher thrust due to a higher velocity, followed by the 1 cm inward curved case. The 2 cm inward curved fence shows values similar to the 2 cm Vertical case due to comparable velocity profiles between the two cases.

9.3.2 Performance coefficients

Wind turbine performance coefficients such as the power and thrust coefficients are important parameters used to evaluate the efficiency of the turbine and to estimate its wake
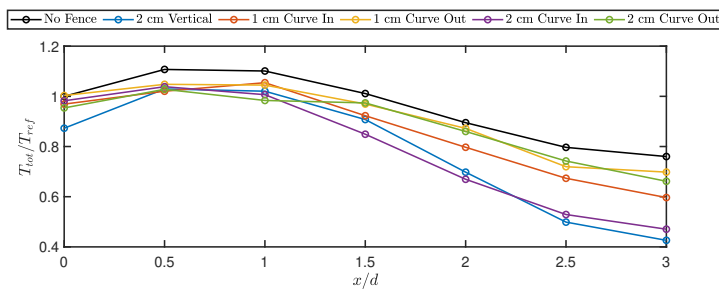
Figure 9.23: Comparison of the normalized mean thrust force between cases with different fence curvatures.

characteristics. The power coefficient C_P is defined as:

$$C_P = \frac{P}{\frac{1}{2}\rho A U^3}, \tag{9.1}$$

where ρ is the air density, A is the rotor swept area and U is a reference wind velocity. In a similar fashion, the thrust coefficient C_T can be defined as:

$$C_T = \frac{T}{\frac{1}{2}\rho A U^2}. \tag{9.2}$$

For wind turbine manufacturers, it is a common practice to provide reference power curves for the turbines. However, it has been reported in the literature that wind turbine performance decreases in the urban environment compared to the manufacturer-provided data (see e.g., (Pagnini et al., 2015)). According to the IEC 61400-12-1 standard (Commission et al., 2005), the wind velocity at the hub height can be used as a reference wind velocity in the evaluation of the wind turbine power and thrust curves. However, this approach of defining the performance coefficients only works if the wind shear in the flow is approximately constant (Van Sark et al., 2019). In an urban environment, especially on rooftops, the wind shear is not constant due to the development of a shear layer from the roof leading edge (as discussed in detail in this article). For a flow with a variable shear, the idea of a rotor equivalent wind speed is proposed (Wagner et al., 2014). For urban wind turbines, currently, there is no comparison of the two approaches, and no standard approach exists. For instance, in Jooss et al. (2022a, 2022b), the inflow velocity upstream of the building is used to compute the power coefficient. However, it can be argued that such an approach does not capture the velocity variation on the roof itself and assumes that the power available to the rotor is the same in any position on the building as it is upstream of the building.

Our goal here is to perform a comparison of the performance coefficients of the turbine accounting for the local variations in the wind speed. For this purpose, we use the time-averaged hub height velocity magnitude and the time-averaged rotor equivalent velocity magnitude (computed using the method described in Wagner et al., 2014). Using the velocity
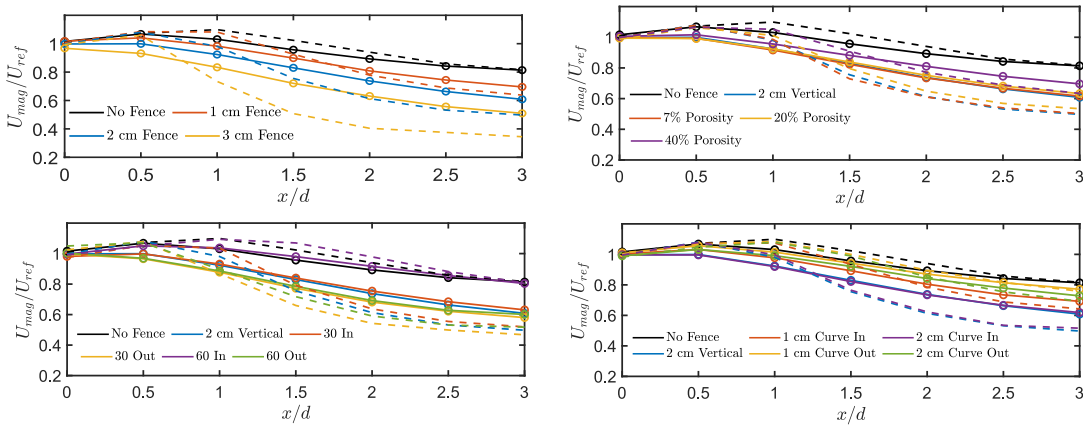
Figure 9.24: Comparison between the normalized averaged velocity magnitude at the hub height (dashed lines) and the rotor equivalent one (solid lines).

magnitude enables us to account for the resultant velocity based on the horizontal and vertical velocity experienced by the rotor. Figure 9.24 compares the normalized averaged velocity magnitude at the hub height of the prospective turbine, and the rotor equivalent one. The building with no fence shows the least difference between the rotor equivalent and hub height velocity magnitude. Close to the roof leading edge, the hub height velocity tends to be higher than the rotor equivalent one, whereas it drops below the rotor equivalent one towards the back end of the building for the majority of the cases. This can be related to the growth of the shear layer. When the shear layer center lies close to the bottom tip of the rotor, the rotor equivalent velocity magnitude is lower than the hub height one. However, as the shear layer center approaches the hub height, the rotor equivalent velocity magnitude tends to be higher than the hub height one. This can be explained by the fact, that if the hub height lies outside the shear layer, the hub height velocity magnitude does not account for the sharp gradient of velocity in the shear layer, which leads to a higher value of the velocity magnitude than the rotor equivalent one.

Figure 9.25 compares the power coefficient computed from the two reference velocities for different fence shapes. Focusing on the power coefficient based on the hub height velocity magnitude (figure 9.25 (a,c,e,g)), one can observe that, for the No Fence case, the computed power coefficient shows the least amount of variation with turbine position. It first tends to decrease with an increase in the distance from the roof leading edge, and then after $x/d = 2$ starts to increase again. For the vertical fence cases, the power coefficient shows a value similar to the No Fence case close to the roof leading edge ($x/d = 1$ for 1 cm and 2 cm Vertical cases and $x/d = 0.5$ for 3 cm Vertical case). Away from the roof leading edge, the power coefficient shows unrealistically high values, which even exceed the Betz limit for certain cases. This is because, for such positions, the hub height lies within the shear layer and cannot represent the actual available energy to the turbine. For the porous fences, a similar behavior is observed, where the 40% porous case shows values closer to the No Fence case than the other cases. For

the angled fences, the 60° inward fence shows the power coefficient similar to the No Fence case. The rest of the cases exceed the Betz limit at $x/d \geq 1.5$, showing that the power coefficient definition breaks down at these positions. A similar observation can be made regarding the curved fences, where the outward-curved fences show lesser variation in the power coefficient with turbine position, and the inward-curved ones show an increase in the power coefficient with distance for $x/d > 1$. In general, it can be concluded that the hub height velocity does not yield a reliable estimate of the power coefficient for streamwise positions where the shear layer center is close to the turbine hub height and the velocity profile has a variable shear across the majority of the rotor swept area.

We now compare the power coefficient based on the rotor equivalent velocity magnitude in figure 9.25 (b,d,f,h). Immediately, one can observe that the nonphysical variation in the power coefficient observed earlier is resolved by this method of computing the reference velocity. For the vertical fences, the 1 cm Vertical fence shows the same trend as the No Fence case, whereas for the higher fences, the power coefficient first increases with the distance from the leading edge, followed by a gradual decrease. Among other factors, this can be due to the additional blockage caused by the fence at the back end of the building. For porous fences, the 7% and 20% porous cases show the highest power coefficient at $x/d = 1.5$, whereas the 40% porous case shows values comparable to the No Fence case. For the angled fences, the 60° inward fence shows the same power coefficient as the No Fence case, whereas the rest of the cases show an increasing-decreasing trend, with peak values at $x/d = 1.5$. Finally, for the curved fences, the 2cm inward curved fence shows a trend similar to the 2 cm Vertical fence due to similarities in the flow fields, whereas the rest of the cases show trends similar to the No Fence case with differences in the power coefficient values. Overall, the power curves show two types of trends: for the cases with the shear layer center approximately below the bottom one-third of the rotor, the power coefficient shows a steady increase in value with an increase in the streamwise distance from the roof leading edge; whereas for the cases where the shear layer center reaches approximately the hub height of the turbine, the power coefficient first shows an increase in the value with distance up to $x/d = 1.5$, followed by a decrease for $x/d > 1.5$. Although the mean power results showed similar trends for all the cases, the turbine efficiency shows a rather complex behavior. This can, in part, be related to the fact that the turbine placement can have an effect on the surrounding flow, which can change the power available to the turbine compared to the one estimated from the base flow. It is known in the literature that the turbine wake can have an effect on the turbine power curve (Troldborg et al., 2022), especially in complex environments. As the turbine wake development can differ based on turbine position and fence shape, this could help explain the different trends in the power coefficient. However, the lack of experimental data on the wake flow warrants future investigation on the subject.

Figure 9.26 compares the turbine thrust coefficient obtained from the two methods. Similar observations as to the power coefficient can be made regarding the comparison between the two approaches. Regarding the thrust coefficient obtained based on the rotor equivalent velocity magnitude, certain cases show thrust coefficients close to or higher than 1. This
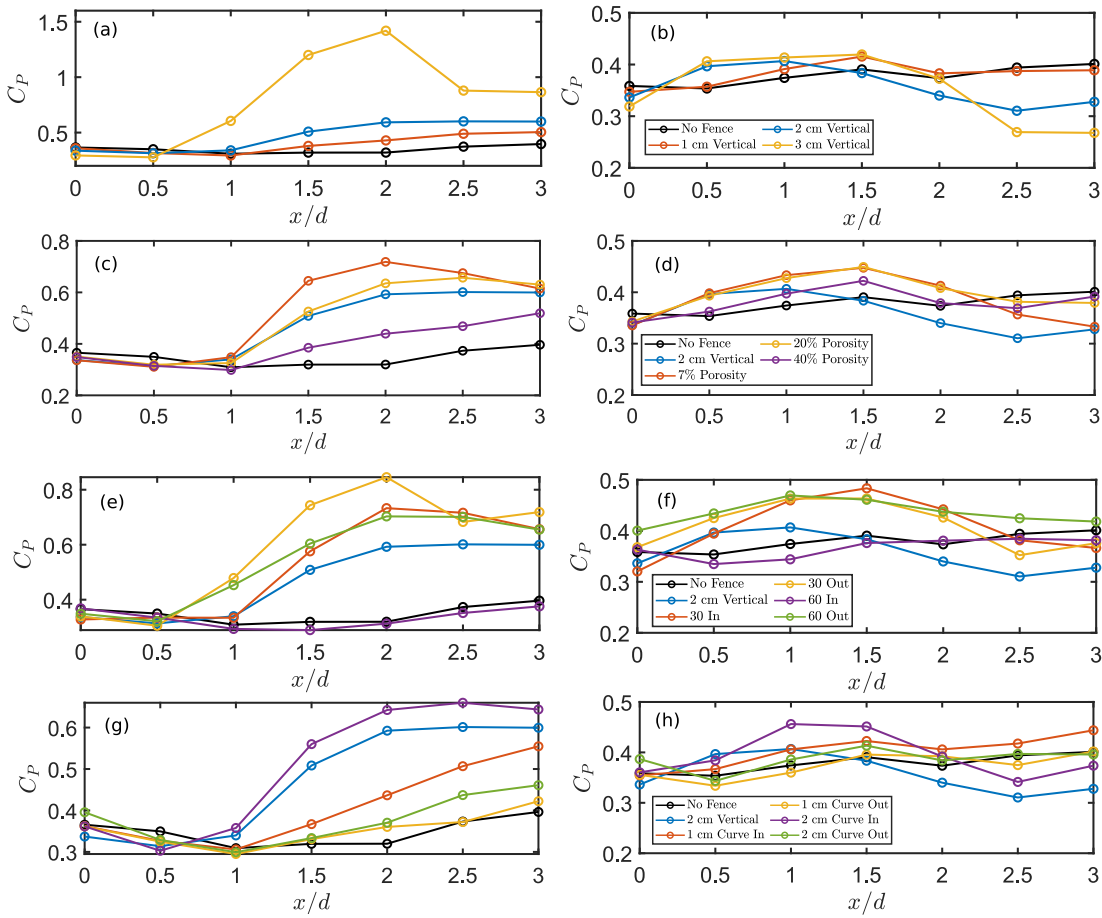
Figure 9.25: Comparison of turbine power coefficient computed with hub height velocity magnitude (left column) and rotor equivalent velocity magnitude (right column) for vertical (a,b), porous (c,d), angled (e,f), and curved (g,h) fences.
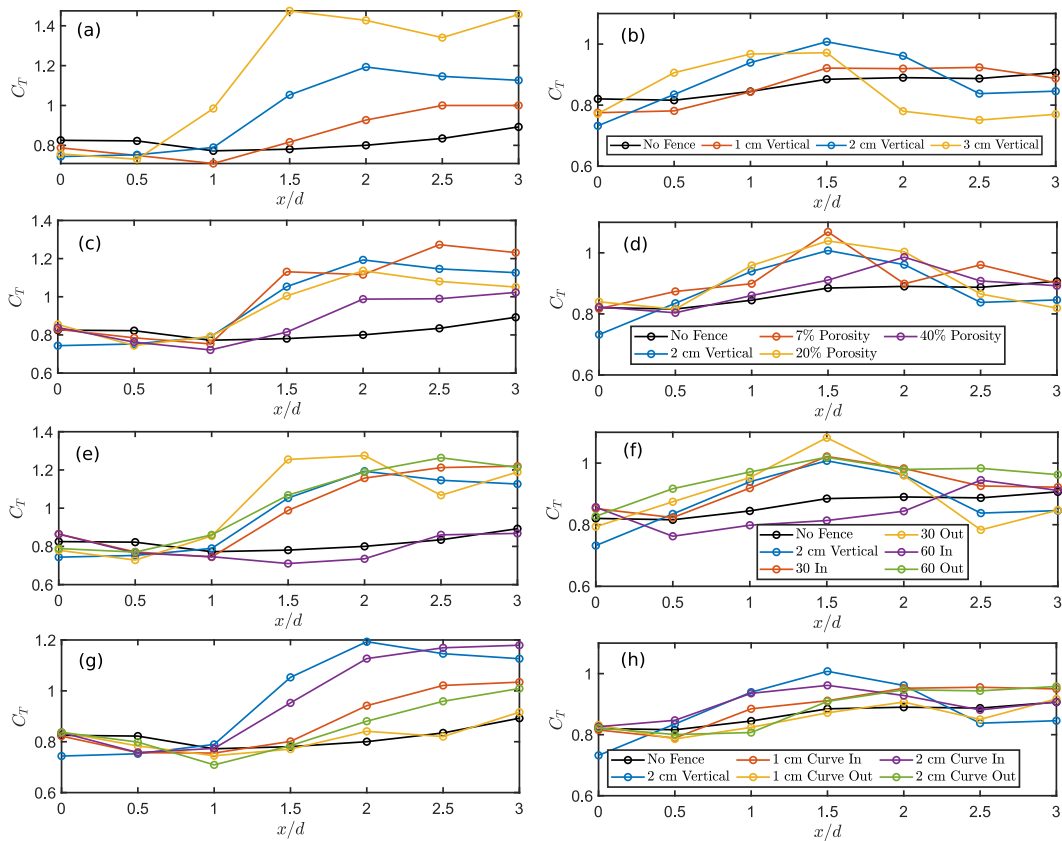
Figure 9.26: Comparison of turbine thrust coefficient computed with hub height velocity magnitude (left column) and rotor equivalent velocity magnitude (right column) for vertical (a,b), porous (c,d), angled (e,f), and curved (g,h) fences.

indicates a potential reverse flow in the turbine wake. Indeed, in Dar et al. (2022), the solid fence case showed negative velocity in the turbine wake. If the reverse flow in the wake becomes strong enough, it could block the flow going through the rotor, which could also help explain the drop in the power coefficient after a certain streamwise distance from the roof leading edge.

9.4   Conclusions

Urban wind energy offers a potential for renewable energy generation close to the end consumer. Rooftops are ideal for turbine placement in an urban environment due to high wind resources over buildings. Building aerodynamics plays a crucial role in determining the flow over it. Boundary fences are an integral safety feature of buildings, however, their effect on the flow over buildings and on the performance of roof-mounted wind turbines is not well understood. In this article, we performed a systemic study on the effect of fence height, porosity, angle, and curvature on the flow over a building and on the turbine sited at several positions

on the building. A building with no boundary fence was used as a reference base case for comparison.

The key findings of the study can be summarized as follows:

1. Fence shape can affect the flow separation and consequently the growth of the shear layer from the roof leading edge. This has a direct effect on the available power across the rotor-swept area.

2. Fence porosity has a considerable effect on the flow for a porosity higher than 20%.

3. Inward-angled fences have the smallest separation bubble for a fixed fence height, with an angle of 60° yielding a flow similar to the building with no boundary fence.

4. For curved fences, the outward-curved fences show better flow conditions for a given fence height compared to the inward-curved ones.

5. In terms of normalized mean power and thrust, certain cases such as the 60° inward-angled fence and the outward-curved fences show values very close to the No Fence case, making them ideal fence shapes for urban wind energy.

6. Although none of the fence shapes yield a mean power higher than the No Fence case, several cases, such as the inward-angled and outward-curved fences have lesser normalized standard deviation in power than the No Fence case at certain turbine positions. This indicates lesser variation in power production and lower fatigue loads on the turbine and can be related to the distribution of turbulence intensity in the base (without turbine) flow.

7. Power and thrust coefficients based on the hub height and rotor equivalent velocity magnitude are compared. The hub height velocity magnitude only gives reasonable results if the shear layer center lies within the lower 1/3 of the rotor height. The rotor equivalent velocity magnitude yields more consistent results for all cases.

8. Based on the power and thrust coefficients computed from the rotor equivalent velocity magnitude, two trends are identified: for cases with shear layer centers close to the bottom tip of the turbine, the coefficients show a slight but gradual increase in value with the increase in turbine's distance from the roof leading edge. For cases where the shear layer center gets close to the turbine hub height, the performance coefficients show an increase-decreasing trend with the streamwise location of the turbine, and maximum value at $x/d = 1.5$ is observed.

10 Overall summary and future perspectives

10.1 Overall summary

This work presents a collection of experimental and analytical studies on wind turbines in complex terrain. Some key findings of these studies are summarized in the following:

- We performed a combination of tomographic and stereoscopic particle-image velocimetry measurements to investigate the effect of the windward side shape of an escarpment on the wake of a wind turbine sited on it. Two types of escarpments were studied: forward facing step (FFS) escarpments, for which the leading edge curvature was varied, and sinusoidal ramp-shaped escarpments, for which the ramp slope was varied. The turbine wake showed a high sensitivity to the escarpment shape, with a faster recovery in the FFS escarpments than in the ramp-shaped ones. The presence of the wind turbine suppressed the development of the flow separation from the escarpment leading edge in the FFS cases. The meandering of the wake was observed to be stronger for the wind turbine wake on the FFS escarpments than on the ramp-shaped ones due to high turbulence kinetic energy. Moreover, the tip and hub vortices shed by the turbine were observed to be broken much more quickly in the FFS escarpment case than in the ramp-shaped one.

- The effect of wind direction on the flow over a cliff and its interaction with a wind turbine wake were then investigated using stereoscopic particle-image velocimetry. The flow became increasingly three-dimensional with a cross-stream flow separation with the increase in the obliqueness in the wind direction. The wake shape, recovery, and deflection were affected by the cross-stream flow separation and by the change in the distribution of streamwise velocity and turbulence kinetic energy in the base flow. The analysis of the streamwise momentum in the wake was performed to investigate the physical mechanism behind the change in the wake recovery.

- An analytical modeling framework that accounts for the effect of pressure gradient on the turbine wake velocity deficit was developed. In this context, an estimation of the

maximum near-wake velocity deficit under a pressure gradient was made using 1-D momentum theory, and coupled with a model for the far wake velocity deficit. The analytical model was validated with the measurements of the wake velocity deficit on the escarpments with different windward side shapes.

- A systematic investigation of wind turbine wakes exposed to linear flow speed-up and slow-down from its induction region to the far wake region was performed. The study showed that, for a range of pressure gradients from adverse to zero to favorable ones, the wake of a wind turbine responds in a systematic manner. The wake velocity deficit increased for the adverse pressure gradient (APG) and decreased for the favorable (FPG) one compared to the zero pressure gradient (ZPG). The near wake length and the wake growth rate behaved in a quasi-linear fashion with the change in the pressure gradient. A new relation for the near wake length under pressure gradient was introduced, which together with the analytical model developed earlier, was used to model the turbine wakes.

- The cumulative wake of multiple wind turbines under a pressure gradient was experimentally investigated. A new analytical approach to model the cumulative wake of multiple turbines was proposed. The new approach accounts for the effect of the pressure gradient imposed by the upstream turbine(s) on the wake velocity deficit of a downstream one. It also eliminates the need for superposition of wake velocity deficit of standalone turbines and was shown to work for wind farms in flat and complex terrain.

- For roof-mounted wind turbines in an urban environment, the effect of roof edge shape on the power and wake of a wind turbine was investigated. The turbine on a roof with a rounded edge shape performed best, whereas the one on a roof with a solid boundary fence performed worst. The turbine wake was also shown to be affected by the roof edge shape. As boundary fences are an integral part of building safety, a parametric study on the effect of fence shape on the performance of a wind turbine was performed. The study revealed that several fence shapes, including inward-angled and outward-curved shapes, significantly improved the turbine performance.

10.2   Future perspectives

The work carried out within this thesis can be expanded into multiple dimensions. Some interesting areas of future research are suggested below:

- All work carried out in this thesis was under neutral atmospheric stability. In reality, the atmosphere is predominantly either under stable or convective stability. The work done under neutral conditions is a good starting point, and most often the only possibility in wind-tunnel studies. However, with the new thermal control system at the WiRE wind tunnel, it is possible to develop stable and convective boundary layers. It will, therefore, be of great interest if some of the studies performed in this thesis are extended to different thermal stability conditions. In this context, a validation of the analytical modeling framework under different types of thermal stability will also be useful for low-order modeling of wind turbine wakes in different atmospheric conditions.

- In terms of terrain, two-dimensional topographical features such as escarpments and ramps were considered in this thesis. Three-dimensional hills are another important topographical feature. Therefore, A natural extension of the current work will be to study wind turbine wakes on symmetric and asymmetric three-dimensional hills. In addition, the topography is often multi-scale, therefore, it will be interesting to investigate wind turbine wakes on multi-scale topography.

- For urban wind energy, a single high-rise building surrounded by an urban canopy was used. It is important to consider the effect of surrounding buildings with comparable heights on the performance of a wind turbine sited on a high-rise building. In addition, a case study resembling a real urban terrain can provide useful insights into the effect of surrounding buildings on the performance of a roof-mounted wind turbine.

Bibliography

Abkar, M., & Porté-Agel, F. (2014). Mean and turbulent kinetic energy budgets inside and above very large wind farms under conventionally-neutral condition. *Renewable Energy, 70,* 142–152.

Abkar, M., & Porté-Agel, F. (2015). Influence of atmospheric stability on wind-turbine wakes: a large-eddy simulation study. *Physics of fluids, 27*(3).

Abkar, M., & Porté-Agel, F. (2016). Influence of the coriolis force on the structure and evolution of wind turbine wakes. *Physical Review Fluids, 1*(6), 063701.

Abkar, M., Sharifi, A., & Porté-Agel, F. (2016). Wake flow in a wind farm during a diurnal cycle. *Journal of Turbulence, 17*(4), 420–441.

Abkar, M., Sørensen, J. N., & Porté-Agel, F. (2018). An analytical model for the effect of vertical wind veer on wind turbine wakes. *Energies, 11*(7), 1838.

Abohela, I., Hamza, N., & Dudek, S. (2013). Effect of roof shape, wind direction, building height and urban configuration on the energy yield and positioning of roof mounted wind turbines. *Renewable Energy, 50,* 1106–1118.

Alfredsson, P. H., & Segalini, A. (2017). Introduction wind farms in complex terrains: an introduction. *Philosophical Transactions of the Royal Society A, 375*(2091), 20160096.

Allaerts, D., & Meyers, J. (2015). Large eddy simulation of a large wind-turbine array in a conventionally neutral atmospheric boundary layer. *Physics of Fluids, 27*(6).

Al-Quraan, A., Stathopoulos, T., & Pillay, P. (2016). Comparison of wind tunnel and on site measurements for urban wind energy estimation of potential yield. *Journal of Wind Engineering and Industrial Aerodynamics, 158,* 1–10.

Astolfi, D., Castellani, F., & Terzi, L. (2018). A study of wind turbine wakes in complex terrain through rans simulation and scada data. *Journal of Solar Energy Engineering, 140*(3), 031001.

Awasthi, M., Devenport, W. J., Glegg, S. A. L., & Forest, J. B. (2014). Pressure fluctuations produced by forward steps immersed in a turbulent boundary layer. *Journal of Fluid Mechanics, 756,* 384–421.

Baidya Roy, S., Pacala, S. W., & Walko, R. L. (2004). Can large wind farms affect local meteorology? *Journal of Geophysical Research: Atmospheres, 109*(D19).

Barthelmie, R. J., & Pryor, S. C. (2019). Automated wind turbine wake characterization in complex terrain. *Atmospheric Measurement Techniques, 12*(6), 3463–3484.

Barthelmie, R. J., & Pryor, S. (2018). The impact of wind direction yaw angle on cliff flows. *Wind Energy, 21*(12), 1254–1265.

Barthelmie, R. J., Wang, H., Doubrawa, P., Giroux, G., & Pryor, S. C. (2016). Effects of an escarpment on flow parameters of relevance to wind turbines. *Wind Energy, 19*(12), 2271–2286.

Bastankhah, M., & Porté-Agel, F. (2014). A new analytical model for wind-turbine wakes. *Renewable Energy, 70*, 116–123.

Bastankhah, M., & Porté-Agel, F. (2016). Experimental and theoretical study of wind turbine wakes in yawed conditions. *Journal of Fluid Mechanics, 806*, 506–541.

Bastankhah, M., & Porté-Agel, F. (2017a). A new miniature wind turbine for wind tunnel experiments. part i: design and performance. *Energies, 10*(7), 908.

Bastankhah, M., & Porté-Agel, F. (2017b). Wind tunnel study of the wind turbine interaction with a boundary-layer flow: upwind region, turbine performance, and wake region. *Physics of Fluids, 29*(6).

Bastankhah, M., & Porté-Agel, F. (2017c). A new miniature wind turbine for wind tunnel experiments. part ii: wake structure and flow dynamics. *Energies, 10*(7), 923.

Bastankhah, M., Welch, B. L., Martínez-Tossas, L. A., King, J., & Fleming, P. (2021). Analytical solution for the cumulative wake of wind turbines in wind farms. *Journal of Fluid Mechanics, 911*, A53.

Bastine, D., Witha, B., Wächter, M., & Peinke, J. (2015). Towards a simplified dynamic wake model using pod analysis. *Energies, 8*(2), 895–920.

Bayoumi, M., Fink, D., & Hausladen, G. (2013). Extending the feasibility of high-rise façade augmented wind turbines. *Energy and buildings, 60*, 12–19.

Bechmann, A., Sørensen, N. N., Berg, J., Mann, J., & Réthoré, P.-E. (2011). The bolund experiment, part ii: blind comparison of microscale flow models. *Boundary-Layer Meteorology, 141*(2), 245–271.

Bempedelis, N., & Steiros, K. (2022). Analytical all-induction state model for wind turbine wakes. *Physical Review Fluids, 7*(3), 034605.

Berg, J., Mann, J., Bechmann, A., Courtney, M. S., & Jørgensen, H. E. (2011). The bolund experiment, part i: flow over a steep, three-dimensional hill. *Boundary-Layer Meteorology, 141*(2), 219–243.

Berg, J., Troldborg, N., Sørensen, N. N., Patton, E., & Sullivan, P. P. (2017). Large-eddy simulation of turbine wake in complex terrain. *Journal of Physics: Conference Series, 854*(1), 012003.

Bergeles, G., & Athanassiadis, N. (1983). The flow past a surface-mounted obstacle. *Journal of Fluids Engineering, 105*, 461–463.

Bhaganagar, K., & Debnath, M. (2014). Implications of stably stratified atmospheric boundary layer turbulence on the near-wake structure of wind turbines. *Energies, 7*(9), 5740–5763.

Bianchi, S., Bianchini, A., Ferrara, G., & Ferrari, L. (2014). Small wind turbines in the built environment: influence of flow inclination on the potential energy yield. *Journal of Turbomachinery, 136*(4), 041013.

Bossuyt, J., Scott, R., Ali, N., & Cal, R. B. (2021). Quantification of wake shape modulation and deflection for tilt and yaw misaligned wind turbines. *Journal of Fluid Mechanics, 917.*

Bowen, A. J., & Lindley, D. (1977). A wind-tunnel investigation of the wind speed and turbulence characteristics close to the ground over various escarpment shapes. *Boundary-Layer Meteorology, 12*, 259–271.

Britter, R. E., Hunt, J. C. R., & Richards, K. J. (1981). Air flow over a two-dimensional hill: studies of velocity speed-up, roughness effects and turbulence. *Quarterly Journal of the Royal Meteorological Society, 107*(451), 91–110.

Brogna, R., Feng, J., Sørensen, J. N., Shen, W. Z., & Porté-Agel, F. (2020). A new wake model and comparison of eight algorithms for layout optimization of wind farms in complex terrain. *Applied energy, 259*, 114189.

Brugger, P., Fuertes, F., Vahidzadeh, M., Markfort, C., & Porté-Agel, F. (2019). Characterization of wind turbine wakes with nacelle-mounted doppler lidars and model validation in the presence of wind veer. *Remote Sensing, 11*(19), 2247.

Cai, T., Cheng, S., Segalini, A., & Chamorro, L. P. (2021). Local topography-induced pressure gradient effects on the wake and power output of a model wind turbine. *Theoretical and Applied Mechanics Letters, 11*(5), 100297.

Calaf, M., Higgins, C., & Parlange, M. B. (2014). Large wind farms and the scalar flux over an heterogeneously rough land surface. *Boundary-layer meteorology, 153*, 471–495.

Calaf, M., Meneveau, C., & Meyers, J. (2010). Large eddy simulation study of fully developed wind-turbine array boundary layers. *Physics of fluids, 22*(1).

Camp, E. H., & Cal, R. B. (2016). Mean kinetic energy transport and event classification in a model wind turbine array versus an array of porous disks: energy budget and octant analysis. *Physical Review Fluids, 1*(4), 044404.

Castro, I. P., Cheng, H., & Reynolds, R. (2006). Turbulence over urban-type roughness: deductions from wind-tunnel measurements. *Boundary-Layer Meteorology, 118*, 109–131.

Chamorro, L. P., Arndt, R. E. A., & Sotiropoulos, F. (2011). Turbulent flow properties around a staggered wind farm. *Boundary-layer meteorology, 141*, 349–367.

Chamorro, L. P., Arndt, R. E. A., & Sotiropoulos, F. (2012). Reynolds number dependence of turbulence statistics in the wake of wind turbines. *Wind Energy, 15*(5), 733–742.

Chamorro, L. P., & Porté-Agel, F. (2009). A wind-tunnel investigation of wind-turbine wakes: boundary-layer turbulence effects. *Boundary-layer meteorology, 132*, 129–149.

Chamorro, L. P., & Porté-Agel, F. (2010). Effects of thermal stability and incoming boundary-layer flow characteristics on wind-turbine wakes: a wind-tunnel study. *Boundary-layer meteorology, 136*, 515–533.

Cheng, W.-C., & Porté-Agel, F. (2015). Adjustment of turbulent boundary-layer flow to idealized urban surfaces: a large-eddy simulation study. *Boundary-Layer Meteorology, 155*(2), 249–270.

Cheng, W.-C., & Porté-Agel, F. (2018). A simple physically-based model for wind-turbine wake growth in a turbulent boundary layer. *Boundary-Layer Meteorology, 169*, 1–10.

Clark, T. L. (1977). A small-scale dynamic model using a terrain-following coordinate transformation. *Journal of Computational Physics, 24*(2), 186–215.

Commission, I. E., et al. (2005). Wind turbines-part 12-1: power performance measurements of electricity producing wind turbines. *IEC 61400-12-1.*

Cooney, C., Byrne, R., Lyons, W., & O'Rourke, F. (2017). Performance characterisation of a commercial-scale wind turbine operating in an urban environment, using real data. *Energy for Sustainable Development, 36*, 44–54.

Council, G. W. E. (2020). Gwec global wind report 2019. *Global Wind Energy Council: Bonn, Germany.*

Crespo, A., Manuel, F., Grau, J. C., Hernández, J., Garrad, A., Palz, W., & Scheller, S. (1993). Modelization of wind farms in complex terrain. application to the monteahumada wind farm. *Proceedings of the 1993 European community wind energy conference, Travemünde, Germany*, 436–439.

Crespo, A., Hernandez, J., & Frandsen, S. (1999). Survey of modelling methods for wind turbine wakes and wind farms. *Wind Energy: An International Journal for Progress and Applications in Wind Power Conversion Technology, 2*(1), 1–24.

Dai, J., Tan, Y., Yang, W., Wen, L., & Shen, X. (2017). Investigation of wind resource characteristics in mountain wind farm using multiple-unit scada data in chenzhou: a case study. *Energy conversion and management, 148*, 378–393.

Dai, S. F., Liu, H. J., & Peng, H. Y. (2022). Assessment of parapet effect on wind flow properties and wind energy potential over roofs of tall buildings. *Renewable Energy, 199*, 826–839.

Dar, A. S., Armengol Barcos, G., & Porté-Agel, F. (2022). An experimental investigation of a roof-mounted horizontal-axis wind turbine in an idealized urban environment. *Renewable Energy, 193*, 1049–1061.

Dar, A. S., Gertler, A. S., & Porté-Agel, F. (2023). An experimental and analytical study of wind turbine wakes under pressure gradient. *Physics of Fluids, 35*(4), 045140.

Dar, A. S., & Porté-Agel, F. (2020). Three-dimensional wind-turbine wake characterization via tomographic particle-image velocimetry. *Journal of Physics: Conference Series, 1618*(6), 062045.

Dar, A. S., & Porté-Agel, F. (2022a). An analytical model for wind turbine wakes under pressure gradient. *Energies, 15*(15), 5345.

Dar, A. S., & Porté-Agel, F. (2022b). Wind turbine wakes on escarpments: a wind-tunnel study. *Renewable Energy, 181*, 1258–1275.

Dar, A. S., Berg, J., Troldborg, N., & Patton, E. G. (2019). On the self-similarity of wind turbine wakes in a complex terrain using large eddy simulation. *Wind Energy Science, 4*(4), 633–644.

Desa, U., et al. (2016). Transforming our world: the 2030 agenda for sustainable development.

de Sá S., F. I. P., Oliveira, J. L. G., & Passos, J. C. (2022). Impact of atmospheric stability, wake effect and topography on power production at complex-terrain wind farm. *Energy, 239*, 122211.

Deshpande, R., & Marusic, I. (2021). Characterising momentum flux events in high reynolds number turbulent boundary layers. *Fluids, 6*(4), 168.

Diebold, M., Higgins, C., Fang, J., Bechmann, A., & Parlange, M. (2013). Flow over hills: a large-eddy simulation of the bolund case. *Boundary-Layer Meteorology, 148*(1), 177–194.

Division, U. N. P. (2001). World urbanization prospects (no. 216). *United Nations, Department of International Economic and Social Affairs.*

Drew, D., Barlow, J., & Cockerill, T. (2013). Estimating the potential yield of small wind turbines in urban areas: a case study for greater london, uk. *Journal of Wind Engineering and Industrial Aerodynamics, 115*, 104–111.

Elgendi, M., AlMallahi, M., Abdelkhalig, A., & Selim, M. Y. (2023). A review of wind turbines in complex terrain. *International Journal of Thermofluids*, 100289.

Elsinga, G., Kuik, D. J., Van Oudheusden, B., & Scarano, F. (2007). Investigation of the three-dimensional coherent structures in a turbulent boundary layer with tomographic-piv. *45th AIAA aerospace sciences meeting and exhibit*, 1305.

Elsinga, G. E., Scarano, F., Wieneke, B., & van Oudheusden, B. W. (2006). Tomographic particle image velocimetry. *Experiments in fluids, 41*(6), 933–947.

EMBER. (2023). Global electricity review 2023.

Emejeamara, F., & Tomlin, A. (2020). A method for estimating the potential power available to building mounted wind turbines within turbulent urban air flows. *Renewable Energy, 153*, 787–800.

Emery, K. O., & Kuhn, G. G. (1982). Sea cliffs: their processes, profiles, and classification. *Geological Society of America Bulletin, 93*(7), 644–654.

Essel, E. E., & Tachie, M. F. (2017). Upstream roughness and reynolds number effects on turbulent flow structure over forward facing step. *International Journal of Heat and Fluid Flow, 66*, 226–242.

Evans, B., Parks, J., & Theobald, K. (2011). Urban wind power and the private sector: community benefits, social acceptance and public engagement. *Journal of environmental planning and management, 54*(2), 227–244.

Fan, X., Ge, M., Tan, W., & Li, Q. (2021). Impacts of coexisting buildings and trees on the performance of rooftop wind turbines: an idealized numerical study. *Renewable Energy, 177*, 164–180.

Farrell, A., King, J., Draxl, C., Mudafort, R., Hamilton, N., Bay, C. J., Fleming, P., & Simley, E. (2021). Design and analysis of a wake model for spatially heterogeneous flow. *Wind Energy Science, 6*(3), 737–758.

Fernando, H. J. S., Mann, J., Palma, J. M. L. M., Lundquist, J. K., Barthelmie, R. J., Belo-Pereira, M., Brown, W. O. J., Chow, F. K., Gerz, T., Hocut, C. M., et al. (2019). The perdigão: peering into microscale details of mountain winds. *Bulletin of the American Meteorological Society, 100*(5), 799–819.

Finnigan, J., Ayotte, K., Harman, I., Katul, G., Oldroyd, H., Patton, E., Poggi, D., Ross, A., & Taylor, P. (2020). Boundary-layer flow over complex topography. *Boundary-Layer Meteorology, 177*(2), 247–313.

Frandsen, S., Barthelmie, R. J., Pryor, S., Rathmann, O., Larsen, S., Højstrup, J., & Thøgersen, M. (2006). Analytical modelling of wind speed deficit in large offshore wind farms.

Wind Energy: An International Journal for Progress and Applications in Wind Power Conversion Technology, 9(1-2), 39–53.

Frandsen, S. (2007). Turbulence and turbulence-generated structural loading in wind turbine clusters. *Risoe*, RISO-R–1188(EN).

Ge, M., Gayme, D. F., & Meneveau, C. (2021). Large-eddy simulation of wind turbines immersed in the wake of a cube-shaped building. *Renewable Energy, 163*, 1063–1077.

Ge, M., Zhang, S., Meng, H., & Ma, H. (2020). Study on interaction between the wind-turbine wake and the urban district model by large eddy simulation. *Renewable Energy, 157*, 941–950.

Ghaemi, S., & Scarano, F. (2011). Counter-hairpin vortices in the turbulent wake of a sharp trailing edge. *Journal of Fluid Mechanics, 689*, 317–356.

Göçmen, T., Van der Laan, P., Réthoré, P.-E., Diaz, A. P., Larsen, G. C., & Ott, S. (2016). Wind turbine wake models developed at the technical university of denmark: a review. *Renewable and Sustainable Energy Reviews, 60*, 752–769.

Gong, W., Taylor, P. A., & Dörnbrack, A. (1996). Turbulent boundary-layer flow over fixed aerodynamically rough two-dimensional sinusoidal waves. *Journal of Fluid Mechanics, 312*, 1–37.

Graziani, A., Kerhervé, F., Martinuzzi, R. J., & Keirsbulck, L. (2018). Dynamics of the recirculating areas of a forward-facing step. *Experiments in Fluids, 59*(10), 1–18.

Graziani, A., Lippert, M., Uystepruyst, D., & Keirsbulck, L. (2017). Scaling and flow dependencies over forward-facing steps. *International Journal of Heat and Fluid Flow, 67*, 220–229.

Grieser, B., Sunak, Y., & Madlener, R. (2015). Economics of small wind turbines in urban settings: an empirical investigation for germany. *Renewable Energy, 78*, 334–350.

GWEC. (2021). Global wind report 2021. *Global wind energy council.*

GWEC. (2022). Global wind report 2022. *Global wind energy council.*

GWEC. (2023). Global wind report 2023. *Global wind energy council.*

Haller, G. (2005). An objective definition of a vortex. *Journal of fluid mechanics, 525*, 1–26.

Han, X., Liu, D., Xu, C., & Shen, W. Z. (2018). Atmospheric stability and topography effects on wind turbine performance and wake properties in complex terrain. *Renewable energy, 126*, 640–651.

Hansen, M. (2015). *Aerodynamics of wind turbines*. Routledge.

Helmis, C. G., Papadopoulos, K. H., Asimakopoulos, D. N., Papageorgas, P. G., & Soilemes, A. T. (1995). An experimental study of the near-wake structure of a wind turbine operating over complex terrain. *Solar energy, 54*(6), 413–428.

Herman, G. T., & Lent, A. (1976). Iterative reconstruction algorithms. *Computers in biology and medicine, 6*(4), 273–294.

Hesp, P. A., & Smyth, T. A. G. (2021). Cfd flow dynamics over model scarps and slopes. *Physical Geography, 42*(1), 1–24.

Higgins, S., & Stathopoulos, T. (2021). Application of artificial intelligence to urban wind energy. *Building and Environment, 197*, 107848.

Hill, P. G., Schaub, U. W., & Senoo, Y. (1963). Turbulent wakes in pressure gradients. *Journal of Applied Mechanics, 30*(4), 518–524.

Howard, K. B., Singh, A., Sotiropoulos, F., & Guala, M. (2015). On the statistics of wind turbine wake meandering: an experimental investigation. *Physics of Fluids, 27*(7).

Howland, M. F., Bossuyt, J., Martínez-Tossas, L. A., Meyers, J., & Meneveau, C. (2016). Wake structure in actuator disk models of wind turbines in yaw under uniform inflow conditions. *Journal of Renewable and Sustainable Energy, 8*(4).

Hu, H., Yang, Z., & Sarkar, P. (2012). Dynamic wind loads and wake characteristics of a wind turbine model in an atmospheric boundary layer wind. *Experiments in fluids, 52,* 1277–1294.

Hu, W., Yang, Q., Chen, H.-P., Guo, K., Zhou, T., Liu, M., Zhang, J., & Yuan, Z. (2022). A novel approach for wind farm micro-siting in complex terrain based on an improved genetic algorithm. *Energy, 251,* 123970.

Hunt, J. C. R., Leibovich, S., & Richards, K. J. (1988). Turbulent shear flows over low hills. *Quarterly Journal of the Royal Meteorological Society, 114*(484), 1435–1470.

Hwangbo, H., Johnson, A. L., & Ding, Y. (2018). Spline model for wake effect analysis: characteristics of a single wake and its impacts on wind turbine power generation. *IISE Transactions, 50*(2), 112–125.

Hyvärinen, A., & Segalini, A. (2017a). Effects from complex terrain on wind-turbine performance. *Journal of Energy Resources Technology, 139*(5).

Hyvärinen, A., & Segalini, A. (2017b). Qualitative analysis of wind-turbine wakes over hilly terrain. *Journal of Physics: Conference Series, 854*(1), 012023.

IEC, I. (2005). 61400-1: wind turbines part 1: design requirements. *International Electrotechnical Commission, 177.*

IRENA. (2020). The international renewable energy agency, abu dhabi. *Renewable Power Generation Costs in 2019.*

IRENA. (2021). Renewable power generation costs in 2020. report.

Ishihara, T., Hibi, K., & Oikawa, S. (1999). A wind tunnel study of turbulent flow over a three-dimensional steep hill. *Journal of Wind Engineering and Industrial Aerodynamics, 83*(1-3), 95–107.

Ishihara, T., & Qian, G.-W. (2018). A new gaussian-based analytical wake model for wind turbines considering ambient turbulence intensities and thrust coefficient effects. *Journal of Wind Engineering and Industrial Aerodynamics, 177,* 275–292.

Jackson, P. S., & Hunt, J. C. R. (1975). Turbulent wind flow over a low hill. *Quarterly Journal of the Royal Meteorological Society, 101*(430), 929–955.

Jensen, N. O. (1983). A note on wind generator interaction.

Jooss, Y., Bolis, R., Bracchi, T., & Hearst, R. J. (2022a). Flow field and performance of a vertical-axis wind turbine on model buildings. *Flow, 2,* E10.

Jooss, Y., Rønning, E. B., Hearst, R. J., & Bracchi, T. (2022b). Influence of position and wind direction on the performance of a roof mounted vertical axis wind turbine. *Journal of Wind Engineering and Industrial Aerodynamics, 230,* 105177.

Juan, Y.-H., Rezaeiha, A., Montazeri, H., Blocken, B., Wen, C.-Y., & Yang, A.-S. (2022). Cfd assessment of wind energy potential for generic high-rise buildings in close proximity: impact of building arrangement and height. *Applied Energy, 321*, 119328.

Juan, Y.-H., Wen, C.-Y., Li, Z., & Yang, A.-S. (2021). Impacts of urban morphology on improving urban wind energy potential for generic high-rise building arrays. *Applied Energy, 299*, 117304.

Kaldellis, J. K., Triantafyllou, P., & Stinis, P. (2021). Critical evaluation of wind turbines' analytical wake models. *Renewable and Sustainable Energy Reviews, 144*, 110991.

Katic, I., Højstrup, J., & Jensen, N. O. (1986). A simple model for cluster efficiency. *European wind energy association conference and exhibition, 1*, 407–410.

Kilpatrick, R., Hangan, H., Siddiqui, K., Parvu, D., Lange, J., Mann, J., & Berg, J. (2016). Effect of reynolds number and inflow parameters on mean and turbulent flow over complex topography. *Wind Energy Science, 1*(2), 237–254.

Kiya, M., & Sasaki, K. (1983). Structure of a turbulent separation bubble. *Journal of Fluid Mechanics, 137*, 83–113.

Kooiman, S., & Tullis, S. (2010). Response of a vertical axis wind turbine to time varying wind conditions found within the urban environment. *Wind Engineering, 34*(4), 389–401.

Lange, J., Mann, J., Berg, J., Parvu, D., Kilpatrick, R., Costache, A., Chowdhury, J., Siddiqui, K., & Hangan, H. (2017). For wind turbines in complex terrain, the devil is in the detail. *Environmental Research Letters, 12*(9), 094020.

Lanzilao, L., & Meyers, J. (2022). A new wake-merging method for wind-farm power prediction in the presence of heterogeneous background velocity fields. *Wind Energy, 25*(2), 237–259.

Largeau, J. F., & Moriniere, V. (2007). Wall pressure fluctuations and topology in separated flows over a forward-facing step. *Experiments in Fluids, 42*(1), 21–40.

Ledo, L., Kosasih, P., & Cooper, P. (2011). Roof mounting site analysis for micro-wind turbines. *Renewable energy, 36*(5), 1379–1391.

Lee, J. H., & Chu, V. (2012). *Turbulent jets and plumes: a lagrangian approach* (Vol. 1). Springer Science & Business Media.

Li, L., Huang, Z., Ge, M., & Zhang, Q. (2022). A novel three-dimensional analytical model of the added streamwise turbulence intensity for wind-turbine wakes. *Energy, 238*, 121806.

Li, S., Li, Y., Yang, C., Wang, Q., Zhao, B., Li, D., Zhao, R., Ren, T., Zheng, X., Gao, Z., et al. (2021). Experimental investigation of solidity and other characteristics on dual vertical axis wind turbines in an urban environment. *Energy Conversion and Management, 229*, 113689.

Lissaman, P. B. S. (1979). Energy effectiveness of arbitrary arrays of wind turbines. *Journal of Energy, 3*(6), 323–328.

Liu, L., & Stevens, R. J. A. M. (2020a). Effects of two-dimensional steep hills on the performance of wind turbines and wind farms. *Boundary-Layer Meteorology, 176*, 251–269.

Liu, L., & Stevens, R. J. A. M. (2020b). Wall modeled immersed boundary method for high reynolds number flow over complex terrain. *Computers & Fluids, 208*, 104604.

Liu, L., & Stevens, R. J. A. M. (2021). Effects of atmospheric stability on the performance of a wind turbine located behind a three-dimensional hill. *Renewable Energy, 175*, 926–935.

Liu, X., Thomas, F. O., & Nelson, R. C. (2002). An experimental investigation of the planar turbulent wake in constant pressure gradient. *Physics of Fluids, 14*(8), 2817–2838.

Liu, Z., Lu, S., & Ishihara, T. (2021). Large eddy simulations of wind turbine wakes in typical complex topographies. *Wind Energy, 24*(8), 857–886.

Longo, R., Nicastro, P., Natalini, M., Schito, P., Mereu, R., & Parente, A. (2020). Impact of urban environment on savonius wind turbine performance: a numerical perspective. *Renewable energy, 156*, 407–422.

Lopez, D., Kuo, J., & Li, N. (2019). A novel wake model for yawed wind turbines. *Energy, 178*, 158–167.

Lutz, T., Schulz, C., Letzgus, P., & Rettenmeier, A. (2017). Impact of complex orography on wake development: simulation results for the planned windfors test site. *Journal of Physics: Conference Series, 854*(1), 012029.

Mann, J., Angelou, N., Arnqvist, J., Callies, D., Cantero, E., Arroyo, R. C., Courtney, M., Cuxart, J., Dellwik, E., Gottschall, J., et al. (2017). Complex terrain experiments in the new european wind atlas. *Philosophical Transactions of the Royal Society A: Mathematical, Physical and Engineering Sciences, 375*(2091), 20160101.

Manwell, J. F., McGowan, J. G., & Rogers, A. L. (2010). *Wind energy explained: theory, design and application.* John Wiley & Sons.

Mason, P. J. (1994). Large-eddy simulation: a critical review of the technique. *Quarterly Journal of the Royal Meteorological Society, 120*(515), 1–26.

Mason, P. J., & Sykes, R. I. (1979). Flow over an isolated hill of moderate slope. *Quarterly Journal of the Royal Meteorological Society, 105*(444), 383–395.

Mattuella, J., Loredo-Souza, A., Oliveira, M., & Petry, A. (2016). Wind tunnel experimental analysis of a complex terrain micrositing. *Renewable and Sustainable Energy Reviews, 54*, 110–119.

Medici, D., & Alfredsson, P. H. (2006). Measurements on a wind turbine wake: 3d effects and bluff body vortex shedding. *Wind Energy: An International Journal for Progress and Applications in Wind Power Conversion Technology, 9*(3), 219–236.

Menke, R., Vasiljević, N., Hansen, K. S., Hahmann, A. N., & Mann, J. (2018). Does the wind turbine wake follow the topography? a multi-lidar study in complex terrain. *Wind Energy Science, 3*(2), 681–691.

Micallef, D., & Van Bussel, G. (2018). A review of urban wind energy research: aerodynamics and other challenges. *Energies, 11*(9), 2204.

Mickle, R. E., Cook, N. J., Hoff, A. M., Jensen, N. O., Salmon, J. R., Taylor, P. A., Tetzlaff, G., & Teunissen, H. W. (1988). The askervein hill project: vertical profiles of wind and turbulence. *Boundary-Layer Meteorology, 43*, 143–169.

Mithraratne, N. (2009). Roof-top wind turbines for microgeneration in urban houses in new zealand. *Energy and Buildings, 41*(10), 1013–1018.

Nai-Zhi, G., Ming-Ming, Z., & Bo, L. (2022). A data-driven analytical model for wind turbine wakes using machine learning method. *Energy Conversion and Management, 252,* 115130.

Nakayama, A. (1987). Curvature and pressure-gradient effects on a small-defect wake. *Journal of Fluid Mechanics, 175,* 215–246.

Nedjari, H. D., Guerri, O., & Saighi, M. (2017). Cfd wind turbines wake assessment in complex topography. *Energy conversion and management, 138,* 224–236.

Niayifar, A., & Porté-Agel, F. (2016). Analytical modeling of wind farms: a new approach for power prediction. *Energies, 9*(9), 741.

Pagnini, L. C., Burlando, M., & Repetto, M. P. (2015). Experimental power curve of small-size wind turbines in turbulent urban environment. *Applied Energy, 154,* 112–121.

Pearse, J. R., Lindley, D., & Stevenson, D. C. (1981). Wind flow over ridges in simulated atmospheric boundary layers. *Boundary-Layer Meteorology, 21,* 77–92.

Pellegrini, M., Guzzini, A., & Saccani, C. (2021). Experimental measurements of the performance of a micro-wind turbine located in an urban area. *Energy Reports, 7,* 3922–3934.

Politis, E. S., Prospathopoulos, J., Cabezon, D., Hansen, K. S., Chaviaropoulos, P. K., & Barthelmie, R. J. (2012). Modeling wake effects in large wind farms in complex terrain: the problem, the methods and the issues. *Wind Energy, 15*(1), 161–182.

Pope, S. B. (2000). *Turbulent flows.* Cambridge university press.

Porté-Agel, F., Bastankhah, M., & Shamsoddin, S. (2020). Wind-turbine and wind-farm flows: a review. *Boundary-Layer Meteorology, 174*(1), 1–59.

Porté-Agel, F., Wu, Y.-T., & Chen, C.-H. (2013). A numerical study of the effects of wind direction on turbine wakes and power losses in a large wind farm. *Energies, 6*(10), 5297–5313.

Porté-Agel, F., Wu, Y.-T., Lu, H., & Conzemius, R. J. (2011). Large-eddy simulation of atmospheric boundary layer flow through wind turbines and wind farms. *Journal of Wind Engineering and Industrial Aerodynamics, 99*(4), 154–168.

Qian, G.-W., & Ishihara, T. (2019). Numerical study of wind turbine wakes over escarpments by a modified delayed detached eddy simulation. *Journal of Wind Engineering and Industrial Aerodynamics, 191,* 41–53.

Radünz, W. C., Sakagami, Y., Haas, R., Petry, A. P., Passos, J. C., Miqueletti, M., & Dias, E. (2021). Influence of atmospheric stability on wind farm performance in complex terrain. *Applied Energy, 282,* 116149.

Radünz, W. C., Sakagami, Y., Haas, R., Petry, A. P., Passos, J. C., Miqueletti, M., & Dias, E. (2020). The variability of wind resources in complex terrain and its relationship with atmospheric stability. *Energy Conversion and Management, 222,* 113249.

Ren, H., & Wu, Y. (2011). Turbulent boundary layers over smooth and rough forward-facing steps. *Physics of Fluids, 23*(4), 045102.

Rezaeiha, A., Montazeri, H., & Blocken, B. (2020). A framework for preliminary large-scale urban wind energy potential assessment: roof-mounted wind turbines. *Energy Conversion and Management, 214,* 112770.

Ritchie, H., & Roser, M. (2018). Urbanization. *Our world in data.*

Rogers, M. M. (2002). The evolution of strained turbulent plane wakes. *Journal of Fluid Mechanics, 463*, 53–120.

Rolin, V. F. C., & Porté-Agel, F. (2018). Experimental investigation of vertical-axis wind-turbine wakes in boundary layer flow. *Renewable energy, 118*, 1–13.

Rowcroft, J., Burton, D., Blackburn, H. M., & Sheridan, J. (2016). Siting wind turbines near cliffs—the effect of wind direction. *Wind Energy, 19*(8), 1469–1484.

Rowcroft, J., Burton, D., Blackburn, H. M., & Sheridan, J. (2019). Siting wind turbines near cliffs: the effect of ruggedness. *Journal of Fluids Engineering, 141*(3), 031104.

Roy, S. B. (2011). Simulating impacts of wind farms on local hydrometeorology. *Journal of Wind Engineering and Industrial Aerodynamics, 99*(4), 491–498.

Ruiz, C. A., Kalkman, I., & Blocken, B. (2021). Aerodynamic design optimization of ducted openings through high-rise buildings for wind energy harvesting. *Building and Environment, 202*, 108028.

Sanderse, B. (2009). *Aerodynamics of wind turbine wakes: literature review.* ECN.

Schulz, C., Klein, L., Weihing, P., & Lutz, T. (2016). Investigations into the interaction of a wind turbine with atmospheric turbulence in complex terrain. *Journal of Physics: Conference Series, 753*(3), 032016.

Shamsoddin, S., & Porté-Agel, F. (2017a). Turbulent planar wakes under pressure gradient conditions. *Journal of Fluid Mechanics, 830.*

Shamsoddin, S., & Porté-Agel, F. (2018a). A model for the effect of pressure gradient on turbulent axisymmetric wakes. *Journal of Fluid Mechanics, 837.*

Shamsoddin, S., & Porté-Agel, F. (2018b). Wind turbine wakes over hills. *Journal of Fluid Mechanics, 855*, 671–702.

Shamsoddin, S., & Porté-Agel, F. (2017b). Large-eddy simulation of atmospheric boundary-layer flow through a wind farm sited on topography. *Boundary-layer meteorology, 163*, 1–17.

Shapiro, C. R., Starke, G. M., Meneveau, C., & Gayme, D. F. (2019). A wake modeling paradigm for wind farm design and control. *Energies, 12*(15), 2956.

Sherry, M., Jacono, D. L., & Sheridan, J. (2010). An experimental investigation of the recirculation zone formed downstream of a forward facing step. *Journal of Wind Engineering and Industrial Aerodynamics, 98*(12), 888–894.

Siedersleben, S. K., Lundquist, J. K., Platis, A., Bange, J., Bärfuss, K., Lampert, A., Cañadillas, B., Neumann, T., & Emeis, S. (2018). Micrometeorological impacts of offshore wind farms as seen in observations and simulations. *Environmental Research Letters, 13*(12), 124012.

Sørensen, J. N. (2016). *General momentum theory for horizontal axis wind turbines* (Vol. 4).

Stathopoulos, T., Alrawashdeh, H., Al-Quraan, A., Blocken, B., Dilimulati, A., Paraschivoiu, M., & Pilay, P. (2018). Urban wind energy: some views on potential and challenges. *Journal of Wind Engineering and Industrial Aerodynamics, 179*, 146–157.

Stefanatos, N. C., Voutsinas, S., Rados, K., Zervos, A., & Tsipouridis, J. L. (1994). A combined experimental and numerical investigation of wake effects in complex terrain. *Proc EWEC, 94*, 484–90.

Stevens, R. J. A. M., & Meneveau, C. (2017). Flow structure and turbulence in wind farms. *Annual Review of Fluid Mechanics, 49*, 311–339.

Stevens, R. J. A. M., Gayme, D. F., & Meneveau, C. (2015). Coupled wake boundary layer model of wind-farms. *Journal of renewable and sustainable energy, 7*(2).

Stevens, R. J. A. M., Gayme, D. F., & Meneveau, C. (2016). Generalized coupled wake boundary layer model: applications and comparisons with field and les data for two wind farms. *Wind Energy, 19*(11), 2023–2040.

Stull, R. B. (1988). *An introduction to boundary layer meteorology* (Vol. 13). Springer Science & Business Media.

Sun, H., Gao, X., & Yang, H. (2019). Validations of three-dimensional wake models with the wind field measurements in complex terrain. *Energy, 189*, 116213.

Sykes, R. I. (1980). An asymptotic theory of incompressible turbulent boundary layer flow over a small hump. *Journal of Fluid Mechanics, 101*(3), 647–670.

Tabib, M., Rasheed, A., & Fuchs, F. (2016). Analyzing complex wake-terrain interactions and its implications on wind-farm performance. *Journal of Physics: Conference Series, 753*(3), 032063.

Takahashi, T., Kato, S., Murakami, S., Ooka, R., Yassin, M. F., & Kono, R. (2005). Wind tunnel tests of effects of atmospheric stability on turbulent flow over a three-dimensional hill. *Journal of Wind Engineering and Industrial Aerodynamics, 93*(2), 155–169.

Taylor, G. J., & Smith, D. (1991). Wake measurements over complex terrain. *Proceedings of the 13th BWEA Conference: Wind Energy Conversion*, 10–12.

Taylor, P. A., Mason, P. J., & Bradley, E. F. (1987). Boundary-layer flow over low hills. *Boundary-Layer Meteorology, 39*(1), 107–132.

Taylor, P. A., & Teunissen, H. W. (1987). The askervein hill project: overview and background data. *Boundary-Layer Meteorology, 39*(1), 15–39.

Thomas, F. O., & Liu, X. (2004). An experimental investigation of symmetric and asymmetric turbulent wake development in pressure gradient. *Physics of Fluids, 16*(5), 1725–1745.

Tian, W., Ozbay, A., Yuan, W., Sarakar, P., Hu, H., & Yuan, W. (2013). An experimental study on the performances of wind turbines over complex terrain. *51st AIAA aerospace sciences meeting including the new horizons forum and aerospace exposition*, 7–10.

Toja-Silva, F., Colmenar-Santos, A., & Castro-Gil, M. (2013). Urban wind energy exploitation systems: behaviour under multidirectional flow conditions—opportunities and challenges. *Renewable and Sustainable Energy Reviews, 24*, 364–378.

Toja-Silva, F., Lopez-Garcia, O., Peralta, C., Navarro, J., & Cruz, I. (2016). An empirical–heuristic optimization of the building-roof geometry for urban wind energy exploitation on high-rise buildings. *Applied energy, 164*, 769–794.

Toja-Silva, F., Peralta, C., Lopez-Garcia, O., Navarro, J., & Cruz, I. (2015). On roof geometry for urban wind energy exploitation in high-rise buildings. *Computation, 3*(2), 299–325.

Troldborg, N., Andersen, S. J., Hodgson, E. L., & Meyer Forsting, A. (2022). Brief communication: how does complex terrain change the power curve of a wind turbine? *Wind Energy Science, 7*(4), 1527–1532.

Troldborg, N., Sorensen, J. N., & Mikkelsen, R. (2010). Numerical simulations of wake characteristics of a wind turbine in uniform inflow. *Wind Energy: An International Journal for Progress and Applications in Wind Power Conversion Technology, 13*(1), 86–99.

Uchida, T. (2017). Cfd prediction of the airflow at a large-scale wind farm above a steep, three-dimensional escarpment. *Energy and Power Engineering, 9*(13), 829–842.

Vahidi, D., & Porté-Agel, F. (2022a). A new streamwise scaling for wind turbine wake modeling in the atmospheric boundary layer. *Energies, 15*(24), 9477.

Vahidi, D., & Porté-Agel, F. (2022b). A physics-based model for wind turbine wake expansion in the atmospheric boundary layer. *Journal of Fluid Mechanics, 943*, A49.

van der Laan, M. P., & Sørensen, N. N. (2017). Why the coriolis force turns a wind farm wake clockwise in the northern hemisphere. *Wind Energy Science, 2*(1), 285–294.

Van Sark, W. G., Van der Velde, H. C., Coelingh, J. P., & Bierbooms, W. A. (2019). Do we really need rotor equivalent wind speed? *Wind Energy, 22*(6), 745–763.

Veers, P., Dykes, K., Lantz, E., Barth, S., Bottasso, C. L., Carlson, O., Clifton, A., Green, J., Green, P., Holttinen, H., et al. (2019). Grand challenges in the science of wind energy. *Science, 366*(6464), eaau2027.

Vermeer, L. J., Sørensen, J. N., & Crespo, A. (2003). Wind turbine wake aerodynamics. *Progress in aerospace sciences, 39*(6-7), 467–510.

Vermeulen, P. E. J. (1980). An experimental analysis of wind turbine wakes. *3rd international symposium on wind energy systems*, 431–450.

Vogel, C. R., Willden, R. H. J., & Houlsby, G. T. (2018). Blade element momentum theory for a tidal turbine. *Ocean Engineering, 169*, 215–226.

Vollmer, L., Steinfeld, G., Heinemann, D., & Kühn, M. (2016). Estimating the wake deflection downstream of a wind turbine in different atmospheric stabilities: an les study. *Wind Energy Science, 1*(2), 129–141.

Voutsinas, S., Rados, K., & Zervos, A. (1990). On the analysis of wake effects in wind parks. *Wind Engineering*, 204–219.

Wagner, R., Cañadillas, B., Clifton, A., Feeney, S., Nygaard, N., Poodt, M., St Martin, C., Tüxen, E., & Wagenaar, J. (2014). Rotor equivalent wind speed for power curve measurement–comparative exercise for iea wind annex 32. *Journal of Physics: Conference Series, 524*(1), 012108.

Walker, S. L. (2011). Building mounted wind turbines and their suitability for the urban scale—a review of methods of estimating urban wind resource. *Energy and Buildings, 43*(8), 1852–1862.

Wan, F., & Porté-Agel, F. (2011). Large-eddy simulation of stably-stratified flow over a steep hill. *Boundary-layer meteorology, 138*, 367–384.

Wieneke, B. (2008). Volume self-calibration for 3d particle image velocimetry. *Experiments in fluids, 45*(4), 549–556.

Wieneke, B. (2015). Piv uncertainty quantification from correlation statistics. *Measurement Science and Technology, 26*(7), 074002.

Wu, Y.-T., & Porté-Agel, F. (2012). Atmospheric turbulence effects on wind-turbine wakes: an les study. *Energies, 5*(12), 5340–5362.

Xie, S., & Archer, C. (2015). Self-similarity and turbulence characteristics of wind turbine wakes via large-eddy simulation. *Wind Energy*, *18*(10), 1815–1838.

Xie, S., & Archer, C. L. (2017). A numerical study of wind-turbine wakes for three atmospheric stability conditions. *Boundary-Layer Meteorology*, *165*(1), 87–112.

Xu, D., Ayotte, K. W., & Taylor, P. A. (1994). Development of a non-linear mixed spectral finite difference model for turbulent boundary-layer flow over topography. *Boundary-Layer Meteorology*, *70*(4), 341–367.

Xu, W., Li, G., Zheng, X., Li, Y., Li, S., Zhang, C., & Wang, F. (2021a). High-resolution numerical simulation of the performance of vertical axis wind turbines in urban area: part i, wind turbines on the side of single building. *Renewable Energy*, *177*, 461–474.

Xu, W., Li, Y., Li, G., Li, S., Zhang, C., & Wang, F. (2021b). High-resolution numerical simulation of the performance of vertical axis wind turbines in urban area: part ii, array of vertical axis wind turbines between buildings. *Renewable Energy*, *176*, 25–39.

Yang, A.-S., Su, Y.-M., Wen, C.-Y., Juan, Y.-H., Wang, W.-S., & Cheng, C.-H. (2016). Estimation of wind power generation in dense urban area. *Applied Energy*, *171*, 213–230.

Yang, H., Lang, B., Du, B., Jin, Z., Li, B., & Ge, M. (2022). Effects of the steepness on the evolution of turbine wakes above continuous hilly terrain. *IET Renewable Power Generation*, *16*(6), 1170–1179.

Yang, X., Howard, K., Guala, M., & Sotiropoulos, F. (2015). Effects of a three-dimensional hill on the wake characteristics of a model wind turbine. *Physics of Fluids*, *27*(2), 025103.

Zehtabiyan-Rezaie, N., Iosifidis, A., & Abkar, M. (2022). Data-driven fluid mechanics of wind farms: a review. *Journal of Renewable and Sustainable Energy*, *14*(3).

Zhang, W., Markfort, C. D., & Porté-Agel, F. (2012). Near-wake flow structure downwind of a wind turbine in a turbulent boundary layer. *Experiments in fluids*, *52*, 1219–1235.

Zhang, Z., Huang, P., Bitsuamlak, G., & Cao, S. (2022). Large-eddy simulation of wind-turbine wakes over two-dimensional hills. *Physics of Fluids*.

Zhou, H., Lu, Y., Liu, X., Chang, R., & Wang, B. (2017). Harvesting wind energy in low-rise residential buildings: design and optimization of building forms. *Journal of Cleaner Production*, *167*, 306–316.

Zong, H., & Porté-Agel, F. (2020a). A point vortex transportation model for yawed wind turbine wakes. *Journal of Fluid Mechanics*, *890*.

Zong, H., & Porté-Agel, F. (2020b). A momentum-conserving wake superposition method for wind farm power prediction. *Journal of Fluid Mechanics*, *889*, A8.

Zou, Q., Li, Z., Zou, F., Zeng, X., Wang, C., & Pan, Y. (2021). A study on the characteristics of roof wind field by wind tunnel test. *Journal of Building Engineering*, *43*, 103155.

Arslan Salim Dar

Avenue du Léman 89
1005 - Lausanne
Switzerland

Phone: +41 77 95 89 829
E-mail: arslan.dar@epfl.ch

Research Interests

Turbulence, Wind Energy, Boundary Layers, Wakes, Experimental Fluid Mechanics.

Education

2019– 2023	**Doctor of Philosophy (Ph.D.) in Mechanical Engineering**
	Swiss Federal Institute of Technology Lausanne (EPFL), Switzerland
	Advisor: Prof. Fernando Porté-Agel.
2016– 2018	**European Wind Energy Master** - Dual Degree Program
	M.Sc. Engineering (Specialization: Wind Energy), Technical University of Denmark (Grade Average: 10.588/12.0)
	M.Sc. Engineering Physics, Carl von Ossietzky University of Oldenburg, Germany (Grade Average: 1.38/5.0)
2011– 2015	**B.Sc. Mechanical Engineering** - University of Engineering & Technology, Lahore, Pakistan
	CGPA: 3.611/4.0

Experience

Feb. 2019– Present	**Doctoral Assistant** - Wind Engineering and Renewable Energy Laboratory (WiRE), EPFL.
	Incharge and safety correspondent (COSEC) of Boundary-layer wind tunnel, WiRE, EPFL
	Teaching assistant for M.Sc. course ´Environmental Transport Phenomena' and B.Sc. course ´Engineering Fluid Mechanics'
	Supervised four M.Sc. thesis and two M.Sc. students for semester project/internship
Feb. 2017– June 2017	**Research Intern** - Energy Meteorology Group, ForWind, University of Oldenburg
July 2015–Oct. 2015 Sep. 2014–Dec. 2014	**Intern** - Alternate Energy Research & Innovation Lab, UET Lahore

Peer-reviewed Journal Publications

---

1. **Dar, A. S.**, Waridel, F. & Porté-Agel, F. Effect of roof fence shape on the flow over a building and its impact on wind turbine performance, *to be submitted.*

2. **Dar, A. S.**, & Porté-Agel, F. Wind turbine wake superposition under pressure gradient. *Physics of Fluids, under review.*

3. **Dar, A. S.**, & Porté-Agel, F. Influence of wind direction on the flow over a cliff and its interaction with a wind turbine wake. *Physical Review Fluids, under review.*

4. Duan, G., **Dar, A. S.**, & Porté-Agel, F. (2023). A wind tunnel study on cyclic yaw control: power performance and wake characteristics. *Energy Conversion and Management,* 293, 117445.

5. **Dar, A. S.**, Gertler, A. S., & Porté-Agel, F. (2023). An experimental and analytical study of wind turbine wakes under pressure gradient. *Physics of Fluids,* 35(4), 045140.

231

6. **Dar, A. S.**, & Porté-Agel, F. (2022). An analytical model for wind turbine wakes under pressure gradient. *Energies,* 15(15), 5345.

7. **Dar, A. S.**, Barcos, G. A., & Porté-Agel, F. (2022). An experimental investigation of a roof-mounted horizontal-axis wind turbine in an idealized urban environment. *Renewable Energy,* 193, 1049-1061.

8. **Dar, A. S.**, & Porté-Agel, F. (2022). Wind-turbine wakes on escarpments: a wind-tunnel study. *Renewable Energy,* 181, 1258-1275.

9. **Dar, A. S.**, Berg, J., Troldborg, N., & Patton, E. G. (2019). On the self-similarity of wind turbine wakes in a complex terrain using large eddy simulation. *Wind Energy Science,* 4(4), 633-644.

10. **Dar, A. S.**, & von Bremen, L. (2019). Short-term forecasting of wake-induced fluctuations in offshore wind farms. *Energies,* 12(14), 2833.

Peer-reviewed Conference Publications

1. **Dar, A. S.**, Majzoub, R. & Porté-Agel, F. The effect of rotor to nacelle size on the wake of a miniature wind turbine. *Journal of Physics: Conference Series, under review.*

2. **Dar, A. S.**, & Porté-Agel, F. (2020). Three-dimensional wind-turbine wake characterization via tomographic particle-image velocimetry. *Journal of Physics: Conference Series,* 1618, 062045.

Distinctions

Received Erasmus Mundus Scholarship for EWEM

Presentations & Exhibitions

April 2023	Represented WiRE at EPFL Open Doors.
Sept. 2022	Represented WiRE at ENAC 20 exhibition.
June 2022	Poster presentation at IIE Green Days on PhD thesis work.
May 2021	Oral presentation of the work on surface roughness effect in Wind Energy Science Conference 2021.
Sept. 2020	Oral presentation of the paper on tomo-PIV in Torque 2020 conference.

Skills

Experimental Techniques
Particle-image velocimetry | Laser-doppler velocimetry | Thermal anemometery | Cobra probe | Force measurements
Software
MATLAB | LabView | Latex | Ansys Fluent | WAsP | Solid Edge
Languages
English | Urdu | French (A1)